UNIVERSITY OF OKLAHOMA

GRADUATE COLLEGE

SIGNAL PROCESSING TECHNIQUES AND CONCEPT OF OPERATIONS
FOR POLARIMETRIC ROTATING PHASED ARRAY RADAR

A DISSERTATION

SUBMITTED TO THE GRADUATE FACULTY

in partial fulfillment of the requirements for the

Degree of

DOCTOR OF PHILOSOPHY

By

DAVID SCHVARTZMAN
Norman, Oklahoma
2020

SIGNAL PROCESSING TECHNIQUES AND CONCEPT OF OPERATIONS
FOR POLARIMETRIC ROTATING PHASED ARRAY RADAR

A DISSERTATION APPROVED FOR THE
SCHOOL OF ELECTRICAL AND COMPUTER ENGINEERING

BY THE COMMITTEE CONSISTING OF

Dr. Tian-You Yu, Chair

Dr. Sebastián Torres, Co-chair

Dr. Jorge Salazar

Dr. Mark Yeary

Dr. Ying Wang

Dedicated to my parents, José and Delia Schvartzman

Acknowledgments

"So I have just one wish for you – the good luck to be somewhere where you are free to maintain the kind of integrity I have described, and where you do not feel forced by a need to maintain your position in the organization, or financial support, or so on, to lose your integrity. May you have that freedom."

Richard P. Feynman

First and foremost I would like to express my deep gratitude to my advisers Dr. Sebastián Torres and Dr. Tian-You Yu. Through their continuous encouragement, I was able to overcome challenging research questions that allowed me to grow and mature as a scientist. I feel fortunate to have worked with such experienced and knowledgeable scientists. I always enjoyed our technical discussions and philosophical brainstorming sessions about advanced radar signal processing concepts. I am very grateful for all the time they invested reviewing my dissertation, and the feedback they provided which greatly enhanced the technical contributions of this dissertation. My ultimate professional goal is to become an innovative scientist in the radar field, all of which would some day be possible thanks to them.

I would like to thank and acknowledge Dr. Jorge Salazar, Dr. Mark Yeary, and Dr. Ying Wang; members of my Ph.D. committee who provided valuable feedback that improved the outcomes of this work. I appreciate their feedback and continuous encouragement throughout this journey, and I look forward to learning more from them in possible future collaborations.

indebted to my colleagues from the Radar Engineering and Development Team at NSSL, who supported me on several data collection activities; special thanks to Christopher Schwarz, Rafael Mendoza, and Daniel Wasielewski. My interactions with Dr. Henry Thomas and Dr. Mark Weber (MIT-Lincoln Laboratory), and with John "Chip" Murdock (General Dynamics Mission Systems) which indirectly contributed to the development of this dissertation, are highly appreciated. Finally, I would like to acknowledge the contributions of numerous engineers, students, scientists, and administrators who have supported the development of the Phased Array Radar technology in the Norman community over the last decade.

My time during the Ph.D. program would not have been the same without my friends. Thanks to my friends from the Advanced Radar Research Center: Tony Segalés, Gustavo Azevedo, Rodrigo Lebrón, Arturo Umeyama, Jose David Díaz, Javier Ortiz, Jorge Duarte, Andrew Byrd, Robin Irazoqui, Alessio Mancini, and David Lucking. I treasure all of our game nights, trips, and fun nights out. It fills me with happiness to see all of you pursuing your dreams and becoming successful radar experts. And I look forward to getting together later on for our yearly PASotF reunions.

My most sincere and deepest appreciation goes to Kristi and to my family. It is through them that I was able to overcome several difficulties encountered along the way and was able to stay focused to reach my goals. They made the past few years fly by through several fun trips and family reunions around the world. These precious moments of joy gave me the energy to stay on track and complete this dissertation work. This work is dedicated to my parents José and Delia Schvartzman. For their endless love, support and encouragement throughout my life. All I have and will accomplish are only possible due to their love and sacrifices.

Table of Contents

List of Tables

List of Figures

Abstract

The Weather Surveillance Radar 1988 Doppler (WSR-88D) network has been operational for over 30 years and is still the primary observational instrument employed by the National Weather Service (NWS) forecasters to support their critical mission of issuing severe weather warnings and forecasts in the United States. Nevertheless, the WSR-88Ds have exceeded their engineering design lifespan and are projected to reach the end of operational lifetime by 2040. Technological limitations may prevent the WSR-88D to meet demanding functional requirements for future observational needs. The National Oceanic and Atmospheric Administration (NOAA) has started considering radar systems with advanced capabilities for the eventual replacement of the WSR-88D. Unique and flexible capabilities offered by Phased Array Radar (PAR) technology support the required enhanced weather surveillance strategies that are envisioned to improve the weather radar products, making PAR technology an attractive candidate for the next generation of weather radars. If PAR technology is to replace the operational WSR-88D, important decisions must be made regarding the architecture that will be needed to meet the functional requirements. A four-faced planar PAR (4F-PAR) is expected to achieve the requirements set forth by NOAA and the NWS, but deploying and maintaining an operational network of these radars across the U.S. will likely be unaffordable. A more affordable alternative radar system is based on a single-face Rotating PAR (RPAR) architecture, which is capable of exceeding the functionality provided by

the WSR-88D network. This dissertation is focused on exploring advanced RPAR scanning techniques in support of meeting future radar functional requirements. A survey of unique RPAR capabilities is conducted to determine which ones could be exploited under an RPAR Concept of Operations (CONOPS). Three capabilities are selected for further investigation: beam agility, digital beamforming, and dwell flexibility. The RPARs beam agility is exploited to minimize the beam smearing that results from the rotation of the antenna system over the collection of samples in the coherent processing interval. The use of digital beamforming is investigated as a possible way to reduce the scan time and/or the variance of estimates. The RPAR's dwell flexibility capability is explored as a possible way to tailor the scan to meteorological observations with the goal of improving data quality. Three advanced RPAR scanning techniques are developed exploiting these capabilities, and their performance in support of meeting the radar functional requirements is quantified. The proposed techniques are implemented on the Advanced Technology Demonstrator (ATD), a dual-polarization RPAR system at the National Severe Storms Laboratory (NSSL) in Norman, OK. Data collection experiments are conducted with the ATD to demonstrate the performance of the proposed techniques for dual-polarization observations. Results are verified by quantitatively comparing fields of radar-variable estimates produced using the proposed RPAR techniques with those produced by a well-known collocated WSR-88D radar simultaneously collecting data following an operational Volume Coverage Pattern (VCP). The techniques introduced are integrated to operate simultaneously, and used to design an RPAR CONOPS that can complete a full volume scan in about one minute, while achieving other demanding functional requirements. It is expected that the findings in this dissertation will provide valuable information that can support the design of the future U.S. weather surveillance radar network.

Chapter 1

Introduction

"We are at the very beginning of time for the human race. It is not unreasonable that we grapple with problems. But there are tens of thousands of years in the future. It is our responsibility as scientists, to do what we can, learn what we can, improve the solutions, and pass them on."

Richard P. Feynman

1.1   Background

The Next Generation Weather Radar (NEXRAD) program completed the deployment of the Weather Surveillance Radar - 1988 Doppler (WSR-88D) network delivering 160 high-resolution, S-band, Doppler weather radars operated and maintained by the National Weather Service (NWS). This network of Doppler weather radars was upgraded in 2012 to simultaneously transmit and receive electromagnetic waves in both horizontal (H) and vertical (V) polarizations, which provided these radars with dual-polarization capability [1]. The received signals on the H and V polarization channels are used to estimate spectral moments (reflectivity Z_h, Doppler velocity v_r, and spectrum width σ_v), and polarimetric variables (differential reflectivity Z_{DR}, differential phase Φ_{DP}, co-polar correlation coefficient ρ_{hv}). This

enables the classification of meteorological scatterers (e.g., rain, graupel, large hail, snow) and non-meteorological targets (e.g., insects, birds, and chaff), which can improve the downstream algorithms such as quantitative precipitation products [2, 3]. Polarimetric radars have become a fundamental tool for better interpretation and forecasting of hazardous weather events, and improving the quality of estimates which is critical to support the NWS mission: "to provide weather, water, and climate data, forecasts and warnings for the protection of life and property and enhancement of the national economy"[1]. Figure 1.1 shows the location and coverage of these radars across the United States.

NEXRAD COVERAGE BELOW 10,000 FEET AGL
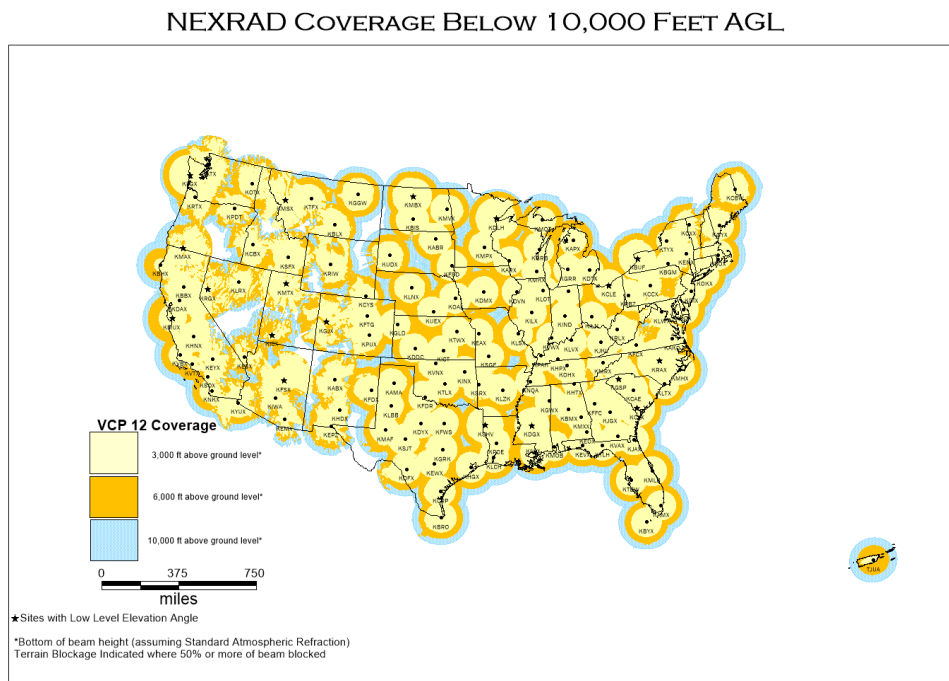
Figure 1.1: Coverage of the NEXRAD network, from NOAA[2]

---

[1]Source: http://www.weather.gov/about

[2]This image was obtained from the National Oceanic and Atmospheric Administration's website: http://www.roc.noaa.gov/WSR88D/Maps.aspx

Data from the WSR-88D are also used to support research efforts, which aim to improve the radar's data quality and help the understanding of weather phenomena [4–12]. For instance, Brown et al. [4] used the KOUN radar, an experimental WSR-88D at the National Severe Storms Laboratory (NSSL), to develop a sampling technique which improves the azimuthal resolution of data and ultimately increases the tornado vortex detection capabilities of the WSR-88D. Similarly, Ivić et al. [6] used archived WSR-88D time series IQ data to develop a radial-based noise power estimation technique that significantly improved the quality of spectral moments and polarimetric variables. After years of research and development, these techniques are transferred to the NEXRAD network and are used in the default operational modes across the WSR-88D fleet.

Compared to the previous non-Doppler weather radars, the introduction of the NEXRAD Network has shown to improve the warning lead time of severe weather events [13]. The network has surpassed its engineering design life span but through continuous upgrades, the service life of the WSR-88D has been significantly extended beyond 2030. Even though the NEXRAD network has shown an impressive performance in comparison to previous radar networks, it also has some limitations [14]. For rotating-reflector radars such as the WSR-88D, most scanning parameters are fixed for a given VCP and the coverage of desired scan sectors is driven by the mechanical rotation of the antenna. These prevent the WSR-88D from achieving a significant reduction in scan-update times in support of the need for more frequent observations. Therefore, it is challenging to support NWS forecasters in their decision-making process for issuing severe weather warnings and forecasts.

The WSR-88D surveys the atmosphere by mechanically rotating a parabolic-reflector antenna following one of the pre-defined scanning patterns denominated Volume Coverage Patterns (VCP). The radar beam covers $360°$ in azimuth and a

variable number of elevations depending on the VCP being used, which can take 4 to 10 minutes to complete. Faster updates are desirable for better understanding and forecasting of the fast-evolving convective precipitation systems[15, 16]. It can be argued that the better understanding of the formation and evolution of severe weather, resulting from radar data with high temporal resolution, may increase lead warning times [17, 18].

Intrinsic architecture limitations may prevent parabolic-reflector systems (such as the WSR-88D) from attaining the performance levels required to meet the set of next-generation radar functional requirements specified by the National Oceanic and Atmospheric Administration (NOAA), and more advanced system capabilities may be needed. One of the most demanding functional requirements involves the volumetric scan-update times, which are optimally expected to be on the order of 1 min. The fastest volume scans currently achieved by the WSR-88D are on the order of 4 mins, and a significant reduction in scan time (maintaining the data quality and spatial sampling capabilities) is not possible without the use of radar capabilities only feasible with more advanced radar architectures. NOAA has been exploring advanced radar systems for the eventual replacement of the operational WSR-88D, which is projected to reach the end of its operational lifetime by 2040 [19]. In addition to the current operational capabilities of the WSR-88D to detect, estimate, and classify returns from meteorological scatterers with high sensitivity and spatial resolution, NOAA has defined performance requirements that involve a more rapid update of volumetric data [20].

Unique and flexible capabilities offered by Phased Array Radar (PAR) technology have the potential to improve the weather radar products, making PAR technology an attractive candidate for the next generation of weather radars [21]. Although PAR technology was initially conceived in the early 1900's [22], tremendous ad-

vancement of the technology was motivated by the need for advanced air defense capabilities during he World War II. Over the past few decades, this technology has greatly matured in the context of air surveillance and defense applications, making PAR technology more accessible to other applications [22]. Key PAR capabilities that support the needs of advanced weather surveillance include: the ability to almost instantly steer the radar beam to an arbitrary direction within the scan sector (i.e., beam agility), the flexibility to dynamically redefine the sampling parameters for each beam position in the scan, and the ability to digitally form multiple simultaneous beams in different directions. Ongoing research efforts that began in the early 2000's at NSSL have aimed at demonstrating unique PAR capabilities for weather surveillance. Research studies have demonstrated that the use of adaptive scanning techniques can reduce the scan time of a stationary planar PAR system [23]. Further, Yu et al. [24] demonstrated an advanced PAR scanning technique that exploits the electronic beam steering agility and can lead to reduced scan times and/or improved data quality. The Phased Array Radar Innovative Sensing Experiment [17] was designed to demonstrate the advantages of rapid-scan PAR data to improve forecasters' ability of warning severe weather. [25] demonstrated the use of a mobile, single-polarization X-band rotating PAR (RPAR) system leveraging an existing military radar, the Mobile Weather Radar 2005 X-band Phased Array (MWR-05XP), to produce rapid volumetric observations of convective storms. Rapid-scan PAR data from the MWR-05X was used in the second Verification of the Origins of Rotation in Tornadoes Experiment (VORTEX2) to analyze the physical processes of tornadogenesis, which advanced the understanding of tornadoes, including tornadogenesis, tornado structure, and improving forecasts [26]. Researchers have also reported that PAR rapid scan data is expected to enhance the effectiveness of radar data-assimilation and numerical weather prediction systems [27].

A single-polarization PAR was installed at the National Weather Radar Testbed (NWRT) in Norman, Oklahoma in 2003 to explore the feasibility of using PAR technology for weather observations [28, 29]. This was the first PAR dedicated to weather observations, and it was made possible through a collaborative effort that initiated at NSSL. The single-polarization PAR system (based on a SPY-1A passive antenna) was made available to research communities in September 2003 [30], and it was decommissioned on May 31, 2016, to make way for newer technology[3]. Significant progress towards evaluating the possibility of adopting PAR technology for weather observations was made with the PAR at the NWRT, however, this system did not have dual-polarization capabilities. Considering that dual-polarization capabilities are a non-negotiable NWS requirement for a future network of weather surveillance radars, the feasibility of producing high-accuracy dual-polarization PAR observations has to be investigated. This important question has recently gained attention in the research community, and scientists have began investigating challenges associated with the implementation and calibration of dual polarization technology on PARs [31].

The recently installed Advanced Technology Demonstrator (ATD) radar system at the NWRT, is a full-size, active, S-band, planar, dual-polarization PAR. It was funded jointly by the NOAA and the Federal Aviation Administration (FAA), and it is being developed by the NSSL, the Cooperative Institute for Mesoscale Meteorological Studies (CIMMS) at the University of Oklahoma, Massachusetts Institute of Technology – Lincoln Laboratory (MIT–LL), and General Dynamics Mission Systems [32–34]. The NWRT site and the ATD antenna are shown in Figure 1.2. The antenna is composed of 76 panels, where each panel consists of an 8×8 set of radi-

---

[3]Source: NOAA National Severe Storms Laboratory, https://www.nssl.noaa.gov/about/history/nwrt-decommission/
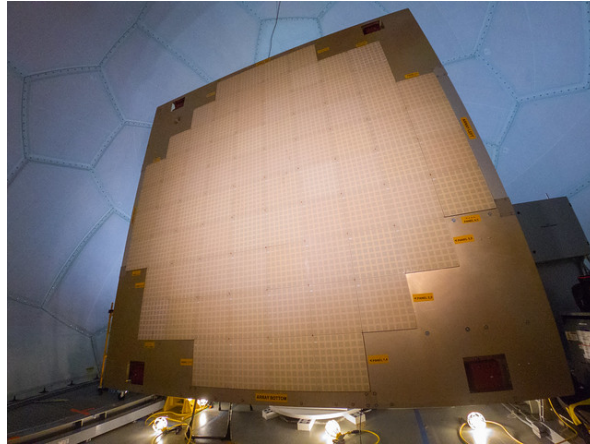
(a) NWRT

(b) ATD Antenna

Figure 1.2: (a) NWRT PAR in Norman, OK, and (b) the ATD at the NWRT.[4].

ating patch-antenna elements with dual linear polarization (H and V), for a total of 4,864 elements. The peak power for each antenna element is 6 W per polarization, which results in $\sim$ 29 kW of peak transmit power for the system. The system makes use of pulse compression to meet sensitivity and range-resolution requirements [35, 36], achieving a sensitivity of approximately 0 dBZ at 50 km. The antenna elements in the ATD have been approximately spaced by half wavelength, which results in a $\sim$4$\times$4 m aperture that produces a 1.58° half-power beamwidth (HPBW) on broadside. On receive, the antenna is partitioned into overlapped subarrays (consisting of 8 panels each, 2 in azimuth by 4 in elevation) to produce lower sidelobes and suppress grating lobes outside of the main beam of the subarray pattern [37]. The multi-channel receiver architecture enables the ATD with beamforming capabilities: it can form up to 24 simultaneous digitally formed beams. This key capability will be exploited to demonstrate techniques that can reduce scan-update times. The main purpose of this advanced dual-polarization radar system is to evaluate the feasibility of PAR technology for weather observations. The full integration, calibration, and testing of the ATD is expected to be completed by the Spring of

2021, after which it will become available to research communities with so-called Initial Operational Capabilities (IOC). There are plans beyond IOC to continuously upgrade these capabilities to support the research and demonstration of additional unique capabilities.

1.2 Motivations

The NOAA Radar Functional Requirements (RFR) document [38] specifies the functionality and expected performance for a future weather surveillance radar system. The document's *Threshold* Functional Requirements are used to define the minimum expected performance of the future system, while its *Optimal* Functional Requirements define the desired system performance. It is likely that advanced scanning and digital signal processing techniques will be needed to meet these demanding requirements. To this end, unique PAR capabilities must be exploited under a certain Concept of Operations (CONOPS). For instance, one of the most demanding optimal requirements is the 1-min update time to complete a volume scan "*with no degradation of the sensitivity, spatial resolution or standard deviation of measurement for radar-variable estimates*". With the conventional dwell times used for weather observations (such as those defined in the WSR-88D VCPs), advanced capabilities such as agile electronic-steering, digital beamforming, and/or adaptive scanning are possible means to reduce the scan update times. A summary of the NOAA/NWS Radar Functional Requirements from [38] most relevant to this work is provided in Table 1.1.

From previous studies mentioned, a stationary four-faced planar PAR architecture has been the prime candidate system that would simultaneously support several

---

[4]Figures 1.2(a) and 1.2(b) were obtained from the NOAA NSSL website: https://www.nssl.noaa.gov/tools/radar/atd/

Category	Threshold Requirements	Optimal Requirements
Weather Radar Variables	Z_h, v_r, σ_v, Z_{DR}, Φ_{DP}, ρ_{hv}	
Wavelength	10 cm (S-Band)	
HPBW	1.0° beamwidth in azimuth and elevation	
Effective Angular Resolution	1.1°	
Coverage	A maximum unambiguous range of 460 km for Z_h, and 300 km for v_r and polarimetric variables	
Scan Strategy Adaptability	Multiple clear air and precipitation mode VCPs with adaptable parameters	One minute or less volume coverage time with no degradation of the sensitivity, spatial resolution or standard deviation of measurement for radar variable estimates
Minimum Detectable Signal	0.0 dB SNR for a -9.5 dBZe target at 50 km in short pulse (1.57 μs)	
Dynamic Range	93 dB	97 dB
Beam Elevation and Azimuth Positioning Accuracy	0.15°	0.0055°
Two-way sidelobes	First sidelobe: ≤ -70 dB relative to the peak of the main lobe	
Standard deviation of radar-variable estimates	Z_h: ≤ 1 dB for target with true σ_v of 4 m s^{-1} and SNR ≥ 10 dB v_r: ≤ 1 m s^{-1} for target with true σ_v of 4 m s^{-1} and SNR 8 dB σ_v: ≤ 0.5 m s^{-1} for target with true σ_v of 2 m s^{-1} and SNR 10 dB Z_{DR}: 0.4 dB for target with true σ_v of 2 m s^{-1}, ρ_{hv} of ≥ 0.99, dwell time of 50 ms and SNR ≥ 20 dB Φ_{DP}: 2.5° for target with true σ_v of 2 m s^{-1}, ρ_{hv} of ≥ 0.99, dwell time of 50 ms and SNR ≥ 20 dB ρ_{hv}: 0.006 for target with true σ_v of 2 m s^{-1}, ρ_{hv} of ≥ 0.99, dwell time of 50 ms and SNR ≥ 20 dB	

Table 1.1: Summary of the NOAA/NWS Radar Functional Requirements [38] most relevant to this work.

missions [32] under the Multi-function Phased Array Radar (MPAR) concept. Nevertheless, the discrepancies among interagency deployment timelines (aided by the insufficient maturity of polarimetric PAR technology for weather observations) resulted in the MPAR concept being abandoned. Consequently, current efforts are now centered on single-mission systems. While a four-faced PAR is likely capable of achieving the optimal requirements set forth by NOAA, deploying and maintaining an operational network of these radars across the U.S. will likely be unaffordable.

A more affordable alternative radar system is based on a single-face RPAR architecture [20], which is capable of meeting the threshold requirements and exceeding the capabilities of the current reflector-based WSR-88D network. The RPAR architecture has been used for air surveillance and defense applications since the late 1970's [39–41] but was only introduced for weather surveillance in recent years [42–45]. The CONOPS for these weather RPAR systems consist of either imitating the operation of a conventional reflector radar with continued mechanical azimuthal rotation and discretely increasing elevation with each rotation or performing a straightforward electronic scan in elevation while mechanically rotating in the azimuthal direction. These limited operational concepts, which were only demonstrated on single-polarization systems, fall short of exploiting all of RPAR's unique capabilities and are not likely to meet demanding functional requirements such as the more rapid update volumetric data. Dual-polarization is one of the strictly required functional capabilities, therefore, advanced techniques compatible with dual-polarization technology are developed in this dissertation.

Advanced capabilities offered by the RPAR are explored in this dissertation as a means to design advanced scanning techniques to address some of NOAA's Optimal radar functional requirements. Specifically, RPAR techniques that support

10

the requirements in effective angular resolution, adaptive scanning strategies, and statistical data quality are developed. First, the RPAR's beam agility is used to compensate for the mechanical rotation of the antenna in azimuth, which minimizes the negative impact of rotation on the effective azimuthal resolution. Then, digital beamforming capabilities are used to develop a technique that supports a significant reduction in scan time and/or in the standard deviation of radar-variable estimates. Lastly, a concept that supports the reduction of scan times and enables the use of adaptive scanning to improve data quality is introduced.

As a potential solution to achieve current and future needs to support the NWS mission, advanced RPAR CONOPS for weather surveillance using these techniques will be investigated. Impacts from these CONOPS on the quality of radar-variable estimates will be understood and quantified. These results could be used to design an RPAR system that supports the desired CONOPS meeting the functional requirements and results in minimal degradation in the quality of radar data.

1.3 Contributions

The overarching goal of this dissertation is to explore and quantify the main advantages and limitations of the RPAR architecture with respect to the rotating-reflector radar (RR) and the stationary 4-faced PAR (4F-PAR), respectively; and to provide valuable information for the design of a CONOPS capable of meeting the NOAA/NWS functional requirements in support of the U.S. weather surveillance mission. Advanced scanning and signal processing techniques developed in this dissertation can be used as building blocks to design an RPAR CONOPS in an operational network of RPARs. The main contributions of this work include:

- An analysis on radar scanning and signal processing techniques that are fea-

sible with the RPAR architecture, and discussions on their advantages and limitations with respect to the RR and 4F-PAR, respectively.

- A quantitative analysis of the antenna rotation impact on the azimuthal resolution and on the quality of radar-variable estimates for RPAR, as a function of the number of bits in the antenna-element phase shifters and including off broadside pulse-to-pulse beamsteering angles.

- The conceptual development, simulation, and practical implementation of a technique capable of mitigating beam-smearing effects with little-to-no impact on the quality of radar-variable estimates. The performance of the technique is quantified as a function of phase-shifter bits, and includes both quantization and random phase errors. The performance of the technique is verified by comparing observations to those from a well-known WSR-88D system.

- A novel technique that exploits unique PAR beamforming capabilities to reduce the scan time and/or to reduce the standard deviation of estimates. Calibration and practical implementation considerations are provided. The technique is demonstrated using the ATD system for polarimetric weather observations. The performance of the technique is verified by comparing observations to those from a well-known WSR-88D system.

- The conceptual development, implementation, and demonstration of a technique that can be used to reduce the standard deviation of estimates (by tailoring scanned beams to observations) and/or the scan time (by eliminating the need for "split cuts" to mitigate range/velocity ambiguities).

- A concept of operations for the RPAR, which includes the integration and

12

joint use of the three techniques presented, and the development of alternative scan strategies based on these techniques.

1.4 Outline

Chapter 2 presents comparative analyses of unique RPAR capabilities with respect to the RR and the 4F-PAR architectures. Techniques considered are described and a discussion with tradeoff considerations for the three architectures introduced is provided. This discussion motivates the selection of the key techniques investigated in this dissertation. Three unique RPAR capabilities are selected to develop advanced scanning techniques in support of the RPAR CONOPS, namely: (1) beam agility, (2) digital beamforming, and (3) dwell flexibility. A justification for the selected techniques is provided in terms of needs for future radar requirements.

Chapter 3 introduces the *Motion-Compensated Steering* (MCS) technique by which the beam is electronically steered on a pulse-to-pulse basis within the coherent processing interval (CPI) to compensate the antenna motion and maintain the beam pointed at the center of resolution volume being sampled. This leads to a reduction in the effective antenna pattern beamwidth. In turn, mitigating the impact of beam smearing allows for smaller (and more affordable) antenna apertures that can meet angular resolution requirements. Impacts of electronic beam steering off the broadside are quantified in terms of azimuthal resolution and data quality using high-fidelity RPAR simulations. The performance of MCS in mitigating beam smearing may be limited if the beam cannot be pointed with sufficient accuracy. This could be caused by either the accuracy of electronic beam steering or the precision of the mechanical rotator. While increasing the number of bits per antenna element may increase system cost, it is likely that increasing the antenna aperture

(i.e., for an equivalent effective beamwidth) would be more costly. Furthermore, MCS may not be compatible with other advanced PAR scanning techniques (e.g., adaptive beamforming), which may limit the capabilities of the overall system. The MCS technique is implemented on the ATD, practical considerations are provided, and polarimetric data collections are presented. Further, polarimetric calibration methods based on the autocorrelation-correction matrices [46, 47] are integrated with MCS.

Chapter 4 introduces the *Distributed Beams* (DB) technique, which provides a way to reduce the scan time and/or to reduce the variance of radar-variable estimates. It exploits unique PAR beamforming by synthesizing a wide transmit beam and receiving multiple beams simultaneously. This concept has been used on RPARs by using wider transmit beams in the elevation dimension. Here, it is applied in the azimuthal dimension. The DB technique consists in coherently combining receive beams coming from the same location to effectively produce a longer dwell (increased by number of simultaneous beams received). This comes at the expense of 1) increased rotation speed, 2) two-way pattern increased sidelobe levels, 3) reduced sensitivity, and 4) an increased two-way beamwidth due to the wider transmit beam. The technique is demonstrated using the ATD system for polarimetric weather observations. The technique could be implemented as part of an RPAR concept of operations to meet requirements for the future weather surveillance network if certain tradeoffs are accounted for in the radar design process.

Chapter 5 presents the *forward-looking* and *back-scanning* technique (FBT) that exploits the RPAR's beam agility by interleaving beams with different pointing angles and dwell-type definitions. Specifically, forward-looking (short dwell beams) and back-scanning (standard dwell beams) are scheduled as interleaved sets of beams that are scanned as the RPAR rotates. For the forward-looking beams, the

concept is to transmit short-dwell beams ahead of the radar rotation to get sufficient surveillance-type information. The FBT is designed to execute split cuts (similar to those used in the WSR-88D) with a single revolution of the antenna, and to be used in conjunction with real-time adaptive scanning algorithms to reduce the scan time. Further, although the back-scanning beams considered in this work follow an invariant scan, they could conceptually be scheduled adaptively. That is, an adaptive algorithm could use information from the forward-looking beams to tailor the observations on significant weather echoes. Potential data quality improvements that could be achieved by implementing a real-time adaptive scheduling of these beams is discussed. A potential limitation of this technique is that it requires accurate polarimetric calibration for an effective operation, since the forward-looking and back-scanning beams are steered off broadside. The FBT technique is demonstrated using the ATD system for polarimetric weather observations, and data collected with the FBT are re-processed to emulate a simple adaptive scanning algorithm.

Chapter 6 discusses the integration of the presented techniques for a CONOPS that results in reducing the update times while improving data quality, and without degradation in spatial resolution. First, MCS, DB and FBT are integrated and demonstrated. Then, independent sets of receive beams using these techniques are added to simultaneously scan several elevations and further reduce scan times. A CONOPS based on the described techniques is used to develop a scan strategy with a volume scan time of 1.06 min, and which achieves the requirements for spatial sampling and data quality (i.e., standard deviation of estimates). While the use of spoiled transmit beams provides a means to reduce the scan time but it puts more demands on the system design. A system designed to meet the angular resolution requirements ($\sim 1°$) using pencil beams will likely go outside of the requirements when using a spoiled transmit beam. One way to compensate for this loss in reso-

lution is to increase the size of the aperture. While this will increase the cost of the system, it is reasonable to assume that a single-face RPAR with a larger aperture would still be more affordable than a 4F-PAR.

Chapter 7 summarizes the findings and contributions of this dissertation and provides some recommendations in support of an initial deployment of RPAR systems to meet functional requirements. Possible future research paths in support of the RPAR CONOPS are briefly described as well.

Chapter 2

Unique PAR Capabilities

"Let's go invent tomorrow rather than worrying about what happened yesterday."

<div align="right">Steve Jobs</div>

2.1 Radar Architectures

The NOAA RFR document [38] specifies the functionality and performance expected for a future weather surveillance radar system, but does not provide specific implementation details to achieve this functionality. A variety of radar architectures could meet the advanced functionality requirements, but system cost and functionality tradeoffs have to be considered to select an appropriate candidate.

RR systems have been used for many applications since the 1930's. This technology is well known and with advances in signal processing techniques (over the past few decades), it has reached a point where significant performance enhancements are limited by the antenna architecture. As argued in Section 1.1, intrinsic architecture limitations may prevent RR systems (such as the WSR-88D) from attaining the required performance levels. Not only this architecture has little scan-definition flexibility, but it also lacks digital beamforming capabilities that could allow the simultaneous reception of multiple beams to scan regions of interest faster.

With limited degrees of freedom for enhancing current performance, it is unlikely that RR technology will be able to meet optimal functional requirements.

The 4F-PAR has been one of the prime candidates to provide the required functionality for the weather surveillance mission. With sufficiently large apertures to produce the required angular resolution, and with element-level digitization of signals, this architecture would likely achieve the objective requirements set forth in the RFR. With four stationary PAR faces operating independently, each face could finish a volume scan in $\sim$67 seconds using the VCP number 212 scan strategy definition to maintain the required data quality. Exercising advanced PAR scanning capabilities such as digital beamforming and adaptive scanning, the volumetric update time could be further reduced to meet the objective update time of 1 min. While a 4F-PAR is capable of achieving the optimal requirements, deploying and maintaining an operational network of these radars across the U.S. will very likely be unaffordable.

The RPAR architecture consists of a combination of the previously mentioned architectures. It is mechanically rotated in azimuth (and also possibly tilted in elevation) as the RR architecture, but it is equipped with an advanced antenna system similar to that of the 4F-PAR (for 1 or 2 faces). The flexibility provided by PAR technology (e.g., agile electronic beam steering, beamforming, etc.) over the RR system allows for advanced scanning and processing techniques. These advanced capabilities could be leveraged to attempt meeting optimal functional requirements. However, some scan strategies (and their associated CONOPS) may be constrained by the required continuous mechanical rotation of the antenna system in azimuth. Elevation scanning can be accomplished by mechanically tilting the antenna or by electronically steering the beam; the latter requires more accurate polarimetric calibration. It is assumed herein that the RPAR has beamsteering capability in azimuth,

and that elevation scanning is accomplished by either mechanically or electronically scanning in elevation. While it can be argued that this architecture is more affordable than the 4F-PAR, it has fewer degrees of freedom (relative to the 4F-PAR) and it is not certain whether this architecture could meet some or all optimal functional requirements. In this dissertation, the focus is on meeting the volume coverage time, the standard deviation of radar-variable estimates, and spatial sampling requirements.

An illustration of these three radar architectures is presented in Figure 2.1. Although there may be other architectures capable of meeting the requirements (such as the Cylindrical Polarimetric Phased Array Radar, CPPAR, [48, 49]), they are not considered here because our focus is on the RPAR architecture with respect to the simplest architecture (RR) and the most capable one (4F-PAR). Other affordable architectures in between the RR and the 4F-PAR could be considered as possible alternatives to the RPAR; this is beyond the scope of this work. An analysis of possible PAR capabilities as a function of architecture oriented towards achieving functional requirements is carried out next.

Rotating-reflector Radar (RR)   **Rotating PAR (RPAR)**   **4-Faced PAR (4F-PAR)**
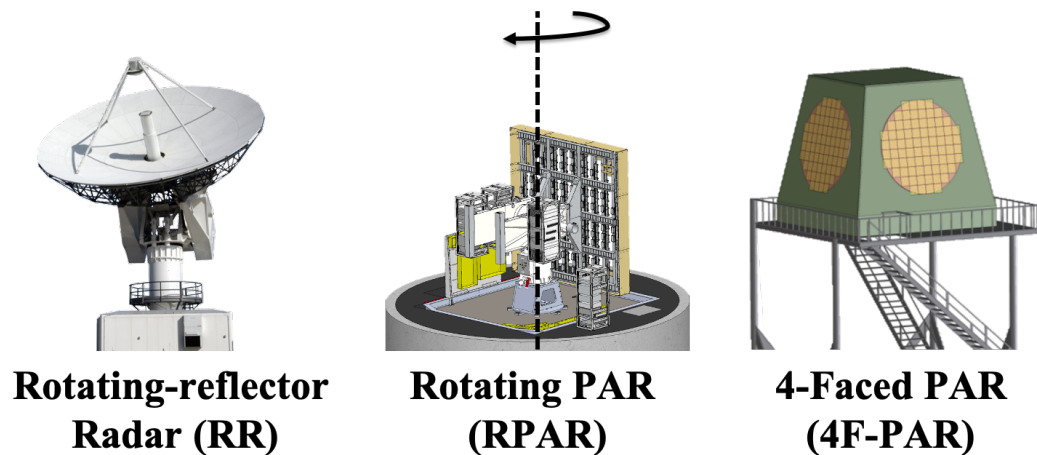
Figure 2.1: Radar Architectures: (left) Rotating-reflector Radar, (center) Rotating PAR, (right) Stationary 4-Faced PAR.

2.2 Radar Capability Analysis

It is of interest to understand the advantages of the RPAR architecture over the RR, and its limitations with respect to the 4F-PAR. We begin by describing relevant radar system capabilities, whether or not these are feasible with the architectures under consideration, and their maturity level in the path to operational implementation. A technique is considered feasible if the architecture can support it, and the maturity level is divided into three simple categories: low, medium, or high. These are meant to represent the state of the technology in terms of their development level; i.e., in initial research phase (low), in testing and demonstration phase (medium), ready for transition to operations (high). Capabilities with a low maturity level are those exploited by techniques for which only theoretical concepts and/or simulations have been presented or published, but no practical implementations or demonstrations are available. For example, the adaptive beam clustering technique proposed by Weber [50] exploits the adaptive scanning and digital beamforming capabilities of the 4F-PAR, and although they provide theoretical concepts and simulations illustrating the technique, it has not been implemented on a weather radar system and would therefore be considered of low maturity level. Capabilities with a medium maturity level are those exploited by techniques for which advanced simulations, proof-of-concept practical implementations, and demonstrations are available in the published literature. For example, the beam multiplexing (BMX [24]) technique exploits the beam agility and dwell flexibility capabilities, and although it has been demonstrated on a weather PAR, further analysis and testing would be needed for an operational implementation (e.g., investigate its compatibility with operational signal processing techniques and scan strategies, and its impacts on polarimetric data quality). Capabilities with a high maturity level are those ex-

ploited by techniques ready for operational implementation or that are already operational on weather radars; that is, those that have been extensively studied and demonstrated, and for which test experiments on operational platforms have been conducted. This may include the involvement of forecasters analyzing the data to ensure that the technique does not impact (and possibly enhances) their ability to issue warnings and forecasts. The Sachidananda-Zrnić range/velocity ambiguity mitigation technique [51] exploits the phase coding capability, and it is considered of high maturity level for the RR since it has been operational in the WSR-88D network for many years. Discussion about the tradeoffs and considerations associated with each capability is provided next with the goal of identifying the most suitable techniques that can be exploited by the RPAR architecture.

2.2.1 Polarimetric Observations

Radars with dual-polarization capability are able to transmit electromagnetic waves in the H and V polarizations. The dual-polarization technology has been operational on the WSR-88D network since 2012, and is therefore considered a mature technology for the RR architecture. These *polarimetric observations* provide information about the type and size of scatterers in the resolution volume (defined herein as the volume of space circumscribed by the 6-dB contour of the two-way antenna pattern in azimuth and elevation and of the range weighting function in range [52]), and have significantly improved precipitation rate estimates, flood warning, hail detection, tornado detection, winter weather warnings and identification of non-meteorological targets. Polarimetric observations and products derived from them have become a fundamental tools for better interpretation and forecasting of hazardous weather events to support the NWS mission [2, 3, 53]. As a result, the

capability to provide high-quality dual-polarization observations has become an indispensable requirement for any future operational weather radar.

Operational implementation of dual-polarization technology requires that scattering properties of precipitation must be measured with high accuracy. One of the major obstacles to the use of polarimetric PAR technology for weather surveillance is the calibration needed to achieve measurements with quality comparable to those of the WSR-88D [31]. This is due to the existence of significant scan-dependent measurement biases, as well as cross-polar antenna pattern contamination, inherent to planar PAR [54, 55]. Scan-dependent system biases in PAR estimates are caused by the H and V copolar antenna patterns, which vary with beamsteering direction. The effects of these variations can be addressed via corrections using appropriate values at each broadside location [56]. If the cross-coupling effects are sufficiently suppressed [57] and given sufficiently narrow antenna main beam, the corrections can be conducted using only the beam peak values of the copolar patterns.

Ongoing research efforts are exploring ways to mitigate both co-polar biases and cross-polar pattern contamination. For example, initial co-polar bias corrections for ATD dual-polarization observations were developed from antenna patterns measured in the near-field chamber at the MIT-LL facilities during March-April 2018 [33]. The beam peaks at all measured locations are shown in Figure 2.2 (left and middle panels), from [47]. Further, by extracting the copolar beam peaks along the horizontal cardinal plane, the copolar beamsteering biases for Z_{h}, Z_{DR}, and Φ_{DP} are computed and shown in Figure 2.2 (right panels). These measurements may not represent the current state of the array with utmost accuracy since they were obtained prior to fielding the array in Norman, OK, but they were tested with ATD data collected during the spring and summer of 2019. Figure 2.3 from [46] shows radar variable estimates of (columns from left to right) Z_{h}, Z_{DR}, Φ_{DP}, and ρ_{hv} for (rows
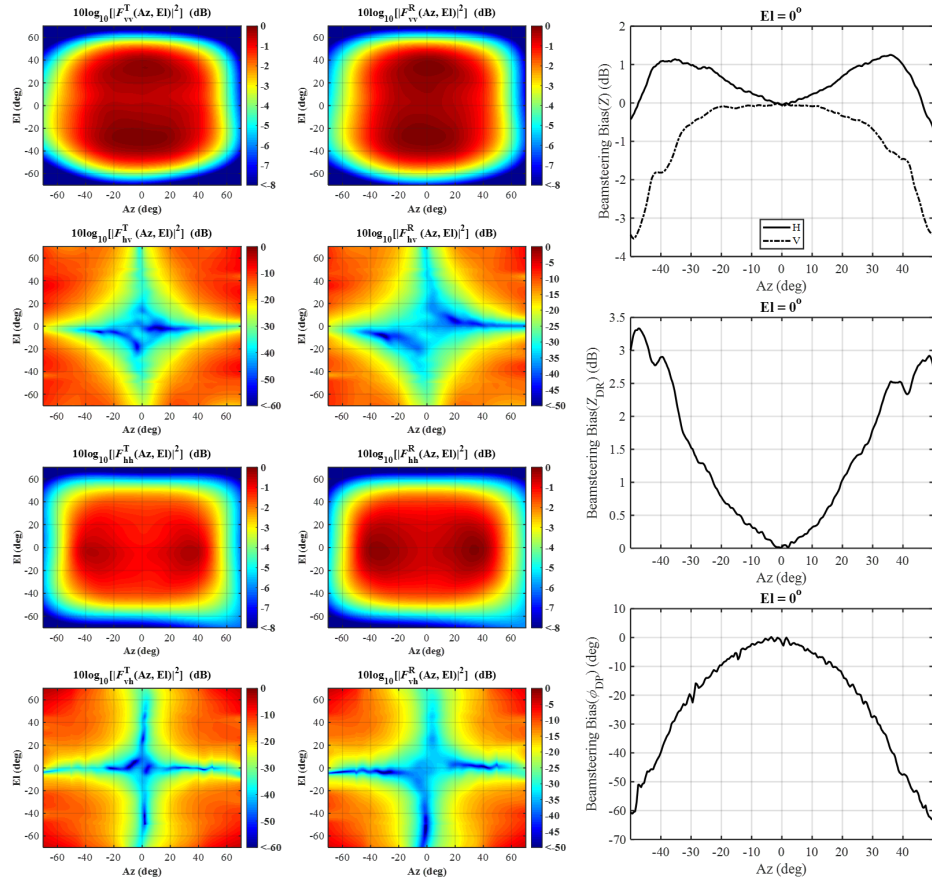
Figure 2.2: (left panels) Transmit embedded element pattern and (middle panels) receive embedded element pattern of the ATD antenna measured in the near-field chamber at Lincoln Laboratories. Near-field measured copolar beamsteering biases derived along horizontal principal plane (right panels), from [47].

from top to bottom) uncorrected ATD data, corrected ATD data using near-field measurements, and data from the closely located Twin Lakes (KTLX) operational WSR-88D radar for reference.

The dual-polarization technology is considered mature for the RR architecture. As discussed previously, PAR antennas are plagued with polarimectric biases induced by co-polar and cross-polar antenna patterns. Recent research efforts show that differences among polarimetric-variable estimates associated with collocated volumes illuminated in rapid succession using distinct electronic steering angles
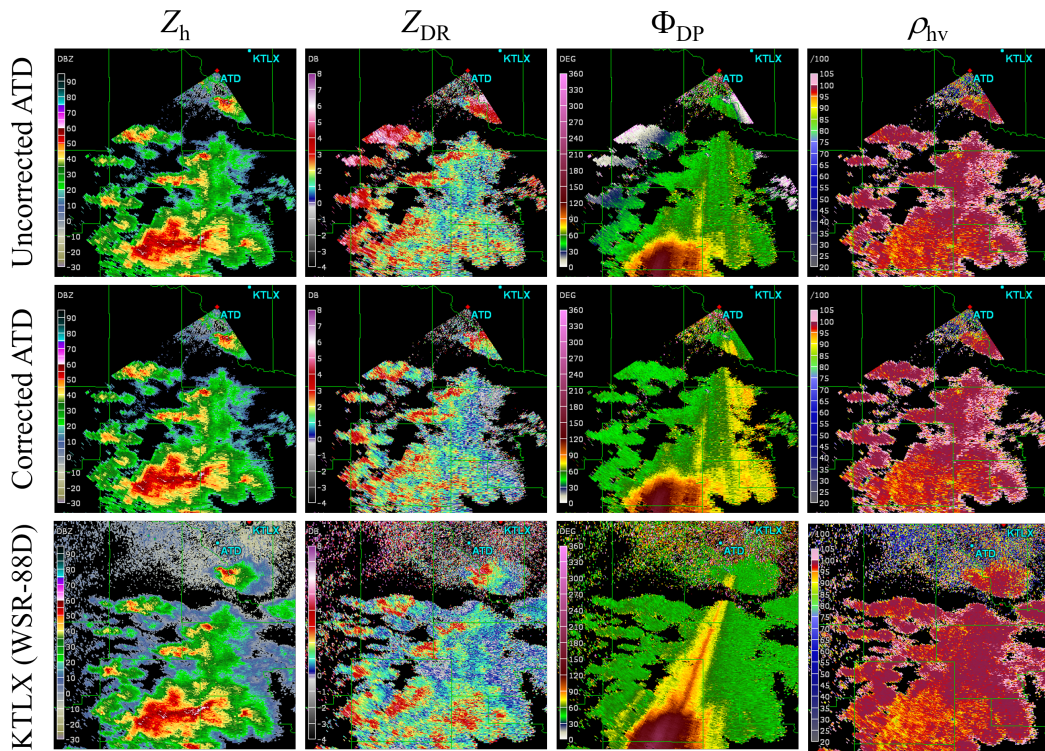
Figure 2.3: ATD reflectivity and polarimetric variable fields on 01 May 2019, without (top row) and with (middle row) bias corrections derived from near-field antenna pattern measurements. The bottom row is concurrent data from the operational WSR-88D in Oklahoma City, OK., from [46].

(the *self-consistency* test) are significantly reduced. This indicates a medium maturity level in the dual-polarization technology for stationary PAR systems such as the 4F-PAR. Polarimetric calibration of the RPAR will depend on the maximum electronic steering angles that will be used in the scan. That is, if beam positions in the scan are sufficiently close to the broadside, calibration will be similar to that of an RR system; and if beam positions in the scan are steered far from the broadside, calibration will be similar to that of the 4F-PAR. If polarimetric calibration is achieved for a stationary PAR system, it would reduce the RPAR's polarimetric calibration procedure to that of an RR system. Nevertheless, the impact of advanced RPAR signal processing techniques (developed in support of meeting functional

radar requirements) on polarimetric-variable estimates will have to be thoroughly evaluated. Considering that dual-polarization has not been operationally demonstrated with PAR technology, this is considered a technology of medium maturity level for RPAR and 4F-PAR.

2.2.2 Pulse Compression

Pulse compression provides increased sensitivity without affecting the range resolution [58]. Initially developed for point targets, it consists of transmitting a long pulse to increase the average power and later compressing it to the desired range resolution at the receiver matched filter. More recently, pulse compression has been implemented on ground-based weather radars [36, 45, 59–61], proving to be an effective technique to improve sensitivity. The use of relatively long pulse-compression waveforms (compared to conventional radar pulsewidths), increases the pulse transmission time, which consequently increases the initial range for echo detection (i.e., the blind range). Researchers have used a combination of a long pulse-compression waveform followed by a short conventional non-compression waveform (at a different frequency) to mitigate this for polarimetric weather observations [60]. Since these waveforms result in different overall system sensitivity, there is a difference in sensitivity in the short-pulse to long-pulse data-transition range. Although this may not pose a critical challenge for the operational use of pulse-compression waveforms on polarimetric weather radars, techniques to blend the sensitivity gap (likely at the expense of data quality) could be devised.

All three architectures support this capability since it operates on the range-time dimension, and it is compatible with rotating and stationary systems. In particular, pulse compression could be used to increase the sensitivity of relatively

low-powered RPAR and 4F-PAR systems to meet functional requirements. Figure 2.4 illustrates the sensitivity improvement of the ATD when using a 78-μs pulse-compression waveform over using a short 1.8-μs pulse (left and center panels), where data from the operational RR KTLX (Twin Lakes, OK) WSR-88D radar is shown for reference (right panel) [36]. Furthermore, since other advanced techniques (such as beamforming) may trade sensitivity for a reduction in scan update times or improvement in the quality of data, pulse compression could be used to compensate for the sensitivity loss. This assumes that the radar transmitter duty cycle is high enough to achieve the required sensitivity when scanning with conventional techniques.

Pulse compression is a well-known technique that is feasible and mature for all three architectures. Considering that pulse-compression operates on range-time, research results developed for the 4F-PAR can be directly implemented on the RPAR. That is, while there are still some open research questions regarding the use of pulse-compression waveforms with PARs, these are not unique for the RPAR and results from PAR-oriented research efforts will be easily transferable to the RPAR. Furthermore, this technique does not directly support reducing the scan time, which
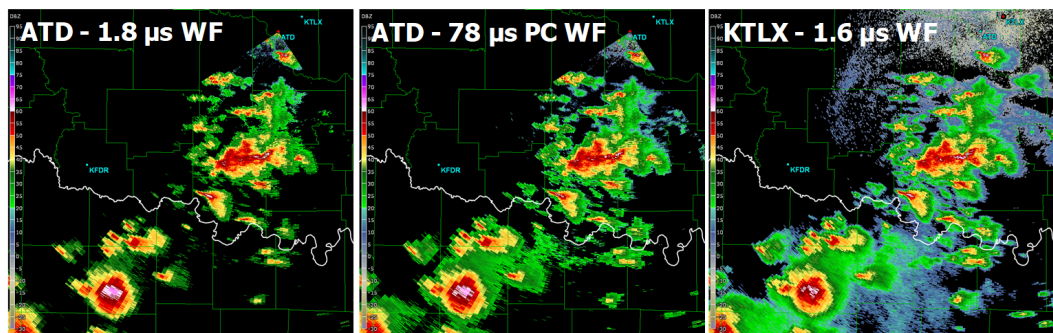
Figure 2.4: Reflectivity fields from the 01 May 2019 weather event at ~19:58:25 UTC (left) ATD using a short waveform (center) ATD using a pulse-compression waveform (right) Operational KTLX WSR-88D for reference from [36].

is one of the most demanding functional requirements. Pulse compression should be considered for RPARs to increase sensitivity of low-powered solid state transmitters, but given its high-maturity level and its value in support of the dissertation goals (novelty and achieving the RFR), it is not considered a unique RPAR capability.

2.2.3 Frequency Diversity

Radars with frequency diversity can transmit signals in separate frequency bands and receive echo signals from all frequency bands transmitted simultaneously. Signals received are separated into their corresponding bands using analog or digital filtering prior to signal processing. This concept is widely used in communication and is known as Frequency Division Multiplexing.

Frequency diversity has been used on RR architectures to either increase the number of independent samples observing a resolution volume [62], or to mitigate the blind range caused by the transmission of a long pulse-compression waveform [60]. Frequency diversity is also very advantageous with systems based on phased array antennas, such as the RPAR and the 4F-PAR. Bluestein et al. [25] demonstrated the use of a mobile, single-polarization RPAR (MWR-05XP), with frequency diversity to increase the number of independent samples. With frequency diversity implemented, a higher antenna rotation rate was possible because independent samples were obtained at a higher rate, reducing the volume sampling time by a factor of 2. Frequency diversity was also implemented on the Rapid-Scanning X-band Polarimetric (RaXPol) radar [63] to increase the number of independent samples and allow faster rotation rates on a mobile RR system.

Nevertheless, the significant growth in wireless broadband applications in re-

cent years has forced the compression of several applications into relatively narrow frequency bands. The high demand for spectrum allocation coupled with the current scarcitiy of available frequency bands resulted in a large increase in spectrum cost, making frequency diversity options for weather radars less feasible. In fact, the Spectrum Efficient National Surveillance Radar (SENSR) program evaluated the possibility of relocating radar systems operating on the 1300–1350-MHz band (L-band) by potentially consolidating weather and aircraft surveillance radar networks into one system operating on the 3 GHz band (S-band) [32].

Frequency diversity has been demonstrated for weather radar applications and provides a way to reduce the scan time or the variance of estimates. However, it is not typically used in operational weather radars due to spectrum availability. Although this technology is feasible with all three canonical architectures considered here and can be considered in a medium-to-high maturity level, the required excessive frequency bandwidth makes it less feasible than other alternatives available with PAR technology. Furthermore, since techniques exercising frequency diversity developed for the 4F-PAR can be readily implemented on the RPAR, it is not considered a unique RPAR capability.

2.2.4   Phase Coding

Phase coding capabilities allow the radar system to impose phase codes on each transmitted pulse in a CPI. Phase coding was initially proposed for the RR architecture in 1980's as a means to resolve range-velocity ambiguities [64, 65], and has been implemented in the WSR-88D network since the early 2000's [51, 66]. In the phase coding technique proposed by Sachidananda and Zrnić [51], transmitted pulses are phase shifted according to a sequence referred to as the switching code.

The received echo samples are multiplied by the conjugate of the switching code sequence to remove the phases of transmit pulses artificially imposed by the switching code. Consequently, the first trip signals are made *coherent* and 2nd (or higher order) trip signals are phase modulated. In general, any one of the overlaid trip signals can be cohered leaving the rest modulated by different codes; the modulation produces a number of spectral replicas. Sachidananda and Zrnić demonstrated that by proper choice of the code, it is possible to spread the spectra of the overlaid signals in a desirable number of replicas.

More recently, pulse-to-pulse phase coding has been proposed to mitigate biases induced by the cross-polar fields of a PAR antenna. Ivić and Doviak [67] investigated the impact of cross-polar fields on Z_{DR} estimates and concluded that the isolation between coaxial cross-polar and copolar beams needs to be in excess of 50 dB to achieve acceptable Z_{DR} biases (i.e., less than 0.1 dB). They proposed a phase coding scheme capable of decreasing Z_{DR} biases without a substantial increase in the standard deviation of estimates. Later, Ivić [68] improved the initial phase coding scheme proposed to maintain the Z_{DR} bias suppression but reducing the ρ_{hv} and Φ_{DP} bias with respect to the originally proposed phase code.

Phase coding schemes have been operationally implemented on the WSR-88D network since the early 2000's; thus it is considered a mature technology for RR systems. Ongoing research on PAR technology shows promise that phase coding technology can be used to mitigate contamination from cross-polar antenna patterns. This would be applicable to both RPAR and 4F-PAR architectures, although more research could be needed to evaluate the impact of phase coding operating in conjunction with advanced scanning techniques for RPAR (e.g., motion-compensated steering), therefore, it is considered a technology of medium maturity level in this dissertation. Similar to previous capabilities discussed, this is not

unique to RPAR, and it is likely that most techniques developed for the 4F-PAR can be implemented on the RPAR. For these reasons, it is not considered a unique RPAR capability in this work.

2.2.5 Dwell Flexibility

The dwell time is defined as the total time the radar spends scanning a given beam position. For a beam defined with a single Pulse Repetition Time (PRT), this is determined by the product of the PRT (T_s) and the number of samples (M). For a multi-PRT beam, the dwell time is the sum of all M and T_s products in the multi-PRT definition. This definition is independent from the beam pointing angle and it supports advanced scanning techniques such as BMX ([24]). The *dwell flexibility* capability discussed in this dissertation refers to the ability to dynamically change T_s and M on a beam-position by beam-position basis. This capability could be exploited by the radar to spend less time dwelling on regions without meteorological targets of interest.

Dwell flexibility is feasible but very limited with the RR architecture because of the mechanical rotation in the azimuth plane and the lack of beamsteering capability. That is, the mechanical rotation rate in azimuth is assumed to be constant for each elevation cut when scanning in the plane-position indicator (PPI) mode, given that it determines the beamwidth-normalized azimuthal sampling spacing of resolution volumes ($\Delta\phi$). Typically, radar functional requirements are provided in terms of $\Delta\phi$, and the expected variance of radar variable estimates, and therefore the rotation rate (ω) is derived from those,

$$\omega = \frac{\phi_1 \Delta\phi}{M T_s} \quad {}^\circ\text{s}^{-1} \tag{2.1}$$

where ϕ_1 is the HPBW in azimuth. The HPBW is defined herein as the angular width in degrees within which the microwave radiation is greater than one-half of its peak intensity [52]. Although the RR technology allows a dynamic definition of M and T_s, constant variations in the rotation rate would cause significant wear on the rotating pedestal system. Furthermore, these variations in the rotation speed cannot occur instantaneously, they are constrained by mechanical inertia, which makes the concept of changing the rotation speed impractical for an operational RR. This in turn would increase maintenance costs. In short, limitations of this technology (e.g., no beam agility) coupled with the traditional RR CONOPS severely limits this capability on the RR architecture. Consequently, this capability has not been extensively explored on RR systems and is therefore considered of medium maturity level.

Dwell flexibility is naturally feasible with the 4F-PAR architecture. Consider four mutually exclusive sets of beam positions each associated with one of the 4F-PAR faces. A beam position is defined herein as a pair of azimuth and elevation angles (ϕ_{az}, θ_{el}) that could be scanned by the radar. With four stationary PAR faces operated independently, dwell times for beam positions scanned by each PAR face can be trivially executed on a beam-to-beam basis, although the determination of acquisition parameters may be more challenging. Since the azimuthal sampling spacing is independent from the dwell times in the 4F-PAR, this architecture fully supports dwell flexibility. The Adaptive Digital Signal Processing Algorithm for PAR Timely Scans (ADAPTS) algorithm proposed and illustrated by [23] exercised dwell flexibility on a single-face and single-polarization stationary PAR system to reduce the scan update time.

Similar to the RR, the RPAR architecture is subject to the mechanical rotation in the azimuthal plane. Nevertheless, the phased array antenna enables this system

with agile beam steering (i.e., being able to almost instantly switch to arbitrary beam positions), which partially decouples the azimuthal sampling spacing from the mechanical rotation in azimuth. That is, even in a constant azimuthal rotation regime, the radar could scan certain beam positions and maintain a desired sampling spacing with certain restriction on the dwell definition (i.e., acquisition parameters). In contrast to the 4F-PAR, the set of *visible* beam positions constantly changes as the RPAR rotates, which constrains the potential effectiveness of dwell flexibility in reducing the scan time. For example, for an RPAR rotating at $\omega = 30° \text{ s}^{-1}$, the radar only has 3 s to scan a beam position before the visible region sweeps a $90°$ sector across it. While the dwell flexibility is feasible on the RPAR architecture and could be used to reduce the variance of radar-variable estimates or to reduce the scan time, it has not been investigated yet, thus, it is considered of low maturity level.

2.2.6 Transmission Mode Flexibility

The transmission mode flexibility defined in this work refers to the ability of the radar system to schedule the transmission of electromagnetic pulses and the reception of echoes from those (and for the H and V polarizations) in a flexible and relatively arbitrary way. While RR systems have some transmission mode flexibility, PAR systems are generally more flexible and allow an almost arbitrary scheduling of transmit pulses. This is because PAR antenna elements can be controlled independently for the H and V polarizations. Three transmission modes are described next.

The simultaneous transmission and reception of electromagnetic waves with horizontal and vertical (SHV) polarizations has been chosen as the main mode for

polarimetric observations on the the WSR-88D weather radar network [69]. In this mode, six weather radar variables are measured in each resolution volume: Z_h, v_r, σ_v, Z_DR, Φ_DP, and ρ_hv. The performance of radar-variable estimators for these variables measured using the SHV mode has been thoroughly studied [1, 52, 70]. Most research efforts that use dual-polarization weather radars adopt this mode of operation because of the high performance of estimators with respect to alternative modes [71].

Research efforts over the past decade have been focused on implementing and testing the SHV mode on PAR systems [32, 33, 55, 72, 73]. This is more challenging than for RR systems for three reasons: (1) as opposed to RR systems, PARs consist of arrangements of antenna elements, which collimate the electromagnetic beams in H and V. Therefore, consistent fabrication and initial calibration procedures have to be employed to produce sufficiently matched H/V beams; (2) as opposed to RR systems, PARs are designed to electronically steer the beam in any direction within the field of view. Due to intrinsic differences in the (cartesian) earth coordinate system and the (polar) antenna coordinate system, the H and V polarizations are not orthogonal when scanning away from the array broadside (i.e., direction perpendicular to the array face), which introduces biases in radar-variable estimates (3) cross-polarization contamination [74] increases significantly as the beam is steered away from the principal planes. Although there are challenges with calibration of the H and V polarization channels to attain the required accuracy of polarimetric-variable estimates, recent research efforts show that it is possible to mitigate biases induced by the antenna system to obtain reasonable polarimetric-variable estimates [46].

An alternate transmission and simultaneous reception of electromagnetic waves with horizontal and vertical (AHV) polarizations has been proposed as a possible

alternative to increase cross-polar isolation of the H and V antenna patterns [75–77]. In this mode, the polarization of transmitted electromagnetic fields is alternated on a pulse-to-pulse basis. Figure 2.5 from [77] illustrates the pulse sequences in the SHV and AHV modes. Although cross-couplings of H and V fields are reduced
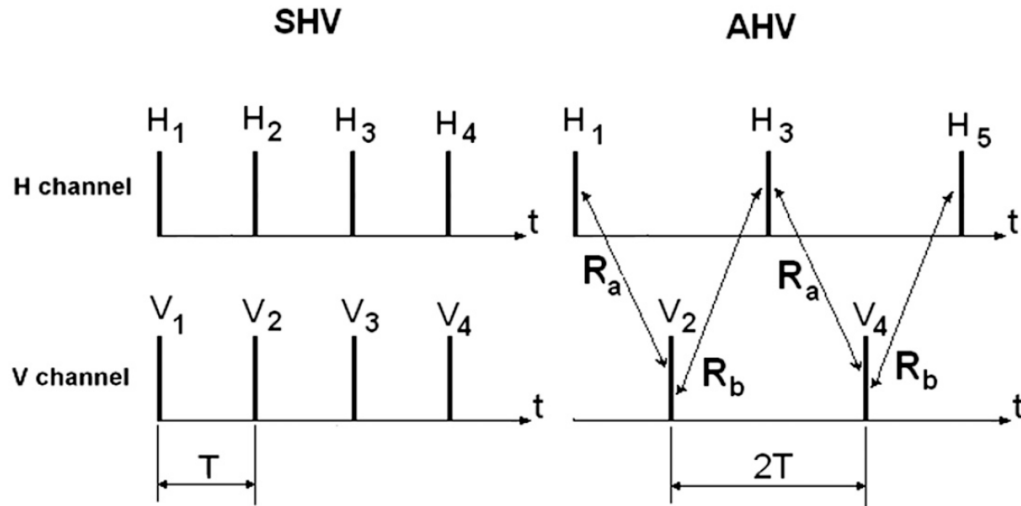
Figure 2.5: Schematic representation of pulse sequences in the SHV and AHV modes from [77].

in the AHV mode, the quality of polarimetric estimates is significantly degraded. This is because H and V weather signals rapidly decorrelate, and a time lag of T_s between these signals in the AHV measurements is enough to introduce large biases in polarimetric estimates. As concluded by [77], the quality of polarimetric-variable estimates in the AHV mode is vastly inferior to what is routinely achieved in the surveillance SHV mode on the WSR-88D. Although the AHV mode may not be suitable for polarimetric weather surveillance, it could be used for some research applications in radar meteorology.

Another transmission mode option proposed by [77] is the Quasi-SHV (QSHV) mode. It consists of a fast switching of polarizations on transmission, whereby after transmitting a horizontally polarized wave, the transmission is quickly switched to

the vertical polarization. If the time between these H and V pulses is short ($\ll T_s$), good correlation of the H and V signals is preserved and the quality of polarimetric variables may be acceptable. While this mode has been presented as an alternative to the SHV mode on PAR systems to increase cross-polar isolation, ongoing research efforts are still evaluating the feasibility of this mode for polarimetric weather surveillance.

Transmission mode flexibility is feasible with the three systems considered, although PAR technology provides a higher level of flexibility than RR systems. Three transmission modes have been proposed, but since the quality of polarimetric-variable estimates is generally lower using modes other than SHV [77, 78], there is little interest in AHV or QSHV. Given that there are many open questions with modes other than SHV, this capability is considered in a medium level of maturity for the three systems. Considering that it is unlikely that the mechanical rotation of the radar will have a significant impact on the performance of a transmission mode (because it is mostly controlled by the decorrelation of signals in sample time), this is not considered a unique capability for the RPAR and is not discussed in this dissertation hereafter.

2.2.7 Agile Beam Steering

Agile beam steering refers to the capability of steering the radar beam to illuminate a different beam position within the scan sector almost instantly (in the order of μs) without mechanical inertia. Beam agility is only possible with phased array antennas, and is one of the key advantages of stationary PAR systems over RR systems. The agile beam capability provides PARs with the ability to quickly switch the scan sector to observe different regions of interest. This concept is illustrated

in Figure 2.6, extracted from [21]. It may be possible to operate an RR system to scan only certain regions with meteorological targets of interest [79] (without beam agility, by mechanically scanning), this would take a longer time than an agile-beam PAR would take to scan the same regions (with the same acquisition parameters). This mode of operating RR systems introduces significant wear in the mechanical system and is not conventionally used in operations. Several applications that ex-
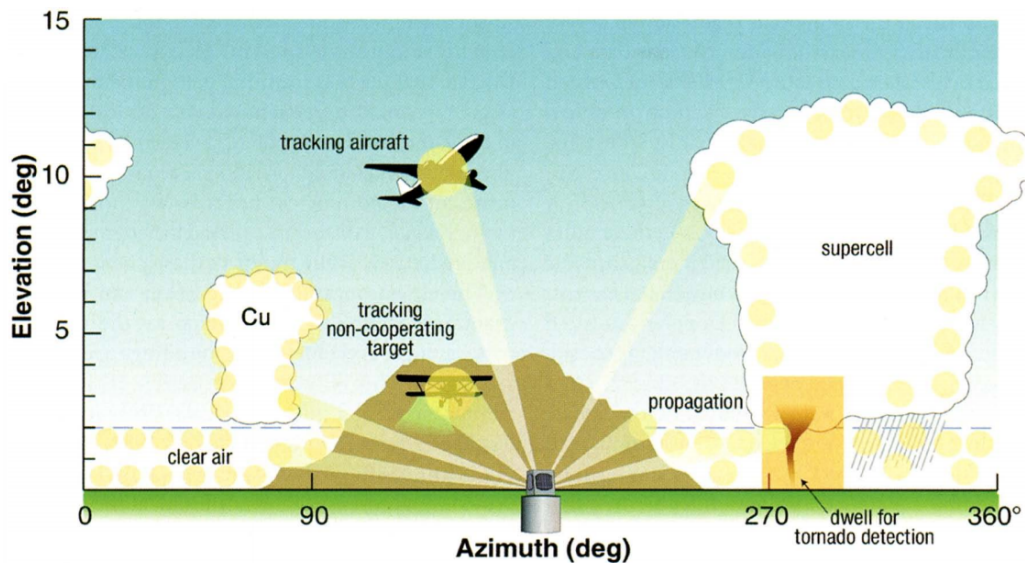
Figure 2.6: Illustration of the agile beam steering capability offered by Phased Array Radars, from [21].

ercise the agile beam steering capability of PARs have been proposed for weather observations. For instance, Yu et al. [24] demonstrated the use of *beam multiplexing* (BMX), whereby the PARs beam agility is exploited to reduce the number of samples needed to achieve the required data accuracy, resulting in a reduction of the scan time. Furthermore, the beam agility capability can greatly increase the effectiveness of adaptive scanning techniques, by which the scanning strategy is dynamically evolving to improve observations of meteorological echoes of interest (this is discussed in section 2.2.9).

Beam agility is not feasible with the RR architecture, but can be readily exploited with a 4F-PAR architecture. While the RPAR is capable of beam agility, exploiting this capability may not be trivial due to the continuous mechanical rotation of the antenna in azimuth. For example, the RPAR's beam agility could be used to reduce beam smearing effects (i.e., an increase in the effective beamwidth), resulting from the continuous antenna rotation coupled with the need to perform coherent processing of multiple samples. That is, by electronically steering the beam to the same earth-relative angular location for all the pulses within the CPI, beam smearing effects from a rotating platform can be mitigated. Bluestein et al. [25] demonstrated the "back scanning" capability with the MWR-05XP to produce rapid volumetric observations of convective storms. This back-scanning technique was implemented through frequency hopping and allowed the beam to dwell at a nearly fixed azimuth angle to collect the required samples. Although they briefly described this motion-compensation concept, they did not provide sufficient evidence quantifying the trade-offs associated with the technique nor to verify its performance. Furthermore, the impact of electronically steering the beam for samples within a CPI on polarimetric-variable estimates was not investigated. An effective implementation of this technique on a dual-polarization RPAR could reduce beam smearing and allow for smaller (and more affordable) antenna apertures that can meet effective-beamwidth requirements. This capability can be exploited by an RPAR to reduce beam smearing effects, but the impact on polarimetric-variable estimates will have to be investigated. In summary, beam agility is not feasible with RR's but it can be considered of medium maturity level for the RPAR and high maturity level for the 4F-PAR.

2.2.8 Digital Beamforming

Digital beamforming is the capability of forming radar beams by means of digitally combining signals received from spatially separated subarrays or antenna elements. This concept was initially proposed by [80] and [81] in the 1980's and has been widely used to develop advanced scanning and signal processing techniques for applications including wireless communications [82], air surveillance and defense [41, 83, 84], biomedical [85], and weather radar observations [42, 44, 86–88].

A common application of digital beamforming for weather observations involves the transmission of a *spoiled* beam to illuminate a wide sector, and the simultaneous reception of multiple beams within the spoiled envelope. Spoiled transmit beams are commonly synthesized by varying the magnitude and phase of transmit signals at each individual array element (commonly referred to as *tapering*) in an active PAR. Other types of antennas can be used to transmit wide beams, as demonstrated by [86] with the Atmospheric Imaging Radar (AIR), where a slotted waveguide passive array is used to transmit a fixed "fan" beam. Because of the wider transmit beam, this comes at the expense of increased two-way antenna sidelobe levels, reduced two-way antenna gain, and slightly increased beamwidth. A schematic from Kurdzo et al. is reproduced in Figure 2.7 to illustrate this concept, referred to as *radar imaging*.

RR architectures typically consist of a single transmitter and one receiver channel per polarization, and therefore do not support digital beamforming. In contrast, both the 4F-PAR and the RPAR can support digital beamforming capabilities, which can be exploited through advanced scanning techniques to meet the RFR. Kurdzo et al. [44] used a fan beam in elevation to reduce the AIR's scan time and observe
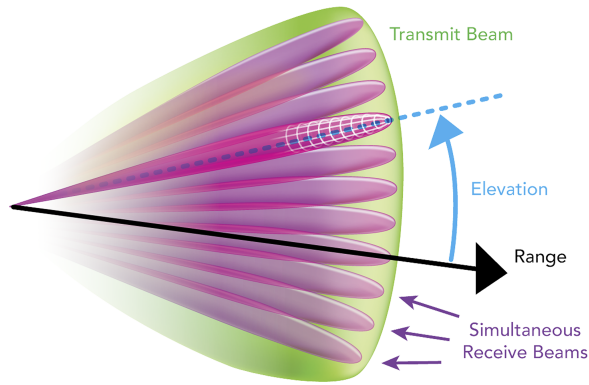
Figure 2.7: Illustration of radar *imaging*, whereby a wide transmit beam in elevation illuminates a large sector and simultaneous receive beams are formed within transmit beam, from [44].

a 120°-wide azimuthal and 20°-wide elevation sector in approximately 8 seconds. This proof-of-concept radar was operated as an RPAR, whereby the antenna was mechanically rotated in azimuth while digitally forming beams in elevation; it is noted that the AIR was not capable of continuously rotating 360° in azimuth, and only sector scans were possible. However, the AIR's fan beam is 20° in elevation, which results in a significant sensitivity loss (capable of detecting ~10 dBZ at 10 km), and relatively high sidelobes (~-13.3 dB with respect to broadside). The key compromise exercised by the AIR system using digital beamforming is the trade of scan-time reduction for degraded sensitivity and spatial resolution (i.e., HPBW and sidelobe levels). That is, the use of narrower spoiled beams will reduce the sensitivity loss at the price of a smaller scan time reduction. Other techniques (such as pulse compression and advanced digital beamforming) can be used to mitigate the sensitivity loss and the increase in sidelobe levels.

The CONOPS implemented on the AIR radar could be considered in the RPAR design phase to account for beamforming tradeoffs, namely: increased sidelobe levels, increased beamwidth, and reduced sensitivity. An important advantage of

this CONOPS is that it is compatible with low mechanical rotation speeds, which reduces the mechanical wear of the pedestal and increases its mean time between failures. Nevertheless, when spoiling the beam and scanning in elevation, the same acquisition parameters must be used for all elevations in the cluster. And while the lower elevations in the WSR-88D's use two scans of the same elevation (with different PRTs) to mitigate range and velocity ambiguities, higher ones do not. Therefore, spoiling a wide fan beam in elevation could impact the quality of estimates at higher tilts or unnecessarily add more time to the scan. For example, surveillance scans at the lower tilts use longer PRTs, this would limit the Nyquist co-interval at some tilts, or the maximum unambiguous range at others. Furthermore, for typical WSR-88D scan strategies, elevation angles scanned at higher altitudes are spread by several degrees. The larger the spoiling factor, the larger the sensitivity loss incurred and the larger the increase in sidelobe levels. Spoiling the beam across angles that are not needed nor typically scanned (i.e., leaving large gaps) will result in an unnecessarily large sensitivity loss.

The concept of digital beamforming was proposed decades ago for PAR systems and has been recently demonstrated for single-polarization weather observations using the stationary PAR and RPAR systems. Nevertheless, digital beamforming capabilities create new CONOPS possibilities that should be investigated for the RPAR architecture. That is, through beam pattern synthesis methods [89], transmit beams could be spoiled in either azimuth only, elevation only, or both azimuth and elevation. While not all of these concepts have been considered for weather observations, they may provide ways to reduce the scan update times by trading other radar resources (e.g., sensitivity, angular resolution). In summary, this capability is not feasible with RR systems but can be considered of medium maturity level for the RPAR and high maturity level for the 4F-PAR.

2.2.9 Adaptive Scanning

The adaptive scanning capability refers to the radars' ability change the scanning strategy (e.g., combining dwell flexibility, beamforming, agile beam-steering) on the fly to focus radar resources on constantly evolving meteorological echoes of interest. Adaptive scanning algorithms are capable of managing radar resources to selectively improve the temporal resolution, spatial sampling and/or data quality of meteorological observations. These algorithms aim to maximize the use of these radar resources to provide users the critical information they need, when they need it [90]. For instance, severe storms (e.g., supercell thunderstorms or hail storms) can develop in a matter of a few minutes [91], which can be very challenging to forecast in real time with relatively slow update times. In fact, current experiments strongly suggest that radar data with high-temporal resolution could be beneficial in the warning decision process of NWS forecasters [92, 93]. Adaptive scanning techniques can lead to faster update times, which in turn supports NWS forecasters conceptual modeling of fast evolving convective storms.

Adaptive scanning techniques have been implemented and tested on the three architectures considered here. Chrisman [94] developed the Automated Volume Scan Evaluation and Termination Automated Volume Scan Evaluation and Termination (AVSET) technique which dynamically controls the number of scanning angles in elevation based on the sampled meteorological returns observed. AVSET terminates the current volume scan if minimum thresholds for reflectivity are not met, shortening the volume scan time. This technique has been operational in the WSR-88D network since the early 2010's. McLaughlin et al. [95] demonstrated adaptive storm sampling capabilities with a small network of X-Band RR systems in the context of the Collaborative Adaptive Sensing of the Atmosphere project. How-

ever, given the limitations of RR systems for dynamically adapting the scan parameters, the advantages of using adaptive scanning techniques to reduce the scan time are not significant. Adaptive scanning techniques are more effective with capabilities provided by the phased array technology. Torres et al. [23] demonstrated the ADAPTS with the single-polarization PAR at the NWRT (SPY-1A), which works by identifying beam positions with significant meteorological returns in real time and scheduling them beams to scan them with the goal of reducing the scan time. Schvartzman et al. [96] proposed an adaptive scanning algorithm, based on a model of the human attention system, capable of defining sectors of meteorological interest to be scanned by the radar.

The effectiveness of adaptive scanning techniques is limited for RR architectures, due to (1) the mechanical inertia of the rotating antenna, and (2) the lack of beam agility and/or beamforming capabilities. PAR technology is more suitable for adaptive scanning techniques due to the additional degrees of freedom it offers. Initial research efforts demonstrated adaptive scanning techniques on stationary PAR systems (similar to the 4F-PAR), but research on adaptive scanning for the RPAR has been more limited. Although the mechanical rotation of the RPARs' antenna may impose limitations that would reduce the effectiveness of adaptive scanning techniques, the additional flexibility provided by phased array technology could allow for a considerable level of flexibility for adaptive scanning (with respect to the RR architecture).

Adaptive scanning is feasible with the three radar architectures considered here, with PAR-based systems being more capable of exploiting it. This capability is not considered very mature in either one of the architectures, although initial research for the 4F-PAR system indicates that adaptive techniques could be used to reduce the scan time and/or the variance of estimates. This capability is considered of

medium-maturity level for the 4F-PAR, but given that the mechanical rotation of the antenna imposes significant constraints on the use of adaptive scanning with RPARs, it is considered of low maturity for this architecture. It is worth exploiting possibilities for adaptive scanning using an RPAR system, as will be discussed later in this dissertation.

2.2.10 Summary of capabilities

The capabilities described are summarized in Table 2.1 for the RR, RPAR, and 4F-PAR architectures.

| Capability | Radar Architecture | | | | | |
| | RR | | RPAR | | 4F-PAR | |
	Feasible	Maturity	Feasible	Maturity	Feasible	Maturity
Polarimetric observations	Yes	High	Yes	Med	Yes	Med
Pulse compression	Yes	High	Yes	High	Yes	High
Frequency Diversity	Yes	High	Yes	Med	Yes	Med
Phase Coding	Yes	High	Yes	Med	Yes	Med
Dwell flexibility	Yes	Med	Yes	Low	Yes	Med
Transmission mode flexibility	Yes	Med	Yes	Med	Yes	Med
Agile Beam Steering	No	N/A	Yes	Med	Yes	High
Digital Beamforming	No	N/A	Yes	Med	Yes	High
Adaptive scanning	Yes	Low	Yes	Low	Yes	Med

Table 2.1: Radar capabilities for each architecture

2.3 Capabilities Selected for the RPAR

The previous section provided an overview of possible radar capabilities that could support the design of an RPAR CONOPS. In this section, three unique RPAR capabilities are selected to develop scanning and associated signal processing methods. Selected capabilities should support achieving the following goals (1) to enhance the angular resolution of the RPAR with respect to a 4F-PAR with equal aperture size, (2) to reduce the scan update time, and (3) to reduce the standard deviation of radar-variable estimates.

The selected capabilities are: agile beam steering (Section 2.2.7), digital beam-forming (Section 2.2.8), and dwell flexibility (Section 2.2.5). Although previous research efforts have explored these capabilities to some extent, they are exploited in this dissertation to develop novel scanning and signal processing techniques in support of the RPAR CONOPS. First, the capabilities are used to develop, quantify, and demonstrate novel signal processing techniques for RPAR. Then, the techniques are integrated to operate in conjunction. This is ultimately used to design an RPAR CONOPS that, with certain design considerations, meets the radar functional requirements.

2.3.1 Agile Beam Steering

One of the cost-driving threshold requirements specifies the effective angular resolution of the radiation patterns produced by the antenna system. The HPBW is typically reduced by increasing the antenna aperture size. The system is expected to produce a radiation pattern that results in a narrow beamwidth of at most $1°$ in azimuth and elevation, as specified by the threshold requirement. For an RR, due to continuous antenna rotation coupled with the coherent processing of mul-

tiple samples, the resulting effective antenna beamwidth (ϕ_e) is broader than the stationary inherent antenna beamwidth [97] when operating an RR or maintaining the RPAR beam at broadside. The effective beamwidth is controlled by the HPBW (ϕ_1), the antenna rotation rate (ω), and the normalized azimuthal sampling interval ($\Delta\phi$) [52]. Although no optimal requirement is specified in [38] for the effective beamwidth (it is implicit in the CONOPS selected), researchers have demonstrated that the identification of velocity signatures from tornadoes is greatly improved when the effective beamwidth of the radar is 1° or less and the sampling is one half the HPBW [4, 98]. Therefore, it is desirable to design a cost-effective radar system that meets angular resolution requirements and is capable of producing weather observations resulting in an effective beamwidth of at most 1° in azimuth and elevation. Note that if electronic steering is used in elevation, the RPAR antenna has to be designed such that the HPBW in elevation is 1° at the highest elevation angle to be scanned.

The 4F-PAR architecture is not susceptible to beam broadening due to antenna motion and is capable of sampling the same resolution volume for all transmitted pulses within the CPI [21]. Nevertheless, it is well-known that the beamwidth of a stationary planar PAR system varies as a function of steering angle, and it monotonically increases as the beam is steered away from the antenna's principal planes [89]. Brown and Wood [99] simulated the performance of this architecture for detecting tornado vortices. Their study found that the widest antenna beamwidth should be no more than ∼1° in order to provide NWS forecasters with "*at least the same quality of data resolution that is currently available for making tornado and severe storm warnings*". To ensure that the beamwidth on the edges of the scan sector (e.g., typically ±45° in azimuth and 0–20° in elevation) is ∼1°, a broadside beamwidth of 0.758° is needed.

The RPAR architecture is susceptible to beam smearing effects, and large aperture sizes may be required to achieve the desired effective beamwidth requirement. Figure 2.8 illustrates the impact of $\Delta\phi$ on the effective broadside beamwidth of simulated planar RPAR systems with approximately circular apertures of different sizes (where N_x is the total number of antenna elements for a stationary broadside HPBW of $x°$), and a half-wavelength element spacing in a rectangular element lattice. Transmit patterns are simulated using a uniform tapering window, and receive
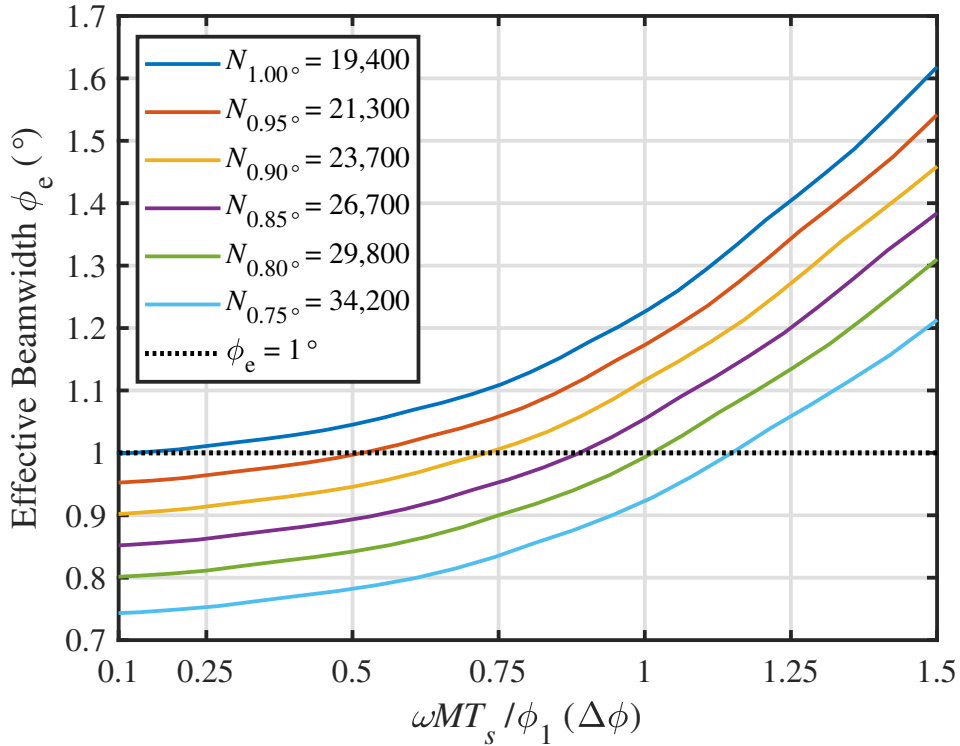
Figure 2.8: Effective broadside beamwidth of planar RPAR systems of different sizes (N_x is the total number of antenna elements for a stationary broadside HPBW of $x°$) as a function of the normalized azimuthal sampling, $\Delta\phi$.

patterns are simulated using a Taylor tapering window to achieve -70 dB two-way antenna sidelobe levels (as indicated in Table 1.1). Notice that $\Delta\phi$ is determined by T_s, M, ω, and ϕ_1. These results indicate that to achieve a ϕ_e of 1° for $\Delta\phi$ of

up to 1 (typically known as the "legacy" sampling in the WSR-88D), an aperture comprising 29,800 elements (or $\sim 85\lambda \times 85\lambda$ where λ is the radar wavelength, and with a true beamwidth of 0.8°) has to be designed. Beam smearing is unavoidable when operating the RPAR with the beam always at broadside (similar to an RR system), since resolution volumes in the CPI are not concentric. However, the RPAR has more capabilities than the RR, which should be used in the most effective way. It is desired to exploit advanced capabilities of the RPAR system to decrease the effective beamwidth, leading to reduced aperture sizes capable of meeting effective beamwidth requirements.

In this dissertation, the RPAR's beam agility is exploited to reduce beam smearing effects under a continuous azimuthal rotation regime. By electronically steering the beam on a pulse-to-pulse basis within the CPI, the motion of the antenna is compensated to maintain the beam pointed at the same earth-relative angular direction. The MCS technique could ideally remove the apparent motion of the antenna and lead to a reduction in the effective beamwidth. In turn, mitigating the impact of beam smearing allows for smaller (and more affordable) antenna apertures that can meet angular resolution requirements. Chapter 3 presents and demonstrates the MCS technique for a dual-polarization RPAR system.

2.3.2 Digital Beamforming

Active PAR technology allows the synthesis of antenna radiation beam patterns on transmission. This capability can be used to produce a wider transmit beam, effectively increasing the beam coverage. For example, an active PAR antenna with an inherent non-tapered radiation pattern that produces a narrow "pencil" beam (as defined by the one-way 3-dB width), can also be used to synthesize wider trans-

mit beams as illustrated in Figure 2.9 [100]. Modern PAR can form multiple received beams within the wide transmitted beam simultaneously through digital multi-channel receivers [101]. The digitally generated beams are received with the
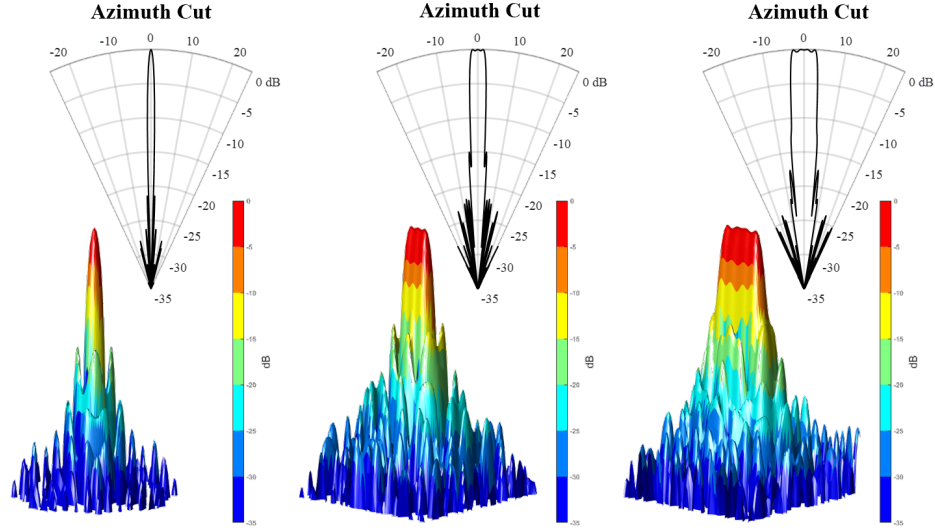
Figure 2.9: Simulated one-way antenna radiation patterns for a narrow pencil beam (left), a beam spoiled by a factor of three (center), and a beam spoiled by a factor of five (right). Sectors correspond to azimuthal cuts of the antenna patterns.

full antenna aperture to produce narrow one-way pencil beams. However, the side-lobe levels of so synthesized two-way beams are typically considerably higher, and the beamwidth is slightly increased compared to two-way patterns obtained when using a narrow beam on both transmission and reception. This is due to both the use of digital beamforming methods, as noted by [86], and the use of a wide spoiled transmit beam, as noted by [102]. For this study, the standard Fourier beamforming method is used to form the receive beams. Considering that digital beamforming is used to form beams within the relatively narrow spoiled beam tapers (worst case for spoiled beams in this work is $\sim \pm 3.5°$ about the broadside), and that the spoiled transmit beams are always on broadside, the increase in sidelobe levels is largely controlled by the spoiled transmit beam taper. Beamforming tradeoff considera-

tions discussed by [102] could be used to design RPARs with acceptable sidelobe levels.

One of the most demanding optimal requirements is the 1-minute update time to complete a volume scan "*with no degradation of the sensitivity, spatial resolution or standard deviation of measurement for radar variable estimates*". Digital beamforming has been used in stationary PAR systems to reduce the volumetric update time by scanning clusters of simultaneous beams. Researchers have demonstrated the use of digitally formed beams in elevation to reduce the volume scan time of an RPAR [26, 42, 44]. Digital beamforming in azimuth has been proposed for stationary PAR systems to reduce the scan time [103] but has not been considered for weather surveillance using RPAR systems.

The novel DB technique introduced in this dissertation provides a way to reduce scan update times or alternatively improve the data quality for an RPAR CONOPS. This is accomplished by synthesizing an azimuthally wide (spoiled) beam on transmission and then using digital beamforming to form several simultaneous beams on reception as the radar rotates (herein, this is referred to as a cluster of receive beams). Returns from subsequent receive beams scanning the same direction are then processed coherently. Specifically, the azimuthal rotation rate of the platform is derived from the duration of the CPI to produce the desired spatial sampling. Consequently, beams from subsequent CPIs are received from approximately the same direction. For example, if the antenna rotates in the clock-wise direction and the receive beams in a cluster are numbered in the same direction, the last receive beam from the first cluster and the second-to-last receive beam from the second cluster both point at the same azimuth. This allows to either reduce the scan time by a factor equal to the number of received beams in a cluster, or to increase the number of available data samples to improve data quality. In this manner, the scan

time can be reduced by a factor equal to the number of receive beams in the cluster (herein referred to as R_F). Examples of transmit beam patterns with spoil factors (F) of 3 and 5, as well as the inherent narrow beam pattern for the array synthesizing them are presented in Figure 2.9. In other words, the DB technique exploits the use of digital beamforming in azimuth and allows a faster rotation rate to be maintained, leading to more rapid updates potentially without degradation in data quality. Alternatively, if the rotation rate is maintained, the number of samples can be increased by a factor of R_F, which leads to reduced variance of radar-variable estimates [104]. Furthermore, scanning a cluster of receive beams in both azimuth and elevation could provide a larger scan-time reduction factor, at the price of reduced sensitivity and angular resolution. Under this concept, the DB technique could be used along the azimuth plane for a specific elevation angle, and applied independently to clusters of receive beams at other elevation angles. Chapter 4 presents a detailed technical analysis of the DB technique.

2.3.3 Dwell Flexibility

Functional requirements state that, while meeting other demanding requirements, there should not be a degradation in the standard deviation of radar-variable estimates. The requirements specifying volume scan time, spatial sampling, and standard deviation of estimates are tightly coupled. For example, to achieve a standard deviation in Z_h estimates of 1 dBZ with $T_s = 1$ ms, a total of $\sim$54 samples are required (computed using theoretical expressions provided by [52]), for the benchmark SNR and σ_v of 10 dB and 4 m s^{-1} (see last row in Table 1.1). This results in a dwell time of 54 ms. If a spatial sampling spacing of one-half beamwidth is used, $\Delta\phi = 0.5$, then the time to scan one elevation in the PPI mode using these

parameters is 38.88 s. With convective precipitation VCPs typically consisting of 14-19 elevation angles [105] (with $\Delta\phi = 0.5$ in the lowest three tilts and $\Delta\phi = 1$ on the higher ones), it is challenging to simultaneously meet the volume scan time (1 min) and standard deviation in Z_h estimates (1 dBZ) requirements.

The dwell flexibility capability is considered in this work as an important tool to trade radar time for improved standard deviation of estimates. Similar to the ADAPTS algorithm introduced by [23], two mechanisms can be employed to reduce the scan time (1) beam positions without weather echoes of interest can be *disabled*, and (2) PRTs could be reduced to scan up to the maximum range of storms observed. Considering an RPAR rotating at a constant rate, the time gained could be used to adaptively increase the number of samples in scanned beam positions, which would reduce the standard deviation of estimates.

Dwell flexibility is exploited in conjunction with beam agility. A scan with CPI-interleaved beams with different dwell definitions can be designed to simultaneously provide acceptable maximum unambiguous range and velocity weather observations. One of the interleaved beams performs the long range surveillance function (typically a $T_s = 3$ ms), and the other one the unambiguous Doppler measurement function (typically a $T_s = 1$ ms). A CONOPS consisting of *forward-looking* surveillance beams scanned ahead of the radar broadside (i.e., positive antenna-relative steering angles) and *back-scanning* Doppler beams scanned behind the radar broadside (i.e., negative antenna-relative steering angles) is defined. One possible application of the FBT is to eliminate the need for two full revolutions of the antenna to collect a split cut (such as those used in the VCPs of WSR-88Ds), and collect these scans in a single revolution of the antenna. In WSR-88D split cuts, the same elevation angle is scanned twice with different PRTs as a means to mitigate range-and-velocity ambiguities. Using the FBT, the forward-looking beams

would collect the surveillance-scan data, and the back-scanning beams would collect the Doppler-scan data; both within a single revolution of the RPAR. This in turn would reduce the wear on the antenna rotator and may increase the lifespan of the antenna pedestal. A better application of FBT would involve its use under an adaptive scanning concept, as mentioned previously, where the backward beams are tailored in real time. Chapter 5 presents a detailed technical analysis of the FBT technique.

2.4   Concept of Operations

The RPAR architecture has been used for air surveillance and defense applications since the late 1970's [39–41] but was only introduced for weather surveillance in recent years [42–45]. The CONOPS for these weather RPAR systems consist of either imitating the operation of conventional RR with continued mechanical rotation and increasing elevation each rotation or performing a straightforward electronic scan in elevation while mechanically rotating slowly in the azimuthal direction. These limited operational concept modes fall short of exploiting all of RPAR's unique capabilities and are not likely to meet demanding functional requirements such as the more rapid-update volumetric data.

Advanced RPAR capabilities can be exploited in different ways to design a CONOPS with the goal of meeting the RFR. Achieving the best tradeoff by balancing advanced capabilities, system cost, and complexity is challenging, and the solution to meet demanding optimal requirements is likely to require a combination of compatible scanning and signal processing techniques. Techniques developed and demonstrated in this work are not only compatible, but complementary, and can be used as building blocks under the RPAR CONOPS to construct scan strate-

gies for weather observations.

The MCS technique is utilized to mitigate beam smearing effects, enhancing the azimuthal resolution (with respect to stationary operation), and allowing for smaller and more affordable antenna apertures that meet the $1°$ azimuthal requirement. The DB technique is utilized to reduce scan times, reduce the standard deviation of radar-variable estimates, or a combination of both. Using the DB technique on the forward-looking beams of the FBT allows to reduce the surveillance scan time, and using adaptive scanning techniques to tailor the back-scanning beams may increase the maximum unambiguous velocity and reduce the standard deviation of estimates. These techniques are integrated to operate in conjunction and to create a large space of design tradeoff considerations to build the RPAR CONOPS. Chapter 6 brings the scanning and signal processing techniques presented together to provide tailored VCPs under the RPAR CONOPS.

Chapter 3

Motion-Compensated Steering

"If the theory turns out to be right, that will be tremendously thick and tasty icing on the cake."

<div align="right">

Brian Greene

</div>

3.1 Introduction

The concept of MCS was initially developed for air surveillance and defense radars in the mid 1970's [106] and has since been widely used for synthetic aperture radar. Initial applications of this concept for meteorological observations were presented in 2002 by Law et al. [107] to compensate for platform motion for a shipborne, vertically pointed, L-band, passive PAR wind profiler system. Their experimental results showed that the electronically stabilized wind profiler measurements were in good agreement with profiles measured by simultaneous rawinsonde balloon launches. As mentioned previously, Bluestein et al. [25] used a mobile radar with a frequency-hoping-based motion-compensation method, but they did not quantify the performance of the technique and did not investigate its feasibility for dual-polarization observations.

As introduced in Section 2.3.1, the motion of the antenna can be compensated

to maintain the beam pointed at the same earth-relative angular direction by electronically steering the beam on a pulse-to-pulse basis within the CPI. MCS could ideally remove the apparent motion of the antenna and lead to a reduction in the effective beamwidth, which in turn, allows for smaller (and more affordable) antenna apertures that can meet azimuthal resolution requirements. Even though it can be ideally assumed the beam pointing directions within a CPI are the same for a dwell of MCS, practical system imperfections (such as the element-level phase noise or the precision of the mechanical rotator) can introduce biases in the pointing direction, which may affect the performance of MCS. Impacts of beam pointing offsets on the performance of MCS should also be investigated.

The purpose of this chapter is to present the concept, simulation, practical implementation, and demonstration of the MCS technique for a dual-polarization RPAR system. A theoretical formulation for the MCS technique is described in Section 3.2, along with a CONOPS for implementing MCS on an RPAR system. A simulation framework to quantify the performance of the MCS technique is presented in Section 3.4. The performance of MCS for the mitigation of beam-smearing effects is quantified first, and then, impacts on the quality of dual-polarization measurements are investigated. Section 3.5 describes the practical implementation of the MCS technique on NSSL's ATD, and presents data collection experiments. Important outcomes of this Chapter are outlined in Section 3.6.

3.2   Theoretical Formulation

To implement MCS, the RPAR's electronic beam agility is exercised on a pulse-to-pulse basis. The radar beam is electronically steered to the same earth-relative angle (i.e., the same azimuth and elevation angles) for all the pulses within the CPI.

In other words, the radar resolution volumes from those pulses are centered at the same location. Note that this concept can be implemented using either pencil or spoiled transmit beam patterns. We begin with a pencil beam implementation in this chapter, and later in Chapter 6 we describe the implementation using spoiled transmit beams.

The concept of MCS is depicted in Figure 3.1, in comparison to the conventional sampling of a mechanically scanning antenna (i.e., No Beam Steering). Notice that as the RPAR's beam is electronically steered away from broadside, the HPBW is broadened as a function of steering angle. Therefore, as opposed to the displaced uniform volumes sampled with the broadside scanning beam (top panel in Figure 3.1), the concentric volumes sampled by MCS are not the same size (bottom panel in Figure 3.1). While the RPAR can also scan without beam steering, it is beneficial to use MCS to mitigate beam smearing in azimuth, as long as data quality is minimally impacted.

These aspects are studied in detail in the following three subsections. First, the MCS steering angles to maintain beam pointing in azimuth and elevation are derived for the antenna-relative coordinate system. Then, the variation in volume size as a function of steering angle is theoretically modeled to understand its impact in the quality of radar-variable estimates. Lastly, an RPAR CONOPS using MCS is presented.

3.2.1 Steering Angles

Assume that an RPAR is rotating about the z-axis at a rate of ω ($^\circ$ s^{-1}), in a spherical coordinate system with polar axis z vertical, and with x in the direction of North as indicated in Figure 3.2. This coordinate system is tied to the earth, and therefore

No Beam Steering

Volume 1 (ϕ_0, θ_0)
Volume 2 (ϕ_0, θ_0)
Volume 3 (ϕ_0, θ_0)
• Phase Center

(a)

Motion-Compensated Steering

Volume 1 (ϕ_{-1}, θ_{-1})
Volume 2 (ϕ_0, θ_0)
Volume 3 (ϕ_1, θ_1)
• Phase Center
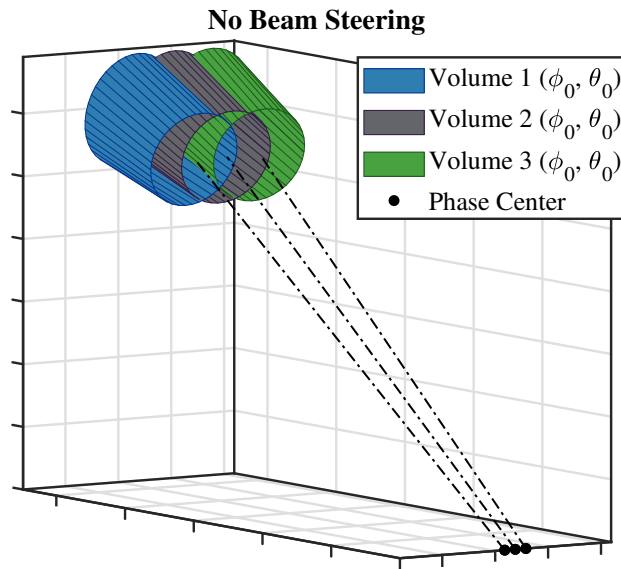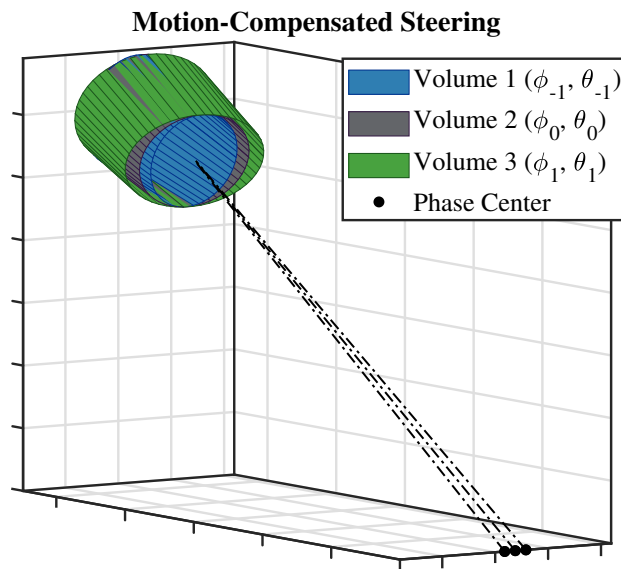
(b)

Figure 3.1: Depiction of the MCS concept. The top panel illustrates the location of resolution volumes being sampled by the antenna without beam steering, while the bottom panel illustrates the location of resolution volumes being sampled with MCS.

the x axis is always directed to North. Note that the antenna lies on a plane that rotates about the z axis and is orthogonal to the x–y plane. This antenna geometry is convenient for modeling arrays designed to scan close to the horizon [108]. Assume the array broadside is pointed in the earth-relative direction (ϕ_N, θ_N). The desired
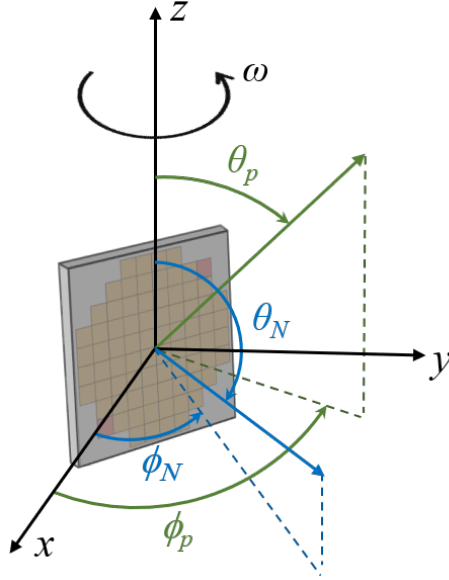
Figure 3.2: Spherical coordinate system used to reference the RPAR scanning with MCS.

scan pointing angle referenced to the earth-relative spherical coordinate system is denoted as (ϕ_p, θ_p). Note that $\phi_p = \phi_{az}$ and $\theta_p = 90° - \theta_{el}$, with θ_{az} and θ_{el} being the conventional earth-relative azimuth and elevation angles, respectively, and are the zenith and azimuth directions to the scatterers. Then, ϕ_N as a function of time is expressed as

$$\phi_N(t) = \phi_0 + \omega t, \tag{3.1}$$

where ϕ_0 is the initial broadside position, and t is time in seconds. If the CPI is defined by M samples spaced by T_s, equation (3.1) can be discretized to produce

the MCS steering angles as,

$$\phi_{MCS}(mT_s) = \phi_p - \phi_N = (\phi_p - \phi_0) + \omega \left[\frac{M-1}{2} - m \right], \qquad (3.2)$$

for $m \in \{0, 1, 2, \ldots, M{-}1\}$, and with $t = mT_s$. For simplicity and without loss of generality, it is assumed that M is odd and that the radar is rotating in the clockwise direction. Note that this ϕ_{MCS} is referenced to the earth's polar coordinate system. If the antenna is tilted by θ_T, with respect to the earth, then the MCS pointing angles relative to the antenna coordinate system are given by (see Appendix B for details),

$$\phi^A_{MCS}(mT_s) = \arctan \left\{ \frac{\sin \theta_p \sin [\phi_{MCS}(mT_s)]}{\sin \theta_p \cos [\phi_{MCS}(mT_s)] \cos(\theta_T) + \cos \theta_p \sin(\theta_T)} \right\}$$

$$\theta^A_{MCS}(mT_s) = \arccos \left\{ - \sin \theta_p \cos [\phi_{MCS}(mT_s)] \sin(\theta_T) + \cos \theta_p \cos(\theta_T) \right\},$$
$$(3.3)$$

where the superscript A indicates these angles are relative to the antenna. Thus, to maintain the beam pointed at the desired earth-relative scan angle (ϕ_p, θ_p), equations in (3.3) should be used to determine the steering angles to command the antenna.

3.2.2 Impact on Signal Power and Copolar Correlation Coefficient Estimates

It is of interest to study the effects of varying resolution volume locations (caused by beam pointing errors) and sizes introduced by the copolar antenna patterns when using MCS on radar-variable estimates. First, we investigate the effects of resolution volume locations on signal power estimates. Then, we investigate biases (i.e., with respect to the broadside beam of a stationary PAR) in the SHV copolar correlation coefficient as a function of resolution volume sizes. This accounts for 1) impacts

from the varying two-way radiation pattern beamwidths for pulses within the CPI, and 2) impacts from beam pointing offsets that could be caused by a number of reasons (e.g., quantization of steering angles, phase noise, precision of the mechanical platform). It is assumed herein that if sidelobe levels are sufficiently low (e.g., $\leq$-70 dB 1.1) biases in radar-variable estimates resulting from MCS are dominated by the mainlobe of the copolar radiation patterns in H and V. The one-way antenna patterns as a function of steering angles (in the antenna-relative coordinate system) can be described as [74],

$$F_i(\phi, \theta) = \sqrt{g_i(\phi, \theta)} f_i(\phi, \theta), \qquad (3.4)$$

where $f_i(\phi, \theta)$ is the normalized one-way electric field antenna pattern, and $g_i(\phi, \theta)$ is the one-way power gain, and i is either 'h' or 'v' to indicate polarization. For system design purposes, it is a common practice to assume that the scan loss from a planar array has a $\cos^{3/2}(\phi, \theta)$ dependence [89], hence,

$$g_i(\phi, \theta) = \cos^{3/2}(\phi - \phi_s) \cos^{3/2}(\theta - \theta_s), \qquad (3.5)$$

where (ϕ_s, θ_s) is the steering angle relative to broadside in the antenna coordinate system (as shown in Figure 3.2). For simplicity, axially symmetric Gaussian functions are used to model the mainlobe of copolar H and V radiation patterns [52]. Since MCS operates mostly in ϕ, changes in θ (within the CPI) are ignored so this dimension is omitted to simplify the notation. Assume that the standard deviation of the Gaussian patterns are σ_h and σ_v, and that the difference in pointing direction of the H and V beams is Δ_ϕ. Note that pointing offsets could come from many sources (e.g., phase shifters or mechanical bias) and therefore Δ_ϕ is treated here

as a uniformly distributed random variable. Then, the power-normalized one-way power pattern of the mainlobe electronically steered at ϕ_s can be expressed as

$$f_h^2(\phi) = \frac{1}{2\sigma_h\sqrt{\pi}} \exp\left[-\frac{(\phi - \phi_s + \Delta_\phi/2)^2}{4\sigma_h^2}\right] \tag{3.6a}$$

$$f_v^2(\phi) = \frac{1}{2\sigma_v\sqrt{\pi}} \exp\left[-\frac{(\phi - \phi_s - \Delta_\phi/2)^2}{4\sigma_v^2}\right]. \tag{3.6b}$$

These widths are proportional to the HPBWs in H and V, and are expressed as $\sigma_i^2 = \phi_{1i}^2/16\ln 2$ [52]. Furthermore, PAR beamwidth variations as a function of steering angle (relative to the array broadside) can be approximated by [89]

$$\phi_{1i}(mT_s) \approx \frac{\phi_{1i}(0)}{\cos[\phi_s(mT_s)]} \quad \text{and} \quad \theta_{1i}(mT_s) \approx \frac{\theta_{1i}(0)}{\cos[\theta_s(mT_s)]}, \tag{3.7}$$

where $\phi_{1i}(0)$ and $\theta_{1i}(0)$ are the broadside beamwidths in ϕ and θ, respectively. This expression indicates that when using MCS, volume sizes for every pulse in the CPI are slightly different and the change is approximately proportional to $[\cos(\phi_s)\cos(\theta_s)]^{-1}$. Note that this change is negligible for small values of ϕ_s and θ_s.

Of interest is to compute signal power estimate as a function of steering angle and for the copolar antenna pattern functions adopted. The signal power estimate is computed as the average of M instantaneous signal-power samples. For signal power estimates, we assume a point target to obtain an upper bound on largest biases from varying resolution-volume locations. Using (3.4), (3.6a) with $g_i(\phi, \theta)$ expressed as a function of time as in (3.7), σ_h as a function of $\phi_{1h}(mT_s)$, and as-

suming a high SNR,

$$\hat{P}_h = \frac{1}{M}\sum_{m=0}^{M-1}|V_h(mT_s)|^2 \approx \frac{1}{M}\sum_{m=0}^{M-1}\int_{\phi,\theta}|F_h(\phi_m)|^4 d\phi = \frac{1}{M}\sum_{m=0}^{M-1}g_h(mT_s)^2\cdots$$

$$\cdots\frac{2}{\phi_{1h}(mT_s)}\sqrt{\frac{\ln(2)}{\pi}}\int_{\phi}\exp\left\{-\frac{[\phi-\phi_s(mT_s)+\Delta_\phi(m)/2]^2}{\phi_{1h}^2(mT_s)/2\ln 2}\right\},$$

(3.8)

where, $\hat{P}_h$, $V_h(mT_s)$, $\phi_s(mT_s)$, $g_i(mT_s)$, and $\phi_{1h}(mT_s)$ are the signal power esti-
mate in H, the received complex voltage for the horizontal polarization, the steering
angle, the power gain, and the HPBW as a function of sample number, respectively.
Note that $\Delta\phi$ is a function of m. The bias of power estimates (with respect to the
broadside and with no antenna motion) is computed as,

$$\frac{\delta P_h}{P_h} = \frac{P_h}{P_h} - \frac{\hat{P}_h}{P_h} = 1 - \frac{1}{M}\sum_{m=0}^{M-1}g_h(mT_s)^2\cdots$$

$$\cdots\frac{2}{\phi_{1h}(mT_s)}\sqrt{\frac{\ln(2)}{\pi}}\int_{\phi}\exp\left\{-\frac{[\phi-\phi_s(mT_s)+\Delta_\phi(m)/2]^2}{\phi_{1h}^2(mT_s)/2\ln 2}\right\}.$$

(3.9)

For a constant ϕ_s this expression represents the bias of power estimates from an
RPAR scanning a fixed electronic beam pointed at ϕ_s. In particular for $\phi_s = 0°$, it
represents the bias introduced by sampling slightly shifted uniform resolution vol-
umes, as in the conventional scan of a reflector-antenna radar. Similarly, selecting
$\phi_s(mT_s) = \phi_{MCS}^A(mT_s)$ in (3.3) provides an expression for the bias in power es-
timates arising form the changes in copolar patterns of the RPAR scanning when
using MCS. Note that (3.9) accounts for the scan loss (i.e., gain variations as a
function of steering angle) as well as the change in volume size as a function of
sample.

The estimator for the copolar correlation coefficient, ρ_{hv}, in the SHV mode is

defined as [69],

$$\hat{\rho}_{\mathrm{hv}} = \frac{\left| \frac{1}{M} \sum\limits_{m=0}^{M-1} V_{\mathrm{h}}^*(mT_s) V_{\mathrm{v}}(mT_s) \right|}{\sqrt{\hat{S}_{\mathrm{h}} \hat{S}_{\mathrm{v}}}}, \tag{3.10}$$

where $V_v(mT_s)$, $\hat{S}_h$, and $\hat{S}_v$ are the echo voltage, the estimated signal power in H, and the estimated signal power in V, respectively. We assume high SNR, and approximate the signal powers in H and V by $S_h \approx P_h$ and $S_v \approx P_v$. For the following analysis, assume that resolution volumes are homogeneously filled with identical scatterers so that in case of perfectly matched beams in width and pointing direction, the true copolar correlation coefficient is equal to ρ_{hv}, despite the changes in size and location of resolution volumes in an MCS CPI. That is, we are focusing on the impacts of imperfect matching between the H and V patterns. The bias of ρ_{hv} due to copolar mainlobe differences between the H and V polarizations is given by [109],

$$\frac{\delta \rho_{\mathrm{hv}}}{\rho_{\mathrm{hv}}} = \frac{1}{M} \sum_{m=0}^{M-1} \left[\frac{\int\limits_{\phi,\theta} F_{\mathrm{h}}^2 F_{\mathrm{v}}^2}{\sqrt{\int\limits_{\phi,\theta} F_{\mathrm{h}}^4 \int\limits_{\phi,\theta} F_{\mathrm{v}}^4}} - 1 \right]. \tag{3.11}$$

The integrals in (3.11) are 2-dimensional over the hemispheric solid angle defined by ϕ and θ. A closed-form expression can be derived for the case of interest (i.e., narrow beams) using (3.4)– (3.6a),

$$\frac{\int\limits_{\phi,\theta} F_{\mathrm{h}}^2 F_{\mathrm{v}}^2}{\sqrt{\int\limits_{\phi,\theta} F_{\mathrm{h}}^4 \int\limits_{\phi,\theta} F_{\mathrm{v}}^4}} = \frac{2\phi_{1\mathrm{h}}\phi_{1\mathrm{v}}}{\phi_{1\mathrm{h}}^2 + \phi_{1\mathrm{v}}^2} \exp\left[-\frac{4\Delta_\phi^2 \ln(2)}{\phi_{1\mathrm{h}}^2 + \phi_{1\mathrm{v}}^2} \right], \tag{3.12}$$

and then inserting into (3.11) to get,

$$\frac{\delta \rho_{\mathrm{hv}}}{\rho_{\mathrm{hv}}} = \frac{1}{M} \sum_{m=0}^{M-1} \left\{ \frac{2\phi_{1\mathrm{h}}\phi_{1\mathrm{v}}}{\phi_{1\mathrm{h}}^2 + \phi_{1\mathrm{v}}^2} \exp\left[-\frac{4\Delta_\phi^2 \ln(2)}{\phi_{1\mathrm{h}}^2 + \phi_{1\mathrm{v}}^2} \right] - 1 \right\}. \tag{3.13}$$

The dependency of ϕ_{1h} (and θ_{1h}) with sample time is omitted to simplify notation, but it is emphasized that beamwidths are a function of sample time as described by (3.7). Similarly, it is emphasized that each realization (m) results in a different value of Δ_ϕ, although this is not explicit in the expression. A quick check of this expression indicates that, for zero beam offset and equal beam widths in H and V, $\delta\rho_{hv} = 0$. In deriving (3.13), it is implicitly assumed that the antenna beams are circular ($\phi_{1h} = \theta_{1h}$). For elliptical beam patterns, which represent the more general shapes of H and V beams of a PAR, the pertinent equation (3.13) becomes

$$\frac{\delta\rho_{hv}}{\rho_{hv}} = \frac{1}{M} \sum_{m=0}^{M-1} \left\{ \frac{2\phi_{1h}\phi_{1v}}{\phi_{1h}^2 + \phi_{1v}^2} \exp\left[-\frac{4\Delta_\phi^2 \ln(2)}{\phi_{1h}^2 + \phi_{1v}^2} \right] - 1 \cdots \atop \cdots \frac{2\theta_{1h}\theta_{1v}}{\theta_{1h}^2 + \theta_{1v}^2} \exp\left[-\frac{4\Delta_\theta^2 \ln(2)}{\theta_{1h}^2 + \theta_{1v}^2} \right] \right\}, \qquad (3.14)$$

where Δ_ϕ and Δ_θ are offsets in ϕ and θ, and are uniformly distributed random variables in sample time.

For illustration, assume that beamwidths in H and V are matched ($\phi_{1h} = \phi_{1v}$) in (3.13), but there is an offset in beam-pointing directions ($\Delta_\phi \neq 0$), as follows

$$\Delta_\phi \leqslant \pm\varepsilon\phi_{1v}, \qquad (3.15)$$

where ε is an upper bound on the beam pointing offset normalized to the beamwidth, which is assumed to be much smaller than 1. Inserting these conditions into (3.13), and assuming that the pointing offset causes reduction of the correlation, we arrive at

$$\chi \triangleq \frac{\delta\rho_{hv} + \rho_{hv}}{\rho_{hv}} \leqslant \exp\left[-2\ln(2)\varepsilon^2 \right], \qquad (3.16)$$

which represents a correlation reduction factor due to a beam pointing mismatch

64

$\Delta_\phi \leq \pm \varepsilon \phi_{1h}$. Next, solving (3.16) for ε leads to

$$\varepsilon \leqslant \pm \sqrt{-\frac{1}{2\ln(2)}\ln(\chi)}. \tag{3.17}$$

This expression can be used to determine the maximum pointing offset between H and V that is allowed for a required bias in ρ_{hv}. For example, for the required bias[1] of 0.01, a $\chi \geq 0.99$ results in $|\varepsilon| \leq 0.085$. And for a beamwidth of $\sim 1°$, $|\Delta_\phi| \leq 0.085°$. Considering the demanding requirement imposed by the bias of ρ_{hv}, which is very sensitive to measurement errors, it is reasonable to assume that this pointing accuracy should be sufficient to achieve similar requirements for other polarimetric variables. This important result has to be considered in the design of an RPAR; as will be discussed in the next section, the choice of phase shifters will impact the achievable accuracy of ρ_{hv} estimates. Another important aspect that needs to be considered is the mismatch of H and V beamwidths, which is conveniently represented by their ratio, defined here as $\psi = \phi_{1h}/\phi_{1v}$ (only ϕ_{1i} is considered here).

Biases in signal power and correlation coefficient due to copolar mainlobe differences within the CPI estimated using (3.9) and (3.13) are shown in Figure 3.3 as a function of the normalized azimuthal sampling Δ_ϕ, and for different values of ε and ψ. Note that the bias in ρ_{hv} is expressed as 1 - χ, since this is a more conventional scale for ρ_{hv} and can be directly related to the RFR. Figure 3.3(a) shows that for zero beam offset (i.e., $\varepsilon = 0$), the signal power estimates from both methods are negatively biased, with the bias of MCS being lower than that when scanning with no beam steering (e.g., a mechanical scanning antenna). For a uniformly distributed offset with $|\varepsilon| \leq 0.085$, the power bias from MCS is comparable to that

---

[1]Specified in the NOAA Radar Functional Requirements document p. 13
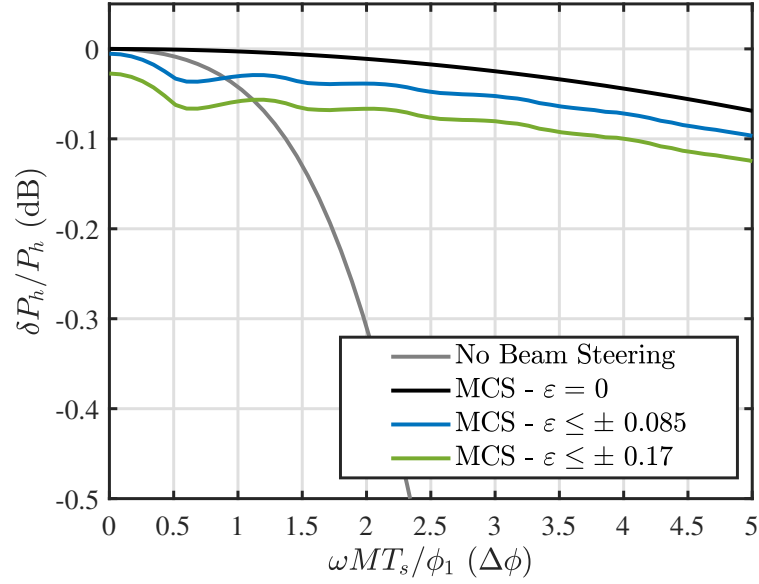
(a) Bias in signal power estimates
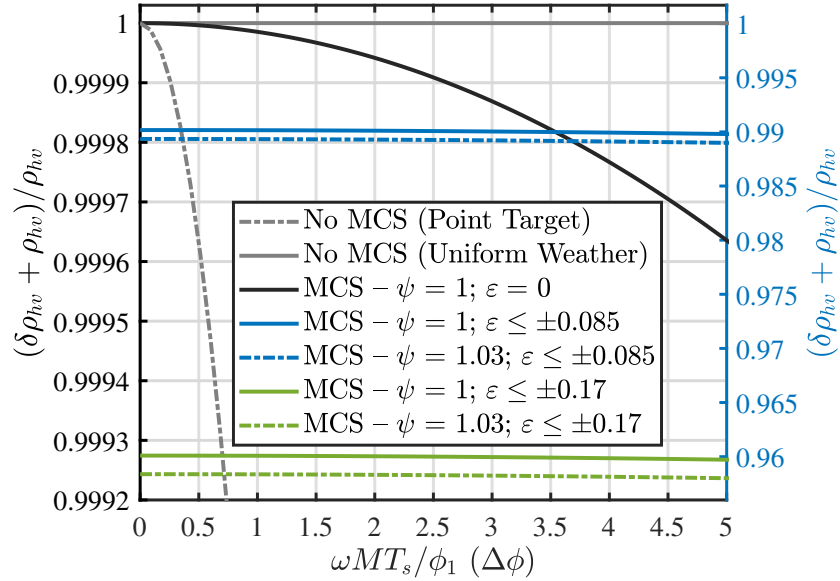
(b) Bias in ρ_{hv} estimates

Figure 3.3: Biases due to copolar mainlobe differences within the CPI estimated using (3.9) and (3.13) for (a) signal power, and (b) correlation coefficient. Note that for (b) the left ordinate axis (in black) is used for the ideal cases (i.e., $\varepsilon = 0$ and $\psi = 1$) and the right one (in blue) for all others.

66

resulting with no beam steering up to $\Delta_\phi \sim 1$, and lower for $\Delta_\phi > 1$. A similar conclusion can be drawn from the case when ε is twice that value (i.e., $|\varepsilon| \leq 0.17$). Figure 3.3(b) shows that with zero beam offset (i.e., $\varepsilon = 0$) and perfectly matched beamwidths (i.e., $\psi = 1$), the bias in ρ_{hv} from MCS is negligible ($\delta\rho_{hv} < 0.0004$), while the estimates when scanning with no beam steering are unbiased. Note that the left ordinate axis (in black) is used for the ideal cases (i.e., $\varepsilon = 0$ and $\psi = 1$) and the right axis (in blue) for all others. For a uniformly distributed ε, with $|\varepsilon| \leq 0.085$, and $\psi = 1$ or $\psi = 1.03$, the expected bias is $\delta\rho_{hv} \sim 0.01$ (as designed with $\chi = 0.99$), and there is little-to-no dependence with the normalized azimuthal sampling. Similarly, for $|\varepsilon| \leq 0.17$, and $\psi = 1$ or $\psi = 1.03$, $\delta\rho_{hv} \sim 0.04$. It is apparent from these curves that the differential beam pointing offsets considered have a larger impact on ρ_{hv} estimates than a 3% mismatch in H and V beamwidths (i.e., $\psi = 1.03$). In summary, these results show that for relatively accurate beam pointing (i.e., $|\Delta_\phi| \leq 0.085\,\phi_{1h}$), MCS achieves the required data quality on signal power and correlation coefficient estimates. Otherwise, it would result in unacceptable data quality degradation for larger pointing offsets (e.g.,$|\Delta_\phi| > 0.085\,\phi_{1h}$).

3.3   MCS Concept of Operations

Here we define a CONOPS that uses the MCS technique. Provided that the beam pointing offset is sufficiently small (e.g.,$|\Delta_\phi| \leq 0.085\,\phi_{1h}$) and that the H and V beams are adequately matched (i.e., $\phi_{1h} = \phi_{1v}$), MCS could improve azimuthal resolution without impacting the quality of radar-variable estimates. The CONOPS discussed in this subsection was implemented in the ATD system to demonstrate its feasibility.

3.3.1 Broadside MCS

A straightforward implementation of MCS can be achieved by using (3.13) with $\phi_p = 0°$ and $\theta_p = 90° - \theta_{el}$. That is, we assume that the center pulse in the CPI coincides with the broadside beam and that others are adjacent to it. For illustration, assume the antenna is not tilted (i.e., $\theta_T = 0°$) and θ_{el} is a small angle (e.g., 0.5°) such that $\sin(\theta_p) \approx 1$ and $\cos(\theta_p) \approx \theta_p$, this reduces (3.13) to

$$
\begin{aligned}
\phi_{BMCS}^A(mT_s) &= \omega\, T_s \left[\frac{(M-1)}{2} - m \right] \\
\theta_{BMCS}^A(mT_s) &= \theta_p,
\end{aligned}
\tag{3.18}
$$

where the subscript indicates Broadside MCS (BMCS). This expression provides the electronic steering angles for transmit and receive pulses within the CPI defined by M and T_s, and it results in a normalized azimuthal sampling of $\Delta\phi = \omega M T_s / \phi_1$. That is, as the RPAR rotates, motion is compensated by the steering angles in (3.18) such that all resolution volumes defined by samples in each CPI are centered at $\phi_k = k(\omega M T_s)$ where $k \in 0, 1, 2, \ldots$ and it represents a CPI index number.

There are a couple of major advantages of this CONOPS with respect to an adaptive 4F-PAR CONOPS. First, since the steering angles are relatively small and remain close to the antenna's principal planes, it is expected that a simple broadside calibration (i.e., similar to that of a rotating reflector-antenna radar) will be sufficient for the required accuracies of radar-variable estimates (see beamsteering biases at $\phi leq \pm 1°$ from broadside in [47]). Second, considering that the set of pointing angles resulting from (3.18) for a pre-defined CPI are deterministic, this results in an invariant scan strategy that mitigates beam smearing effects with negligible data quality impact, and does not require additional signal processing for implementation.

Nevertheless, the simplicity of this CONOPS does not make full use of the RPAR's resources to meet the prescribed functional requirements. That is, this CONOPS only tackles one of the requirements (azimuthal resolution) and does not exploit RPAR capabilities to improve data quality or reduce the volume update times. A more advanced CONOPS that uses MCS and could be used to also improve data quality is discussed in Chapter 5.

3.4   Performance of MCS

High-fidelity RPAR simulations were developed to evaluate the performance of MCS to enhance azimuthal resolution, and to quantify its impact on the bias and standard deviation of polarimetric-variable estimates. One set of simulations is used to evaluate the performance of MCS on enhancing azimuthal resolution (i.e., decrease the effective beamwidth); these are designed to quantify the importance of beam pointing accuracy to achieve a significant reduction in the effective beamwidth. The other set of simulations is used to quantify the impact of MCS on data quality; these are designed to capture the combined effects of sampling concentric non-uniform resolution volumes and antenna radiation patterns. Data produced with both sets of simulations are compared to RPAR simulations that do not use MCS as well as to PAR operation in a stationary mode.

3.4.1   Azimuthal Resolution

As argued before, the angular resolution gained by MCS can have have important implications in the size of the antenna aperture needed to meet angular-resolution requirements. That is, as illustrated in Figure 2.8, an antenna aperture with a stationary beamwidth of $1°$ on broadside results in a $\sim 1.23°$ effective beamwidth when

sampling at $\Delta\phi = 1$. Thus, an aperture with a stationary beamwidth of $0.8°$ on broadside is needed for an effective beamwidth of $1°$ at $\Delta\phi = 1$. However, this can result in a significant increase in aperture size (e.g., $N_{1°} = 19{,}400$ to $N_{0.8°} = 29{,}800$), which would increase system complexity and cost. The use of MCS could result in a reduction of the effective beamwidth, thus potentially reducing system cost. It is important to note that the performance of MCS to enhance the RPAR's angular resolution is mostly determined by beam-pointing accuracy (dictated by the pointing offset Δ_ϕ) and knowledge of the platform's mechanical position.

The beam pointing accuracy of a phased array antenna is dictated by the performance of phase shifters in the antenna elements [110]. Phase shifters control the phase of the signals at each radiating element to electronically form a collimated beam in the desired direction. A digitally controlled phase shifter with n bits has 2^n phase states separated by phase steps of $2\pi/(2^n)$ [89]. This phase quantization introduces an error in the steering phase at the element level and may cause a distortion of the resulting antenna pattern. Two major adverse effects from phase quantization have been the subject of several research efforts: increase in antenna sidelobe levels and beam-pointing accuracy [111].

Phase quantization errors are predictable and are typically considered in the design of phased array antennas. Nevertheless, imperfections in antenna fabrication and other sources of error (e.g., differences in the power divider network, failed bits in phase shifters, mutual coupling between elements, thermal noise, etc.) introduce random phase errors that are well approximated by a Gaussian probability density function with zero mean [89, 112, 113]. These random phase fluctuations have to be considered to quantify the impact of beam pointing accuracy as a function of n on the effective beamwidth achieved by MCS. The simulation developed for this analysis includes phase quantization errors and also random phase errors. The

70

transmit and receive antenna patterns are generated as the product of a measured embedded element pattern and a simulated array factor [89]. The array factor is generated using the Fourier method. The measured embedded element pattern[2] is used to enhance the fidelity of simulations and corresponds to that of an element designed for the ATD system [33]. Steering phases at the element level are produced by quantizing Gaussian random variables with a mean equal to the desired quantized steering phase (rounded to the nearest bit as a function of n) and a standard deviation of 5° [89]. As is done conventionally, transmit patterns are generated with a uniform taper to maximize sensitivity and receive patterns are tapered with a Taylor window to reduce sidelobe levels. This simulation captures the systematic and random phase errors and includes effects from both copolar and cross-polar antenna radiation patterns.

The procedure described is used to simulate M patterns steered in ϕ using MCS as described in (3.2). Without loss of generality, ϕ_p is assumed to be 0°, which corresponds to broadside MCS. Results can be scaled by $1/\cos(\phi_p)$ for the effective beamwidth at a pointing angle $\phi_p \neq 0°$. RPAR rotation is simulated by shifting each pattern in ϕ by $-\omega m T_s$, which assumes a uniform antenna rotation rate in azimuth. The effective antenna pattern is obtained by adding these M patterns, from which the effective beamwidth is measured. Results for $n = 5$, 6, and 7 bits are presented in Figure 3.4 as a function of the normalized azimuthal sampling Δ_ϕ. It is apparent from the results in Figure 3.4(a) that due to phase errors (dominated by quantization errors), 5-bit phase shifters are not sufficient to mitigate beam smearing effects considerably. In this case, an antenna aperture with a stationary beamwidth of 1° on broadside results in a $\sim$1.20° effective beamwidth when sampling at $\Delta_\phi = 1$.

---

[2]Measurements were obtained in the near field chamber at the MIT-LL facilities during March-April 2018.

This indicates that the pointing offset for $n = 5$ was relatively large and the centers of resolution volumes could not be aligned with the required precision. The

(a) $n = 5$ bits

(b) $n = 6$ bits
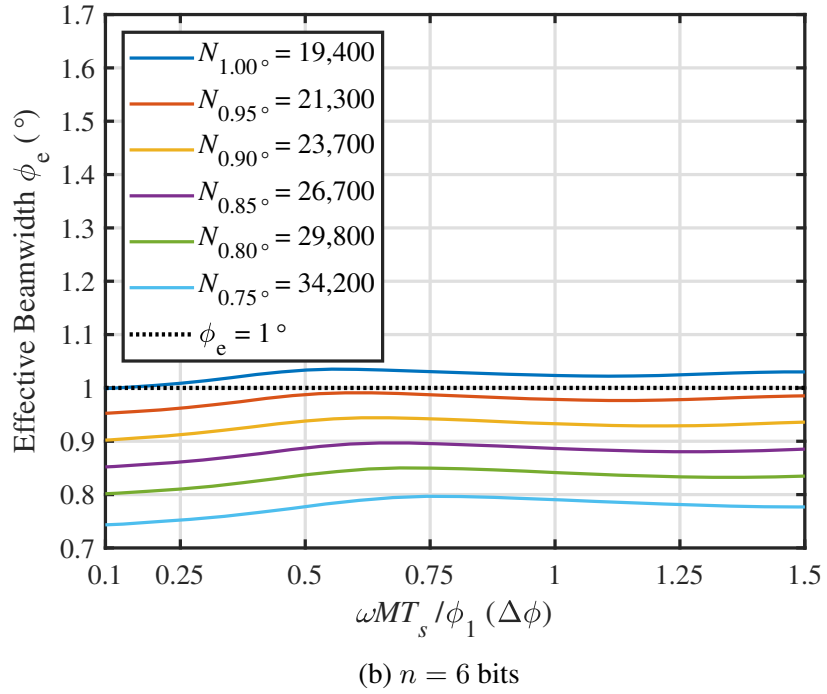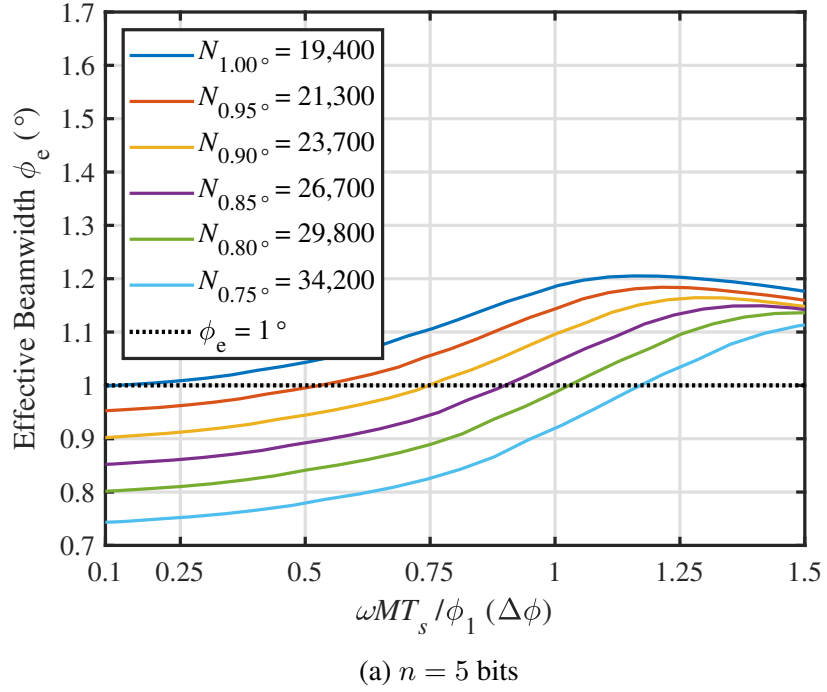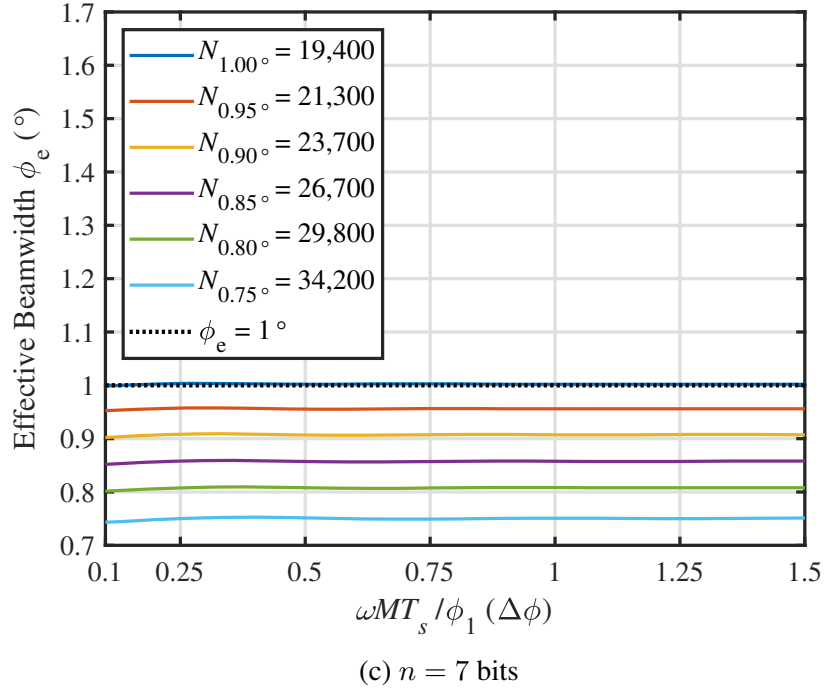
Figure 3.4: Effective beamwidth as a function of the normalized azimuthal sampling Δ_ϕ for (a) $n = 5$, (b) $n = 6$, and (c) $n = 7$ phase shifter bits. The stationary beamwidth for all cases is for the broadside position.

effective beamwidth was greatly reduced with $n = 6$, as shown in Figure 3.4(b). While not completely mitigated, beam smearing effects are largely reduced with 6-bit phase shifters, being the effective beamwidth within $0.1°$ from the stationary beamwidth for all N_x and all Δ_ϕ. Lastly, Figure 3.4(c) indicates that for $n = 7$ beam smearing effects are negligible and the effective beamwidth is approximately equal to the stationary beamwidth. Results presented in this subsection quantify the performance of MCS in enhancing azimuthal resolution by mitigating beam smearing effects as a function of phase shifter bits. It is expected that 6-bit phase shifters (Figure 3.4(b) are sufficient for achieving satisfactory MCS performance, while 7-bit phase shifters would be ideal.

3.4.2 Data Quality

The simulations used to evaluate the impact of MCS on data quality are based on the approach proposed by [108], which combines the effects of simulated or measured radiation patterns with simulated time series signals. It applies the well-established backscattering matrix model [68, 74] that includes bulk statistical properties of scatterers within a resolution volume over the dwell time coupled with electromagnetic wave propagation and radar system effects. In addition to the copolar biases quantified in Section 3.2.2, the simulation can be used to quantify the effects from both the copolar and cross-polar antenna radiation patterns. The present work considers copolar antenna patterns only.

The RPAR simulation procedure is similar to that discussed in the previous section. A set of M simulated transmit and receive patterns are steered in ϕ using MCS as described in (3.2), and rotation is simulated by shifting each pattern in ϕ by $-m\omega T_s$. The two-way patterns are sampled at the desired pointing angle ϕ_p and θ_p for every m. It is assumed that the pointing angle (relative to the earth coordinate system) is constant for the duration of the CPI, and that steering angles for simulated patterns may change as a function of sample m. RPAR simulations for the case where constant beam steering is used (i.e., no MCS) are also generated for reference using the same procedure. An illustration of the copolar transmit beam peaks resulting from this simulation procedure is shown in Figure 3.5, where the beam pointing angle is $\phi_{az} = 45°$ and $\theta_{el} = 20°$ ($\phi_{az} = \phi_p$, and $\theta_{el} = 90° - \theta_p$), the rotation rate is $\omega = 21.15° s^{-1}$, $M = 15$, and T_s = 3 ms. The top row shows the beam peaks with constant beam steering (i.e., no MCS) as a function of steering angle relative to the array broadside for samples m = 1, 8, and 15, while the bottom row is analogous but using MCS. Note that since the steering angle for this example

(a) No Beam Steering

(b) MCS
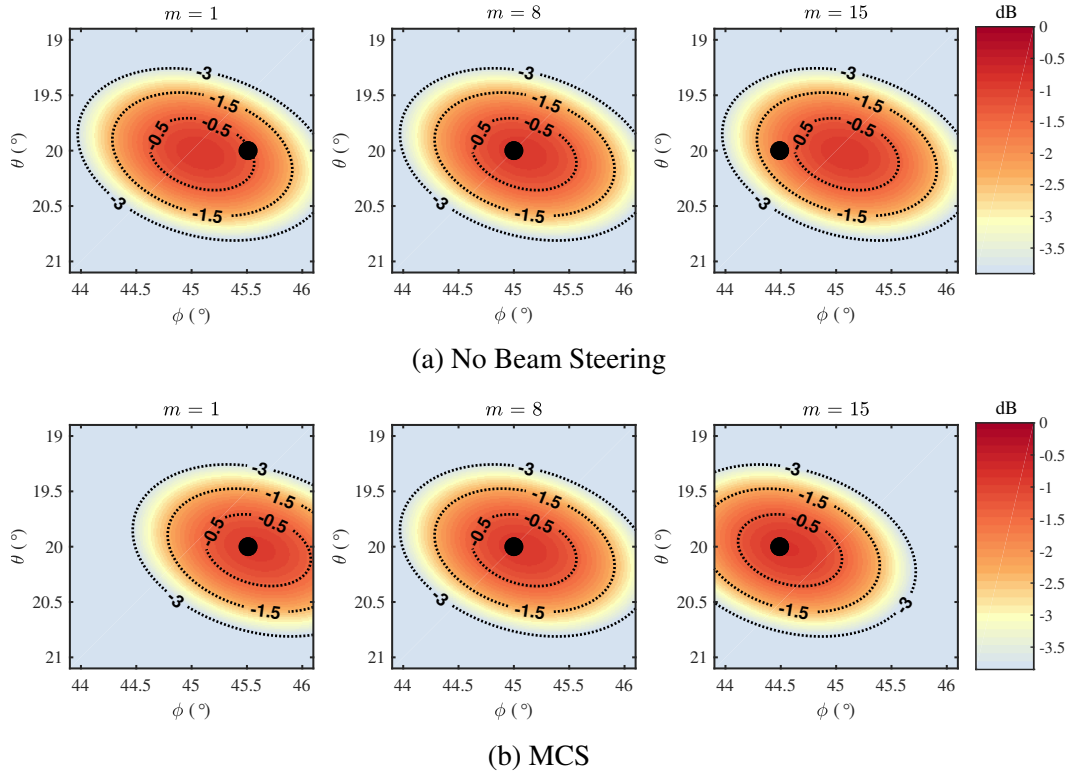
Figure 3.5: Copolar beam peaks for the transmit antenna pattern of the simulated RPAR pointed at $\phi_{az} = 45°$ and $\theta_{el} = 20°$, with a rotation rate of $\omega = 21.15°s^{-1}$, $M = 15$, and $T_s = 3$ ms (a) Beam peaks corresponding to constant beam steering for samples $m = 1$, 8, and 15 (b) Beam peaks corresponding to MCS for the same samples. The black dot represents the desired pointing angle ϕ_{az} and θ_{el} (earth-relative coordinates), which is constant in earth-relative coordinates for the duration of the CPI.

is far from the broadside, there is a scan loss of ~ 1 dB. Black dotted lines delineate contour levels of constant power with respect to the beam peak (in dB). The black dot represents the desired pointing angle ϕ_{az} and θ_{el}, which is constant in earth-relative coordinates for the duration of the CPI. It can be observed in the top-left ($m = 1$) and top-right ($m = 15$) panels that the beam is not accurately pointed at the desired angle. For example, this would translate into a loss of ~ 0.5 dB in power if scanning a point target. Although this would generally have little impact on uniformly distributed weather targets, it could introduce biases in large reflectivity

gradients such as those observed in tornado vortices. Applying MCS results in more accurate pointing towards the center of the resolution volume compared to constant beam steering (i.e., no MCS) and a negligible power loss (with respect to the peak of the pattern) due to the pointing offset. The complex samples obtained from two-way patterns at the desired pointing angle are used in the backscattering matrix model, which includes statistical properties of meteorological scatterers. This generates the simulated time series of complex voltages, from which spectral moments and polarimetric variables are estimated.

To understand the impact of MCS on the quality of variables using the described simulation procedure over the scan volume, the space of pointing angles $\phi_{az} \in [-45°, 45°]$ and $\theta_{el} \in [0°, 20°]$ is simulated, with a grid spacing for both θ_{el} and ϕ_{az} of $1°$. For simplicity, assume the antenna is not tilted ($\theta_T = 0°$). As before, constant beam steering is simulated for reference over the scan sector. It represents a RPAR scanning with a set of M identical electronic beams steered a constant angle (in the antenna-relative coordinate system) as the radar rotates. Antenna characteristics based on the ATD system are adopted for this analysis since this system is used to demonstrate MCS in Section 3.5. The ATD antenna elements are designed with 6-bit phase shifters. It is assumed that the antenna tilt angle is $0°$, that is, the broadside is perpendicular to the z axis. Simulation results quantifying the copolar beamsteering biases are presented in Figure 3.6. Columns from left-to-right correspond to a stationary PAR (e.g., 4F-PAR), an RPAR not using MCS, and an RPAR using MCS, respectively. From top-to-bottom, the rows correspond to biases of Z_h, Z_{DR}, and ρ_{hv}. Absolute calibration constants for the broadside beam are derived from the stationary PAR for unbiased powers on both polarization channels (H and V) and applied to all three cases. Comparing the results for Z_h on the first row, it is apparent that positive biases for the RPAR not using MCS are higher along

76

the azimuth planes at $\sim\pm38°$, with respect to both the stationary PAR and the RPAR using MCS. Negative biases along the azimuth plane at $\sim0°$ are lower than those for the stationary PAR and the RPAR using MCS (specially at higher elevations). Comparing the results for Z_{DR} on the middle row, it is apparent that all three cases have very similar performance. To understand this, consider Z_{DR} that is the ratio of the H and V signal powers, each of which is estimated by averaging M signal power samples from potentially non-concentric or non-uniform volumes. Volume locations or sizes for the H and V polarizations may change in a relatively similar manner as a function of steering angle. The resulting relative changes in signal powers from a set of M non-concentric or non-uniform resolution volumes are thus similar, and differences cancel out in the ratio. Lastly, comparing the results for ρ_{hv} on the last row, it is apparent that estimates for the stationary PAR and the RPAR using MCS are unbiased, and there are small negative biases for the RPAR not using MCS. Biases for the RPAR not using MCS come from differences between the cross-correlation power (the numerator in (3.10)) and the geometric mean of H and V signal powers. The bias magnitude for ρ_{hv} increases as a function of steering angle relative to the broadside, with unbiased estimates at $\phi_{az} \sim \pm8°$ and $\theta_{el} \sim 0°$ $- 6.5°$, and the largest biases in the scan sector at $\phi_{az} \sim \pm45°$ and $\theta_{el} \sim 20°$. Nevertheless, the largest bias magnitudes obtained for the RPAR not using MCS are on the order of 0.003, which are small enough and meet the requirements for the weather surveillance mission [38].

Absolute bias differences between the stationary PAR and the RPAR using MCS are shown in Figure 3.7. Panels from top-to-bottom correspond to differences in the absolute value of biases for Z_h ($\delta|\text{B}[Z_h{}^{Co}]|$), Z_{DR} ($\delta|\text{B}[Z_{DR}{}^{Co}]|$) and ρ_{hv} ($\delta|\text{B}[\rho_{hv}{}^{Co}]|$), respectively. Notice that the color map scales are an order of magnitude smaller than the corresponding ones in Figure 3.6. It is apparent from the top and
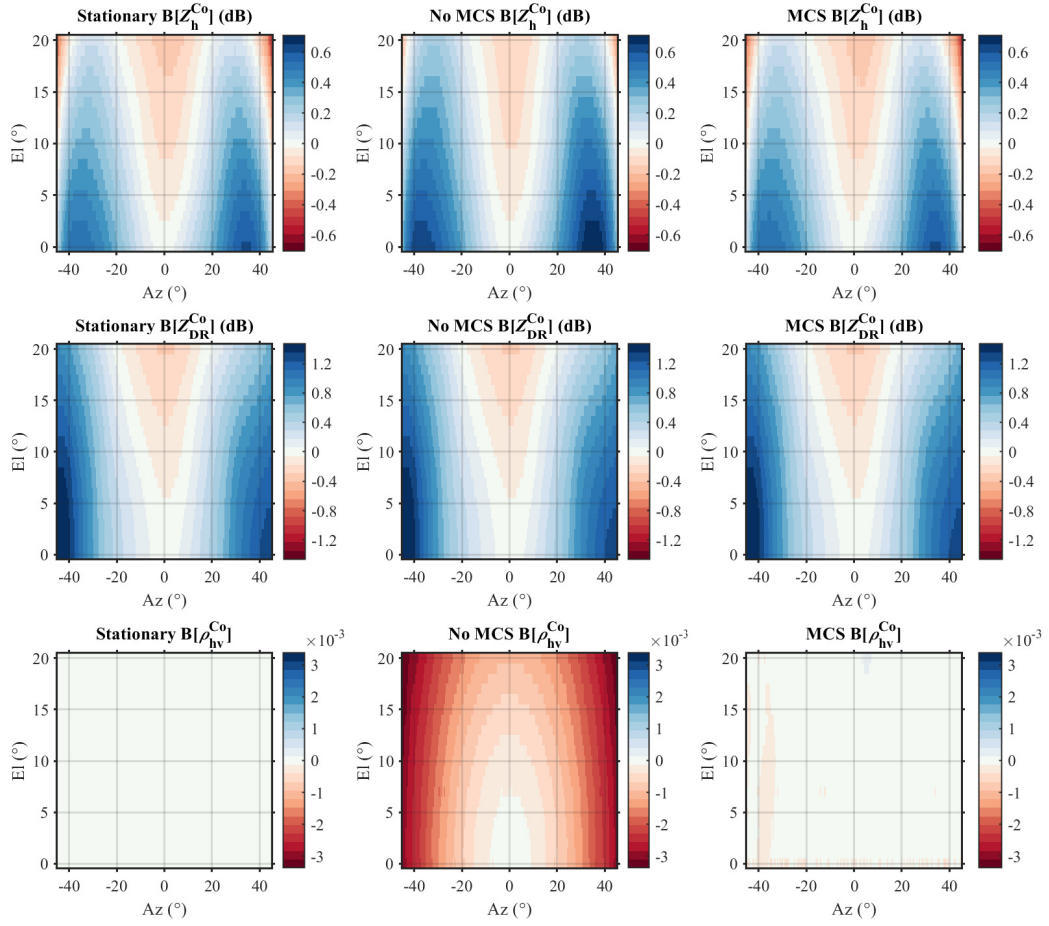
Figure 3.6: Columns from left-to-right correspond to a stationary PAR, an RPAR not using MCS, and an RPAR using MCS, respectively. From top-to-bottom, the rows correspond to biases of Z_h, Z_{DR}, and ρ_{hv}. Absolute calibration constants for the broadside beam are derived from the stationary PAR for unbiased powers on both polarization channels (H and V) and applied to all three cases.

center panels that biases of the stationary PAR and the RPAR using MCS for Z_h and Z_{DR} are very similar. The bottom panel shows that there may be small biases in ρ_{hv} for the RPAR using MCS in some areas of the scan sector, but these are negligible ($\sim 10^{-4}$) and are therefore ignored herein. These results show that a system designed with sufficient pointing accuracy can be operated as an RPAR using MCS, and the impact on radar-variable estimates is comparable to that obtained when operating the same system as a stationary PAR. That is, by using MCS
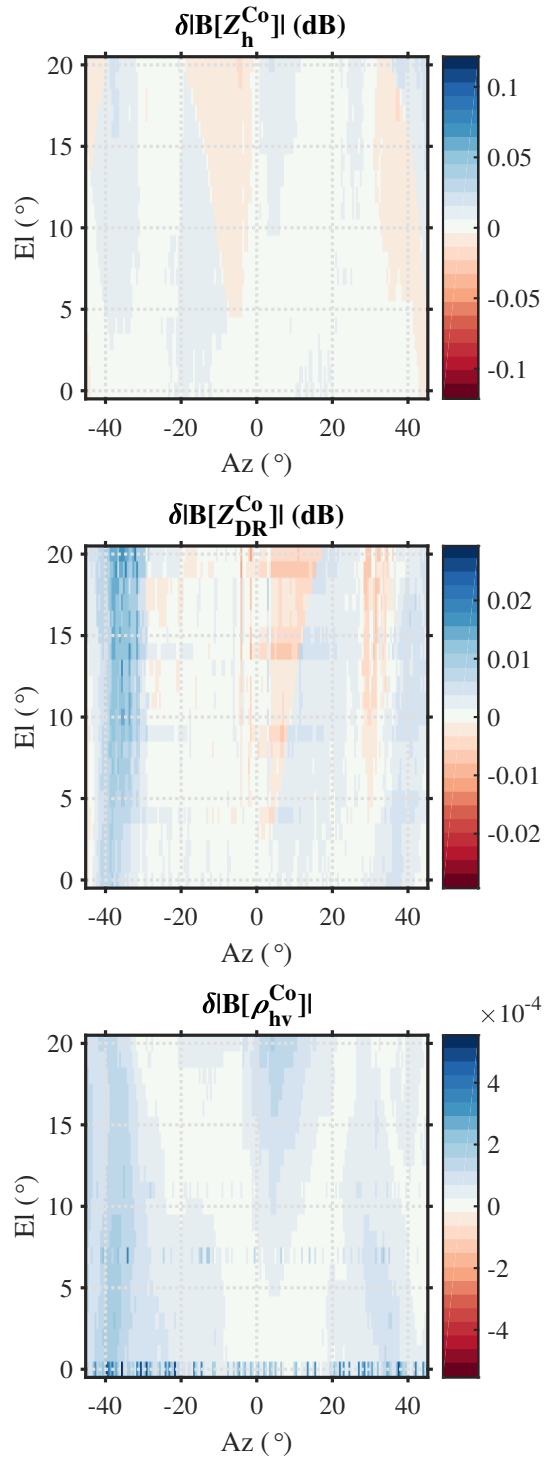
Figure 3.7: Absolute bias differences between the stationary PAR and the RPAR using MCS (left) Z_h, (middle) Z_{DR}, and (right) ρ_{hv}. The notation $\delta|B[\cdot]|$ is used to denote the difference in the absolute value of biases.

and compensating for antenna motion, the radar matches the performance of a stationary PAR system. Nevertheless, intrinsic scan-dependent measurement biases coming from the copolar antenna patterns (present in both the stationary PAR and MCS-RPAR, as show in in Figure 3.6) must be addressed.

It is understood that stationary PAR systems are subject to scan-dependent measurement biases coming from the antenna patterns as they are electronically steered in various directions [54]. These are caused by the H and V copolar antenna patterns that vary with beamsteering direction and are quantified on the first column of Figure 3.6 for the ATD system when it is operated as a stationary PAR system. The effects of these variations can be addressed via corrections using appropriate values at each broadside location. If the cross-coupling effects are sufficiently suppressed with phase coding [57] and given a sufficiently narrow antenna main beam, the corrections can be conducted using only the measurements of the copolar pattern peaks [56]. Considering that biases in the stationary PAR and the RPAR using MCS are comparable, radar-variable corrections for the copolar biases of the ATD operated as a stationary system derived by [46, 47] are used to demonstrate the RPAR using MCS in the next section.

3.5 Demonstration of MCS

The BMCS technique was implemented on the ATD to demonstrate these concepts in an experimental research environment. First, a point target was scanned with BMCS to validate the practical implementation and to quantify the beam pointing offset. Then, the BMCS was used to illustrate the MCS technique for polarimetric weather observations.

3.5.1 Point Target Experiment

Implementation and calibration of the MCS technique were verified by rotating past a stationary point target located in the vicinity of the ATD. Specifically, a set of data were collected with the ATD rotating over a $\sim 20°$ sector at $\omega = 4°$ s^{-1}, $M = 65$, and $T_s = 3$ ms. The radar broadside was commanded to rotate from 290° to 310° azimuth with respect to North, with the target located at 31.65 km in range and approximately 300.96° azimuth with respect to North. The system was commanded to mechanically tilt the antenna so that the broadside would point at the 0.5° elevation angle. Two subsequent scans were conducted 1) the transmit and receive beams were electronically maintained at broadside in azimuth and elevation (i.e., no MCS), and 2) the transmit and receive beams were electronically steered in azimuth and elevation using the BMCS in Section 3.3.1. The pointing angles for 2) were initially obtained using the theoretical expression (3.18), but were not sufficiently accurate as the pedestal positioner was not able to maintain a perfectly constant rotation speed. A model of the ATD's mechanical motion in azimuth was derived by fitting 3$^{\text{rd}}$ order polynomials to pedestal positions measured at a rate of 10 Hz when the system was commanded to rotate at the speeds of 2, 4, and 8° s^{-1}. This model agreed well with the theoretical expression in (3.18) for the linear and constant terms,

$$
\begin{aligned}
\tilde{\phi}_{BMCS}^{A}(mT_s) &= 0.0034(mT_s)^3 + \cdots \\
\cdots &+ 0.052(mT_s)^2 + \omega\, T_s \left[\frac{(M-1)}{2} - m \right],
\end{aligned}
\tag{3.19}
$$

and was adopted for the practical implementation of MCS on the ATD under both CONOPS presented as the pedestal motion is independent of electronic steering angle.

81

The Signal-to-Noise Ratio (SNR) of signals received by the ATD on the H polarization while rotating past the target as a function of the pedestal (i.e., mechanical) azimuth is presented in Figure 3.8. The pedestal azimuth positions (with respect to North) are used to compare the SNRs measured with MCS with those from a mechanically scanning antenna (i.e., not using MCS). Solid lines show the single-pulse SNR estimates and dot markers show the SNRs estimated by averaging those from the M samples in each CPI (herein referred to as the CPI estimate). The blue line represents the SNRs for the RPAR not using MCS and its shape resembles the mainlobe of the two-way antenna patterns. The solid black line represents the single-pulse SNRs of the RPAR using MCS and its shape resembles a staircase plot where the SNRs at each step are sampling approximately the same resolution volume, and therefore the returned powers are approximately constant. The inset plot shows that the CPI estimate obtained using MCS is 71.81 dB while that obtained without MCS is 71.16 dB. It is apparent that CPI estimates obtained using MCS are closer to true SNRs, since estimates are closer to the single-pulse SNRs on the blue curve, in particular, the peak SNR return from the point target which is 71.82 dB. Furthermore, the standard deviation of single-pulse SNRs for the samples in the CPI that contains the peak return ($\sim301°$) is 0.033 dB with MCS, and 0.61 dB without MCS. This order of magnitude reduction in the variance of SNRs from a point target indicates that power estimate biases arising from approximately concentric non-uniform resolution volumes are much smaller than those from non-concentric uniform volumes. The mean standard deviation of absolute azimuth pointing angles (i.e., the summation of the mechanical and electronic azimuths) of samples within CPIs is $0.008°$ with MCS, and $0.21°$ without MCS. This average standard deviation of pointing angles measured when using MCS is used to characterize the pointing offset, which is consistent with that obtained in the simulations
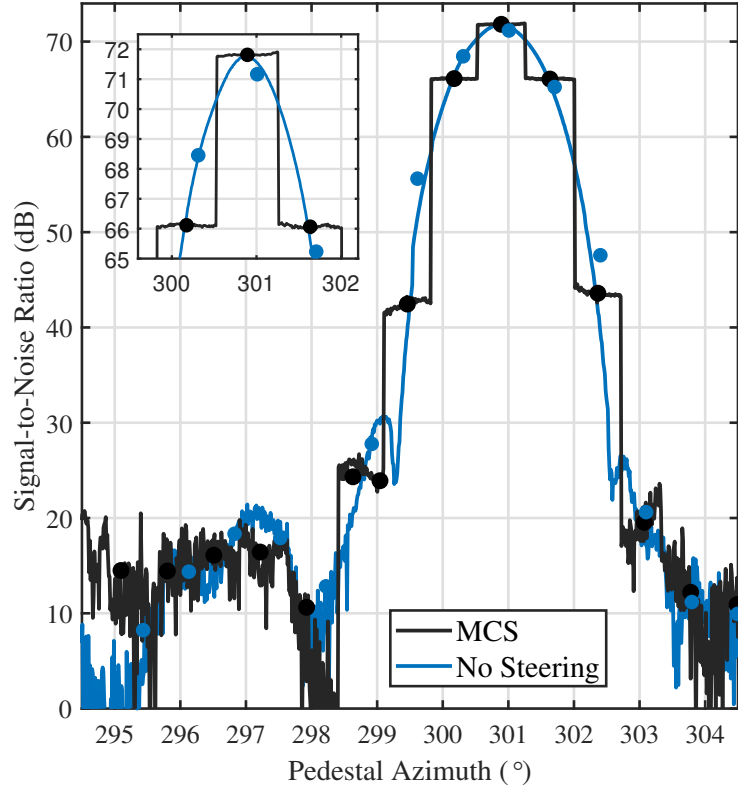
Figure 3.8: SNR of signals received by the ATD system on the H polarization while rotating past the target as a function of the pedestal (i.e., mechanical) azimuth. Solid lines show the single-pulse SNR and dot markers show the SNRs estimated by averaging those from the M samples in each CPI.

presented in Section 3.4.1 ($\sim$0.006°). The small difference between simulated and measured standard deviation of pointing angles is largely due to mechanical system imperfections, which were not considered in the simulations. Using $\varepsilon \leq \pm 0.085$ (for $\chi = 0.99$), and (3.15) with $\phi_{1h} = 1.58°$, a pointing offset of $\Delta_\phi \leq \pm 0.143°$ is obtained for the ATD system. Since this pointing offset is much larger than the measured standard deviation of MCS pointing angles, the performance is considered acceptable to largely mitigate beam smearing using the ATD system without impacting polarimetric data quality.

3.5.2 Polarimetric Weather Observations

This experiment is used to illustrate the BMCS CONOPS whereby MCS is used to compensate the radar motion for samples within a CPI centered on the elevation principal plane. Sector scans were collected in rapid succession using the STSR mode on 05 May 2020 to sample a rapidly evolving mesoscale convective system at a range of approximately 100 km. For scan 1, the ATD rotated at $\omega = 4°$ s^{-1}, the transmit and receive pencil beams were maintained at broadside ($\phi_{az} = 0°$, $\theta el = 0°$), mimicking the operation of a conventional reflector-based radar. Data from this scan were collected at 00:44:25 Z, and are used here to verify the BMCS data. For scan 2, the ATD rotated at $\omega = 4°$ s^{-1}, the transmit and receive pencil beams were collected using BMCS. Data from this scan were collected 22 seconds after scan 1, at 00:44:47 Z. For these scans, the radar broadside was commanded to mechanically rotate clockwise from 130° to 170° in azimuth, at constant 0.9° elevation, with a continuous pulse transmission at T_s = 3 ms. For a normalized azimuthal sampling of $\Delta\phi = 0.5$, the number of samples M was set to 65 on both scans. Receiver range-time samples were produced at a rate of 4 MHz, which results in a range sampling interval of 37.5 m. Range-time processing was set to incoherently average samples from 6 consecutive range gates, which results in a range sampling spacing for the radar variables of 225 m

Data produced with this technique were verified by comparing them to data from a WSR-88D radar system, that has an inherently better angular resolution than the ATD. The KCRI radar in Norman, OK is operated and maintained by the Radar Operations Center and it is collocated with the ATD. The KCRI radar was following the operational VCP number 212, for which the antenna is rotated at 21.5° s^{-1} when scanning the 0.9° elevation angle. For this elevation, the CPIs from the surveillance

scan consist of 15 samples at $T_s = 3$ ms, with $\Delta\phi = 0.5$ (i.e., an azimuthal sampling of $0.5°$ since the HPBW of this system is approximately $1°$), and a ϕ_e $1.1°$. Data for the $0.9°$ elevation of the VCP were collected with the KCRI radar at 00:44:36 Z, and IQ data from the same azimuthal sector were extracted for processing. There are several architectural differences between the ATD and KCRI systems, but since the KCRI has better effective angular resolution it is considered here as a reference to verify the angular resolution enhancement of the MCS technique. Radar system parameters and scan strategies for these experiments are summarized in Table 3.1. Fields of radar-variable estimates resulting from processing the data from these scans are presented in Figure 3.9. Panels are organized as follows: the top row corresponds to scan 1, the middle row corresponds to scan 2, and the bottom row corresponds to scan 3; the columns from left to right show fields of radar Z_h, Z_{DR}, Φ_{DP}, and ρ_{hv}. Qualitative comparison of radar-variable estimates from scans 1 and 2 shows there are no apparent artifacts in the data from scan 2 (MCS), and both datasets appear to have similar meteorological features as that of scan 3. Data from scans 1 and 2 have a smoother texture than data from scan 3, likely due to the higher number of samples, which results in reduced standard deviation of radar-variable estimates. Regions with well-defined meteorological features are highlighted with black arrows for discussion. Comparing the highlighted regions on fields of Z_h, it is apparent that the line of high Z_h (> 50 dBZ) presents a finer structure in the field estimated with MCS data. This is also apparent in other areas

Scan #	Radar System	Time (Z)	Beam Type	Scanned Sector	Mechanical Elevation	ϕ_1	M	T_s	$\omega °\,s^{-1}$
1	ATD	00:44:25	Broadside Pencil	130° - 170°	0.9°	1.58°	65	3	4
2	ATD	00:44:47	BMCS	130° - 170°	0.9°	1.58°	65	3	4
3	KCRI	00:44:36	Broadside Pencil	0° - 360°	0.9°	1°	16	3	21.15

Table 3.1: Radar system parameters and scan strategies for MCS experiment.
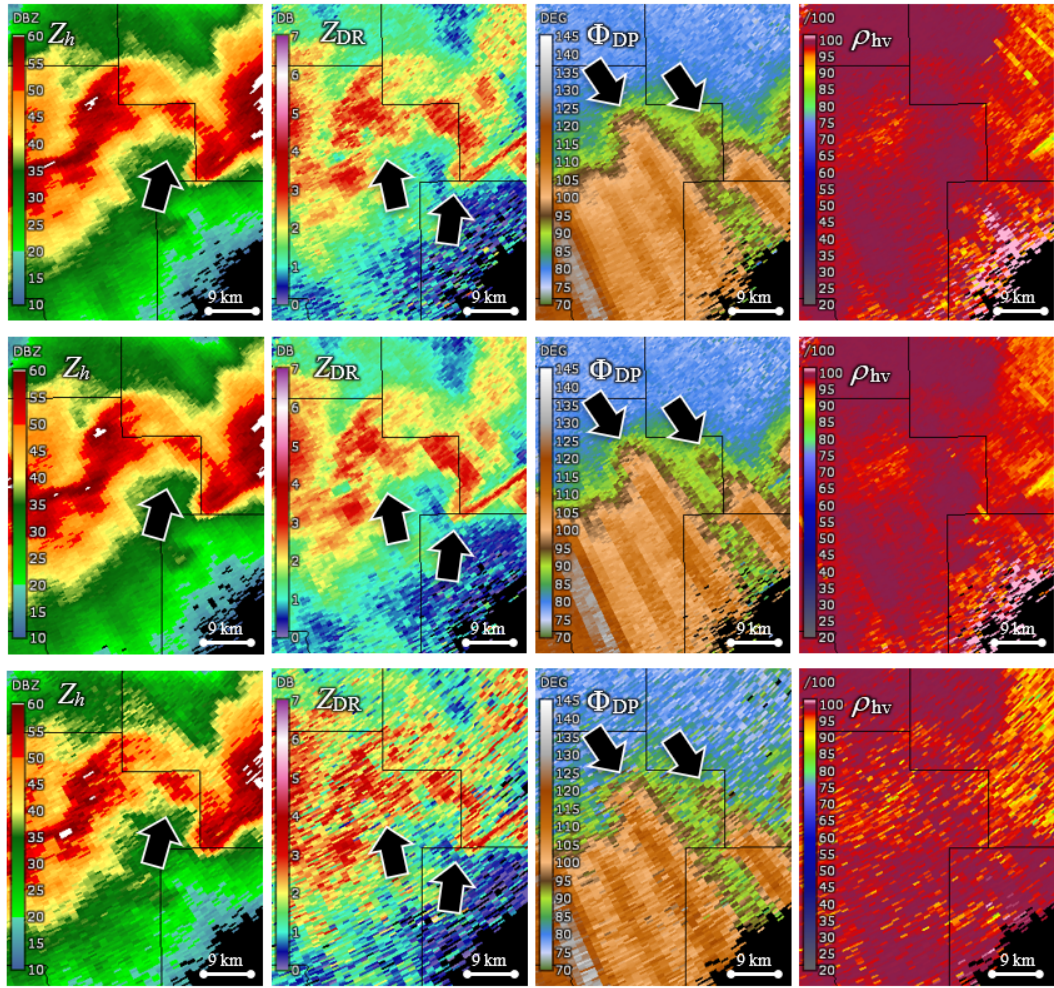
Figure 3.9: Radar-variable estimates obtained from three scans collected in rapid succession. Panels are organized as follows: the top row corresponds to scan 1 (ATD – No MCS), the middle row corresponds to scan 2 (ATD BMCS), and the bottom row corresponds to scan 3 (KCRI – No MCS); the columns from left to right show fields of Z_h, Z_{DR}, Φ_{DP}, and ρ_{hv}, respectively.

on fields of Z_h, consistent with the hypothesis that MCS reduces beam smearing. Similar conclusions are drawn from a qualitative comparison of fields of Z_{DR} (specially in regions highlighted with black arrows). Comparing the fields of Φ_{DP} from scans 1 and 2 in this region, it is apparent that scan 2 exhibits a narrower and more defined line with increasing values of Φ_{DP} along the beams with high Z_h (see black arrows in fields of Φ_{DP}). Since Φ_{DP} represents the difference in phase from the H and V polarizations along the wave propagation path, it typically presents radially oriented features. In this case, it is apparent that the high radially oriented Z_h core attenuates the vertically polarized waves, which results in the increase of Φ_{DP}. The narrower appearance of this feature in the field of Φ_{DP} from scan 2 (i.e., BMCS) resembles that of scan 3. Comparing the fields of ρ_{hv} from scans 1 and 2 in this region, it is observed that scan 2 exhibits generally higher values (i.e., closer to 1). Considering that the time difference between these scans is relatively short ($\sim$22 s) and that the same noise-power estimation technique is used for all three scans [6], the improvement in ρ_{hv} estimates are attributed to the use of MCS.

To quantify the differences in the fields of radar-variable estimates produced by scans 1 and 2, the absolute difference of each of these with scan 3 is calculated. Since data from scan 3 inherently has better angular resolution, data from scans 1 and 2 are compared to it by using the absolute difference of estimates. Given that sampling grids are different, a simple nearest neighbor interpolation is used to map the data from scans 1 and 2 on the sampling grid of scan 3. The notation $\delta|x|$ is used, where x is one of the radar variables presented in Figure 3.9. An SNR threshold of 8 dB is used to censor data corresponding to weak returns (painted in gray for reference). Further, to reduce the variance of differences, a running average of 5 gates in range is applied on the direct absolute differences (no averaging in azimuth is applied to preserve resolution). Results are presented in Figure 3.10,

where the top row represents the absolute differences between scans 1 and 3, and

the bottom row represents absolute differences between scans 1 and 2. Black arrows
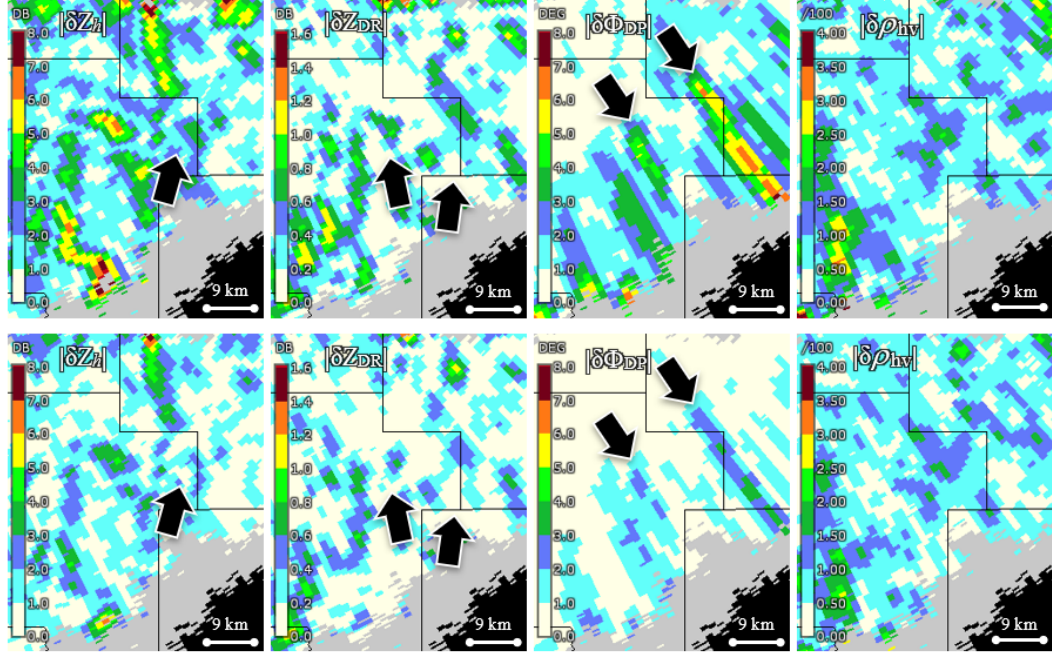
Figure 3.10: Absolute differences between fields of radar-variable estimates in Figure 3.9. The top row represents the absolute differences between scans 1 and 3, and the bottom row represents absolute differences between scans 2 and 3. Columns from left to right show absolute difference fields of Z_h, Z_{DR}, Φ_{DP}, and ρ_{hv}, respectively.

are used to highlight regions corresponding to those discussed in Figure 3.9. Fields

of $\delta|Z_h|$, $\delta|Z_{DR}|$ and $\delta|\Phi_{DP}|$ reveal considerable improvement, i.e., lower absolute

differences in estimated fields with respect to the KCRI estimates. For the $\delta|Z_h|$

fields, there is a reduction from ~3-4 dB (scan 1) to ~1-2 dB (scan 2) in the

highlighted region. For the $\delta|Z_{DR}|$ fields, there is a reduction from ~0.6-0.8 dB

(scan 1) to ~0.4-0.6 dB (scan 2) in the highlighted region. For the $\delta|\Phi_{DP}|$ fields,

there is a reduction from ~4-7° (scan 1) to 1-3° (scan 2) in the highlighted regions.

As noted when comparing fields of ρ_{hv} estimates, there appears to be no significant

differences in the field $\delta|\rho_{hv}|$.

Results presented show that data produced using the BMCS CONOP has better azimuthal resolution than that obtained with no beam steering. Furthermore, no apparent data artifacts were observed in the polarimetric estimates obtained using MCS, which is consistent with the conclusions from Section 3.2.2.

3.6 Chapter 3 Summary

The MCS technique presented in this dissertation provides a way to reduce the RPARs effective beamwidth and potentially meet NWS requirements with a smaller antenna aperture. By exploiting a PAR's unique dynamic capabilities in conjunction with the application of advanced signal processing techniques, we demonstrated that it is possible to design an RPAR CONOPS capable of enhancing the angular resolution of the system. That is, by electronically steering the beam on a pulse-to-pulse basis within the CPI, the motion of the antenna can be compensated to maintain the beam pointed at the center of resolution volume being sampled. MCS can reduce the apparent motion of the antenna and lead to a reduction in the effective beamwidth. In turn, mitigating the impact of beam smearing allows for smaller (and more affordable) antenna apertures that can meet effective-beamwidth requirements, which could translate into a simpler and less costly radar system.

The MCS technique was introduced and expressions for the MCS pointing angles were provided for the general case with the antenna plane tilted with respect to earth. A theoretical analysis of the impact of MCS on the quality of signal power and copolar correlation coefficient estimates was done to derive simple expressions that provide the upper bound for beam pointing offset to achieve the required bias in correlation coefficient estimates. The BMCS CONOPS, which produces sampling of concentric non-uniform resolution volumes centered around the elevation princi-

pal plane, was introduced and discussed. Through high fidelity RPAR simulations we quantified the effectiveness of MCS in mitigating beam smearing as a function of antenna phase shifter bits, antenna size, and normalized azimuthal sampling. It was demonstrated that for relatively large planar RPARs, 6-bit phase shifters provide sufficient pointing accuracy to effectively implement MCS and mostly mitigate beam smearing, while 7-bit phase-shifters would be desirable to largely eliminate smearing effects. Further, the impacts of copolar beamsteering biases resulting from the use of MCS were quantified over a large scan sector using simulations and were found to be negligible with respect to stationary operation of the same RPAR. These simulations were tailored for the architecture of the polarimetric ATD radar system in Norman, OK. The BMCS was implemented on the ATD system to demonstrate the MCS technique. First, a point target located in the vicinity of the ATD system was scanned without electronic beam steering (i.e., mimicking a parabolic-reflector antenna) and with BMCS. It was shown that the BMCS implementation on the ATD provides sufficient pointing accuracy to mitigate beam smearing effects. The BMCS CONOPS introduced was demonstrated by scanning meteorological scatterers. Fields of polarimetric-variable estimates were compared to those obtained when scanning without beam steering. These results were verified by quantifying absolute radar-variable-estimate differences with respect to a WSR-88D system (KCRI) that has inherently better azimuthal resolution. The BMCS data were shown to produce fields of radar-variable estimates with generally narrower features (more apparent in reflectivity and differential phase).

Chapter 4

The Distributed Beams Technique

"A technique is a trick that works."

Gian-Carlo Rota

The purpose of this chapter is to introduce the novel DB technique, which provides a way to reduce scan update times or alternatively improve the data quality for an RPAR CONOPS and can facilitate meeting the NOAA RFR for a future weather surveillance network if certain tradeoffs are accounted for in the radar design process. It is noted that the DB technique is presented in this chapter independently from the MCS technique presented in the previous chapter. These techniques are integrated in Chapter 6.

This chapter is structured into five sections as follows. Section 4.1 provides a detailed technical description of the DB technique and illustrates the two previously discussed applications. Section 4.2 then describes the practical implementation of DB, including calibration methods and important considerations for a successful operation. Section 4.3 takes the theoretical analysis further using the experimental implementation for a comparative demonstration of the DB technique by capturing and presenting actual polarimetric weather observations. Both applications of the DB technique presented in Section 4.1 are illustrated via observation of a mesoscale

convective precipitation system three times in rapid succession using the ATD system. Section 4.4 provides the analysis and verification of the radar-variable estimates produced using DB by comparing the data quality to those obtained from data that was collected simultaneously using NSSL's collocated experimental WSR-88D (KOUN) radar system. Section 4.5 summarizes the contributions of this chapter and discusses some alternative RPAR CONOPS techniques using the DB technique.

4.1 Distributed Beams Concept

Researchers demonstrated the use of spoiled beams and digital beamforming in elevation to reduce the volume scan time of an RPAR [42, 44]. Since operational weather radars typically scan by rotating in the azimuth plane and acquisition parameters such as the PRT are naturally defined as a function of elevation, an advantage for spoiling the beam in azimuth is that operational scanning strategies used by radars with rotating reflector antennas can be replicated in an RPAR system. That is, by scanning in azimuth only, identical acquisition parameters (M and T_s) as those in operational scan strategies can be used. When spoiling the beam and scanning in elevation, the same acquisition parameters must be used for all elevations in the cluster. And while lower-elevation angles in the WSR-88D's are scanned twice with different PRTs (i.e., split cuts) to mitigate range and velocity ambiguities, higher ones are not. Therefore, spoiling a wide fan beam in elevation could impact the quality of estimates at higher tilts or unnecessarily add more time to the scan. For example, surveillance scans at the lower tilts use longer PRTs, this would limit the Nyquist co-interval at some tilts, or the maximum unambiguous range at others. Furthermore, for typical WSR-88D scanning strategies, elevation angles scanned at higher altitudes are spread by several degrees. The larger the spoiling

factor, the larger the sensitivity loss incurred and the larger the increase in sidelobe levels. Spoiling the beam across angles that are not needed nor typically scanned (i.e., leaving large gaps) would result in an unnecessarily large sensitivity loss. The DB technique could help in these situations by fully utilizing the energy transmitted when spoiling in azimuth.

A CONOPS for the RPAR using the DB technique is now defined. Assume the antenna is rotating in azimuth at a constant speed of ω [$^\circ$ s^{-1}], a broadside transmit beam is spoiled by a factor F, and R_F beams are simultaneously generated with digital beamforming techniques [86]. Typically, the azimuthal sampling for weather surveillance is set to either one beamwidth (ϕ_1) as illustrated in Figure 4.1 (for a factor F = 5, and R_F = 5), or one-half beamwidth ($0.5\phi_1$, for a factor F = 5, and R_F = 9). The two-way beamwidth, which includes the effects on transmit and receive patterns, is defined as the angular width in degrees within which the microwave radiation is at least one-quarter of its peak intensity. For this chapter, the two-way beamwidth definition is adopted and simply referred to as the beamwidth. Finally, let us assume that the data quality requirement sought in terms of bias and standard deviation of the radar-variables estimates defines the optimal CPI as a set of M PRT of T_s seconds. With this, the optimal radar rotation speed ω can be set to,

$$\omega = \frac{\phi_1 \Delta\phi}{MT_s} \quad [^\circ \text{ s}^{-1}], \tag{4.1}$$

in order to collect the desired CPI (MT_s) over the specified normalized angular sampling spacing of $\Delta\phi$. It is noted that due to continuous antenna rotation coupled with the need to perform coherent processing of multiple samples, the resulting effective antenna beamwidth is broader than the stationary inherent antenna beamwidth (i.e., beam smearing as described in Chapter 3). As demonstrated in this

reference, beam smearing effects are not controlled only by the rotation speed, but rather by the normalized azimuthal sampling spacing, $\Delta\phi$. The value of $\Delta\phi$ for all cases illustrated in this chapter is 0.5, the same as that used in the WSR-88D super-resolution scans. That is, if the CPI is designed using equation 4.1 and with $\Delta\phi$ of 0.5 or 1, beam smearing effects incurred with the DB technique are analogous to those incurred by the WSR-88D. As mentioned before, there are two applications being considered for the DB CONOPS: A) Scan Time Reduction and B) Variance Reduction. The key difference between these applications is in the RPAR rotation speed and the dwell acquisition parameters. In A), the RPAR rotates R_F times faster and the number of samples per CPI is reduced by R_F, and DB increases the number of available samples by R_F (back to the desired number). In B), the RPAR speed and acquisition parameters are maintained, and DB increases the number of available samples by R_F.
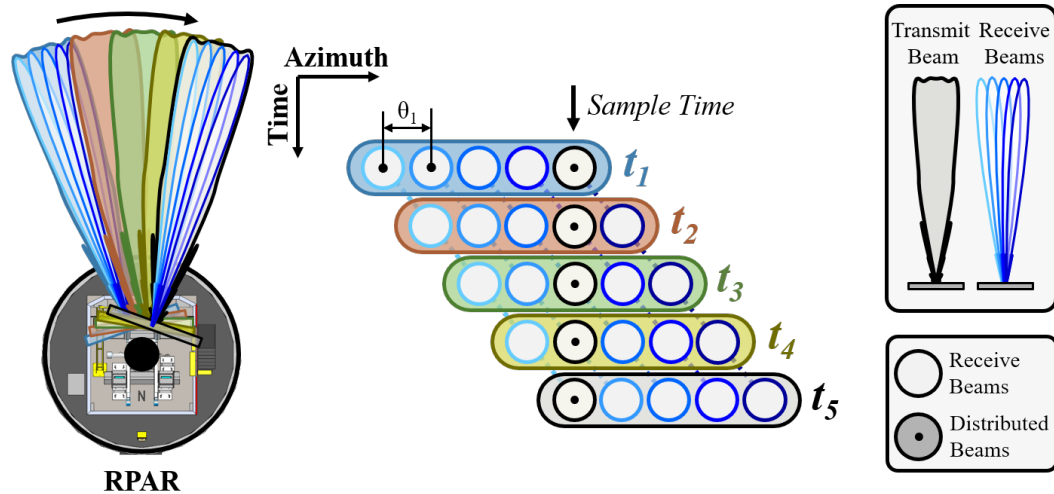
Figure 4.1: Illustration of the DB technique. On the left, a top view of an RPAR system illustrates the radiation of wide transmission beams for which multiple simultaneous beams are received (note that the beams are not drawn to scale). On the center, the diagram shows how receive beams from subsequent transmissions can be grouped to increase the number of samples in a CPI.

4.1.1 Scan Time Reduction

Applying the DB scan-time reduction strategy requires an increase in the rotation speed. This causes the number of transmitted pulses per CPI to be reduced to $M_{DB} = M/R_F$, and the DB rotation speed to be increased by a factor of R_F to $\omega_{DB} = R_F\omega$. As the RPAR rotates at ω_{DB}, a pulse train defined by the CPI is continuously transmitted every T_s seconds, and M_{DB} samples are received per CPI on each digitally generated receive beam. Given that the antenna broadside beam position shifts at $\omega_{DB}M_{DB}T_s = \phi_1\Delta\phi$ degrees per CPI, and the azimuthal sampling of the R_F receive beams is set to $\phi_1\Delta\phi$, subsequent receive beams (as illustrated in Figure 4.1) sample approximately the same azimuth location. That is, in a continuous rotation regime, ω_{DB} is such that the centers of resolution volumes (defined by the effective beamwidths in azimuth and elevation, and the range resolution) sampled by the set of R_F beams received every $M_{DB}T_s$ seconds (from distinct spoiled transmit beams) are associated with the same location in space. Each of the samples received on these different transmit-receive beams can then be coherently combined to get the $M_{DB}R_F = M$ samples required to obtain the desired data quality. In summary, operating the radar under this DB CONOPS results in reducing the scan time by a factor R_F while maintaining the same variance of radar-variable estimates.

Comparing this DB CONOPS to that from a conventional radar with a parabolic-reflector antenna, the DB technique exploits the RPAR beamforming capability to reduce the scan time. This comes at the expense of 1) increased rotation speed, 2) two-way pattern increased sidelobe levels [102], 3) reduced sensitivity, and 4) an increased two-way beamwidth due to the wider transmit beam. However, it is believed that some of the listed limitations can be mitigated in a straightforward manner. The rotation speed increase is technically possible as argued by [114] since

the rotating machinery has been around for a long time and has a high technology-readiness level. This reduces the risk of deploying and maintaining RPAR pedestals capable of rotating at higher rates. A larger aperture would be required to reduce the increased beamwidth and sidelobe levels, to implement this CONOPS and meet the RFR. This would entail the use of a more aggressive taper on the receiving array to lower sidelobe levels [89] and such that the resulting two-way beamwidth and side-lobe levels meet the desired requirements [38]. This should be considered at the RPAR's design stage and is beyond the scope of this work. The amount by which the aperture has to be increased to achieve similar sidelobe levels as those obtained when using narrow beams on transmit and receive depends on the array size, the spoiling factor used, and the pattern synthesis algorithm. A larger and heavier aperture consuming more power requiring a pedestal that can support higher rotation rates will increase the cost, but this is dependent on the selection of R_F. For example, for an RPAR with a two-way stationary $1°$ broadisde beamwidth when using narrow transmit-receive beams, the aperture would need to be increased by ∼19% in azimuth for a spoiling factor of $F = 3$ if the resolution is to be maintained (i.e., the transmit-receive combination results in an effective beamwidth of $1°$ at broadside). And finally, the sensitivity loss could be recovered by increasing the power radiated by each array element, which may increase the cost of the antenna panels. For example, there is a sensitivity loss relative to the narrow beam of ∼6.2 dB when spoiling the transmit beam by a factor of 3, and ∼8.5 dB by a factor of 5 for the illustrative antenna patterns presented in Figure 2.9. These sensitivity losses, which are greater than the theoretical loss of $10 \log_{10}(F)$, result from the pattern synthesis technique used to produce the spoiled transmit beams [115].

4.1.2 Variance Reduction

For the second possible application, the number of samples per CPI and the rotation speed are maintained at M and ω, respectively. And similar to the previous scenario, operation is in a constant rotation regime of R_F receive beams being digitally generated every MT_s seconds (but now from distinct transmit beams). The receive beams are still directed at approximately the same space location, since $\omega MT_s = \phi_1 \Delta \phi$ and the receive beams are spaced exactly by $\phi_1 \Delta \phi$. Samples received on these beams can be coherently processed to obtain $M_{DB} = M R_F$ samples. Thus, increasing the number of samples by the factor R_F can result in a significant reduction in the variance of radar-variable estimates [52]. The reduction factor depends on the dwell times and several signal characteristics, but it is mostly controlled by the SNR, the σ_v, and ρ_{hv} for the reflectivity and polarimetric-variable estimates. It is noted that at high SNR, the reduction factor is directly proportional to R_F and independent of spectrum width or other signal characteristics.

To illustrate the potential data quality improvement, Figure 4.2 shows the standard deviation of signal power estimates as a function of the number of samples, M, computed from simulated time-series data for a 10-cm wavelength radar with with $T_s = 3$ ms (typically used in surveillance scans), $\sigma_v = 2$ m s^{-1}, a maximum unambiguous velocity $v_a = 24.6$ m s^{-1}. A set of SNR are selected to account for the spoil factors ($F = 1$ or pencil, $F = 3$, $F = 5$) and the potential sensitivity reduction incurred when spoiling the transmit beam. SNRs of 2 and 20 dB are selected for the pencil beam ($F = 1$) as a reference, and SNRs for the spoiled beams are derived reducing those by the corresponding sensitivity loss (i.e., 6.2 dB for $F = 3$ and 8.5 dB for $F = 5$). The markers on each curve illustrate the potential reduction in the standard deviation of power estimates for the application of DB with spoiled factors

of 3 and 5, and with $0.5\phi_1$ sampling (i.e., $R_F = 5$ and $R_F = 9$, respectively), with respect to the pencil beam without using DB. Specifically, the circles on the curve show the standard deviation of power estimates when using DB to improve data quality with $F = 3$ and $R_F = 5$, and the stars show the standard deviation of power estimates with $F = 5$ and $R_F = 9$. At medium-to-high SNRs ($>\sim 8$ dB), a reduction of 0.5-1 dB in the standard deviation of estimates can be achieved using DB. Even though this only shows the improvement for signal power estimates, increasing the number of samples also reduces the bias and standard deviation of all spectral moments and polarimetric variables. The CONOPS presented by this application of the DB also exploits the RPAR beamforming capability, but now to reduce the variance of radar-variable estimates. In comparison to a similar pencil-beam CONOPS, this application would not require an increase in the rotation speed and has the potential of significantly reducing the fluctuation of estimates in the fields of radar products (and thus improving interpretation of the displayed fields).
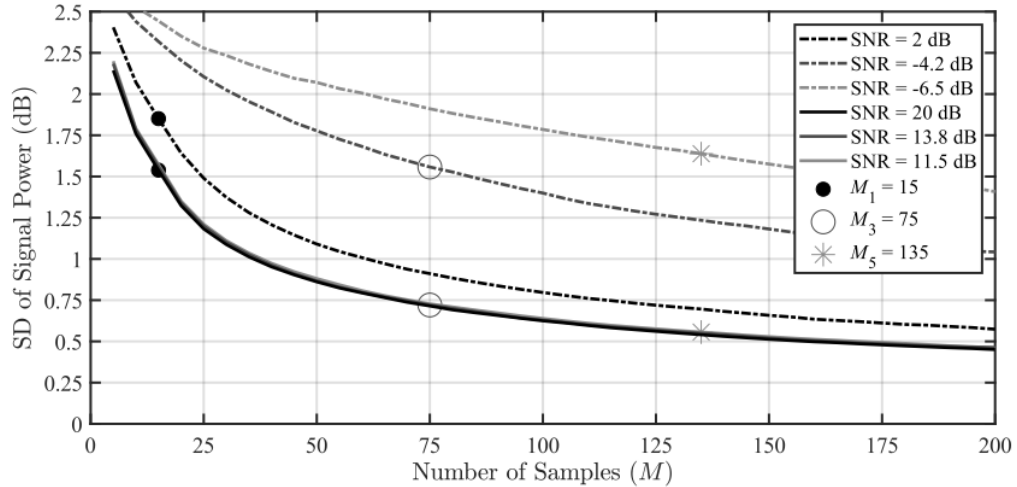
Figure 4.2: Standard deviation of signal power estimates as a function of M for T_s = 3 ms, $\sigma_v = 2$ m s^{-1}, and several representative SNRs. The dot markers at $M_1 = 15$ represent the typical number of samples for the surveillance scan of VCP 12. Circle and star markers represent the number of samples obtained with DB for $\Delta\phi = 0.5$, and with $F = 3$ and $F = 5$, respectively.

These two applications of the DB technique may be highly suitable for advance in observations of different precipitation systems. That is, VCPs for observing fast-evolving convective precipitation systems could use the first application of the DB technique with its higher rotating speed, while VCPs for stratiform precipitation systems could use the second application collecting the higher number of sample realizing reduced weather data variance.

For example, consider the WSR-88D operational VCP number 212 for convective precipitation, which takes approximately 4.5 minutes to complete the operation [105]. An RPAR using 4.1.1 with a spoil factor $F = 1.5$, $R_F = 3$ ($\Delta\phi = 0.5$), and rotating three times faster than the WSR-88D could complete the VCP in about 1.5 minutes, maintaining the same variance of estimates using all of the same radar parameter constraints established for the operation. Considering that the spoil factor in this example is small, if not mitigated, the increase in sidelobe levels and loss of sensitivity would also be relatively small (thus maintaining the overall data quality comparable to that of using RPAR as parabolic reflector). However, this would require that the radar rotate three times faster on every elevation scan. Alternatively, consider the VCP number 32 for clear-air or weak precipitation situations, which takes approximately 9.5 minutes to complete [105]. An RPAR using 4.1.2 with a spoil factor $F = 3$, $R_F = 5$ ($\Delta\phi = 0.5$), and rotating at the same speed could complete the VCP in the same period, but there would be a significant reduction in the standard deviation of estimates ($\sqrt{R_F}$ at high SNR [52]). As noted, this is especially important for weak precipitation VCPs where coherent processing of a large number of samples is required to detect and estimate signals with low SNR. Furthermore, given that these systems do not normally present strong reflectivity gradients, there would be little impact from the higher two-way pattern sidelobe levels. As discussed previously, spoiling the transmit beam leads to a reduction

in sensitivity (e.g., $\sim$6.2 dB) which should be accounted for in the antenna design process to get the desired detectability of the weaker echoes. The increase in the number of samples results in variance reduction and facilitates the reduction in censoring thresholds [5] that in turn partially compensates for the spoiled beam sensitivity loss. This is effectively a signal processing gain that increases the detectability of echoes and should also be accounted for in the antenna design. This can be seen on Figure 4.2 by comparing the standard deviation of power estimates in the black dot marker found on the solid line (M_1 = 15 at SNR = 20 dB) compared with the circle marker on the dotted line (M_3 = 75 at SNR = -4.2 dB) where the SNR is 6.2 dB lower, yet the standard deviation of estimates of M_3 is better.

Of course, the limitations related to the use of spoiled transmit beams have to be considered for an operational use of the DB technique. That is, important aspects have to be considered in the design of the rotating pedestal and the antenna. Pedestals would be required to rotate the antenna at higher rates (based on the scan-time reduction factor desired), and the antenna aperture would have to be increased so that the two-way sidelobes can be lowered (tapering the receive array) to meet the prescribed requirements. One alternative proposed for future research is to investigate the use of adaptive beamforming methods [102] in conjunction with the DB technique to reduce increased sidelobe levels. Both of these applications of the DB technique are possible and are illustrated in Section 4.3. The next section will advance the theoretical aspects of DB by presenting a proof-of-concept implementation of the technique and discuss important antenna calibration considerations.

Of course, the limitations related to the use of spoiled transmit beams have to be considered for an operational use of the DB technique. That is, important aspects have to be considered in the design of the rotating pedestal and the antenna. Pedestals would be required to rotate the antenna at higher rates (based on the scan-

time reduction factor desired), and the antenna aperture would have to be increased so that the two-way sidelobes would meet the prescribed requirements. Sill, both of these applications of the DB technique are possible and illustrated in Section 4.3. The next section will advance the theoretical aspects of DB by presenting a practical implementation of the technique and discuss important antenna calibration considerations.

4.2 Practical Implementation, Calibration, and Verification

4.2.1 Implementation on the ATD

Through element-level control of the magnitude and phase of transmitted signals, this system is capable of synthesizing different beam patterns on transmission. Therefore, the ATD can be used to implement the DB technique in an experimental research environment. The DB technique was implemented in the ATD using $F = 3$ with $R_F = 3$ or 5 ($\Delta = 1$ or 0.5) and using $F = 5$ with $R_F = 5$ or 9 ($\Delta = 1$ or 0.5). The next subsection provides some of the important calibration considerations that were taken in the implementation.

Initial array calibration was performed in the anechoic chamber at MIT Lincoln Laboratory, whereby individual element transmit powers and phases were measured. These measurements were used to derive lookup tables that digitally equalize the power of each element and align their phases. The next subsection provides some of the important calibration considerations that were taken in the implementation.

4.2.2 Calibration of Power in DB Implementation

The spoiled transmit beams produced by the ATD are synthesized using phase-only coefficients to maximize the power on transmit [115]. The co-polar main lobes of these antenna patterns were measured using the calibration infrastructure installed in the vicinity of the ATD [56], and those corresponding to the horizontal polarization are shown in Figure 4.3 (axes are scaled to enhance visual interpretation). Azimuth-plane measurements of the horizontal polarization broadside transmit beams, as well as the two-way beams resulting from the use of each of these transmit beams with narrow beams on reception are presented in Figures 4.4b, 4.4c, and 4.4d. Note that two-way beams are normalized using the peak out of the set of digitally formed beams.

Examination of the two-way beams in Figures 4.4c and 4.4d reveals variations in the magnitude of beam peaks. These beam peak differences arise as a consequence of the small ripples in the spoiled transmit beams (Figure 4.4a), which have to be compensated prior to DB processing. The beamwidth and peak-sidelobe level (PSL) of the two-way beams were measured and the results for the horizontal polarization are presented in Tables 4.1 and 4.2, respectively. Similar results were obtained for the vertical polarization beams.

It is apparent from these measurements that the beamwidth is not constant and

Beam Type	Beamwidth (°)								
	φ_{-4}	φ_{-3}	φ_{-2}	φ_{-1}	φ_0	φ_1	φ_2	φ_3	φ_4
$F = 1$ and $R_F = 1$	—	—	—	—	1.58°	—	—	—	—
$F = 3$ and $R_F = 5$	—	—	1.75°	2.15°	2.32°	2.24°	1.76°	—	—
$F = 5$ and $R_F = 9$	1.87°	2.06°	2.42°	2.32°	2.23°	2.36°	2.39°	2.08°	1.77°

Table 4.1: Measured Two-Way Antenna Pattern Beamwidths
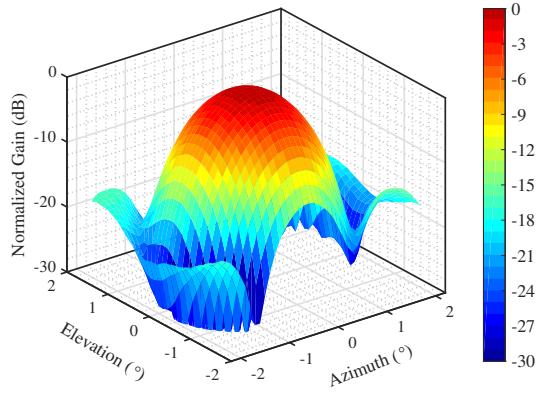
(a)
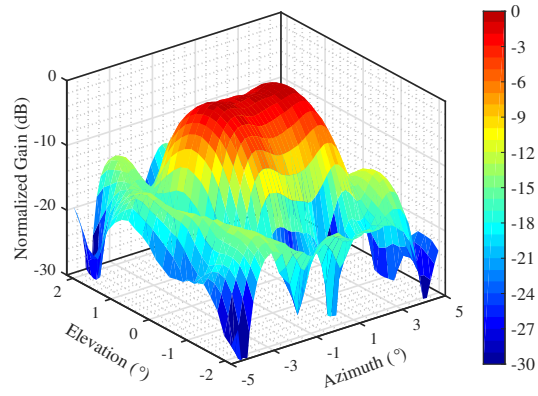
(b)
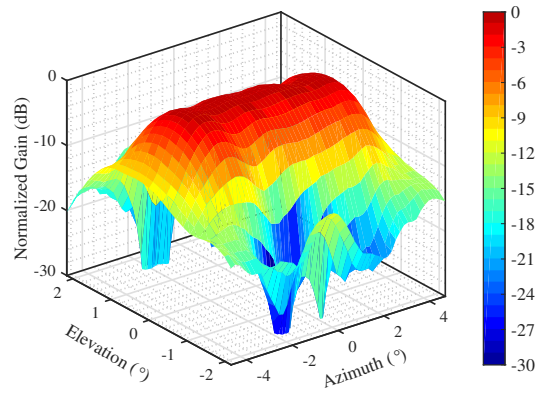
(c)

Figure 4.3: Measured one-way normalized ATD antenna mainlobe transmit patterns (a) narrow beam (b) beam spoiled by $F = 3$, and (c) beam spoiled by $F = 5$.
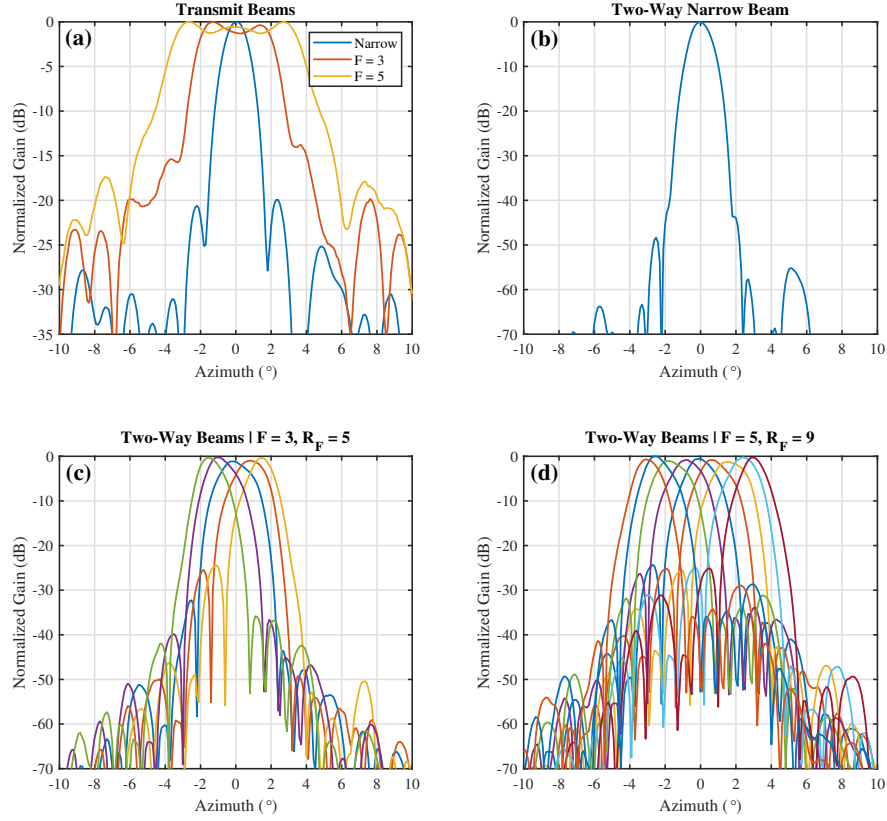
Figure 4.4: Azimuth-plane measurements of ATD horizontal polarization antenna patterns on broadside (a) one-way transmit narrow and spoiled beams for $F = 3$ and $F = 5$, (b) two-way narrow beam, (c) two-way spoiled beams for $F = 3$ and $R_F = 5$, and (d) two-way spoiled beams for $F = 5$ and $R_F = 9$. For (c) and (d), the beam steering angles are computed for $0.5\phi_1$ sampling.

Beam Type	Peak Sidelobe Level (dB)								
	φ_{-4}	φ_{-3}	φ_{-2}	φ_{-1}	φ_0	φ_1	φ_2	φ_3	φ_4
$F = 1$ and $R_F = 1$	—	—	—	—	-48.4	—	—	—	—
$F = 3$ and $R_F = 5$	—	—	-35.8	-36.6	-31.8	-25.5	-24.4	—	—
$F = 5$ and $R_F = 9$	-29.0	-28.7	-31.1	-26.3	-24.3	-25.2	-24.1	-24.7	-24.8

Table 4.2: Measured Two-Way Antenna Pattern Peak Sidelobe Levels

that two-way beams near the edge of the spoiled transmit beam's mainlobe are narrower. This is due to the sharp decay in mainlobe energy (from the spoiled transmit beam) on the digitally formed receive beams near the edges. Given that the beamwidth determines the resolution volume, where most of the mainlobe energy is concentrated, it is important to consider these variations for both the horizontal and vertical polarizations to produce accurate polarimetric measurements using the DB technique. It is also noted that the PSL increases significantly with the use of spoiled transmit beams. Specifically, the measurements indicate an average increase of approximately 17.52 dB for $F = 3$ and 21.88 dB for $F = 5$, both with respect to the narrow beam. The PSL of the two-way beams near the edges for negative azimuth angles appears to be consistently lower (for both $F = 3$ and $F = 5$). This is explained by observing that even though the narrow transmit beam (blue trace in Figure 4.4a) has good symmetry, the two-way narrow beam does not (Figure 4.4b). The appearance of the first sidelobe on the two-way narrow beam pattern at approximately –2.6° in azimuth, indicates that the one-way receive beam sidelobe levels are higher on the negative azimuth angles. As the one-way receive beam is digitally steered towards negative azimuth angles, the first sidelobe gets suppressed by the decaying mainlobe on the spoiled transmit beam. The presence of this first sidelobe was confirmed by examining the one-way receive beam pattern (not shown here).

Power calibration for the DB technique was performed to ensure that the powers measured by receive beams of each polarization (H and V calibrated independently) are equal for the same target. Considering that this is a weather radar, a calibration procedure for volumetric targets was carried out. First, mainlobe (null to null) powers for the measured two-way beams (single cuts shown in Figures 4.4b, 4.4c, and 4.4d) were integrated in azimuth and elevation. Then, using the center beam as a

reference and normalizing its integrated power to 0 dB, other beams were digitally compensated by the relative difference between their integrated mainlobe power with respect to that of the center beam. This ensures that the integrated powers of all mainlobes are equal. The approach is similar to that discussed by [46, 47], although mainlobe integrated powers are used here instead of beam peaks. Notice that given the significant beamwidth variations (as presented in Table 4.1), which leads to resolution volumes of different sizes, compensating with the two-way beam peak differences only would not be sufficient for distributed weather targets. Details about polarimetric calibration using the DB technique are not presented here and are left for future research.

The measurements presented in this subsection motivate the importance of accurate calibration of signal power to successfully implement the DB technique. The calibration procedure for signal phase is outlined in the next subsection.

4.2.3 Calibration of Phase in DB Implementation

In addition to correcting for signal power differences as a function of steering angle, the phases of the two-way beams may have to be aligned to ensure a coherent transition across the R_F receive beams for Doppler processing. Achieving phase calibration requires two considerations. First, similar to the power calibration, instantaneous phases of the two-way beam peaks were measured and digitally aligned. It consists of measuring signal phases at the peak of each of the two-way beams and deriving a set of phase alignment coefficients such that all two-way beam-peak phases are equal (arbitrarily set to 0° here). Then, phase alignment coefficients are applied digitally at the signal processor. Second, a deterministic phase difference arises because the antenna plane does not contain the center of rotation (due to the

antenna arm used to attach the antenna to the pedestal, which displaces the antenna from the rotation center). That is, the phase centers for consecutive two-way distributed beams are shifted by

$$2\pi \frac{d}{\lambda} \left[1 - \cos(\omega M_{DB} T_s)\right] \quad \text{[rad]} \tag{4.2}$$

where d is the distance between the center of rotation and the array phase center, and λ is the radar wavelength. This deterministic phase compensation factor aligns the phase centers for the two-way distributed beams. It is noted that this depends on the particular RPAR design, and it may not be necessary if the antenna and the axis of rotation are in the same plane. Phase calibration is critical for the DB technique. If the phases of signals from DB samples are not coherent across two-way beam transitions, the combined time-series data cannot be coherently processed. Any loss of coherency from sample to sample would prevent the use of conventional pulse-pair or spectral processing methods (e.g., clutter filtering).

Calibration allowed the implementation of DB to demonstrate both applications proposed in Section 4.1, namely, (4.1.1) scan time reduction and (4.1.2) variance reduction. The proof-of-concept implementation of the DB technique on the ATD allows for $F = 3$ or $F = 5$ with $R_F = 5$ or 9, respectively ($0.5\phi_1$ sampling), and a rotation speeds of $\omega = 4$ or $8\,°\,\text{s}^{-1}$. Additionally, a narrow beam mode that mimics the operation of a reflector-antenna radar was implemented to validate the results from using the DB technique.

4.2.4 Verification of Implementation and Calibrations

Calibration is verified by digitally applying calibration corrections derived in Section 4.2.2 to volumetric weather targets. A sector scan was collected on 27 March

2020 at 18:07:45 Z, by commanding the ATD system to mechanically rotate clockwise from $300°$ to $340°$ in azimuth at $\omega = 4°\text{s}^{-1}$, and a constant $0.5°$ elevation angle. A total of 64 pulses were collected per CPI at a PRT of 3 ms, resulting in a $0.5\phi_1$ azimuthal sampling spacing. The broadside transmit beam was spoiled with $F = 5$, and $R_F = 9$ beams were generated for each polarization on reception. The data recording period for every pulse was set to capture samples from 100 μs to 450 μs, which correspond to ranges between 15 to 67.5 km. Note that this receive window was set to collect meteorological echoes of interest only and reduce data size.

Data from all receive beams observing the convective precipitation system were initially processed without applying calibration corrections. Fields of reflectivity produced for individual uncalibrated receive beams are shown in the top row of Figure 4.5. Comparing the panels from either one of the edge beams (φ_{-4} and φ_4) with the center beam (φ_0), noticeable differences ($\sim$2–3 dB) can be seen in the estimated fields although the time lag between them is only 0.768 s. Differences for other receive beams are present as well, but they may not be as apparent in this qualitative comparison.

Analogous fields of reflectivity derived by applying power calibration correc-
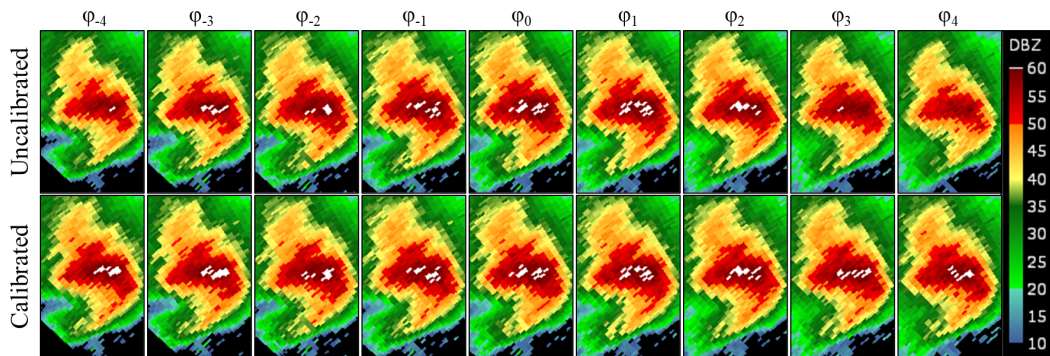
Figure 4.5: Fields of reflectivity produced from two-way beams with $F = 5$ and $R_F = 9$, (top row) uncalibrated, and (bottom row) calibrated.

tions are shown in the bottom row of Figure 4.5. No apparent qualitative differences are observed in reflectivity estimates from these panels even though they come from beams with different spatial resolution, which corroborates the effectiveness of calibration corrections given that observations from all receive beams are similar.

A quantitative evaluation of calibration corrections is carried out to confirm these results. Gate-to-gate differences between reflectivity fields estimated from each beam (φ_i) with respect to the center beam (φ_0) are computed for the uncalibrated and calibrated cases to produce histograms of reflectivity differences (δZ), presented in Figure 4.6. Considering the relatively slow evolution of the weather with respect to the time differences amongst these beams (<1 s), it is expected that δZ should be zero-mean with a standard deviation roughly dictated by the radar's acquisition parameters (M and T_s) and signal characteristics (SNR and σ_v). Panel (a) shows the histograms of δZ for uncalibrated reflectivities while panel (b) shows the same for calibrated reflectivities. Results in (a) show that, on average, receive beams φ_{-4} and φ_4 (which are symmetric about the broadside) are equally biased by $\sim$-2.5 dB, while other receive beams also present lower negative biases on average ($\sim$1.5 dB for $\varphi_{\pm 3}$, 0.7 dB for $\varphi_{\pm 2}$, and <0.25 dB for $\varphi_{\pm 1}$). These negative biases are consistent with the power calibration corrections derived for the receive beams. Results in (b) verify the effectiveness of calibration corrections, as the histograms corresponding to all beams are centered more closely around zero with mean values < 0.054 dB.

To verify phase calibration, samples from a resolution volume containing a stationary point target were extracted from all 9 two-way beams and were coherently processed to form a DB-CPI of 576 samples (9×64). The target is located at 31.65 km in range and approximately $300.96°$ azimuth with respect to North. These were used to estimate the targets' Doppler spectrum. The uncalibrated and calibrated
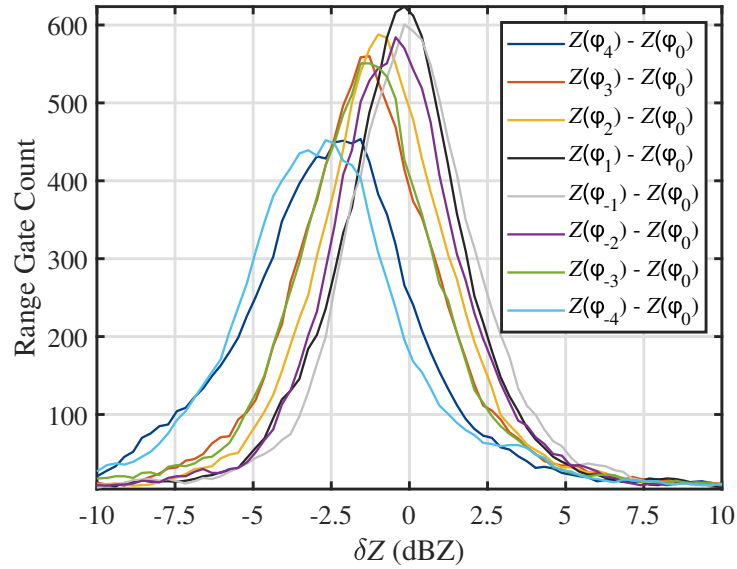
(a) Uncalibrated DB beams
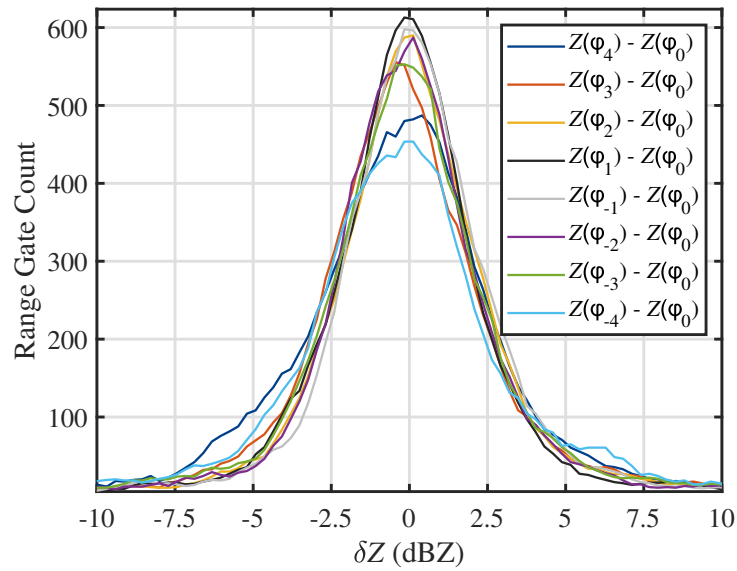
(b) Calibrated DB beams

Figure 4.6: Histograms of reflectivity differences (δZ) computed from gate-to-gate differences between reflectivity fields shown in Figure 4.5. (a) uncalibrated beams and (b) calibrated beams. Differences are computed with respect to the center beam, φ_0.

spectra are shown in Figure 4.7. Both phase corrections were applied to estimate the calibrated spectrum. It is apparent that phase discontinuities in the uncalibrated time-series IQ data results in the appearance of spurious harmonics, which are not present after phase calibration. In the next section, both DB applications are illustrated by scanning actual weather events and completing a quantitative analysis of the results.
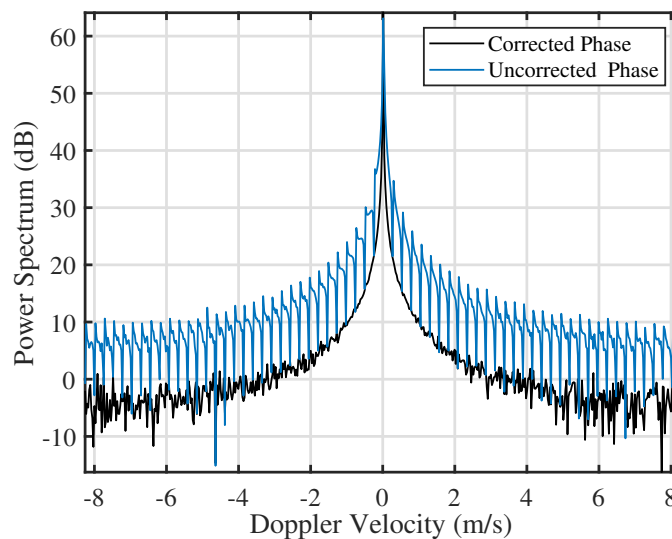
Figure 4.7: Doppler spectra for the stationary point-target without phase calibration (blue curve) and with phase calibration (black curve).

4.3 Demonstration of DB

After implementation of the DB technique, data were collected with the ATD system to demonstrate both applications proposed in Section 4.1. Radar calibration parameters derived using the procedure described in Section 4.2 are applied in the digital signal processor for these demonstration experiments.

4.3.1 Experimental Sector Scans

For the first experiment, three sector scans were collected in rapid succession on 19 March 2020. For scan 1, the ATD rotated at $\omega_1 = 4° \text{ s}^{-1}$, the broadside transmit beam (i.e., no MCS) was spoiled with $F = 3$, and $R_F = 5$ beams were generated for each polarization on reception. Data from this scan were collected at 17:48:54 Z, and are used to demonstrate the DB technique for data quality improvement (Section 4.1.2). For scan 2, the ATD rotated at $\omega_2 = 4° \text{ s}^{-1}$, both the transmit and receive beams were broadside narrow, mimicking the operation of a conventional reflector-based radar. Data from this scan were collected at 17:49:46 Z, and are used here as a reference to verify the DB data. For scan 3, the ATD rotated at $\omega_3 = 8° \text{ s}^{-1}$, the broadside transmit beam was spoiled with $F = 3$, and $R_F = 5$ beams were generated for each polarization on reception. Data from this scan were collected at 17:50:25 Z and are used to demonstrate the DB technique for scan time reduction by a factor of 2 (Section 4.1.1). It should be noted that using R_F beams, could allow a scan time reduction by a factor of 5, but that would require rotating 5 times faster, which was not possible at the time of this experiment. Thus, data from 3 two-way beams in scan 3 were discarded prior to DB processing to establish a fair performance comparison with scan 2. For all three scans, the radar broadside was commanded to mechanically rotate clockwise from 140° to 166° in azimuth, at constant 0.5° elevation, with a continuous pulse transmission at $T_s = 3$ ms. The settings for scans 1 and 2 result in 64 pulses for $0.5\phi_1$ sampling in azimuth, while settings for scan 3 result in 32 pulses for $0.5\phi_1$ sampling in azimuth since $\omega_3 = 2\omega_1$. The data recording period for every pulse was set to capture samples from 200 μs to 600 μs, which correspond to ranges between 30 to 90 km. Receiver range-time samples were produced at a rate of 4 MHz, which results in a range sampling

interval of 37.5 m.

Data from scans 1 and 3 were processed using the DB technique. That is, IQ data from two-way beams were calibrated in magnitude and phase and CPIs pointed in the same direction where grouped for processing. Radials of DB-CPIs from scan 1 resulted in 320 (5 × 64) IQ samples per range gate, while radials of data from scan 3 resulted in 64 (2 × 32) IQ samples per range gate. Data from scan 2 were processed using conventional signal processing techniques with radials of data with 64 IQ samples per range gate. Range-time processing was set to incoherently average samples from 6 consecutive range gates, which results in a range sampling spacing of 225 m. Fields of radar-variable estimates resulting from processing the data from these scans are presented in Figure 4.8. Panels are organized as follows: the top row corresponds to scan 1, the middle row corresponds to scan 2, and the bottom row corresponds to scan 3; the columns from left to right show fields of radar Z_h, Z_DR, Φ_DP, and ρ_hv.

4.3.2   Demonstration of Variance Reduction

A qualitative comparison of radar-variable estimates from scans 1 and 2 is discussed first. While scan times were the same (∼6.5 sec), the fields from scan 1 are spatially smoother compared to their scan 2 counterparts. This is observed for all fields but is more noticeable in the fields of Z_DR. The smoothness of the fields in scan 1 with respect to the corresponding ones in scan 2 is a result of the combined effects of (1) a reduction in the standard deviation of estimates due to the larger number of available samples, and (2) the degraded spatial resolution; the azimuth beamwidth of scan 1 is ∼2.04°, while that of scan 2 is ∼1.64°. Comparing the fields of Z_h and Z_DR, it is apparent that power calibration for the DB technique was achieved since no
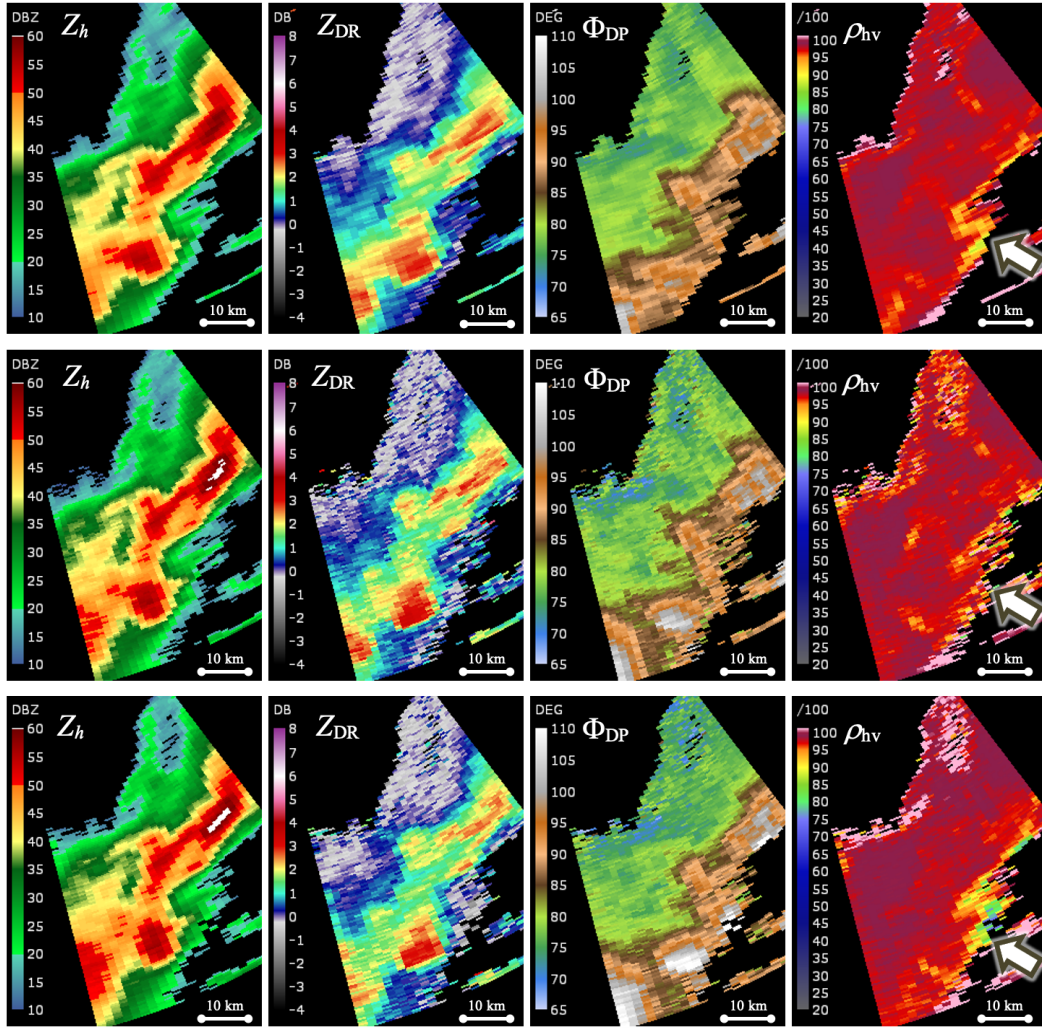
Figure 4.8: Radar-variable estimates obtained from three scans collected in rapid succession. Panels are organized as follows: the top row corresponds to scan 1 (DB with $F = 3$, $R_F = 5$), the middle row corresponds to scan 2 (narrow beam), and the bottom row corresponds to scan 3 (DB with $F = 3$, $R_F = 2$); the columns from left to right show fields of radar reflectivity (Z_h), differential reflectivity (Z_DR), differential phase (Φ_DP), and copolar correlation coefficient (ρ_hv).

apparent artifacts are observed, and estimates from scans 1 and 2 have comparable values. Comparison of the fields of Φ_{DP} from scans 1 and 2 indicate that phase calibration was also achieved successfully. Careful examination of the Z_h and Z_{DR} fields reveals what appears to be sidelobe contamination in the estimates from scan 1. This is observed in the Z_h and Z_{DR} fields from scan 1 in the area surrounding the strong Z_h core ($\sim$57 dBZ) located to the south of the sector (indicated with white arrows in the panels of ρ_{hv}). This can also be inferred by comparing the fields of ρ_{hv} estimates, where lower signal cross-correlation values ($\sim$0.85-0.90) are observed in data from scan 1 around the suspected area with sidelobe contamination. This was expected, considering the significantly higher sidelobes on the two-way patterns resulting from the use of the spoiled transmit beams ($F = 3$), especially in the presence of a strong reflectivity gradient.

The spatial resolution appears to be slightly better on data from scan 2. This was also anticipated, considering the increased beamwidth of the two-way patterns resulting from the use of the spoiled transmit beam ($F = 3$). Finally, a predicted sensitivity difference is observed by comparing the coverage of weather echoes in all radar variables. This difference is smaller than the gain difference between the two-way narrow patterns and the two-way spoiled pattern (with $F = 3$) presented in Section 4.1. This is due to variance reduction resulting from averaging a larger number of second-order estimates. That is, since the default WSR-88D SNR censoring threshold of 2 dB is used to process both datasets, but due to the reduced fluctuation of estimates from the DB data, more samples that would otherwise have been filtered (i.e., without DB), exceed the censoring threshold.

4.3.3   Demonstration for Scan Reduction Times

Next, a comparison of radar-variable estimates from scans 2 and 3 is presented. Scan 3 data were collected in approximately 3.25 s, twice as fast as data from scan 2. Since data from scan 3 were collected at $\omega_3 = 8°$ s^{-1}, a set of $M = (0.5\phi_1)/(\omega_3 T_s)$ = 32 samples were obtained for every two-way beam. Using the DB technique with $R_F = 2$ (ϕ_0 and ϕ_1 in Tables 4.1 and 4.2) and coherently processing IQ data from 2 beams pointed in the same direction resulted in an effective CPI of 64 samples per radial. This CPI matches that of scan 2, and it is expected to result in similar data quality even though it was collected twice as fast. An analogous examination of radar-variable estimates confirms this hypothesis. That is, all fields have similar spatial texture, indicating that the standard deviation of estimates is comparable. And while no data artifacts related to calibration are apparent, the region with suspected sidelobe contamination is present in data from scan 3, as expected. A discussion on possible ways to mitigate the impact on spatial resolution and sensitivity incurred by the use of spoiled transmit beams is provided in the conclusions.

To quantify the variance reduction as a result of using the DB technique, a spatial texture was derived from Z_{DR} fields. Spatial texture fields were produced using a running window of 3 beams in azimuth by 3 gates in range and computing the standard deviation (SD) of estimates in the window. Comparing the left and center spatial SD fields in Figure 4.9 reveals the data quality improvement of the DB technique over the conventional processing, while comparing the center and right spatial SD fields shows that data from scans 2 and 3 have comparable quality. Finally, Figure 4.10 shows the median spatial SD per radial as a function of azimuth, where the blue, black, and green curves represent data from scans 1, 2, and 3,
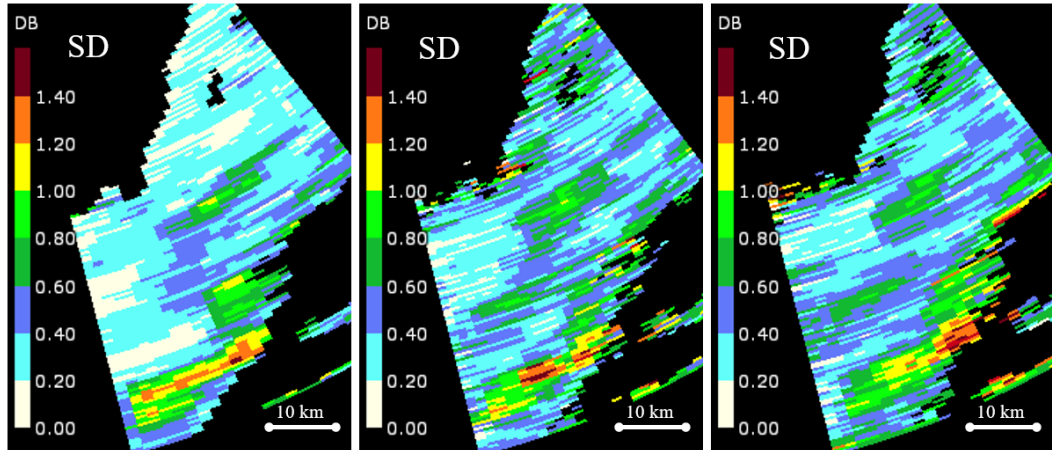
Figure 4.9: Spatial fields of standard deviation (SD) were produced using a running window of 3 beams in azimuth by 3 gates in range. Comparing the left and center fields reveals the data quality improvement of the DB technique over the conventional processing and comparing the center and right fields shows that comparable data quality was achieved by scanning weather echoes twice as fast.

respectively. It is clear from these results that a comparable spatial SD of estimates is achieved when using the DB technique described in Section 4.1.1, and that the spatial SD of estimates is significantly improved when using the DB technique in Section 4.1.2. In the next section, Section V, a qualitative comparative analysis of DB data and WSR-88D data is presented.

4.4 Verification of DB Data with KOUN Radar

With the improvements of the DB technique in scan time or SD reduction illustrated in the previous subsection, data produced with this technique were verified by comparing them to a WSR-88D radar system. The KOUN radar in Norman, OK is operated and maintained by the NSSL and it is collocated with the ATD system. It serves as an experimental testbed for research and development of new techniques. Two simultaneous data collection experiments are presented for the verification process. The first one is used to evaluate the quality of spectral moments, namely Z_h,
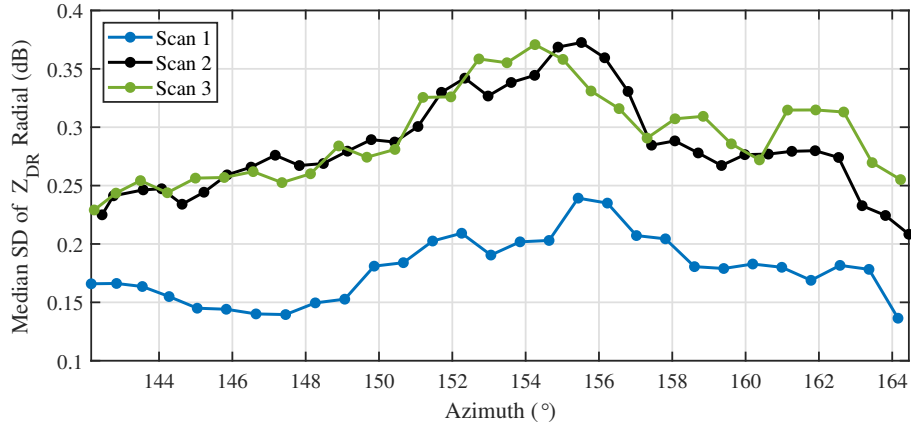
Figure 4.10: Median spatial SD per radial as a function of azimuth. The blue, black, and green curves are derived from scans 1, 2, and 3.

v_r, and σ_v. This case was selected because the Doppler velocities observed for this weather event did not exceed the maximum unambiguous velocity (v_a) on the scan from the ATD radar ($v_a = 8.27$ m s^{-1}). The second experiment was used to evaluate the quality of polarimetric variables, namely, Z_{DR}, Φ_{DP}, and ρ_{hv}. This case was selected because of the widespread nature of the weather event observed, which covered most of the sector observed with the ATD using the DB technique.

4.4.1 Experiment Comparing Quality of Spectral Moments

The first experiment was conducted on 04 March 2020. The ATD system was commanded to rotate at $\omega = 4°$ s^{-1}, the broadside transmit beam was spoiled with $F = 3$, and $R_F = 5$ beams were generated for each polarization on reception. Data from this scan were collected at 02:44:54 Z, as a stratiform precipitation system was advecting from the west and passing south of the radar site. The radar broadside was commanded to mechanically rotate clockwise from 150° to 175° in azimuth and at constant 0.5° elevation, with a continuous pulse transmission at $T_s = 3$ ms.

Similar to the first scan in the previous section, this scan resulted in 64 pulses

for $0.5\phi_1$ sampling in azimuth. The data recording period for every pulse was set to capture samples from 400 μs to 1200 μs, corresponding to ranges of 60 to 180 km. Receiver range-time samples were produced at a rate of 4 MHz, which resulted in a range sampling interval of 37.5 m. The KOUN radar was following the operational VCP number 215, which commands to antenna system to rotate at $21.15°$ s^{-1} at the lowest elevation angle ($0.5°$). For this elevation, the CPIs from the surveillance scan consist of 30 samples at $T_s = 3$ ms^{-1}, with $0.5\phi_1$ azimuthal sampling of $0.5°$, since the beamwidth of this system is approximately $1°$. Data for the lowest elevation of the VCP were collected with the KOUN radar at 02:44:41 Z, and IQ data from the same azimuthal sector (i.e., $150°$ to $175°$) were extracted for processing. Receiver range-time samples were produced at a rate of 0.6 MHz, which resulted in range sampling interval of 250 m.

There are several architectural differences between these two systems, the most relevant ones for this comparison being the antenna system and the scan strategies. However, with access to the received IQ data from both systems, the signal processing can be modified to compensate some system differences for a more fair data quality comparison. First, azimuthal resolution can be made equal by considering the impact of the rotation rate on the antenna patterns. That is, the effective antenna pattern [52] of an antenna rotating at uniform rate can be derived considering the displacement of resolution volumes for every sample in the CPI. This effective pattern defines an effective beamwidth that determines the azimuthal resolution of the data.

Considering the previously mentioned radar parameters for the KOUN radar, it was determined through simulations that to increase KOUN's effective beamwidth to $1.58°$ (and thus match the ATD beamwidth), the samples per CPI should be increased to $M_{\text{KOUN}} = 38$. Since the number of samples per CPI from each two-way

receive beam (i.e., prior to applying DB processing) from the ATD was 64, 24 samples were discarded to get $M_{\mathrm{ATD}} = 38$. Range-time processing was set to use only the third out of every six samples in range, resulting in a range resolution of 225 m but without increasing the effective number of samples through averaging. Finally, azimuthal sampling of data was set to for $0.79°$ for $0.5\phi_1$ sampling. Second order differences such as radar frequency (both are S-Band radars), sensitivity, sidelobe levels, elevation beamwidth, and antenna height with respect to the ground were neglected for this comparison.

Data from these scans were processed with the considerations described, and the DB technique was used on data from the ATD system to improve the data quality. Radar-variable estimates from these scans are presented in Figure 4.11. Panels are organized as follows: the top row corresponds to data from the KOUN radar, while the bottom row corresponds to the data from the ATD radar; columns from left-to-right show fields of estimated Z_{h}, v_{r}, and σ_{v}.

A comparison of corresponding estimates from both radars indicates that despite system differences, fields appear to be very similar with data from the ATD radar having superior SD due to the large number of samples ($5 \times 38 = 190$) per CPI produced by the DB technique. Comparison of v fields shows that velocities from the ATD data estimated using the DB technique are qualitatively similar to velocities estimated from the KOUN data. This provides evidence of accurate phase calibration on the DB data, which comprises alignment of instantaneous two-way beam-peak phases and phase correction for the shifted antenna phase centers.

Also, estimates of σ_{v} from the ATD using the DB technique appear to have significantly lower SD. That is, while the σ_{v} field estimated from KOUN data has a noisy texture (indicating a larger standard deviation of estimates), estimates from the ATD data result in a smoother texture, creating a field that is easier to inter-
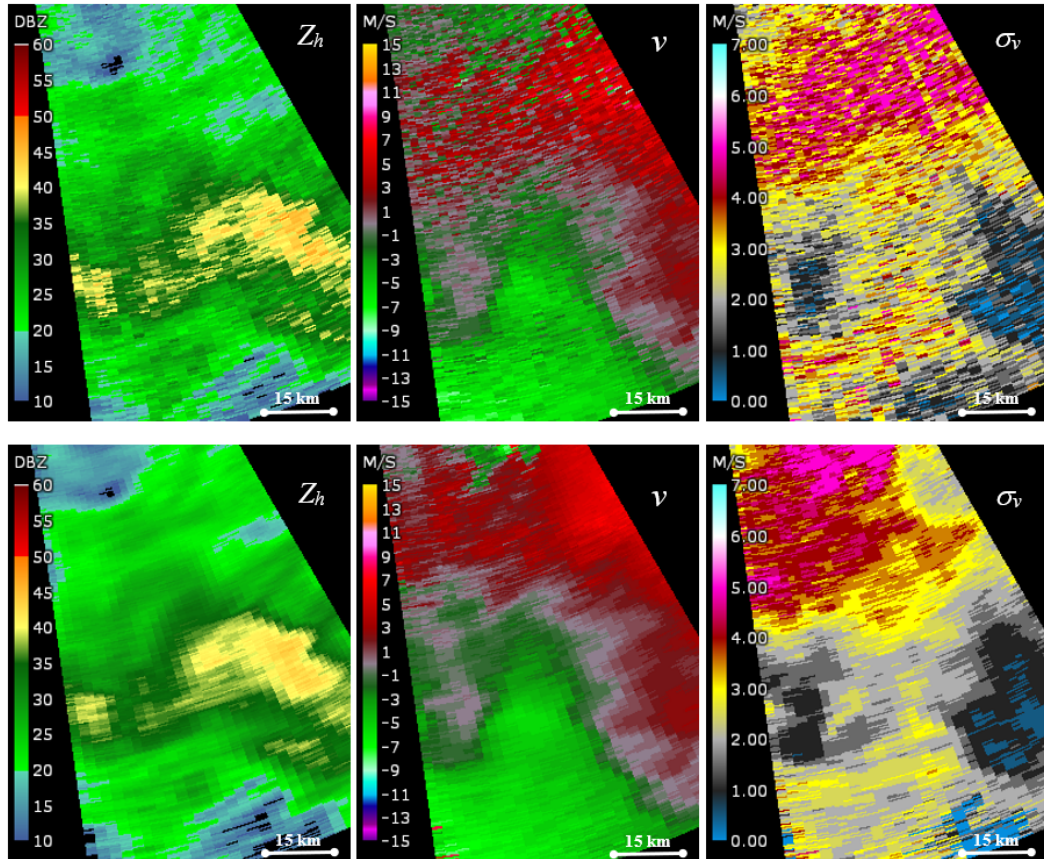
Figure 4.11: Radar-variable estimates from weather echoes observed on 04 March 2020 with (top) the KOUN radar, and (bottom) the ATD radar using the DB technique with $F = 3$ and $R_F = 5$. Columns from left-to-right show fields of estimated Z_h, v, and σ_v.

pret. Accurate estimation of σ_v is typically challenging, especially for narrow spectra [116]. The increased number of available samples obtained with the DB technique seems to significantly improve the performance of the estimator. Examining the Z_h estimates from ATD data, reveals no apparent evidence of sidelobe contamination. This was expected given that the observed precipitation system does not present strong reflectivity gradients that would result in sidelobe contamination. While the sensitivity of the KOUN radar is superior than that of the ATD radar using a beam with $F = 3$ by $\sim$13 dB ($\sim$7.5 dB for two-way narrow beam), it appears

121

that there is no appreciable sensitivity impact on these data.

4.4.2 Experiment Comparing Quality of Polarimetric Variables

The second experiment occurred on 20 November 2019. The ATD system was commanded to rotate at $\omega = 4°$ s^{-1}, the broadside transmit beam was spoiled with F = 5, and R_F = 9 beams were generated for each polarization on reception. Data from this scan were collected at 20:48:26 Z as widespread weak precipitation system was approaching the radar site from the west. The radar broadside was commanded to mechanically rotate clockwise from 260° to 280° in azimuth and at constant 0.5° elevation, with a continuous pulse transmission at T_s = 3 ms. Similar to the previous scans presented, this resulted in 64 transmit pulses for $0.5\phi_1$ sampling in azimuth. The data recording period for every pulse was set to capture range-time samples from 100 μs to 1000 μs, corresponding to ranges from 15 to 150 km. Similar to the previous case, the KOUN radar was following the operational VCP number 215. Data for the lowest elevation of the VCP were collected with the KOUN radar at 20:48:42 Z, and IQ data from the same azimuth sector (i.e., 260° to 280°) were extracted for processing. All other data recording and processing settings are the same as the ones described previously in this subsection.

Radar-variable estimates from the KOUN scan are presented in Figure 4.12(a), and corresponding ones from the ATD scan are presented in Figure 4.12(b). Panels for both figures are organized as follows: top-left shows fields of estimated Z_h (for reference), top-right shows Z_{DR}, bottom-left shows Φ_{DP}, and bottom-right shows ρ_{hv}.

Similar to the analysis for the spectral moments, estimates from both radars appear to be very similar, but data from the ATD radar have superior quality due to the
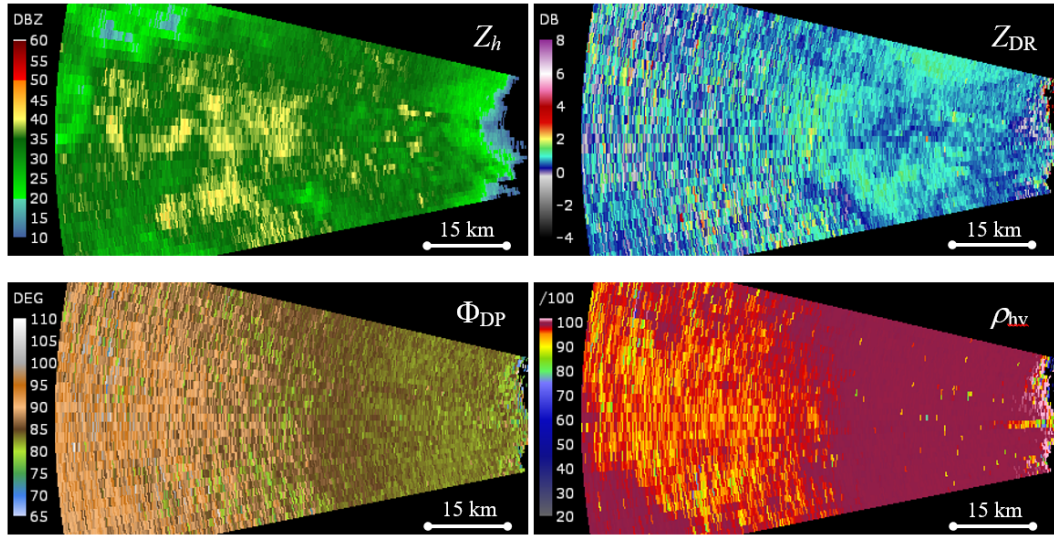
(a) KOUN data
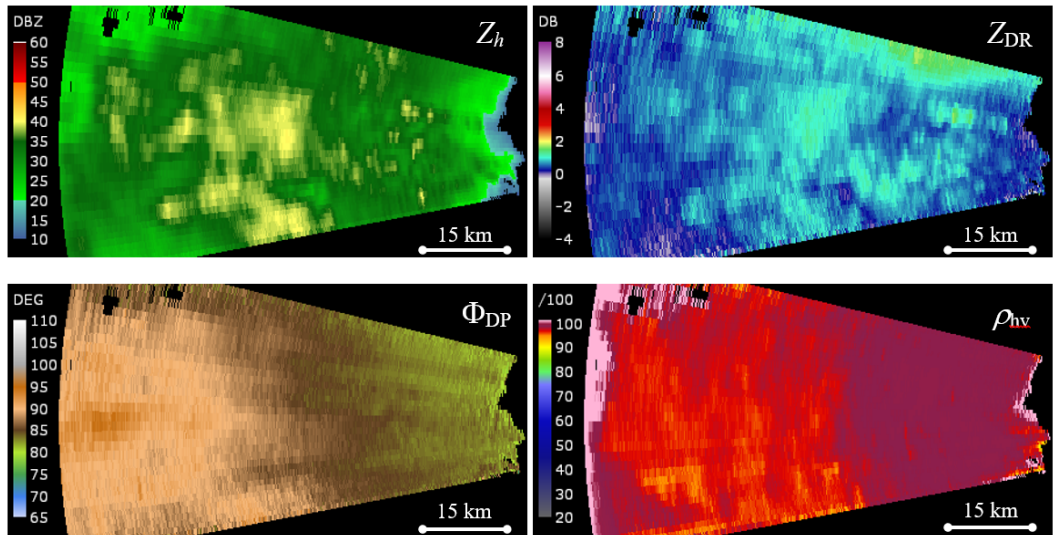
(b) ATD data using the DB technique

Figure 4.12: Radar-variable estimates from weather echoes observed on 20 November 2019 at (a) 20:48:42 Z with the KOUN radar, and (b) 20:48:26 Z with the ATD radar using the DB technique with $F = 5$ and $R_F = 9$

larger number of samples ($9 \times 38 = 342$) per CPI produced by the DB technique. Examination of corresponding Z_{DR} fields shows good agreement in the mean value of estimates up to a range of 102 km. Beyond that range, estimates from KOUN data have very poor quality (i.e., high measurement errors), which lowers the value

of these data for posterior interpretation or quantitative precipitation estimation processing. This is because polarimetric-variable estimates are more sensitive to measurement noise, and higher SNRs are necessary to achieve the precision levels required (SNR $\sim$8–10 dB).

Despite the large sensitivity difference between these radars, the additional reduction of SD achieved by the DB technique allows for more precise estimation of the Z_{DR} field for most of the observed sector. Similarly, there is good agreement between corresponding Φ_{DP} and ρ_{hv} fields, with the ATD data using the DB technique showing superior quality at low SNR (past 102 km in range). There is a small sensitivity difference observed far down range ($\sim$135-150 km), where weak echoes in the Z_h field are censored on the ATD data, and ρ_{hv} estimates become invalid (i.e., $\rho_{hv} > 1$).

The analysis presented in this subsection shows great promise for the DB application for data quality improvements when observing stratiform precipitation systems, where sidelobe contamination is unlikely to be present and spatial resolution is not critical. The increased number of samples available to estimate spectral moments and polarimetric variables provides fields with visibly less noisiness, which could potentially enhance interpretation and posterior processing of the radar base data.

4.5   Chapter 4 Summary

The DB technique presented in this dissertation could provide a way to reduce the RPAR scan times and achieve the required volume scan times, or reduce the variance of estimates to the desired level, or a combination of both. Other digital beamforming techniques have been proposed for RPAR systems; however, the novelty

of the DB technique is that it allows the coherent processing of CPIs from different two-way beams, and it is the first demonstration of digital beamforming in azimuth using dual-polarization weather RPAR. The DB technique was introduced in Section 4.1, and two new CONOPS applications for it were described, namely, the scan-time (4.1.1) and the variance (4.1.2) reduction techniques. The two-way beam patterns for the narrow and spoiled transmit beams were characterized in terms of the spatial resolution (beamwidth and peak sidelobe levels), and sensitivity in Section 4.2. These measurements were used to quantify the impact of using spoiled transmit beams on the data quality, and to provide a calibration procedure for the implementation and testing of the technique. Radar calibration for the DB technique was verified by scanning an external stationary point-target and comparing the measured power and phases of two-way beams prior-to and post applying the calibration procedure. Section 4.3 provided experimental results of using the DB technique with the ATD radar. The first DB application is illustrated in Section 4.3.3 by collecting two scans of data, one using a two-way narrow beam (for reference) rotating at $\omega = 4^\circ$ s^{-1}, and the other using the DB technique and collecting comparable data twice as fast. The second application is illustrated in Section 4.3.2 by collecting two scans of data, one using a two-way narrow beam (for reference) rotating at $\omega = 4^\circ$ s^{-1}, and the other using the DB technique which produced visibly smoother fields of radar products.

Results presented show that the DB technique can be used to reduce the scan time or the variance of radar-variable estimates, at the expense of degraded sensitivity and spatial resolution. The technique could be implemented as part of an RPAR concept of operations to meet demanding requirements for the future weather surveillance network if certain tradeoff compromises are accounted for in the radar design process. An important step to validate the performance of the DB

125

technique was presented in Section 4.4, where data from a collocated WSR-88D radar (KOUN) were collected simultaneously with the ATD using the DB technique. While these systems are different, a procedure for a fairer comparison was used and described in Section 4.4.1. Two cases were presented to compare the quality of spectral moments and polarimetric variables. Qualitative results show a high degree of agreement between the fields of radar variables produced by processing the data from these systems, with the ATD fields (produced using the DB technique) exhibiting improved spatial textures. In particular, polarimetric-variable estimates were shown to greatly benefit from the variance reduction when using the DB technique.

Future PARs that are specifically designed to exploit the use of spoiled transmit beams should account for the increased beamwidth and sidelobe levels to meet the requirements. While this may require increasing the aperture, it also allows for advanced techniques (such as DB) that support meeting demanding requirements with an affordable architecture (compared to the stationary 4F-PAR). A possible consideration is to design an aperture that meets the beamwidth requirements when using narrow beams and increase the size of the receive aperture only to lower sidelobe levels of two-way beams using spoiled transmit tapers. Another alternative is to define an operational mode in which spatial resolution and sensitivity degradations resulting from the use of the DB technique are an acceptable tradeoff to reduce the scan time or the variance of radar-variable estimates.

To achieve large scan-time reduction factors using the DB technique, azimuthal rotation speed has to be increased by the desired reduction factor. Considering the mechanical rotation machinery has a high technology-readiness level, achieving higher rotation speeds with this well-known pedestal technology reduces the risk of designing, building, and deploying RPAR systems with higher rotation rates.

Achieving high reduction factors (e.g., $R_F = 5$) may be the challenging point due to the required rotation speeds, consider that an operational implementation can be designed using a small time-reduction factor (e.g., $R_F = 2$). This relatively low increase in the rotation speed increase would reduce in the volume scan time by a factor of 2, with relatively modest demands on mechanical rotators. This could also result in a relatively smaller increase in the aperture size required to meet two-way sidelobe requirements given that a narrower spoiled transmit beam would be used.

Finally, an important and unique aspect to consider for the deployment of an RPAR is the increase of reflections coming from a water-coated radome. While spherical radomes may be the most suitable candidate for the RPAR because of the symmetric properties of the geometry, they may reflect part of the transmit beam energy on the array when the electronically steered beams reach angles far from the broadside. Internal reflections levels at that point could increase by several decibels since the water layer on the radome increases the radome backscattering cross-section [117]. A direct implementation of the DB technique as presented in this dissertation with the transmit beam always on broadside would reduce the risk of these array-damaging reflections when operating under a wet-radome regime with a spherical radome.

Chapter 5

Forward-looking and Back-scanning Technique

"Every once in a while, a new technology, an old problem, and a big idea turn into an innovation."

<div align="right">

Dean Kamen

</div>

5.1 Exploiting Dwell Flexibility and Beam Agility

One of the key capabilities of PAR systems that has not been investigated for RPAR is the dwell flexibility. As described in Section 2.2.5, dwell flexibility refers to the RPAR capability to dynamically (i.e., in real-time) re-define M and T_s for beam positions in a scan. Herein, we use the term *dwell definition* to describe a specific selection of M and T_s. Note that under this definition a multi-PRT dwell would be defined with multiple pairs of M and T_s. Further, considering that this definition is independent from the beam pointing angle, it supports advanced scanning techniques such as BMX (see 2.2.7), which would consist of one (or many in the case of multi-PRT) dwells with M being the total number of samples collected per beam position. A scan initialized with equal dwell definitions for all beam positions (such as those in the WSR-88D) could be dynamically modified by re-defining the dwells for each beam position based on meteorological observations. That is, the adaptive

scanning algorithms considered in this chapter could tailor dwell definitions to either reduce the scan time (as done by [23] for stationary PAR) or to improve data quality.

This chapter has three objectives. First, to introduce the Forward-looking and Back-scanning MCS (FB-MCS) CONOPS, which uses the FBT in conjunction with MCS and DB to scan beams off broadside (in contrast to the BMCS CONOPS presented in Chapter 3). This CONOPS combines the dwell flexibility, the beam agility, and the beamforming capabilities presented in Chapter 2. Second, to demonstrate the practical implementation of FBT on the ATD and to quantitatively verify the technique using observations from the collocated WSR-88D. The MCS technique (Chapter 3) is used to maintain the earth-relative pointing angles of beams within a CPI, and the DB technique (Chapter 4) is used in conjunction with FBT to reduce the scan time. Third, this chapter proposes and emulates a simple adaptive scanning algorithm using the FBT to quantify potential data quality improvements resulting from this CONOPS. It combines dwell flexibility, beam agility, and digital beamforming; the three main RPAR capabilities investigated in this dissertation. The chapter concludes with a discussion on potential benefits of adaptive scanning using the RPAR architecture.

5.2 The Forward-Looking and Back-Scanning Technique

The CONOPS discussed here uses an invariant pre-defined scan strategy based on the FBT, which is defined using MCS on off-broadside steering angles. Forward-looking beams consist of dwells for which the steering angles are ahead of the radar rotation and back-scanning beams consist of dwells for which the steering angles are less or equal than those from forward-looking beams. In our specific imple-

mentation of this CONOPS, forward-looking beams consist of short-dwell dwells and are designed to provide sufficient surveillance information about the potential regions of interest for the back-scanning beams, while back-scanning beams consist of longer dwells and are designed to provide high-quality weather observations. However, we note that dwells for the forward-looking and back-scanning beams could be designed in different ways (depending on the application) and do not have to follow this specific implementation necessarily (i.e., short-dwell forward beams and longer dwell backward beams). Furthermore, digital beamforming techniques can be coupled with the concept of forward-looking and back-scanning beams to arbitrarily use pencil or spoiled beam patterns (depending on the application) on either beam. In the FB-MCS CONOPS, dwells of forward-looking and back-scanning beams are interleaved. The concept is illustrated in Figure 5.1, where a top view of the RPAR shows a wide spoiled transmit beam used for the forward beams (black pattern) and a narrow pencil beam used for the back-scanning beams (blue pattern). Digital beamforming is coupled with forward-looking beams to increase the coverage of these quick surveillance beams by transmitting a spoiled beam in azimuth and receiving multiple simultaneous beams [86]. MCS beam-pointing angles for these beams are derived using (3.3). In conjunction with the FB-MCS CONOPS, the RPAR's beam agility can be used to focus the scan in regions of interest (using information from the forward-looking beams) within the visible region (e.g., typically $\pm 45°$ from broadside) as the radar rotates. This concept is referred to as *adaptive scanning* (introduced in Section 2.2.9), by which the scan strategy dynamically evolves to make efficient use of the radar resources. The back-scanning beams considered in this work are deterministically scheduled but could conceptually be scheduled adaptively. An adaptive scanning algorithm could schedule these dwells to tailor the backward beams. That is, using information from the forward-
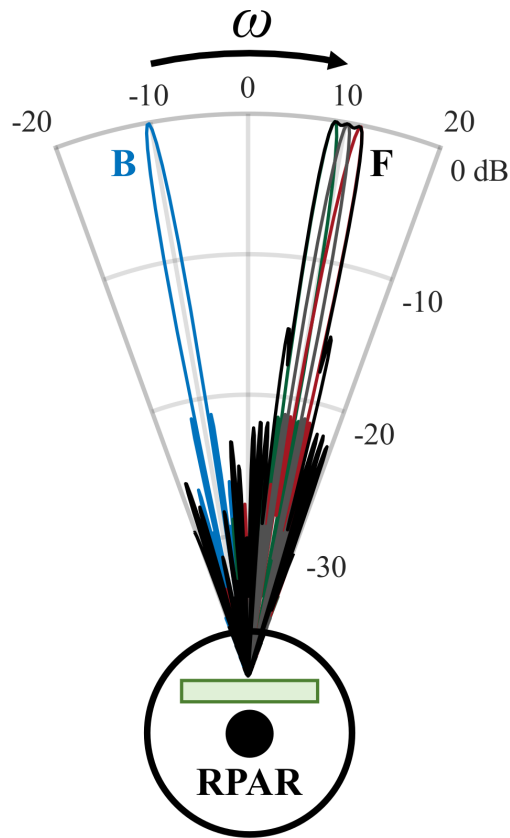
Figure 5.1: Forward-looking and back-scanning MCS CONOPS. The solid black circle represents center of rotation and the green rectangle represents the PAR antenna.

looking beams, the back-scanning beams can be defined (i.e., beam positions and dwell times) to tailor the observations on significant weather echoes. For example, the maximum range of storms could be computed from the forward-looking beams, and the dwells of the back-scanning beams could be designed to match these maximum ranges. While the PRTs of the backward beams are reduced (to match the maximum range of storms) the number of samples would be increased to approximately maintain the dwell time. This would lead to improved radial velocity and spectrum width estimates (due to the extended Nyquist interval), an improvement in the performance of algorithms (due to the increased number of samples; e.g., ground clutter filter), and to a slight reduction in the variance of estimates (due

to the slightly increased dwell time gained from non-significant beam positions not scanned). MCS would be especially beneficial for scheduling back-scanning beams to maximize the use of radar resources with the goal of improving weather observations and meeting functional requirements. A real-time adaptive implementation of the FB-MCS CONOPS is beyond the scope of this work and is proposed for future research.

5.3   Demonstration of FBT

The application of the FBT proposed in this section provides a way to collect a long-range surveillance scan (i.e., using a long PRT) and a large-Nyquist-velocity Doppler scan (i.e., using a short PRT) at the same elevation angle with a single revolution of the antenna (as opposed to two revolutions, as done in the WSR-88D scans). These "split cuts" are used in the WSR-88D VCPs for range and velocity ambiguity mitigation. In split cuts, the same elevation angle is scanned twice using two different PRTs (i.e., there are two $360°$ azimuthal rotations of the antenna at the same elevation angle). A long PRT is used in the first half of the split cut (called the surveillance scan and referred to as the CS scan) for better spatial coverage, and a short PRT is used in the second half of the split cut (called the Doppler scan and referred to as the CD scan) to reduce the occurrence of velocity aliasing. Operationally, Z_h, Z_{DR}, Φ_{DP}, and ρ_{hv} are obtained from the CS scan, whereas v_r and σ_v are obtained from the CD scan using a "range unfolding" technique that relies on the reflectivity from the CS scan. Alternatively, the recently proposed Hybrid Scan Estimators (HSE) [11], designed to choose between the data provided by either one of the two scans in split cuts based on their expected statistical performance, could be used to improve the quality of polarimetric-variable estimates compared to the

conventional estimators. The FBT is designed to execute split cuts (similar to those used in the WSR-88D) with a single revolution of the antenna, and to be used in conjunction with real-time adaptive scanning algorithms.

The FBT interleaves dwells of forward-looking and back-scanning beams as the RPAR rotates. That is, a CPI of forward-looking beams is executed first, and a CPI of back-scanning beams is executed next. The steering angles for the forward-looking and back-scanning beams can be arbitrarily set within the RPAR's visible region (i.e., $\pm 45°$ from the broadside in azimuth, and 0–$20°$ in elevation), although there are some tradeoffs associated with the selection. If an adaptive scanning algorithm operating in real-time uses the data from the forward-looking beams to schedule the back-scanning beams, there should be an angular separation between them such that the time difference is sufficient for the radar processor to modify the back-scanning beams. However, the farther these beams are from the RPAR's broadside, the higher the cross-polarization contamination incurred. Scan time reduction is accomplished by using the DB technique on the forward-looking beams of the FBT, with $T_{sF} = 3$ ms (similar to the CS in typical WSR-88D precipitation strategies) and reducing the number of samples by $R_F = 5$ to meet requirements on the variance of estimates, at the expense of degraded azimuthal resolution. The back-scanning beams are high-resolution narrow pencil beams scanned with $T_{sB} = 1$ ms (similar to the CD in typical WSR-88D precipitation strategies). The back-scanning beams could also use the DB technique (at the price of reduced azimuthal resolution, higher sidelobes and lower sensitivity), but this implementation preserves narrow pencil beams for higher data quality. Note that MCS is used for both the forward-looking and back-scanning beams. In addition to reducing the surveillance scan time, this application of the FBT allows the collection of both the CS and CD scans in a single revolution of the antenna system and leads to reduced

133

pedestal rotation speeds. This is similar to the batch mode used in the WSR-88D VCPs, where the CPIs for the long and short PRTs are transmitted sequentially and scans are collected in one revolution of the antenna.

Two sector scans were collected using the STSR mode in rapid succession on 30 July 2020 through a convective precipitation system approaching the ATD from the West at ranges extending from approximately 35 km to 150 km. For scan 1, the radar rotated at $\omega = 4 \,°\,s^{-1}$, the transmit and receive pencil beams were maintained at broadside ($\phi_{az} = 0°$, $\theta_{el} = 0°$), mimicking the operation of a conventional reflector-based radar. Data from this scan were collected at 22:12:54 Z. The number of samples was set to 65 for a normalized azimuthal sampling of $\Delta\phi = 0.5$ at $T_s = 3$ ms. For scan 2, the ATD rotated at $\omega = 10 \,°\,s^{-1}$, the transmit and receive beams were collected using the FB-MCS CONOPS (Section 5.2). A set of 5 simultaneous forward-looking beams were pointed $+15°$ with respect to broadside and collected with $M_F = 3$ at $T_{sF} = 3$ ms and using a transmit beam spoiled by a factor of 3. The back-scanning beams were pointed $-15°$ with respect to broadside and collected with $M_B = 72$ at $T_{sB} = 1$ ms. The normalized azimuthal sampling for both beams in the scan is $\Delta\phi = \omega(T_{sF}M_F + T_{sB}M_B)/\phi_1(15°) = 0.5$. Notice that the azimuthal sampling spacings for the forward-looking and back-scanning beams can be set arbitrarily and may be different. Data from scan 2 were collected 33 seconds after scan 1, at 22:13:27 Z. For both scans, the radar broadside was commanded to mechanically rotate clockwise from $210°$ to $270°$ in azimuth, at constant $0.9°$ elevation. The forward-looking beams scanned the sector from $225°$ to $285°$ (i.e., $+15°$ from the broadside), and the back scanning beams scanned the sector from $195°$ to $255°$ (i.e., $-15°$ from the broadside). A 78μs pulse-compression waveform with a 52-m range resolution (defined as the 6-dB width of the range weighting function [52]) and low range sidelobes [35] was used to improve sensitivity. Receiver range-time

samples were produced at a rate of 4 MHz, which results in a range sampling interval of 37.5 m. Range-time processing was set to incoherently average samples from 6 consecutive range gates, which results in a range sampling spacing for the radar variables of 225 m

Data produced with the FBT were verified by comparing them to data from the KOUN radar, that has an inherently better angular resolution than the ATD. The KOUN radar was following the operational VCP number 215, which commands the antenna system to rotate at $11.5°$ s^{-1} to collect surveillance scan data and at $17.1°$ s^{-1} to collect Doppler scan data, both at the $0.9°$ elevation angle. For this elevation, the dwell definitions for the CS and CD scans consist of 24 samples at T_{CS} = 3 ms and 64 samples at T_{CD} = 1 ms, respectively. Surveillance scan data for the $0.9°$ elevation of the VCP were collected with the KOUN radar at 22:13:35 Z, and time-series IQ data for the same azimuthal sector as the one scanned by the ATD system were extracted for processing. Radar system parameters and scan strategies for these experiments are summarized in Table 5.1.

Azimuth angles for a subset of pulses in scan 2 are shown in Figure 5.2 as a function of time to illustrate the CONOPS. Dot markers in black represent the back-scanning beams and dot markers in colors represent the forward-looking beams. The DB technique was used to reduce the forward-looking scan time while maintaining the variance of estimates. Markers of different colors in Figure 5.2 represent

Scan #	Radar System	Time (Z)	Beam Type	Scanned Sector	Mechanical Elevation	ϕ_e	M	T_s	ω ° s^{-1}
1	ATD	22:12:54	Broadside Pencil	210° - 270°	0.9°	1.74°	65	3	4
2F	ATD	22:13:27	FB-MCS	225° - 285°	0.9°	2.04°	3	3	10
2B	ATD	22:13:27	FB-MCS	195° - 255°	0.9°	1.64°	72	1	10
3	KOUN	22:13:35	Broadside Pencil	0° - 360°	0.9°	1.1°	24	3	11.5
4	KOUN	22:14:03	Broadside Pencil	0° - 360°	0.9°	1.1°	64	1	17.1

Table 5.1: Radar system parameters and scan strategies for FBT experiment.

the five beams received. Notice that dwells of forward-looking and back-scanning beams are interleaved, and azimuth angles for pulses within a CPI appear to be approximately constant. Inset plots provide close-up views of the azimuth angles from samples within a CPI for each type of beam. For the selected forward-looking CPI, the span of azimuth angles is $0.002°$, and for the selected back-scanning CPI the span of azimuth angles is $0.006°$. The larger spread on the latter one is a consequence of the higher number of samples and a small slope ($\sim 0.083°\ s^{-1}$), caused by practical imperfections in the mechanical motion of the azimuth rotator (considered negligible for the purposes of this work).
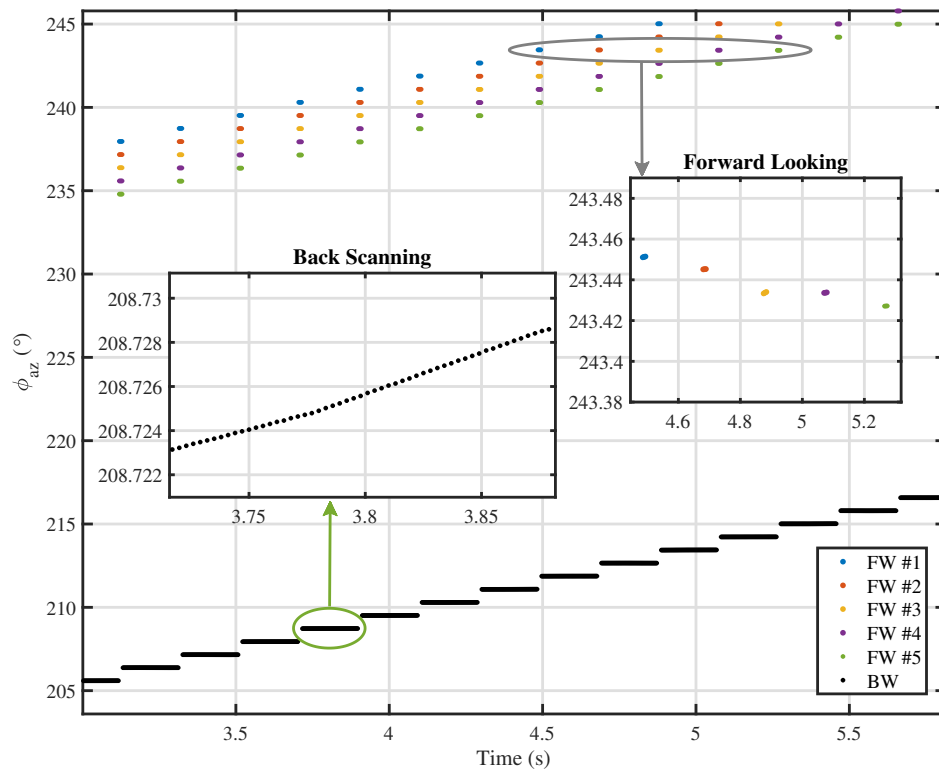
Figure 5.2: Azimuth angles of a subset of pulses in scan 2 as a function of time. These illustrate the scan angles of the FB-MCS CONOPS

Fields of radar-variable estimates resulting from processing the data from these

136

scans are presented in Figure 5.3. Panels are organized as follows: the left column corresponds to scan 1, the center column corresponds to scan 2F (forward-looking beams), and the right column corresponds to the scan 2B (back-scanning beams); the rows from top to bottom show fields of Z_h, v_r, σ_v, Z_DR, Φ_DP, and ρ_hv. Qualitative comparison of radar-variable fields shows no apparent data artifacts from either scan. Note that polarimetric-variable estimates for the forward-looking ($\phi_p = +15°$) and back-scanning ($\phi_p = -15°$) beams were corrected using the methods described in [46].

A qualitative comparison of the fields derived from scan 1 (left column) and those derived from the forward-looking beams in scan 2 (center column) is carried out first. Comparing corresponding fields, it is noted that fields from scan 2F appear to have lower azimuthal resolution and sensitivity than corresponding ones from scan 1. These expected degradations are a consequence of the use of spoiled transmit beams. Specifically, the HPBW increases from $1.64°$ in scan 1 to $\sim 2.04°$ in scan 2F (considering beam smearing effects on the data from scan 1). This was expected and it is a trade-off of the DB technique as described in Chapter 4. As mentioned previously, these tradeoffs should be considered in the radar design process such that the resulting performance meets the RFR. The DB technique increases the number of samples by $R_F = 5$ to $M_{DB} = 15$, such that the resulting variance of estimates in the fields produced by processing scan 2F is comparable to that obtained when processing the CS scan of VCP 212. The PRT used for both cases is 3 ms, and therefore, Doppler-derived estimates (v_r and σ_v) are inaccurate due to the narrow Nyquist interval. Next, a qualitative comparison of the fields derived from scan 1 (left column) and those derived from the back-scanning beams in scan 2 (right column) shows that features appear to be similar for Z_h and Z_DR, although the data in scan 2B are collected with a narrower effective beamwidth achieved by MCS.

This is more apparent in the fields of Φ_{DP}, where a narrow feature along the strong convective cores shows higher values being better resolved. The most significant difference between these scans is in the estimates of the Doppler variables. While v_r and σ_v appear to be inaccurate (e.g., aliased v_r and saturated σ_v) in data form scan 1 due to the low maximum unambiguous velocity (8.27 m s^{-1}), these fields of estimates do not present artifacts resulting from velocity aliasing in scan 2B due to the larger maximum unambiguous velocity (24.81 m s^{-1}).

Three key takeaways are derived from these results. First, Figure 5.2 shows that an implementation of the FB-MCS CONOPS with sufficient beam pointing accuracy for MCS is achievable on the ATD system. Second, results presented in Figure 5.3 show that it is possible to implement MCS at steering angles away from the broadside (but in the horizontal principal plane for the case presented), and to produce calibrated radar-variable estimates without apparent aliasing artifacts. Lastly, it illustrates that data from the forward-looking beams capture the main non-Doppler meteorological features (at a slightly degraded resolution and sensitivity) and could be used by an adaptive algorithm to improve the quality of estimates derived from the back-scanning beams. Information from forward-looking beams could be use to (1) decide if there are significant weather echoes in upcoming back-scanning beam positions and (2) determine the maximum range of storms observed and shorten the PRTs of back-scanning beams to match the maximum unambiguous range with that of the maximum range of observed storms (increasing the Nyquist interval). Future research efforts could implement this CONOPS with a real-time scheduler to adaptively point the back-scanning beams with tailored dwell definitions to improve the quality of estimates.
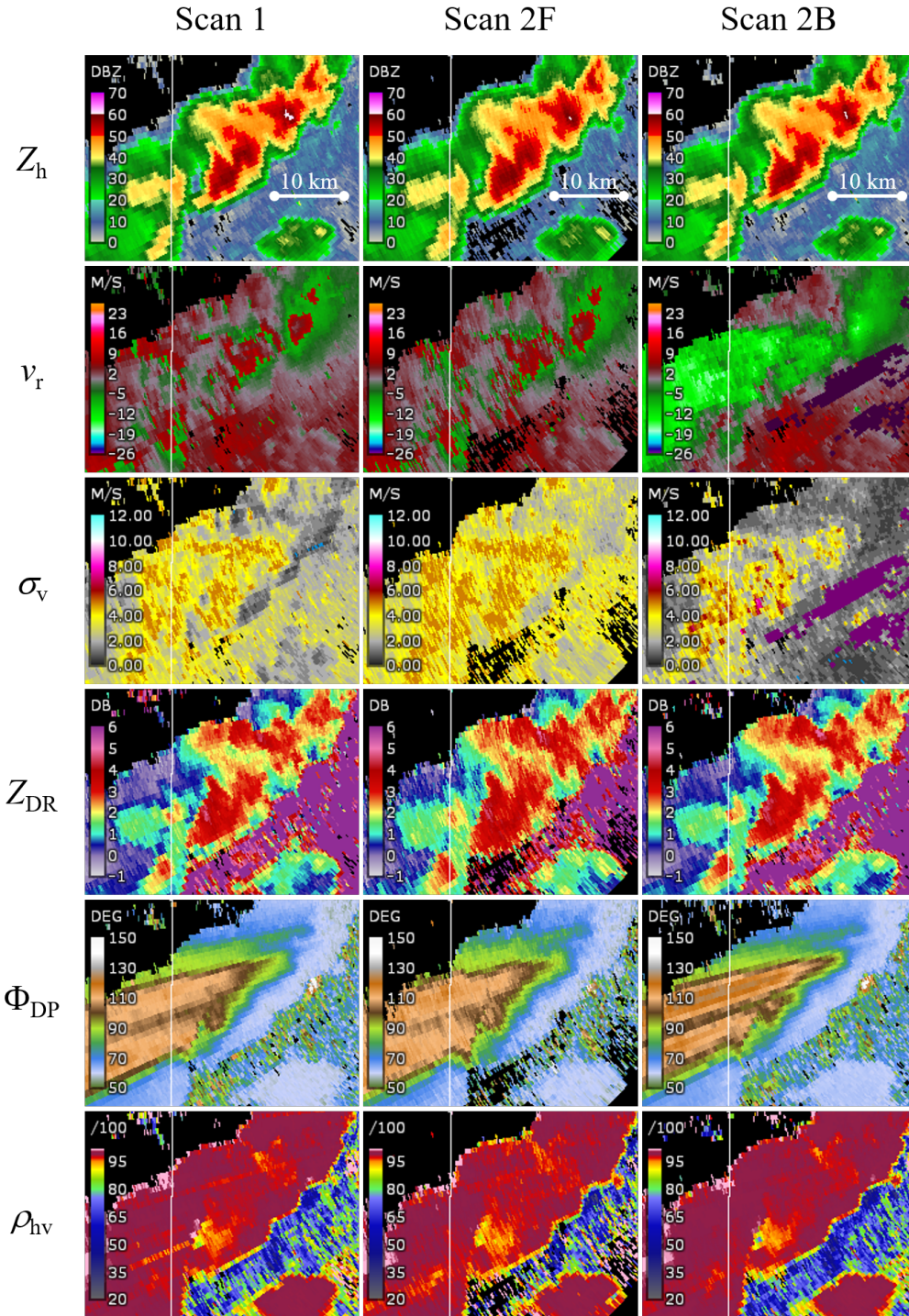
Figure 5.3: Radar-variable estimates obtained from two scans collected in rapid succession ($\sim$33 s apart). Panels are organized as follows: the left column corresponds to scan 1, the center column corresponds to scan 2F (forward-looking beams), and the right column corresponds to the scan 2B (back-scanning beams); the rows from top to bottom show fields of Z_h, v_r, σ_v, Z_DR, Φ_DP, and ρ_hv.

5.3.1 Comparison with KOUN Radar

In this section we compare ATD data from scan 2 with KOUN data from scans CS and CD (3 and 4 in Table 5.1, respectively). ATD data from scans 2F and 2B are processed using the conventional split-cut processing of WSR-88D data [118, 119]; that is, Z_h, Z_{DR}, Φ_{DP}, and ρ_{hv} estimates are derived from the surveillance scan (2F) while v_r and σ_v are derived from the Doppler scan (2B). Data from scan 2F are used to determine if there are overlaid echoes in the Doppler scan data from 2B. If no overlaid echoes are found, or the power ratio between overlaid echoes is more than 5 dB (i.e., the SNR difference between CS and CD signals is more than 5 dB at a specific range location), data from the stronger signal are *range unfolded* and those from the weaker signal are flagged as ambiguous. Otherwise data from both the strong and weak overlaid signals are flagged as ambiguous and estimates in these range locations are deemed invalid.

Fields of radar-variable estimates obtained from ATD scan 2 (selected from Figure 5.3, reproduced here for convenience) and KOUN scans CS (3 in Table 5.1) and CD (4 in Table 5.1) are presented in Figure 5.4. Panels are organized as follows: the left column corresponds to ATD data using the FB-MCS CONOPS and the right column corresponds to KOUN data using a split-cut to mitigate range/velocity ambiguities; the rows from top to bottom show fields of Z_h, Z_{DR}, v_r, and σ_v.

Qualitative comparison of corresponding Z_h and Z_{DR} fields shows very good agreement between meteorological features (spatial structure and values) between both scans. The ATD's limited azimuthal resolution can be readily noticed. This is due to a couple of reasons: (1) the KOUN radar has a narrower true beamwidth, and (2) the use of a spoiled transmit beam for forward-looking beams results in a wider beamwidth, effectively degrading spatial resolution. By qualitatively comparing
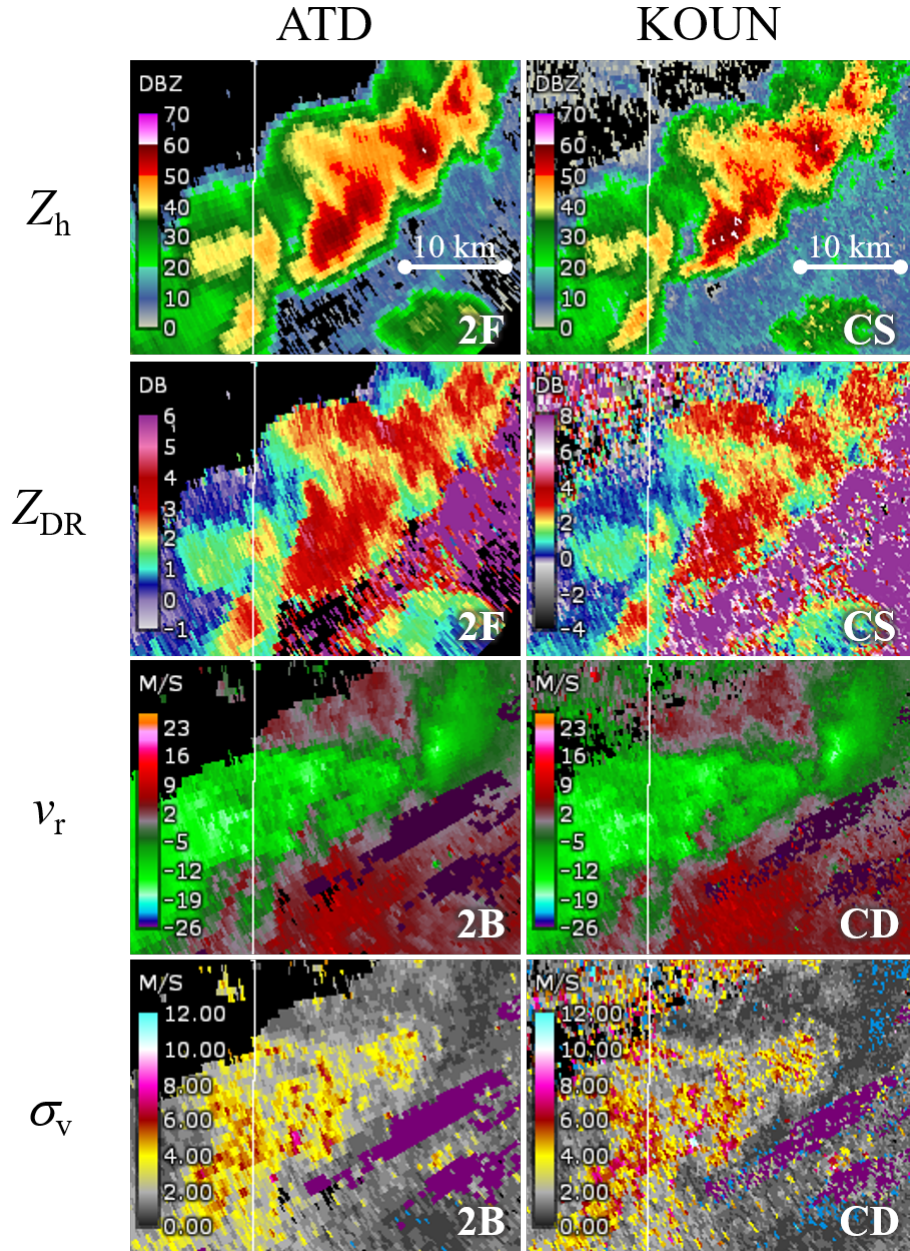
Figure 5.4: Fields of radar-variable estimates obtained from ATD scan 2 and KOUN scans CS (3 in Table 5.1) and CD (4 in Table 5.1). Panels are organized as follows: the left column corresponds to ATD data using the FB-MCS CONOPS and the right column corresponds to KOUN data using a split-cut to mitigate range/velocity ambiguities; the rows from top to bottom show fields of Z_h, Z_{DR}, v_r, and σ_v.

fields of v_r and σ_v, it appears that Doppler data from scan 2B are similar to that from KOUN's CD scan. Doppler velocity fields present zero iso-Doppler regions in approximately the same locations; inbound and outbound radial velocities are present in similar locations and have comparable values (no artifacts or signs of velocity aliasing are apparent); and regions with estimates deemed invalid due to the presence of overlaid echoes (painted in purple on panels of v_r and σ_v) generally coincide in location.

It is of interest to get quantitative verification of the quality of estimates obtained using the FBT with the ATD system with respect to the KOUN system. To this end, the KOUN time-series data were reprocessed using a procedure similar to that outlined in Sections 4.4.1 and 4.4.2, whereby the number of samples per CPI was increased so that effective azimuthal resolution of both systems was made equal. Figure 5.5 shows the effective beamwidth of these radar systems and for the acquisition parameters under consideration. For the ATD's back-scanning beams, to increase KOUN's effective beamwidth to 1.64° using the CD scan parameters, $M_{\text{KOUN-B}} = 87$ samples per CPI are processed per radial. For the ATD's forward-looking beams, the beamwidth is computed as the average of beamwidths of the $R_F = 5$ beams coherently combined by the DB technique, which results in 2.044° (see Table 4.1 in Section 4.2.2). For this case, $M_{\text{KOUN-F}} = 55$ samples per CPI are processed per radial. The number of samples (between 2F and CS, 2B and CD) are matched in a similar way as done in Sections 4.4.1 and 4.4.2. Second order differences such as radar frequency (both are S-band radars), sensitivity, sidelobe levels, elevation beamwidth, and antenna height with respect to the ground were neglected for this comparison.

Fields of radar-variable estimates from the ATD FBT scan are compared to corresponding ones from the KOUN CS/CD scans after reprocessing the time-series.
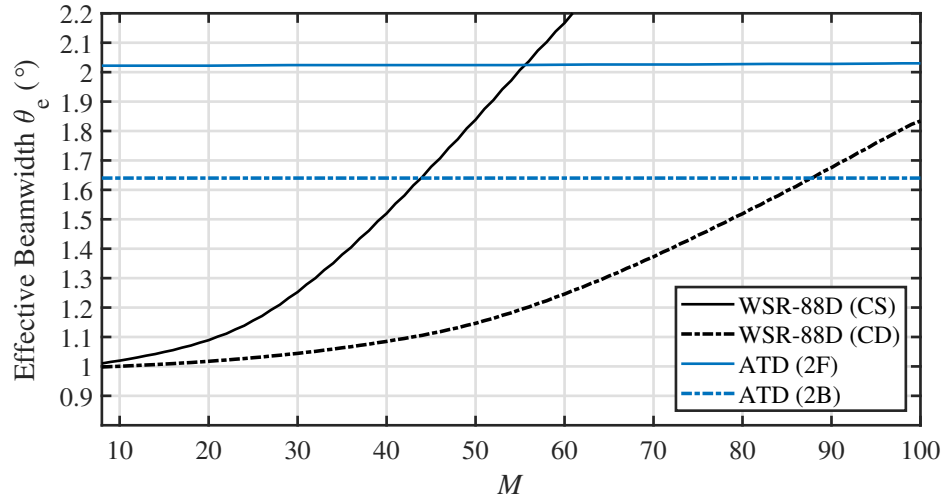
Figure 5.5: Effective beamwidth of the KOUN and ATD radar systems using the dwells defined in the CS, CD and 2F, 2B scans, respectively.

The bivariate density maps in Figure 5.6 are computed from these fields of estimates using an SNR threshold of 10 dB and illustrate the correlation between estimates derived from both systems. These density maps are normalized to approximate a probability density function, that is, the value at each bin is computed as the number of observations in that bin divided by the product of the total number of observations and the area of the bin. The Pearson correlation coefficient r between the estimates is indicated in each sub-figure title. It indicates a significant correlation (i.e., $r > 0.9$) for estimates shown in panels (a) Z_{h}, (b) v_{r}, and (d) Φ_{DP}. Density maps are narrow and symmetric about the $x = y$ line. These impressive correlations between radar-variable estimates from different systems is obtained as a result of the data re-processing methodology described, and the short time difference between the scans (i.e., 8 s between scan 2F and scan 3, and 36 s between scan 2B and scan 4). More importantly, it quantifies the effectiveness of the FBT technique to obtain both the CS and CD scans in one revolution of the antenna and saving time by using the DB technique with the forward-looking beams. Results in panels
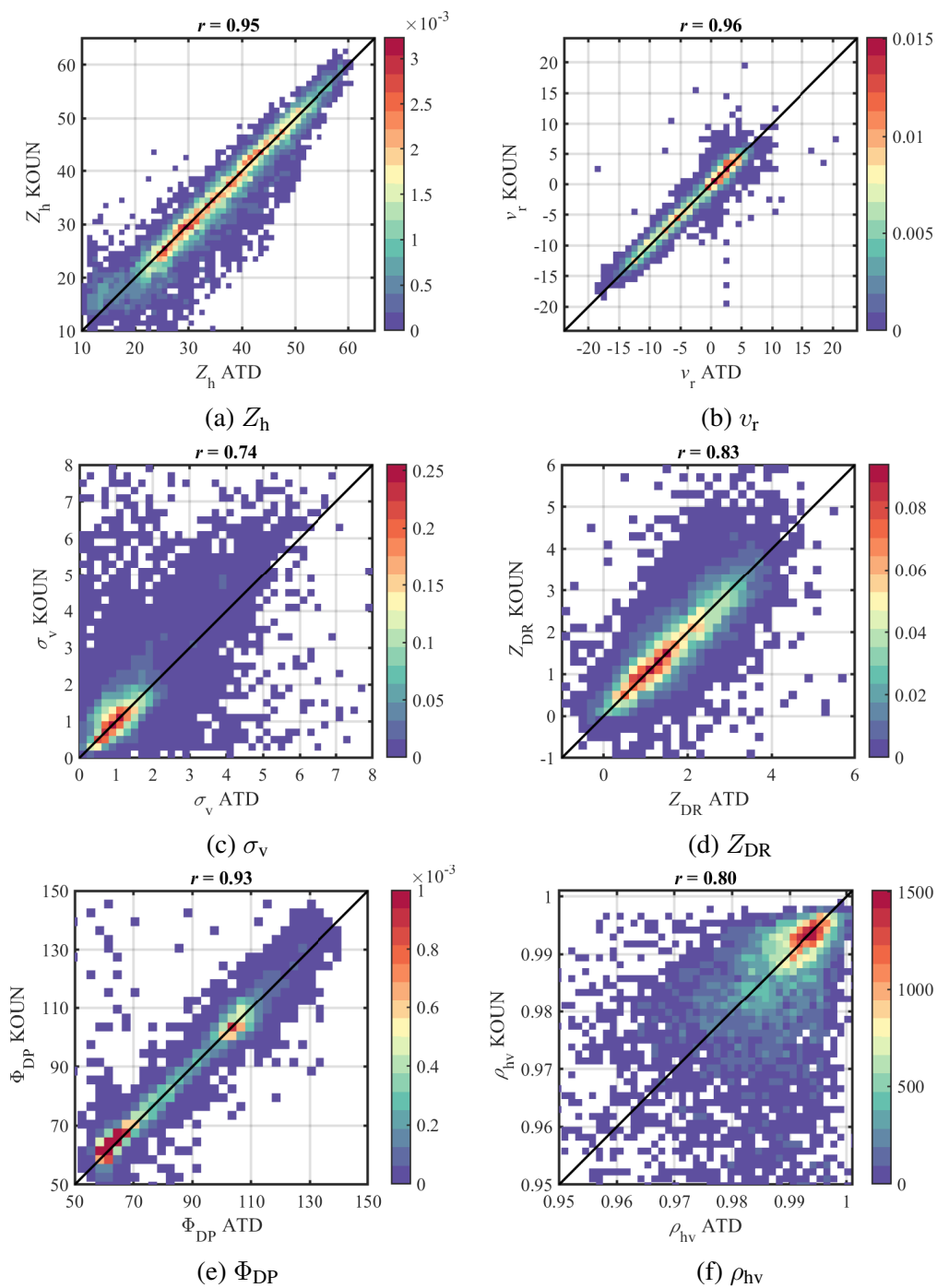
Figure 5.6: Bivariate density maps computed from fields of radar-variables estimates from the ATD and KOUN scans in Figure 5.4. These density maps are normalized to approximate a probability density function. The Pearson correlation coefficient r between the estimates is indicated in each sub-figure title.

(d) Z_{DR} and (f) ρ_{hv} also show considerably high correlation (i.e., $r > 0.8$) between these polarimetric estimates, which are typically very sensitive to noise and estimation error [1]. While these density maps are not as narrow as the ones discussed previously, they are symmetric about the $x = y$ line and most of the estimates lie on or very close to this line. This indicates that estimates from the FBT scan are not biased, and that measurement errors may be larger for these polarimetric variables. Finally, while there is a considerable correlation between σ_v estimates ($r = 0.74$) and most of them lie on the $x = y$ line, the spread about this line is large. As mentioned previously, accurate estimation of σ_v is typically challenging [116]. A more detailed analysis could be conducted to get to the bottom of these differences, this is proposed for future work.

This application of the FB-MCS CONOPS incorporates all three techniques presented in the dissertation, namely MCS, DB, and FBT. The MCS technique is used to mitigate beam smearing and enhance the azimuthal resolution of the RPAR, the DB technique is used to reduce the surveillance scan time (at the expense of degraded spatial resolution and sensitivity), and the FBT is used to interleave surveillance and Doppler scans (which minimizes mechanical rotations and the time difference between CS and CD scans). The FBT is designed to be used under an adaptive scanning concept. As mentioned previously, forward-looking beams could be used to tailor the scan of back-scanning beams with the goal of improving data quality.

5.4 Exploring Adaptive Scanning with FBT

As introduced previously, adaptive scanning consists on efficiently utilizing the radar's resources to focus the scan on regions of interest. One of the most challenging aspects of developing adaptive scanning algorithms is to define which radar

resources will be traded to improve observations. Given that radars have a finite amount of resources (power, time, bandwidth, processing), trading resources can generally improve observations in a certain way, at the expense of degrading them in another. Fundamentally, adaptive scanning techniques can trade between three performance metrics defined in this space: data quality (e.g., variance of estimates), spatial sampling (number and pointing of beam positions), and temporal resolution. For example, the ADAPTS algorithm selects only certain *significant* beam positions to scan, skipping positions that do not have significant echoes of interest. This reduces the scan time and allows for more frequent updates by trading radar time for coverage (trading spatial sampling for better temporal resolution). While scan times are reduced using ADAPTS, new meteorological echoes could develop in the sectors not being scanned, potentially missing significant echoes.

In this section, we use the FBT to develop a simple adaptive scanning algorithm and quantify potential improvements in data quality. Data quality is improved by increasing the maximum unambiguous velocity (which reduces the occurrence of aliasing and saturated σ_v estimates) and by reducing the variance of estimates. This simple adaptive scanning algorithm uses data from the forward-looking beams to modify the dwell definition of the back-scanning beams. The algorithm has three steps to determine the dwells of back-scanning beams. For each beam position: 1) the maximum range of storms is estimated from the forward-looking beams and used to define the PRT for the back-scanning beams. A short time is added to the computed PRT to ensure that meteorological echoes that were possibly not detected (due to the sensitivity/censoring differences) are captured. This may not be necessary for echoes with high SNR, but it could be for weaker echoes. Further, given the short time difference between forward-looking and back-scanning beams scanning the same location ($\sim$1-2 s), storm evolution does not need to be considered

146

for the time padding in range. Since it does not result in a significant increase in scan time ($<1\%$) we use it here; 2) the time gained by shortening the PRT is used to increase the number of samples scanning that beam position; 3) if no meteorological echoes are present in a certain beam position, this beam position is deemed as non-significant and is scanned with a very short dwell time. The time gained by reducing the dwell of non-significant positions is distributed over a set of back-scanning beams and used to increase their number of samples. Additional algorithm parameters include a minimum PRT and a minimum number of samples per back-scanning beam position. This algorithm increases the Nyquist interval of back-scanning beams, reducing the possibility of velocity aliasing. Furthermore, spectral processing techniques (e.g., clutter filtering) are also improved due to the higher number of samples (i.e., better spectral resolution). Lastly, the variance of estimates is maintained or lowered by increasing the number of samples. ATD data presented in the previous section are used to illustrate the algorithm. Conclusions are used to drive a discussion on the potential of using adaptive scanning on RPARs.

5.4.1   A simple adaptive scanning algorithm for RPAR

ATD data from the FBT scan (2F and 2B in Table 5.1) are re-processed to emulate the simple adaptive scanning algorithm described. The reflectivity field in Figure 5.7 illustrates the maximum range of storms determined for the case under consideration (black contour), and the maximum range determined by the adaptive FBT adaptive algorithm (gray contour). At least 5 range gates with reflectivities higher than 10 dBZ are required to classify a beam position as significant. The adaptive FBT algorithm includes a range padding of 2.5 km and an azimuth padding of $1°$. These padding parameters are arbitrarily set here for illustration, and in general

147

do not need to be large since the time-difference between the forward-looking and back-scanning beams is short ($\sim$1 s). A minimum PRT of 0.5 ms is used for both: beam positions with significant echoes within the maximum unambiguous range (r_a) determined by this PRT, and beam positions without significant echoes. For this case, beam positions for $\phi_{az} \leq 259°$ are considered significant, and those for $\phi_{az} > 259°$ are not. This can be seen in Figure 5.8(a), which shows the maximum range of storms as a function of ϕ_{az}, where storm ranges for $\phi_{az} > 259°$ are 0 km. Once the maximum range of storms per beam position is computed, the adaptive FBT PRTs are determined. This, in turn, determines the maximum unambiguous Nyquist velocity ($v_a = \lambda/4T_s$, where λ is the waveform length), which is shown
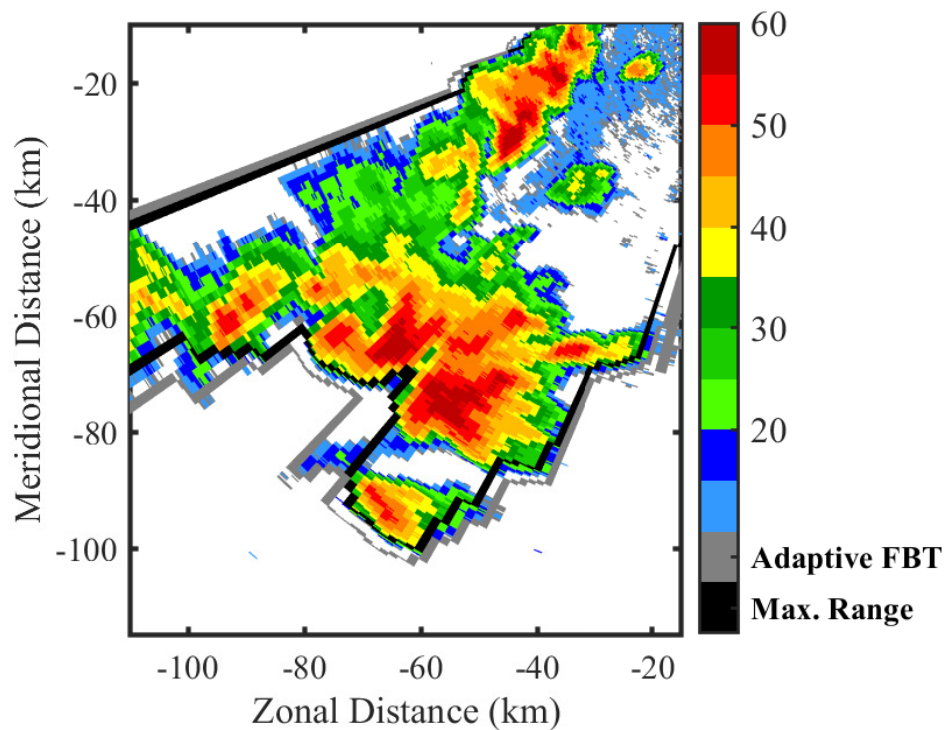
Figure 5.7: Reflectivity field illustrating the maximum range of storms determined for the case under consideration (black contour), and the maximum range used by in the adaptive FBT (gray contour).

in Figure 5.8(b). In this case, the maximum unambiguous velocity was increased considerably in most beam positions, being the average increase of 16.05 m s^{-1}.

(a) Maximum unambiguous range

(b) Maximum unambiguous velocity
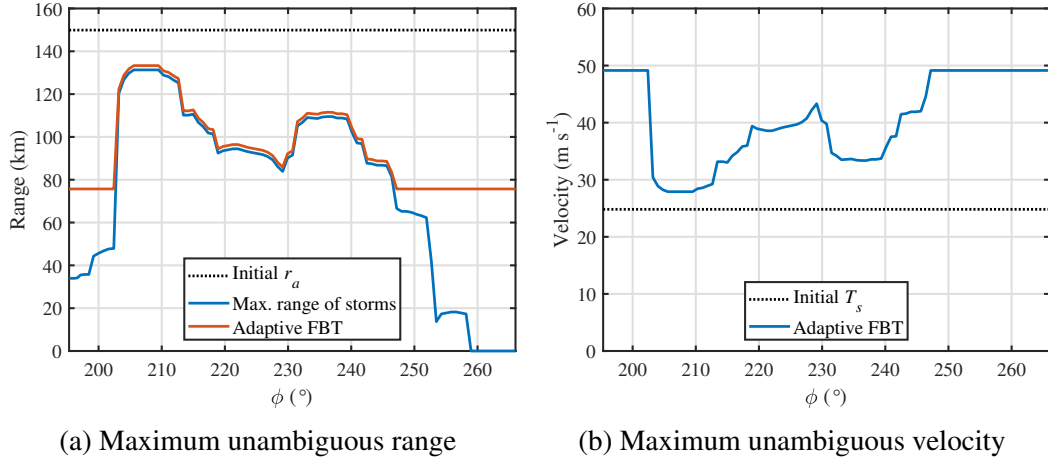
Figure 5.8: Maximum unambiguous range and velocity achieved using the simple adaptive FBT algorithm as a function of azimuth.

The time gained by shortening the PRT of a significant back-scanning beam is used to increase the number of samples for that same beam. The number of samples is increased to maintain the dwell time and achieve a standard deviation of Z_{h} and v_{r} similar to that of the initial dwell definition. Considering that the standard deviation of estimates is controlled by the dwell times (for specific signal conditions), reducing the PRTs while increasing the number of samples does not impact the quality of estimates. For the non-significant beams, the number of samples is set to 5 and the PRT to 0.5 ms (i.e., the minimum PRT). The time gained by reducing the dwells of non-significant beams is distributed equally over a set of upcoming back-scanning beams to reduce the standard deviation of estimates. The number of samples computed emulating the adaptive FBT scan is illustrated in Figure 5.9. Alternatively, it may be desirable to use the time gained to revisit a certain storm region more frequently while maintaining the same variance of estimates. The simple algorithm presented could be modified to include this alternative way of using

149

the time gained. Once the PRTs and number of samples per back-scanning beam
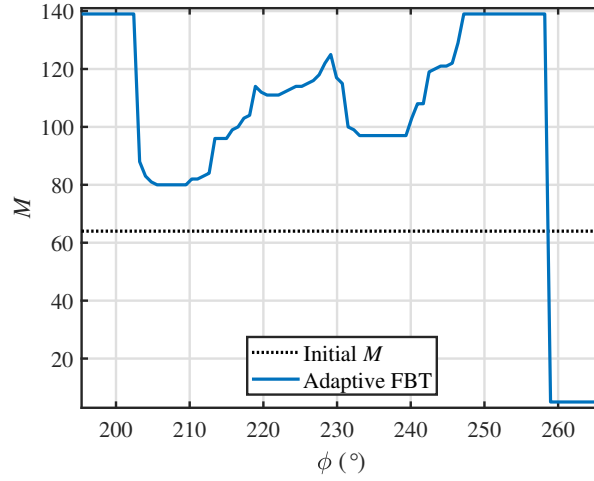
Figure 5.9: Number of samples derived using the simple adaptive FBT algorithm as a function of azimuth.

position are defined, the expected standard deviation of Z_h and v_r can be computed. These are computed from theoretical expressions derived by [52] using the adaptive PRT and M determined for benchmark SNR of 10 dB and $\sigma_v = 4$ m s^{-1}, and are shown in Figures 5.10(a) and 5.10(b), respectively. Results corroborate that for all beam positions with significant weather echoes, the expected standard deviation of Z_h and v_r estimates are less or equal than those in the initial (non-adaptive) scan. It is noted that the initial non-adaptive dwells definitions used here are equal to those in the lowest elevation scan of VCP 212.

The adaptive FBT illustrated in this section improves the data quality in two ways. First, by reducing the PRT to the maximum range of storms (including a small range padding), the maximum unambiguous velocity is increased. This reduces the likelihood of velocity aliasing. Second, while the standard deviation of estimates is controlled by the dwell times and the signal characteristics, increasing the number of samples for the same PRT typically reduces the standard deviation

of estimates. The adaptive FBT technique presented in this section increases the number of samples for a back-scanning to maintain the dwell time (compensating for the reduction in the PRT), and by using the time gained from non-significant beams. This maintains or reduces the standard deviation of estimates. While this technique is simple and exercises only one tradeoff (radar time for data quality), it can be used to improve the quality of estimates without risk of going outside of the requirements.

5.4.2 Discussion on Adaptive Scanning for RPAR

As described in Section 2.2.9, adaptive scanning techniques have been proposed for RRs and for 4F-PARs. The effectiveness of adaptive scanning techniques in reducing the scan time is limited for RR architectures due to the continuous mechanical
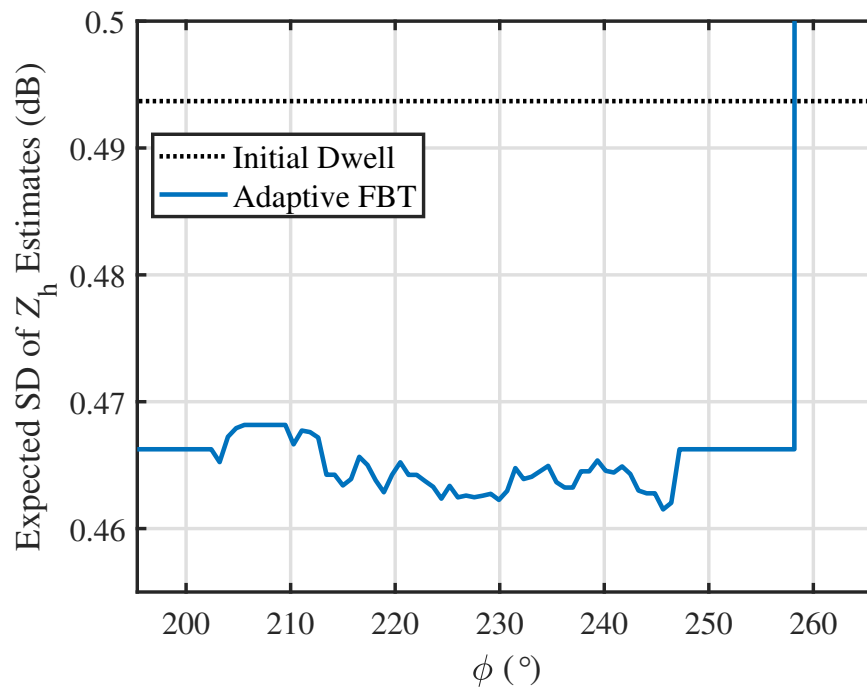
(a) SD of Z_h estimates
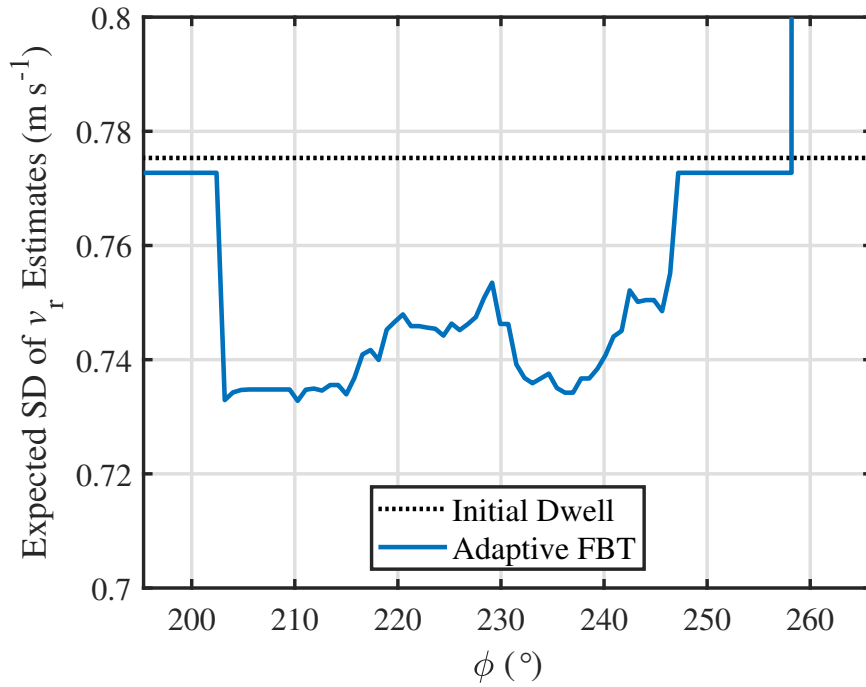
(b) SD of v_r estimates

Figure 5.10: Expected standard deviation of Z_h and v_r estimates computed using the scanning parameters produced by the adaptive FBT technique for the weather event illustrated in Figure 5.7.

inertia of the antenna, and the lack of advanced capabilities such as beam agility and/or beamforming. Research efforts demonstrated adaptive scanning techniques on stationary PAR systems (a single face of the 4F-PAR), but adaptive scanning has not been considered for the RPAR architecture yet. Although the mechanical rotation of the RPARs' antenna may impose limitations that would reduce the versatility of adaptive scanning techniques, the additional flexibility provided by phased array technology could enable dynamic adaptation of scan parameters.

One of the major challenges to develop adaptive scanning algorithms for an RPAR is that the PAR's visible region is continuously changing due to the mechanical rotation. Assuming a visible region of $\pm45°$ in azimuth about the broadside,

the total time the RPAR can scan a specific beam position (within the current revolution) is given by $t_v = 90°/\omega$. If the dwell for each beam position in the scan is $t_{BP} = MT_s$, then $B = t_v/t_{BP}$ beams can be scanned within the available time the beam is visible within the revolution of the antenna. Assuming polarimetric calibration can be achieved and maintained within the scan sector ($\phi_{az} = \pm45°$ and $\theta_{el} = 0°–20°$), t_v provides an upper limit on the time available for an adaptive technique to tailor observations. Figure 5.11 illustrates the number of beam positions that can be scanned by the RPAR within the visible region as a function of rotation speed and dwell time. Dotted lines correspond to the dwell times of beams in the CS (black) and CD (blue) scans for the lowest elevation (0.5°) scan of the VCP 212. These results indicate that for a given dwell time, lower rotation speeds permit larger number of beam positions to be scanned within the antenna revolution. Lower rotation speeds allow more time for adaptive scanning algorithms to operate and may be preferable; however, this would increase the overall volume scan time. Certain CONOPS could be devised to rotate the RPAR at relatively low speeds and still achieve faster updates on the order of one minute.

For illustration, assume that dwell definitions for the lowest elevation (0.5°) scans of the VCP 212; i.e., 15 samples at T_s = 3 ms for the CS scan and 64 samples at T_s = 1 ms for the CD scan, are used in an adaptive RPAR CONOPS. Assume one revolution of the antenna is carried out for each scan (CS and CD). The number of *storm-region revisits* for different storm sizes can be computed by taking ratio of the total number of beam positions (B) as a function of ω (Figure 5.11) over the number of beam positions required to scan the storm region. This is illustrated in Figures 5.12(a) and 5.12(b) for the CS and CD scan parameters. For example, consider a storm region of interest with an extent of 20° in azimuth and 3° in elevation. Assume that the RPAR has a 1 ° HPBW, that half-beamwidth sampling is
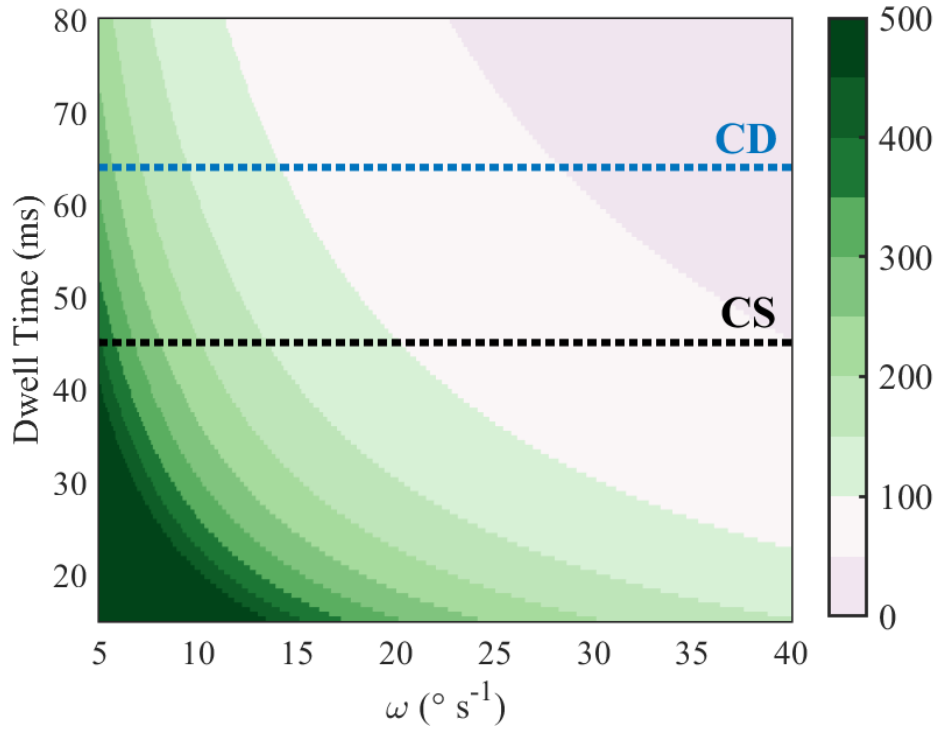
Figure 5.11: Number of beam positions that can be scanned by the RPAR within the visible region as a function of rotation speed and dwell time. Dotted lines correspond to the dwell times of beams in the CS (black) and CD (blue) scans for the lowest elevation (0.5°) scan of the VCP 212.

used in azimuth, and one-beamwidth sampling is used in elevation. Under these considerations, a total of 120 beams would be required to scan this storm region. Figure 5.12(a) indicates that this storm region could be revisited $\sim$1–3 times within one revolution of the antenna in the CS scan depending on the rotation speed. For $\omega \leq 5.5\,°\,\text{s}^{-1}$, the storm could be revisited about three times, for $5.5\,°\,\text{s}^{-1} \leq \omega \leq 8.3\,°\,\text{s}^{-1}$ the storm could be revisited 2–3 times, for $8.3\,°\,\text{s}^{-1} \leq \omega \leq 16.7\,°\,\text{s}^{-1}$ the storm could be revisited 1–2 times, and for $\omega > 16.7\,°\,\text{s}^{-1}$ the storm can only be observed once within the revolution of the antenna. For the CD scan, the storm can be revisited at least twice for $\omega \leq 5.8\,°\,\text{s}^{-1}$, 1–2 times at rotation speeds $5.8\,°\,\text{s}^{-1} \leq \omega \leq 11.8\,°\,\text{s}^{-1}$, and only once for $\omega > 11.8\,°\,\text{s}^{-1}$. Note that the fractional

part of a non-integer number of revisits means that only a partial revisit is possible with the remaining time.

Adaptive scanning considerations are oriented towards reducing the scan update times (i.e., faster revisits), given that volumetric update-time requirements are very demanding. Results presented in this subsection indicate that lower rotation speeds may allow for more flexible and effective adaptive scanning algorithms. Nevertheless, reducing the rotation speed may also increase the volume scan time. A CONOPS that achieves $\sim$1-min update times, and under which the antenna is rotated at relatively low speeds (5-10 $^\circ$ s^{-1}) would be ideal for adaptive scanning algorithms and would also reduce the mechanical wear on the azimuth rotator.

Other adaptive scanning techniques oriented towards improving the data quality could also be devised to improve meteorological RPAR observations. For instance, an adaptive pulse-compression algorithm, whereby the pulse length is adapted to the observations, could improve the sensitivity of the system. That is, longer waveforms could be used to scan meteorological echoes that do not exhibit large reflectivity gradients along range (to minimize range-sidelobe contamination), and shorter waveforms to scan regions with large reflectivity gradients along range. This concept is not specific for the RPAR, and could also be implemented on the 4F-PAR. A comprehensive analysis of adaptive scanning techniques for RPAR is beyond the scope of this dissertation and it is proposed for future work.

5.5   Chapter 5 Summary

This chapter introduced the FBT and demonstrated it using the FB-MCS CONOPS. An application of the FB-MCS CONOPS was presented in Section 5.3, whereby the dwell definition for the forward-looking and back-scanning beams were equal
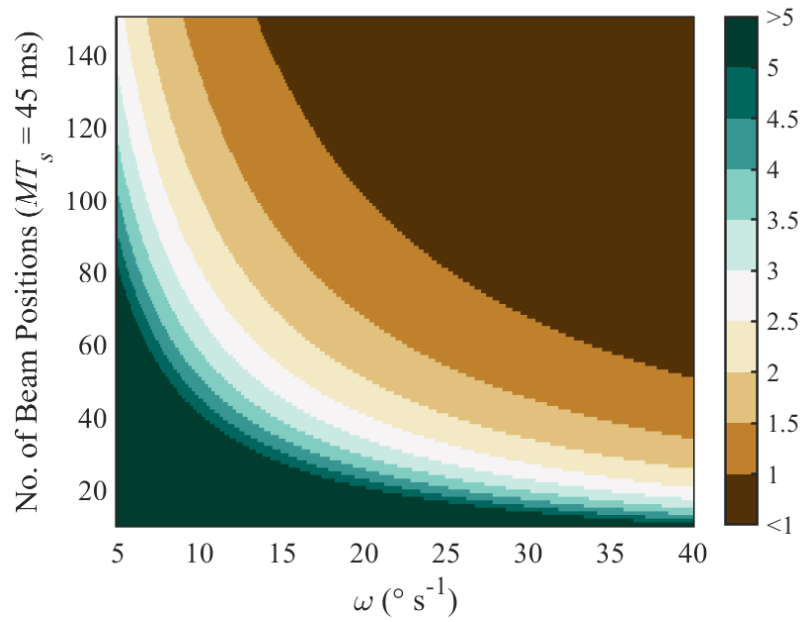
(a) CS scan
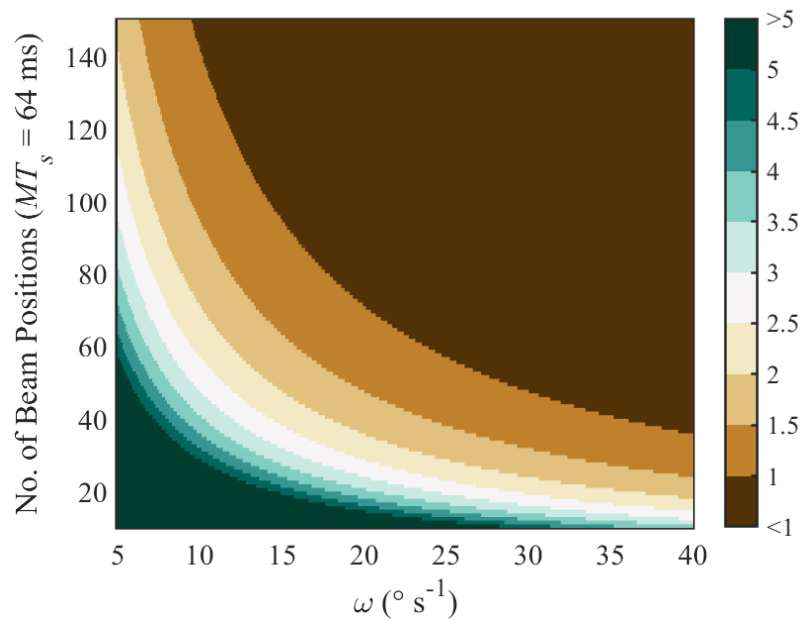
(b) CD scan

Figure 5.12: Number of *storm-region revisits* as a function of the number of beam positions to scan and using the dwell definitions for the lowest elevation scans of the VCP 212 (a) CS scan, and (b) CD scan.

156

to those in the lowest elevation surveillance and Doppler scans of VCP 212, respectively. In addition to illustrating the FBT, the DB (Chapter 4) was used to scan the forward-looking beams and reduce the surveillance scan time. Polarimetric fields of radar-variable estimates produced by the FBT were qualitatively compared to corresponding ones from a straightforward reference pencil-beam scan mimicking an RR system.

Qualitative results indicate that the standard deviation of estimates derived from the FBT scan was comparable to that of the reference pencil-beam scan. Doppler-variable estimates produced with the reference pencil-beam scan were difficult to compare to corresponding ones produced with the FBT due to inherent limitations imposed by the acquisition parameters (i.e., $T_s = 3$ ms). As expected, the spatial resolution of the radar variables derived from the forward-looking beams (namely, Z_h, Z_{DR}, Φ_{DP}, ρ_{hv}) was degraded with respect to the reference pencil-beam scan due to the use of a spoiled transmit beam. The HSE technique mentioned previously [11] could be used with the FBT to improve the quality of estimates and the spatial resolution of polarimetric variables (when data from the back-scanning beams are chosen). While the use of spoiled beams introduces some degradations (e.g., spatial resolution and sensitivity), it provides a means of reducing the scan time through digital beamforming. These degradations should be considered in the radar design process to ensure the use of the FBT meets functional requirements.

Time-series data from a collocated WSR-88D system (KOUN) were used to evaluate the quality of the FBT data collected with the ATD. Polarimetric fields of radar-variable estimates were first qualitatively compared. In this case, the high maximum unambiguous velocity of KOUN's CD scan, provided a valid means for comparison with the Doppler estimates produced with the FBT scan. A specific configuration of the signal processor was used to degrade the spatial resolution

of KOUN's CS scan, for a commensurate comparison with the forward-looking beams of the FBT scan. The quantitative analysis indicated significant correlation between fields of Z_h, v_r, and Φ_DP, and considerable correlation between fields of Z_DR and ρ_hv. Despite architectural differences between these radar systems, this methodology proved to be effective in obtaining meaningful quantitative results of the FBT.

An implementation of the FBT under an adaptive scanning CONOPS was emulated. Data from the forward-looking beams was used to tailor the acquisition parameters of the back-scanning beams. This resulted in increased maximum unambiguous velocities and reduced standard deviation of estimates. The simple adaptive FBT algorithm was described, and results were quantified using theoretical expressions for the standard deviation of Z_h and v_r estimates. Finally, a discussion about the potential of using adaptive scanning to reduce the update times was presented. Results indicate that there is greater potential for adaptive scanning algorithms to reduce storm revisit times when operating the RPAR system at lower rotation speeds.

Chapter 6

RPAR Scanning Strategy and Concept of Operations

"Truly successful decision-making relies on a balance between deliberate and instinctive thinking."

Malcolm Gladwell

Considering the demanding radar functional requirements, it is expected that several advanced RPAR scanning techniques will need to be applied simultaneously to achieve them. In previous chapters, three techniques that exploit different PAR capabilities were introduced: MCS, DB, FBT. Depending on the scanning strategy, these techniques could be used simultaneously by an RPAR to enhance azimuthal resolution while reducing the scan time and the variance of radar-variable estimates. As discussed previously, important tradeoffs have to be considered in the RPAR design process such that angular resolution and sensitivity requirements are met when using these techniques. This chapter brings together the techniques presented in previous chapters with the goal of using them to design a proof-of-concept RPAR CONOPS.

6.1 Integration and Testing of Techniques

To meet functional requirements with an affordable radar architecture, several advanced scanning techniques operating simultaneously may be needed. In this section, we begin by demonstrating the integration of MCS and DB. The former exploits beam agility and the later exploits digital beamforming, both unique PAR capabilities. Although the MCS and DB techniques are not completely independent (i.e., both operate in the angular domain), they exercise different capabilities which can be readily integrated. For MCS, the pointing angles for each pulse in a CPI are computed using the equations presented in Chapter 3 as a function of ω, T_s, M, and $\Delta\phi$. To integrate it with the DB, these MCS pointing angles are applied to each digitally formed receive beam to minimize azimuthal spreading of pulses across all R_F beams.

Implementation on the ATD was relatively straightforward. MCS pointing angles computed for the single-beam case (as in Chapter 3) were added to the predefined pointing angles of each receive beam. For example, for DB with $F = 3$ and $R_F = 5$ (i.e., $\Delta\phi = 0.5$), the relative pointing angles of receive beams are $\varphi_1 = -1.58°$, $\varphi_2 = -0.79°$, $\varphi_3 = 0°$, $\varphi_4 = 0.79°$, $\varphi_5 = 1.58°$. Then, the single-beam MCS pointing angles are added (in azimuth and elevation) to integrate the techniques. Note that this integration is valid for MCS angles computed using either the BMCS or FB-MCS concepts. For example, if the MCS angles were $\phi_{BMS}(1) = 0.02°$, $\phi_{BMS}(2) = 0°$, and $\phi_{BMS}(3) = -0.02°$ (i.e., assume $M = 3$), the angles for the MCS-DB beams would be $\phi_{MCS-DB}(1, k) = -0.02° + \varphi_k$, $\phi_{MCS-DB}(2, k) = \varphi_k$, and $\phi_{MCS-DB}(3, k) = 0.02° + \varphi_k$, where $k \in \{1, 2, 3, 4, 5\}$ represents a digital beam index. The implementation of the MCS-DB integration was tested by rotating past a stationary point target located in the vicinity of the

ATD and using BMCS angles. Specifically, a set of data were collected with the ATD mechanically rotating over a 40° sector at $\omega = 4\,^\circ\,\mathrm{s}^{-1}$, with $F = 3$, $R_F = 5$, $M = 65$, and $T_s = 3$ ms. The radar broadside was commanded to rotate from 280° to 320° azimuth with respect to North, with the target located at 31.65 km in range and approximately 301° azimuth. The antenna was commanded to a 0.5° mechanical elevation angle. The FB-MCS and DB techniques were also integrated and tested in an analogous way.

Azimuth angles for the received samples as a function of time are shown in Figure 6.1. Markers of different colors represent the five beams received. The inset plot presents a closer look at the pointing angles for the MCS-DB CPI that was transmitted in the direction of the point target (~301° in azimuth). It can be seen that the transition from beam to beam is smooth, which ensures that subsequent
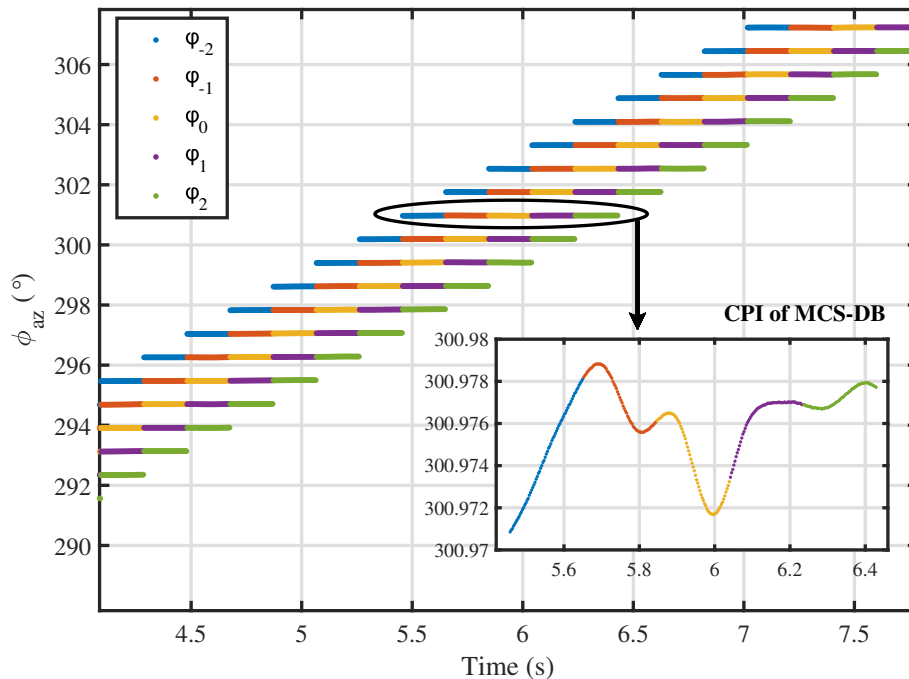
Figure 6.1: Azimuth angles for the received MCS-DB samples as a function of time. Markers of different colors represent the $R_F = 5$ beams received.

beams coherently processed with DB are pointed in approximately the same direction. Further, the spread of angles for samples across all received beams is of 0.0079°. This is consistent with the result obtained in Chapter 3, and it indicates that MCS would be effective in mitigating beam smearing in azimuth across all beams collected and processed with the DB technique. The mean standard deviation of absolute azimuth pointing angles (i.e., the summation of the mechanical and electronic azimuths) of samples within the MCS-DB CPIs is 0.0018°. It is probable that the oscillation observed is caused by practical imperfections in the mechanical system; they are different from one CPI to the next.

The SNR of signals received by the ATD on the H polarization for every receive beam while rotating past the target as a function of the pedestal (i.e., mechanical) azimuth are presented in Figure 6.2. Solid color lines represent the single-pulse SNRs estimated for each receive beam using MCS. Power and phase calibration of these receive beams is performed as described in section 4.2. Similar to the single-beam MCS implementation presented in chapter 3, the shape of the plots resembles a staircase because the returned powers of samples within the CPI are approximately constant. It is important to note that peak SNR estimates are approximately constant across receive beams ($\sim$ 49.1 dB). This indicates that all beams are pointed at the same location (i.e., same radar-cross section) and that beams are power calibrated. The inset plot presents a close up view of the peak returns for all receive beams. Note that the MCS-DB CPI coherently combines samples samples from the $R_F = 5$ beams across these peak returns (which are pointed in approximately the same direction with MCS), for a total of M_{DB} = 325. The standard deviation of SNR estimates for samples across the MCS-DB CPI that contains the peak return is 0.0927 dB. This is slightly higher than the one obtained for the single-beam MCS implementation (0.033 dB in section 3.5.1), but it is much lower than the
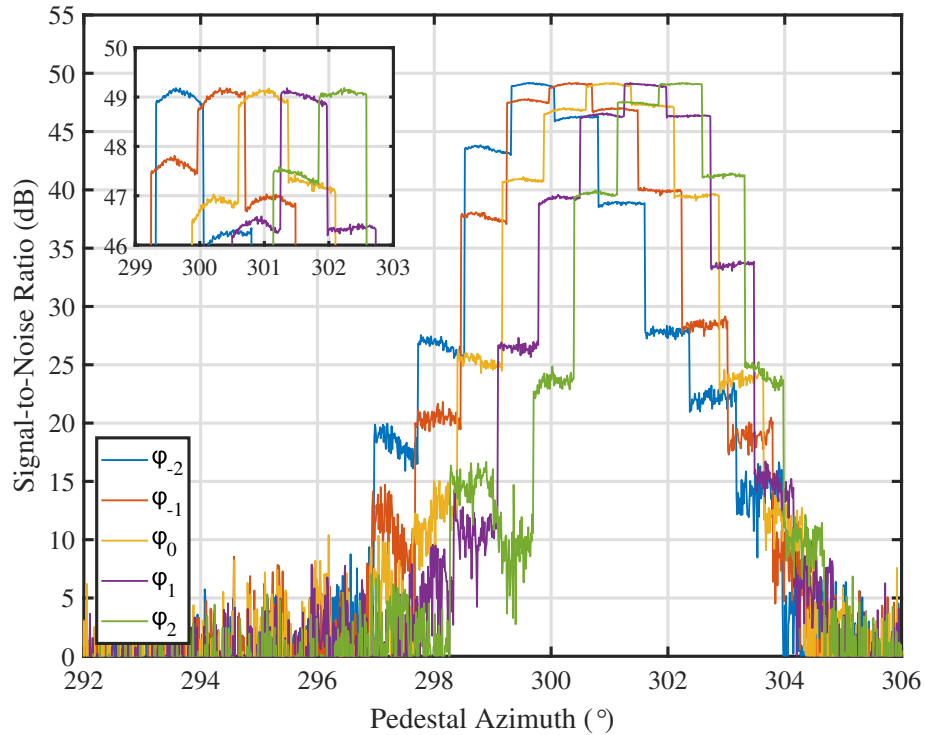
Figure 6.2: Single-pulse SNR of signals received by the ATD on the H polarization while rotating past the target and for every receive beam as a function of the pedestal (i.e., mechanical) azimuth.

expected standard deviation of estimated powers computed using theoretical expressions from [52] (for SNR = 49.1 dB, σ_v = 0.25 m s^{-1}, M_{DB} = 325, and $T_s = 3$ ms), which is 0.52 dB.

Integration of the FBT with the MCS-DB beams was achieved by using the FB-CONOPS described in section 5.2. That is, off-broadside pointing angles are derived for the forward-looking and back-scanning beams using the MCS expressions provided in Chapter 3 and are integrated with the DB technique using the same procedure outlined previously in this section. The last step involves setting different dwell definitions for forward-looking and back-scanning beams. Since this capability operates in sample time, it is independent from the MCS and DB op-

eration. In the ATD implementation, the PRTs for a CPI of FBT beams are specified explicitly in a file which is read by the real-time software. The example presented in section 5.3 exercised the integration of all three techniques.

6.1.1 Beam Types

The integration of all techniques presented in this dissertation is used to define *beam types*. These beam types are determined by the transmit and receive antenna patterns (i.e., spoil factors), the pointing angles of simultaneous receive beams formed, and the techniques used. It is assumed that the RPAR architecture supports these beam types and that effective two-way beams meet the prescribed requirements. Beam types can be used as building blocks to design scanning strategies for the RPAR CONOPS, and although we only present two beam types here (both of which are supported by the ATD), many other beam types using these techniques could be defined. These beam types were designed with several technical considerations and with the practical objective of demonstrating them using the ATD. Technical considerations for the design of beam types include: Polarimetric calibration feasibility and complexity, architecture complexity, and system cost.

As discussed in Chapter 2, the feasibility of achieving high-accuracy polarimetric calibration of PARs is an open question. Ongoing research at NSSL is evaluating the polarimetric calibration corrections derived for the ATD using far-field measurements [120]. Although preliminary results presented show promise [46], deriving the calibration corrections requires a calibration infrastructure used to measure the copolar and cross-polar far-field patterns [47, 56]. Considering the low likelihood that a similar infrastructure could be deployed in every radar site across the US, alternative solutions should be considered. Since beamsteering biases increase as

164

the beam is steered off the radar broadside, smaller steering angles may reduce the impact of these biases on polarimetric measurements. Alternative polarimetric calibration methods could be sufficiently effective at correcting biases from angles closer to broadside to achieve the required accuracy (e.g., near-field-based calibration). Therefore, it is preferable to design beam types that support a CONOPS with small off-broadside steering angles. Additionally, using relatively small steering angles would reduce the risk of array-damaging reflections when operating under a wet-radome regime with a spherical radome.

Digital beamforming methods provide a way to achieve the required volume scan time. However, as discussed previously, the use of spoiled transmit beams can negatively impact data quality as it results in increased two-way sidelobe levels and HPBW, and reduced sensitivity. A possible way to mitigate the former is to design a larger aperture such that the effective antenna pattern meets the requirements. Possible ways to mitigate the latter include increasing the element peak transmit power or using longer pulse-compression waveforms. Although enhancing the antenna to account for these may come at a cost, it provides a solution that permits the use of spoiled transmit beams (which support the required scan-time reduction). Another option is to use the technique proposed by Melnikov et al. [121], which involves the use of concatenated pulse transmissions in multiple directions, followed by simultaneous reception and processing of digitally formed beams in the same directions as the transmit beams. Although the use of this technique does not directly reduce system sensitivity, it requires high-power antenna elements (i.e., not compatible with pulse compression) and a large enough transmitter duty cycle to accommodate all concatenated transmit pulses. Further, the authors argue that an all-digital architecture may be needed to maintain sidelobe levels comparable to those resulting from narrow pencil beams with the same aperture. Considering that the use

of spoiled beams is compatible with pulse compression and can be implemented on a sub-arrayed architecture, it is expected that the architecture supporting these capabilities is more affordable than the all-digital RPAR with high-power elements supporting the alternative technique to reduce the scan time proposed by Melnikov et al. [121]. Therefore, although the use of spoiled transmit beams has to be compensated by increasing the aperture size and the system sensitivity, it is preferable to design beam types exploiting this capability.

Finally, other methods to reduce the scan time, such as frequency division multiplexing, are likely to be more costly than accounting for spoiled-transmit-beam degradations in the RPAR design process.

With these considerations in mind, the beam types defined here are:

1. **MCDB3**: This beam type uses the BMCS CONOPS and incorporates the DB technique, with spoiled transmit beams in both azimuth and elevation. The transmit beam is spoiled in azimuth by $F_{az} = 1.5$ and in elevation by a variable factor F_{el} in the range of 1.5 to 4. Nine simultaneous beams are digitally formed in a 3×3 cluster centered on the broadside. The normalized sampling spacing in azimuth is $\Delta\phi = 0.5$, and it is variable in elevation (as dictated by the VCP). Note that additional independent beams are digitally formed in elevation as well; this relaxes the need for very high rotation speeds while achieving large scan-reduction factors.

2. **FB3**: This beam type makes use of the FB-MCS CONOPS, which includes the FBT on top of MCS and DB; it is designed to execute split cuts (similar to those used in the WSR-88D) with a single revolution of the antenna, and to be used in conjunction with real-time adaptive scanning algorithms (as illustrated with an example in Section 5.4.1). Electronically steered MCDB3

166

beams are used for forward-looking and back-scanning beams, each with a specific dwell definition. Antenna-relative pointing angles for the forward-looking and back-scanning beams can be set arbitrarily (e.g., $\pm 15°$), but staying close to the principal planes will reduce co-polar beam steering biases and cross-polar contamination induced by the RPAR antenna. The angular separation between forward-looking and back-scanning beams could be important since the dwells of back-scanning beams are dynamically redefined by an adaptive scanning algorithm. There should be sufficient time to process the forward-looking beams and to used the derived adaptive scanning products to schedule the back-scanning beams.

These two beam types were implemented on the ATD with $F_{\mathrm{az}} = 3$ and $F_{\mathrm{el}} = 1.5$. While this is not ideal because the transmit beam is illuminating a wider azimuthal sector than needed, which results in an additional sensitivity loss, it is valid to demonstrate the concept. The sampling spacing of simultaneous beams in elevation was set to $0.4°$, such that when mechanically commanding the antenna at the $0.9°$ elevation, the $0.5°$, $0.9°$, and $1.3°$ angles would be simultaneously sampled. These elevation angles are typically used in WSR-88D VCPs, and in particular, are used on the VCP 212 split cuts.

Beam peaks measured using the ATD calibration infrastructure were used to derive power and phase calibration parameters in a similar way as described in previous chapters. Normalized measured two-way uncalibrated ATD antenna mainlobe patterns for the MCDB3 beam type are shown in Figures 6.3(a), and corresponding calibrated beams are shown in Figures 6.3(b). Dotted contour lines delimit the -1 dB level and black dot markers indicate the intended scanning location of the beam.

In summary, the techniques introduced in this dissertation were first integrated
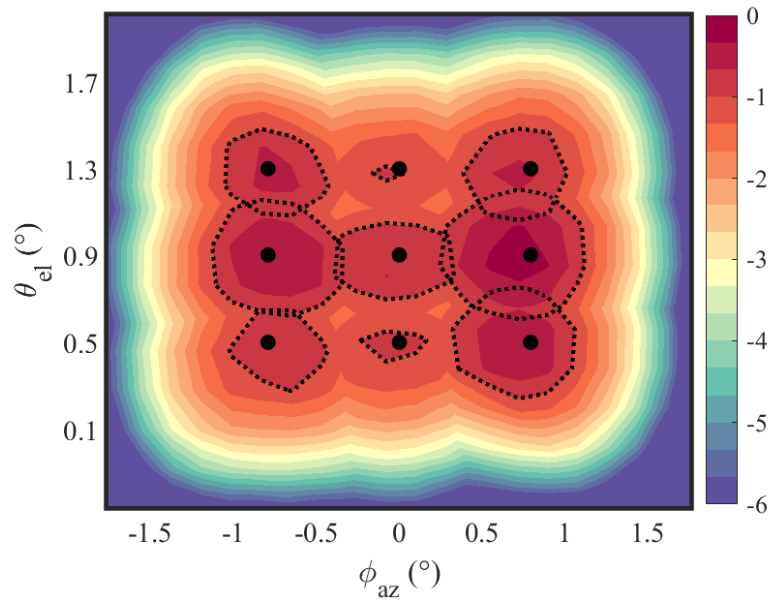
(a) Uncalibrated beams
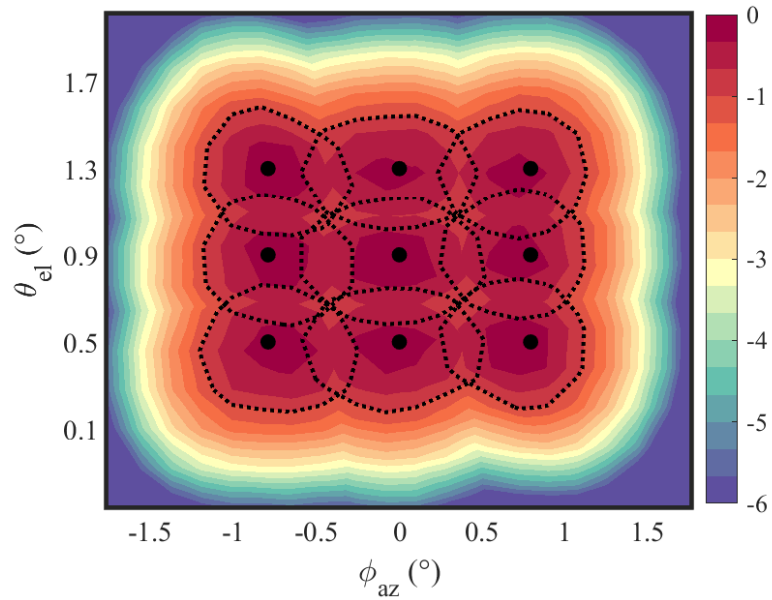
(b) Calibrated beams

Figure 6.3: Gain-normalized measured two-way ATD antenna mainlobe patterns for the MCDB3 beam type (a) Uncalibrated beams (b) Calibrated beams. Dotted contour lines delimit the −1 dB level and black dot markers indicate the intended scanning location of the beam.

and tested on the ATD. Then, the illustrative beam types defined were implemented, independently calibrated, and tested using combinations of the three techniques. With the satisfactory implementation of these beam types, we proceed to design an RPAR scanning strategy and collect polarimetric weather data with the ATD for proof-of-concept demonstration.

6.2 RPAR Scanning Strategy

Advanced scanning and signal processing techniques can be used to construct a scanning strategy for the RPAR. As discussed in Chapter 2, there are several unique RPAR capabilities that could be exploited to enhance the radar performance (e.g., reduce the scan time, improve the quality of estimates, etc.) and meet the RFR. Some important tradeoffs to consider for designing advanced RPAR scanning strategies include (1) transmit beam spoiling factor, and its associated tradeoffs discussed in Chapter 4; (2) the number of simultaneous dual-polarization receive beams required (3) the need for accurate copolar beam peak measurements to achieve polarimetric calibration, specially at steering angles far from the broadside; (4) the increased antenna pattern cross-polarization levels as the RPAR beam is steered far from the principal planes; (5) the maximum pedestal rotation speeds required. These main tradeoffs should be accounted for in the RPAR design process, such that the performance of the RPAR with the defined scanning strategies meets the RFR.

Hereafter, the two beam types introduced in the previous section are used to design an illustrative VCP for the RPAR CONOPS. These are consistent with the scanning strategy frequently used in precipitation-mode, the VCP 212, in terms of the number of beam positions per scan, the PRTs (i.e., same spatial coverage), and

the number of samples per beam position (which determines the standard deviation of estimates). We emphasize that this is not the only possible scanning strategy for the RPAR, but it is one reasonable option designed with consideration of the previously mentioned tradeoffs, and the use of the RPAR techniques developed in this work.

The current VCP 212 definition is presented in Table 6.1 [105], where each scan corresponds to one revolution of the antenna. Subscripts 'S' and 'D' denote the surveillance and Doppler scan parameters. Beam types SZCS, SZCD, B, and CDX correspond to the SZ-2 CS dwells, SZ-2 CD dwells, batch PRTs dwells, and uniform PRTs dwells, respectively. Two columns with the expected standard deviation of Z_h and v_r estimates labeled SD(Z_h) and SD(v_r) are added at the rightmost end of the table. These are computed using theoretical expressions derived by [52] with an SNR of 10 dB for Z_h, an SNR of 8 dB for v_r, and a σ_v of 4 m s^{-1} for both. These benchmark parameters are extracted from the RFR, which specifies that the standard deviation of Z_h estimates should be "$\leq$ 1 dB for a target with true σ_v of 4 m s^{-1} and SNR $\geq$ 10 dB", and for v_r estimates should be "$\leq$ 1 m s^{-1} for a target with true σ_v of 4 m s^{-1} and SNR $\geq$ 8 dB". Cells with the expected standard deviations computed are filled in green for scans that achieve the requirement, and in red for those that do not. It is noted that some scans in VCP 212 do not meet requirements on the standard deviation of Z_h and v_r estimates for the benchmark SNR and σ_v parameters used.

An RPAR VCP is designed for the observation of fast-evolving convective precipitation systems. The proposed RPAR VCP takes 63.5 s (1.06 min.) to complete and is presented in Table 6.2, where each scan corresponds to one revolution of the antenna. This table is similar to the one presented for the conventional VCP 212, with additional columns for R_F (number of simultaneous beams received) and M_{DB}

(effective number of samples) for the surveillance and Doppler scan parameters.

Scan No.	Angle (°)	ω (° s^{-1})	Period (s)	Beam Type	M_S	M_D	T_S (ms)	T_D (ms)	Dwell Time (ms)	$r_{a,S}$ (km)	$r_{a,D}$ (km)	v_a (m s^{-1})	SD(Z_h) (dB)	SD(v_r) (m s^{-1})
1	0.50	21.5	16.8	SZCS	15		3.11		46.60	466			0.63	
2	0.50	17.1	21.0	SZCD		64		0.91	58.45	0	137	30.3		0.91
3	0.90	21.5	16.8	SZCS	15		3.11		46.60	466			0.63	
4	0.90	17.1	21.0	SZCD		64		0.91	58.45	0	137	30.3		0.91
5	1.30	23.3	15.4	SZCS	15		2.86		42.90	429			0.65	
6	1.30	17.1	21.0	SZCD		64		0.91	58.45	0	137	30.3		0.91
7	1.80	28.0	12.9	B	3	28	2.57	1.00	38.29	386	150	27.7	1.40	1.31
8	2.40	28.8	12.5	B	3	28	2.24	1.00	36.96	336	150	27.7	1.47	1.31
9	3.10	29.5	12.2	B	3	28	1.95	1.00	35.81	293	150	27.7	1.55	1.31
10	4.00	28.6	12.6	B	3	30	1.66	1.00	36.64	249	150	27.7	1.65	1.27
11	5.10	27.8	13.0	B	3	31	1.66	1.00	37.64	249	150	27.7	1.65	1.24
12	6.40	27.8	13.0	B	3	31	1.66	1.00	37.64	249	150	27.7	1.65	1.24
13	8.00	28.8	12.5	CDX		38		0.91	34.71	137	137	30.3	0.69	1.18
14	10.00	28.8	12.5	CDX		41		0.85	34.71	127	127	32.7	0.69	1.19
15	12.50	28.8	12.5	CDX		44		0.79	34.76	119	119	35.1	0.69	1.20
16	15.60	28.8	12.5	CDX		44		0.79	34.76	119	119	35.1	0.69	1.20
17	19.50	28.8	12.5	CDX		44		0.79	34.76	119	119	35.1	0.69	1.20
VCP Time:	**4.44**	**min**												

Table 6.1: Current VCP 212 definition. Subscripts 'S' and 'D' denote the surveillance and Doppler scan parameters. Beam types SZCS, SZCD, B, and CDX correspond to the SZ-2 CS, SZ-2 CD, batch PRTs, and uniform PRTs, respectively.

Scan No.	Angle (°)	ω (° s^{-1})	Period (s)	Beam Type	Surveillance			Doppler			T_S (ms)	T_D (ms)	Dwell Time (ms)	$r_{a,S}$ (km)	$r_{a,D}$ (km)	v_a (m s^{-1})	SD(Z_h) (dB)	SD(v_r) (m s^{-1})
					R_F	M_S	M_{DB}	R_F	M_D	M_{DB}								
	0.50				3	5	15	3	22	66	3.11	0.91	35.63	466	137	30.3	0.63	0.90
1	0.90	28.1	12.8	FBD3	3	5	15	3	22	66	3.11	0.91	35.63	466	137	30.3	0.63	0.90
	1.30				3	5	15	3	22	66	3.11	0.91	35.64	467	137	30.3	0.63	0.90
	1.80				3	6	18	3	20	60	2.57	1.00	38.01	386	150	27.7	0.63	0.89
2	2.40	28.2	12.8	MCDB3	3	6	18	3	20	60	2.57	1.00	38.01	386	150	27.7	0.63	0.89
	3.10				3	6	18	3	20	60	2.57	1.00	38.01	386	150	27.7	0.63	0.89
	4.00				3	9	27	3	20	60	1.66	1.00	36.60	249	150	27.7	0.62	0.89
3	5.10	28.6	12.6	MCDB3	3	9	27	3	20	60	1.66	1.00	36.60	249	150	27.7	0.62	0.89
	6.40				3	9	27	3	20	60	1.66	1.00	36.60	249	150	27.7	0.62	0.89
	8.00							3	42	126		0.85	35.56	127	127	32.7	0.41	0.68
4	10.00	28.1	12.8	MCDB3				3	42	126		0.85	35.56	127	127	32.7	0.41	0.68
	12.50							3	42	126		0.85	35.56	127	127	32.7	0.41	0.68
	15.60							3	44	132		0.79	34.76	119	119	35.1	0.41	0.69
5	17.55	28.8	12.5	MCDB3				3	44	132		0.79	34.76	119	119	35.1	0.41	0.69
	19.50							3	44	132		0.79	34.76	119	119	35.1	0.41	0.69
VCP Time	**1.06**	**min**																

Table 6.2: RPAR VCP definition. Subscripts 'S' and 'D' denote the surveillance and Doppler scan parameters. Beam types FBD3 and MCDB3 described previously are used to design the scan.

For each scan in the table, the antenna is mechanically tilted in elevation such that the beam on the center of the cluster is on broadside. That is, the antenna is tilted to the middle elevation angle in the scan. The PRTs are consistent with those of the current VCP 212, but the number of samples is increased to meet the requirements on the standard deviation of Z_h and v_r using the same benchmark parameters as described before. The MCDB3 beam is used in batch mode for scans 2 and 3, that is, the surveillance CPI is collected first and the Doppler CPI is collected after. Further, considering that these beam types are designed to sample three elevations at a time, an additional elevation scan is added with respect to the current VCP 212 (i.e., 17.55° in scan 5), to fully exploit the RPAR's beamforming capabilities. Lastly, a maximum rotation speed of 29 ° s^{-1} is imposed, as this is below the maximum speed currently used in VCP 212, and is below the azimuthal rotation speed limit of the WSR-88D pedestal system (30° s^{-1}). Further, the scans are designed to have approximately the same rotation speed to minimize wear of the pedestal system. In summary, this RPAR scanning strategy results in the same coverage as VCP 212 (with an additional scan at the 17.55° elevation angle), it takes about 1 min to complete, it is designed to meet the standard deviation requirements (unlike VCP 212), and it assumes achievable rotation rates.

An RPAR system supporting this CONOPS would need to have the capability to receive $R_F = 9$ simultaneous beams within maximum spoiling factors of F_{az} = 1.5 and $F_{el} = 4$. It is assumed that the RPAR was designed to meet the requirements when using the MCDB3 and FB3 beams, accounting for the spatial resolution (azimuth/elevation beamwidths and sidelobe levels) and sensitivity degradations incurred. A detailed study of possible RPAR architectures that support his CONOPS is very important, and it is proposed for future work.

6.3 Data Collection Experiment

This experiment is used to illustrate the MCDB3 beam type. Sector scans were collected using the STSR mode in rapid succession on 10 July 2020 to sample a convective precipitation system to the north of the ATD at ranges extending from approximately 50 km to 150 km. For both scans, the radar broadside was commanded to mechanically rotate clockwise from 300° to 355° in azimuth, at constant 0.9° elevation. For scan 1, the MCDB3 beam was used to collect polarimetric weather data at 13:32:45 Z with the ATD rotating at $\omega = 4\,°\,\mathrm{s}^{-1}$. Azimuth and elevation sampling of the digitally formed receive beams in the 3×3 cluster was set to 0.79° (i.e., $\Delta\phi = 0.5$) and 0.4°, respectively. Elevation sampling was set such that the 0.5°, 0.9°, and 1.3° elevation angles were sampled simultaneously (matching the lower elevation angles of VCP 212). For scan 2 the radar rotated at $\omega = 4\,°\,\mathrm{s}^{-1}$, the transmit and receive pencil beams were maintained at broadside, as done for reference in previous data collection experiments. Data from this scan were collected at 13:33:34 Z. Identical dwell definitions were used for both scans with $M = 65$ at $T_s = 3$ ms, resulting in a normalized azimuthal sampling of $\Delta\phi = 0.5$. As with previous experiments, range-time samples were produced at a rate of 4 MHz for a range sampling interval of 37.5 m. Range-time processing was set to incoherently average samples from 6 consecutive range gates, which results in a range sampling spacing for the radar variables of 225 m. Data from the collocated KCRI radar system (WSR-88D) were collected simultaneously to verify the ATD MCDB3 data. The KCRI radar was following the operational VCP number 215; time-series IQ data for the same azimuthal sector and the three elevation angles scanned by the ATD system were extracted for processing. Radar system parameters and scanning strategies for these experiments are summarized in Table 6.3.

Fields of radar-variable estimates resulting from processing scan 1 and scan 2 are presented in Figure 6.4. Panels are organized as follows: the first three columns correspond to scans 1A (0.5°), 1B (0.9°), and 1C (1.3°), respectively, and the right-most column corresponds to scan 2; the rows from top to bottom show fields of radar Z_h, Z_{DR}, Φ_{DP}, and ρ_{hv}.

A qualitative analysis of the three cuts in scan 1 is conducted first. A quick look through the panels for scans 1A, 1B, 1C, confirms that there are no data artifacts. Comparing the Z_h fields, it is apparent that values increase with elevation. Light blue arrows indicate a region in the reflectivity core where this increase is more apparent. An inverse effect is observed by comparing panels of Z_{DR} in the regions indicated with gray arrows, that is, it is apparent that values decrease as elevation increases. These observations are consistent with the storm dynamics, there is higher density (large Z_h) of small spherical water droplets (low Z_{DR}) at higher altitudes, and through the collision-coalescence process they merge (decreases Z_h) and grow into larger drops (increases Z_{DR}) as they are falling [122]. Drag force produces the oblate shape of large drops that gradually increases Z_{DR}. Fields of Φ_{DP} for the three scans are similar and indicate an increase in differential phase of approximately 100° as the polarimetric wave propagates through the heavy precipitation core. In

Scan #	Radar System	Time (Z)	Beam Type	Scanned Az. Sector	Scanned Elevation	ϕ_e	M	T_s	$\omega °\,s^{-1}$
1A					0.5°				
1B	ATD	13:32:45	MCDB3	300° - 355°	0.9°	2.04°	65	3	4
1C					1.3°				
2	ATD	13:33:34	Broadside Pencil	300° - 355°	0.9°	1.64°	65	3	4
3	KCRI	13:32:19	Broadside Pencil	0° - 360°	0.5°	1.1°	28	3	11.5
4	KCRI	13:33:16	Broadside Pencil	0° - 360°	0.9°	1.1°	24	3	13.4
5	KCRI	13:34:08	Broadside Pencil	0° - 360°	1.3°	1.1°	22	3	15.9

Table 6.3: Radar system parameters and scanning strategies for the MCDB3 experiment.
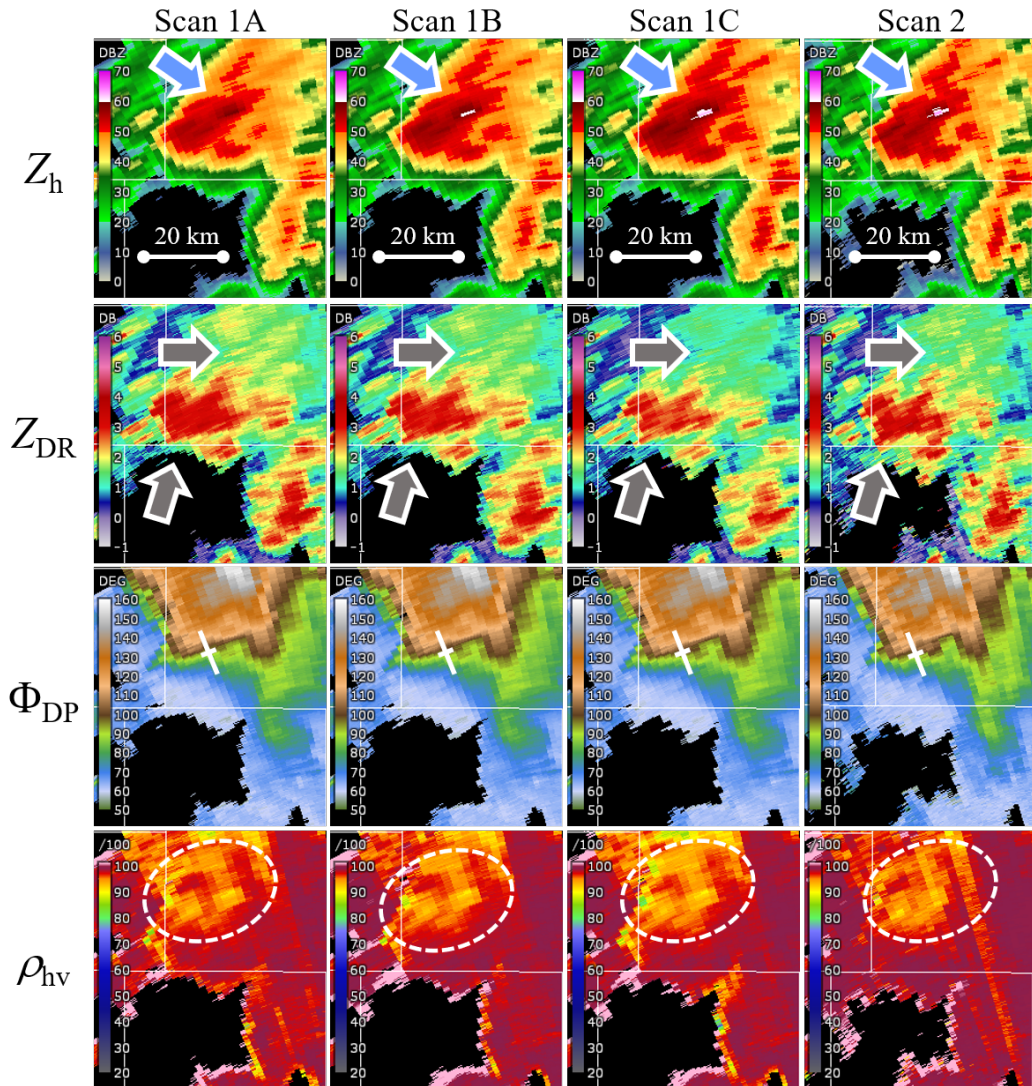
Figure 6.4: Radar-variable estimates obtained from scans 1 and 2 collected in rapid succession. Panels are organized as follows: the left column corresponds to the 0.9° elevation angle of scan 1 and the right column corresponds to scan 2; the rows from top to bottom show fields of Z_h, Z_DR, Φ_DP, and ρ_hv.

particular, a sharp Φ_{DP} gradient is indicated with white lines, where it appears that Φ_{DP} values increase with elevation. A cross-section of the specific differential propagation phase K_{DP} [123] (derived from the ATD's MCDB3 data) is derived from Φ_{DP} along the white lines to verify that Φ_{DP} estimates are well calibrated in elevation, it is presented in Figure 6.5. It shows changes in K_{DP} ranging from $0\,^\circ\,\mathrm{km}^{-1}$ to $4.8\,^\circ\,\mathrm{km}^{-1}$, and a vertical structure that is consistent with the increase in Z_h as a function of altitude. This vertical K_{DP} structure is typically observed with range-height indicator (RHI) scans through heavy precipitation cores [124, 125]. Note that K_{DP} was selected because it reveals changes in Φ_{DP} that otherwise may not be apparent due to the wide range of Φ_{DP} values. Comparing the fields of ρ_{hv}, it is noted that high values ($\rho_{hv} \geq 0.9$) are estimated, as is expected for meteorological scatterers. In the region enclosed with white dotted ellipses, relatively lower values of ρ_{hv} are measured (~ 0.95), and is is apparent that values decrease with increasing elevation. This is probably caused by the path integrated attenuation as the polarimetric wave traverses the high Z_h core and the SNR is < 10 dB [126, 127]. This hypothesis is consistent with the higher Z_h's observed at higher elevations, which causes larger attenuation.

A qualitative analysis of panels from scan 1B and scan 2, both at the 0.9° elevation angle, is provided next. A quick comparison of corresponding panels shows that data collected with the MCDB3 beam type have lower azimuthal resolution and sensitivity. That is, the footprint of Z_h echoes is larger on data from scan 2 (i.e., better sensitivity), and spatial features appear better defined (i.e., better azimuthal resolution) also in data from scan 2 (e.g., the region with the Z_h core indicated by the arrows in the panels of Z_h). This was expected since the use of spoiled transmit beams increases the two-way beamwidth and reduces sensitivity, as discussed in Chapter 4. Qualitative comparison of Z_h fields shows that estimates appear to have
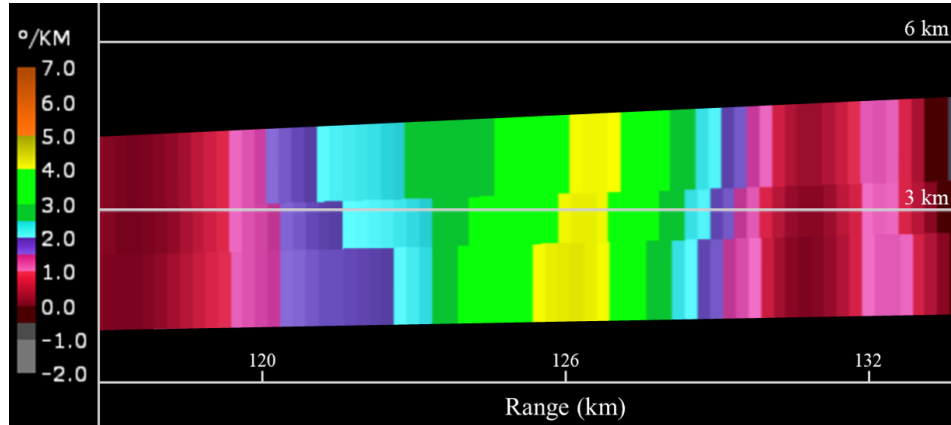
Figure 6.5: Cross-section of the specific differential phase K_{DP} (derived from the ATD's MCDB3 data) along the white lines in Figure 6.4 confirm the presence of a Φ_{DP} gradient.

comparable values, but the texture of the field from scan 1B appears smoother. This is because the DB technique is used to increase the number of coherently processed samples by $R_F = 3$, from $M = 65$ to $M_{\text{DB}} = 195$. Although the degraded azimuthal resolution in scan 1 smears spatial features, this is independent from the standard deviation of radar-variable estimates. The smoothness in the texture of the field, as gauged by the reduction in the "*salt and pepper*" noise [128], is achieved by the larger number of available samples obtained using DB. For the benchmark parameters discussed earlier, namely, SNR = 10 dB and $\sigma_\text{v} = 4$ m s^{-1} (and the same $T_s = 3$ ms), the expected standard deviation of Z_h estimates is reduced from 0.32 dB to 0.18 dB when samples are increased from $M = 65$ to $M_{DB} = 195$. It is also noted that the reflectivity core indicated by the light-blue arrows has larger values ($\sim$1 - 2 dB) in scan 2. A possible hypothesis for this is that the Z_h core in scan 1C descended in elevation (from $1.3°$ to $0.9°$) over the 49 s period between these scans. Similar conclusions can be drawn by comparing fields of Z_{DR}. The difference in azimuthal resolution is more apparent in fields of Φ_{DP}, since radially oriented features are more sharply defined in fields derived from scan 2. Nevertheless, estimated val-

ues are comparable and a similar change in $\Phi_{\rm DP}$ along the $Z_{\rm h}$ core (of $\sim 100°$ as noted previously) is observed in both fields. Comparing the fields of $\rho_{\rm hv}$, it is noted that similar features of lower $\rho_{\rm hv}$ (~ 0.95) are observed in the area enclosed by the white ellipses on fields from both scans. The field of $\rho_{\rm hv}$ estimates from scan 1B also appears to have a smoother texture.

This qualitative analysis indicates that the MCDB3 beam type was effectively implemented and calibrated for polarimetric weather observations. Key takeaways from the analysis are (1) MCS and DB can operate in conjunction to enhance azimuthal resolution and reduce the variance of estimates, without introducing apparent biases or unexpected artifacts in that could affect the quality of radar-variable estimates, (2) the techniques are compatible with sets of simultaneous digitally formed beams in elevation (3) the use of simultaneous beams in elevation provides a complementary way to reduce the scan-time (as concluded by [44, 86]), and relaxes the need for very high rotation speeds to achieve the same scan-time reduction factor as when using DB in azimuth only. The RPAR VCP defined in section 6.2 can be implemented with this beam type to achieve 1.06 min volume scan times. If the RPAR is designed to achieve angular resolution requirements using the MCDB3 and FBD3 beam types, and it can rotate at speeds of $\sim 30° \text{ s}^{-1}$, it would be possible to achieve the NOAA/NWS RFR.

6.3.1 Comparison with KCRI Radar

Data collected with the ATD system using the MCDB3 beam type are now compared to data simultaneously collected with the collocated KCRI WSR-88D radar. KCRI scan parameters are provided in Table 6.3. This analysis is conducted to check the quality of the MCDB3 data against that of a well-known reference radar.

First, data are qualitatively analyzed to verify that the meteorological interpretation of MCDB3 fields is similar to that from KCRI fields. This would indicate that polarimetric calibration of MCDB3 fields was sufficient for interpretation. It is important to remember that these radar systems are different, and known differences in resolution and sensitivity are expected. An RPAR with the same effective resolution and sensitivity as KCRI would not incur these degradations. Furthermore, data from scans 3, 4, and 5, from the KCRI radar are not simultaneously collected and there are periods of 57 s and 52 s between scans 3–4 and 4–5, respectively. Since KCRI's scan 4 (at 0.9° elevation) and the ATD's scan 1B (also at 0.9° elevation) are only 18 s apart, these are used for a quantitative analysis.

Fields of radar-variable estimates resulting from processing scans 3–5 are presented in Figure 6.6. Panels are organized as follows: the first three columns correspond to scans 3 (0.5°), 4 (0.9°), and 5 (1.3°), respectively, and the rightmost column corresponds to scan 1B (i.e., MCDB3 at 0.9°); the rows from top to bottom show fields of radar Z_h, Z_DR, Φ_DP, and ρ_hv. The KCRI time-series data presented in these panels were processed with the conventional super-resolution mode and $\Delta\phi = 0.5$.

Qualitative analysis of the Z_h and Z_DR fields derived from KCRI scans indicates that as elevation increases, there is an increase in estimated Z_h values and a decrease in estimated Z_DR values. This is consistent with corresponding ATD fields derived from MCDB3 data. Fields of Φ_DP estimates also show similar qualitative features; there is an increase from the initial system Φ_DP of 60° to about 160° along the radial crossing the Z_h core (indicated with the light-blue arrow in the panel of Z_h from scan 1B). An apparent decrease in fields of ρ_hv is observed in the region where the Z_h core is (white dotted circle in the panel of ρ_hv from scan 1B). This is also consistent with corresponding ATD fields in Figure 6.4 and is likely a result of
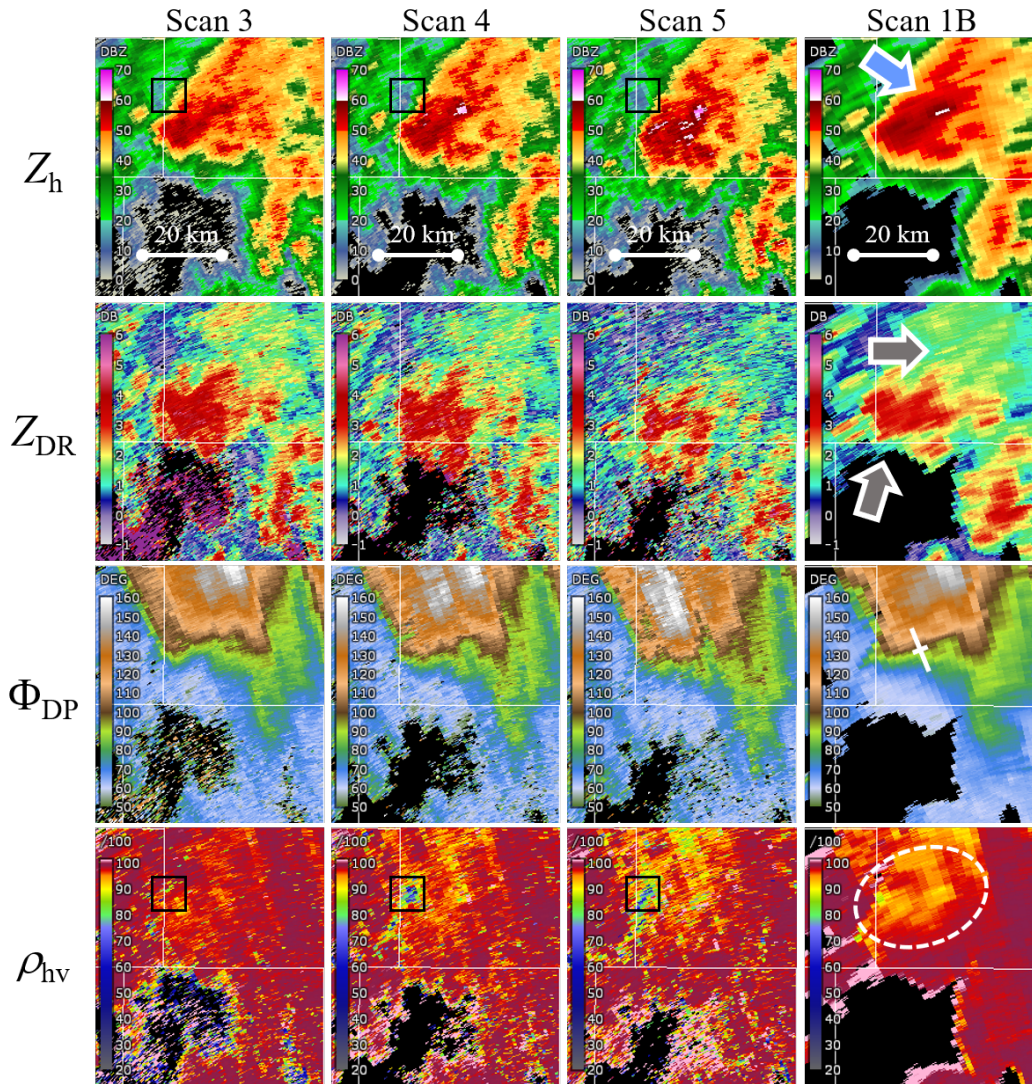
Figure 6.6: Fields of radar-variable estimates resulting from processing scans 3–5. Panels are organized as follows: the first three columns correspond to scans 3 (0.5°), 4 (0.9°), and 5 (1.3°), respectively, and the rightmost column corresponds to scan 1B (i.e., MCDB3 at 0.9°); the rows from top to bottom show fields of Z_h, Z_{DR}, Φ_{DP}, and ρ_{hv}.

attenuation as the wave propagates through the Z_h core. Further, a small region with low ρ_{hv} estimates is indicated with a black square. Corresponding squares are placed in the Z_h fields to show that reflectivities in that region are very low (~ 10 dBZ), and therefore the low ρ_{hv} estimates are likely a result of attenuation and low SNRs from echoes in the region. This analysis indicates similar meteorological characteristics as those observed in the analysis of MCDB3 data.

A qualitative comparison of corresponding fields derived from scans 4 (KCRI) and 1B (ATD) indicates good agreement between estimated values. That is, similar meteorological features are observed in approximately the same location and their values are comparable. A clear difference in angular resolution and sensitivity is observed, as expected. Analogous to previous comparisons, data from KCRI have a larger footprint (i.e., better sensitivity) and spatial features are narrower in the azimuthal direction (i.e., better azimuthal resolution). Fields of estimates from scan 1B appear to have a smoother texture than corresponding ones from scan 2. This is due to the larger number of available samples to process data from scan 1B (i.e., $M_{DB} = 195$), similar to the previous comparison.

Time-series data from the KCRI radar are reprocessed following a similar methodology as that described in section 4.4 for a fair quantitative comparison with ATD data. The bivariate density maps in Figure 6.7 are computed from these fields using an SNR threshold of 15 dB and illustrate the correlation between estimates derived from both systems. As in Chapter 5, these density maps are approximate probability density functions. The Pearson correlation coefficient r between the estimates is indicated in each sub-figure title. It indicates a significant correlation (i.e., $r > 0.9$) for estimates shown in panels (a) Z_h and (c) Φ_{DP}, a considerable correlation for estimates shown in panel (b) Z_{DR}, and a moderate correlation for estimates shown in panel (d) ρ_{hv}. Significant correlations between corresponding Z_h and Φ_{DP}

estimates are very promising; they verify the effectiveness of the MCDB3 scan 1B to retrieve these variable estimates. Correlation between Z_{DR} estimates is considerable (higher than similar results obtained in Chapter 5), and the bivariate density map is well aligned with the $x = y$ line. There is a larger spread of ρ_{hv} estimates about the $x = y$ line, but estimates from both systems appear be well concentrated in the 0.98–0.99 range. Since the standard deviation of the ρ_{hv} estimator increases
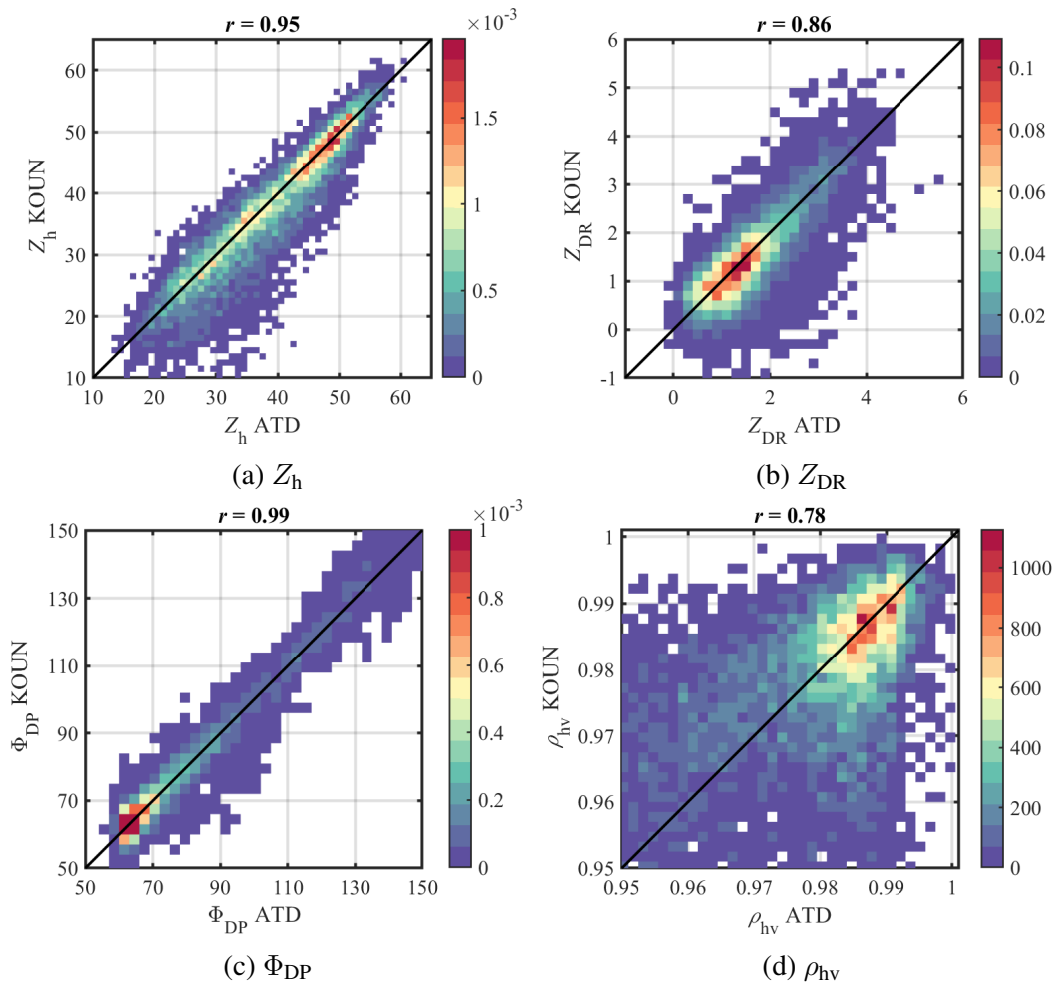
Figure 6.7: Bivariate density maps computed from scans 1B (ATD) and 4 (KCRI). These density maps are normalized to approximate a probability density function. The Pearson correlation coefficient r between the estimates is indicated in each sub-figure title.

from $\sim$0.01 to $\sim$0.04 [11] as the true ρ_{hv} decreases from 0.99 to 0.9 (which are observed in the fields of estimates in Figure 6.6) for $\sigma_{\text{v}} = 2$ m s^{-1} and SNR = 15 dB, it is reasonable to assume this could impact the Pearson correlation between ATD and KCRI fields. Further, although the same noise estimator was used to process both datasets, the radar systems are not the same (e.g., data precision is different). And since the performance of ρ_{hv} is very dependent on the accuracy of estimated noise values for H and V [129], this could also increase the spread of values in the bivariate maps and lower the Pearson correlation. These results are very encouraging and consistent with previous results.

6.4 Chapter 6 Summary

This chapter provides a way to use advanced RPAR scanning techniques to design a CONOPS capable of meeting radar functional requirements. In section 6.1 the RPAR techniques described in chapters 3, 4, and 5 were integrated to operate in conjunction. By jointly utilizing MCS and DB the RPAR's azimuthal resolution is enhanced, and the scan time and/or the variance of estimates can be reduced. The integration of these with FBT exploits dwell flexibility and would enable the use of real-time adaptive scanning techniques to improve data quality. Two *beam types* derived from the integrated techniques were described in section 6.1.1. Digital beamforming in elevation was also exploited in these beam types to scan additional independent beams in elevation. This relaxes the need for very high rotation speeds and provides a way to achieve large scan-time reduction factors.

The RPAR beam types defined in section 6.1.1 are used to design a scanning strategy. The proposed RPAR VCP exploits the techniques introduced in this dissertation and takes 1.06 min to complete. For this VCP to be effective in meeting

the functional requirements, certain tradeoffs must be accounted for in the radar design process. For example, the use of spoiled transmit beams (with digital beam-forming) provides a means to reduce the scan time but it puts more demands on the system design. As discussed previously, one way to compensate for this loss in resolution is to increase the size of the aperture. While this will increase the cost of the system, it is reasonable to assume that a single-face RPAR with a larger aperture would still be more affordable than a 4F-PAR.

The chapter concluded with a demonstration of the MCDB3 beam used for polarimetric weather observations. The MCDB3 beam was implemented such the three elevations sampled simultaneously match the three lowest elevation angles in VCP 212 (i.e., $0.5°$, $0.9°$, $1.3°$). These polarimetric data were calibrated and were compared to data collected with the ATD system sampling the $0.9°$ elevation by mimicking an RR system. Then, a quantitative verification of the results was carried out by comparing the data to that collected with the KCRI system. Key takeaways of this chapter include (1) the techniques presented in this dissertation can be integrated to operate simultaneously, (2) a combination of advanced scanning techniques is needed to achieve the requirements, (3) engineering tradeoffs have to be considered in the RPAR design process to meet the requirements using the proposed CONOPS.

Chapter 7

Epilogue

"We can only see a short distance ahead, but we can see plenty there that needs to be done."

<div align="right">

Alan Turing

</div>

7.1 Summary

This dissertation focused on exploring advanced RPAR scanning techniques in support of meeting future radar functional requirements. A survey of unique PAR capabilities was conducted in Chapter 2 to determine which ones could be exploited under an RPAR CONOPS. Three capabilities were selected for further investigation: beam agility, digital beamforming, and dwell flexibility. The RPARs beam agility was exploited to minimize the beam smearing that results from the rotation of the antenna system over the collection of samples in the coherent processing interval. The use of digital beamforming was discussed as a possible way to reduce the scan time and/or the variance of estimates. The PAR's dwell flexibility capability was explored as a possible way to tailor the scan to meteorological observations with the goal of improving data quality, i.e., increasing the maximum unambiguous velocity (which could reduce the occurrence of aliasing) and reducing the variance

of estimates.

The MCS technique investigated in Chapter 3 provides a way to reduce the RPARs effective beamwidth and potentially meet NOAA/NWS requirements with a smaller antenna aperture than the one that would be needed to achieve the required HPBW if beam smearing is not mitigated. The MCS technique was described and expressions for the MCS pointing angles were provided for the general case with the antenna plane tilted with respect to earth. A theoretical analysis of the impact of MCS on the quality of signal power and copolar correlation coefficient estimates was conducted. This resulted in simple expressions that can be used in the design process of candidate RPAR systems. Through high fidelity RPAR simulations, the effectiveness of MCS in mitigating beam smearing as a function of antenna phase shifter bits, antenna size, and normalized azimuthal sampling was quantified. Further, the impacts of copolar beamsteering biases resulting from the use of MCS were quantified over a large scan sector using simulations and were found to be negligible with respect to stationary operation of the same RPAR. The BMCS CONOPS was implemented on the ATD system to demonstrate the MCS technique. First, a point target located in the vicinity of the ATD system was scanned without electronic beam steering (i.e., mimicking a parabolic-reflector antenna) and with BMCS. This confirmed that the beam pointing accuracy of the BMCS implementation was sufficient to mitigate beam smearing effects. Then, the BMCS CONOPS was demonstrated by scanning meteorological scatterers. Fields of polarimetric-variable estimates from the BMCS CONOPS were compared to those obtained when scanning without beam steering. These results were verified by quantifying absolute radar-variable-estimate differences with respect to a collocated WSR-88D system that has inherently better azimuthal resolution. The BMCS data were shown to produce fields of radar-variable estimates with generally narrower features.

The DB technique introduced in Chapter 4 provides a way to either reduce the scan-update times or to reduce the variance of radar-variable estimates by azimuthally spoiling the transmit beam while receiving multiple digital beams as the radar rotates in azimuth. Specifically, the rotation rate of the platform is derived from the duration of the CPI to produce the desired spatial sampling. This results in beams from subsequent CPIs in approximately the same directions, which increases the number of available data samples for processing. The increased number of available data samples can be coherently processed to reduce the variance of estimates. Alternatively, by reducing the number of samples per CPI and increasing the RPAR's rotation rate, the scan time can be reduced without increasing the variance of estimates. The two-way beam patterns for the narrow and spoiled transmit beams were characterized in terms of the spatial resolution (beamwidth and peak sidelobe levels), and sensitivity. These measurements were used to quantify the impact of using spoiled transmit beams on the data quality, and to provide a calibration procedure for the implementation and testing of the technique. Radar calibration for the DB technique was verified by scanning external targets and comparing the measured power and phases of two-way beams prior-to and post applying the calibration procedure. The DB technique was used to reduce the scan time by collecting two scans of data; one using a two-way narrow beam (for reference) rotating the PAR at $\omega = 4 \; ^\circ \; \mathrm{s}^{-1}$, and the other using the DB technique and collecting comparable data twice as fast. Then, the DB technique was used to reduce the variance of radar-variable estimates. This was accomplished by collecting two scans of data, one using a two-way narrow beam (for reference) rotating the PAR at $\omega = 4 \; ^\circ \; \mathrm{s}^{-1}$, and the other using the DB technique, which produced visibly smoother fields of radar products. Results presented show that the DB technique can be used to reduce the scan time or the variance of radar-variable estimates at the expense of degraded

187

sensitivity and spatial resolution.

The FBT was described and demonstrated in Chapter 5 by exploiting dwell flexibility to scan meteorological echoes with the ATD. Forward-looking beams consist of short-dwell CPIs for which the steering angles are ahead of the radar rotation and are designed to provide sufficient surveillance information about upcoming potential regions of interest. Back-scanning beams consist of longer dwell CPIs for which steering angles are less or equal than those from forward-looking beams and are designed to provide high-quality weather observations. An application of the FB-CONOPS was used to illustrate potential benefits of this technique. In this application, FBT eliminates the need for split cuts used in the WSR-88D VCPs, whereby the antenna scans the same elevation angle twice to obtain unambiguous range and Doppler velocity measurements. That is, dwell definitions for the forward-looking and back-scanning beams were set equal to those in the lowest elevation surveillance and Doppler scans of VCP 212, respectively. This resulted in the collection of surveillance and Doppler scan data in one revolution of the antenna. Further, the DB technique was used with the forward-looking beams to reduce the scan time. Time-series data from a collocated WSR-88D system were reprocessed in a commensurate way to evaluate the performance of the FBT data collected with the ATD system. A quantitative analysis of corresponding fields of polarimetric radar-variable estimates indicated significant correlation between fields of Z_h, v_r, and Φ_DP, and considerable correlation between fields of Z_DR and ρ_hv. This verified the implementation of the FBT on the ATD. An implementation of the FBT under an adaptive scanning CONOPS was emulated. A simple adaptive FBT algorithm was described, and results were quantified using theoretical expressions for the standard deviation of Z_h and v_r estimates. Finally, a discussion about the potential of using adaptive scanning to reduce the update times was presented.

In Chapter 6, the techniques introduced were integrated and used to design an RPAR VCP. By jointly utilizing MCS and DB the RPAR's azimuthal resolution is enhanced and the scan time and/or the variance of estimates can be reduced. The integration of these with FBT exploits dwell flexibility and enables the use of real-time adaptive scanning techniques to improve the data quality. Two beam types derived from the integrated techniques were defined. Digital beamforming in elevation was also exploited in these beam types to scan additional independent beams in elevation. The MCDB3 and FB3 beams are used as building blocks to design an RPAR VCP that takes approximately 1 minute to complete. For this VCP to be effective in meeting the functional requirements, certain tradeoffs must be accounted for in the radar design process. The MCDB3 beam was implemented on the ATD such the three elevations sampled simultaneously match the three lowest elevation angles sampled in VCP 212 (i.e., 0.5°, 0.9°, 1.3°). Polarimetric weather data were collected using the MCDB3 beam and a quantitative verification of the results was carried out by comparing this data to that collected with a collocated WSR-88D.

7.2   Conclusions

The MCS technique is capable of enhancing azimuthal resolution of the RPAR and has shown to be feasible for polarimetric weather radar observations. The technique could be integrated with other advanced complementary techniques (e.g., BMX [24], ADAPTS [23], range oversampling [130]) to attain the performance levels required to meet radar functional requirements. It was demonstrated that for relatively large planar RPARs, 6-bit phase shifters provide sufficient pointing accuracy to effectively implement MCS and mostly mitigate beam smearing, while 7-bit

phase-shifters would be desirable to largely eliminate smearing effects. Further, the impacts of copolar beamsteering biases resulting from the use of MCS were quantified over a large scan sector using simulations and were found to be negligible with respect to stationary operation of the same RPAR. If the pointing accuracy of antenna elements were insufficient, the RPAR would be unable to accurately sample concentric resolution volumes using MCS. While increasing the number of bits per antenna element may increase system cost, it is likely that increasing the antenna aperture (i.e., for an equivalent effective beamwidth) would be more costly.

The DB technique may allow an RPAR-based CONOPS to meet future radar requirements if certain obtainable considerations are incorporated into the basic radar design process. Results presented show that the DB technique can be used to reduce the scan time or the variance of radar-variable estimates, at the expense of degraded sensitivity and spatial resolution (compared to using narrow pencil beams with the same antenna aperture size). To achieve large scan-time reduction factors using the DB technique, the azimuthal rotation speed has to be increased by the desired reduction factor. Considering the mechanical rotation machinery has a high technology-readiness level, achieving higher rotation speeds with this well-known pedestal technology reduces the risk of designing, building, and deploying RPAR systems with higher maximum rotation speeds. Nevertheless, since larger aperture sizes may be needed to compensate the spatial resolution degradation resulting from the use of spoiled transmit beams, it could be challenging to achieve high rotation rates with a larger and heavier antenna. Achieving high reduction factors (e.g., $R_F = 5$) may be challenging due to the required rotation speeds, consider that an operational implementation can be designed using a small time-reduction factor (e.g., $R_F = 2$). This relatively low increase in the rotation speed would reduce the scan time by a factor of 2, with relatively modest demands on mechanical rotators.

190

This could also result in a relatively smaller increase in the aperture size required to meet two-way sidelobe requirements given that a narrower spoiled transmit beam would be used. That is, RPARs that are specifically designed to exploit the use of spoiled transmit beams should account for the increased two-way sidelobe levels to meet the requirements. While this may require increasing the aperture, it also allows for advanced techniques (such as DB) that support meeting demanding requirements with an affordable architecture (compared to the stationary four-faced PAR). A possible consideration is to design an aperture that meets the beamwidth requirements when using narrow beams and increase the size of the receive aperture only to lower sidelobe levels of two-way beams using spoiled transmit tapers. Another alternative is to define an operational mode in which spatial resolution and sensitivity degradations resulting from the use of the DB technique are an acceptable tradeoff to reduce the scan time or the variance of radar-variable estimates.

The FBT could be used to improve data quality under an adaptive scanning CONOPS and to reduce the scan time when coupled with the DB technique for the forward-looking beams. The demonstration of the FB-CONOPS shows that it is possible to implement MCS at steering angles away from the broadside and to produce calibrated radar-variable estimates without apparent radar sampling artifacts caused by MCS. The adaptive FBT algorithm emulated in this dissertation, shows that information from forward-looking beams could be used to decide if there are significant weather echoes in upcoming beam positions, to determine the maximum range of storms observed, and shorten the PRTs of back-scanning beams to match the unambiguous range with that of the maximum range of observed storms (increasing the Nyquist co-interval).

Finally, if certain considerations are incorporated into the basic radar design process, the FB3 and the MCDB3 beams could be implemented to reduce the scan

time to ~1 minute while meeting other radar functional radar requirements. Data produced with the RPAR VCP presented were well correlated with data from a co-located WSR-88D, despite radar system differences. This key result indicates that single-face RPAR's with sufficient capabilities could, in principle, achieve optimal requirements. This RPAR would require a larger aperture than a single-face of a 4F-PAR that meets optimal requirements to compensate for increased beamwidth and sidelobe levels; it would need to support increased sensitivity either by increasing the peak power per antenna element or being able to transmit longer pulse-compression waveforms (i.e., higher duty cycle); and it would need to rotate at speeds comparable to those of the current WSR-88D. Further, it would need to support digital beamforming capabilities to produce a total of 9 simultaneous dual-polarization beams, within relatively narrow spoiled beam factors in azimuth and elevation. In summary, by simultaneously exploiting advanced RPAR capabilities and incorporating certain tradeoffs in the radar design process, it is possible to design RPAR CONOPS capable of achieving demanding radar functional requirements. It is expected that the outcome of this research effort will provide valuable information that can support the design of the future U.S. weather surveillance radar network.

7.3 Future Work

The initial investigation of RPAR capabilities and CONOPS provided in this dissertation is the first step in the direction of exploring possibilities with rotating arrays for polarimetric weather observations. Promising results indicate that further RPAR research would be valuable to explore the feasibility of this architecture in meeting future NWS observational needs. That is, research efforts should be focused

on developing other advanced RPAR scanning techniques, integrating these techniques with existing ones, and exploring RPAR architectures that could support the advanced capabilities required to meet the requirements. Answers to these fundamental questions will be critical to inform NOAA's decision when considering the RPAR architecture as the radar for the future U.S. Weather Surveillance Network.

The flexibility of PAR technology can be exploited in many ways to reduce the scan time or improve the quality of radar-variable estimates. An alternative technique that could be used to reduce the RPAR's scan time involves the use of concatenated pulse transmissions in multiple directions, followed by simultaneous reception and processing of the digitally formed beams. The Multi-Beam Technique (MBT) can be used to achieve a scan-time reduction factor proportional to the number of digitally formed beams [121]. This could be integrated with MCS, and possibly also with the DB technique. Key challenges with the MBT are the suppression of unwanted mainlobe-sidelobe coupling signals and the cross-polar contamination of H and V polarizations as the beams are steered far away from the principal planes. Furthermore, the MBT technique relies on the transmission of temporally concatenated pulses, and thus, may limit the use of long pulse-compression waveforms to achieve sensitivity requirements. Pulse compression would require a significant increase in the duty cycle requirements (proportional to the number of beams transmitted), and long blind ranges would need to be mitigated. A demonstration that the MBT can be used for polarimetric observations and without increased sidelobe interference is critical in validating that meteorological PAR can achieve the desired rapid volume scanning without impacting the quality of its observations [131].

Adaptive scanning algorithms for RPAR could lead to improved data quality or even reduced scan-update times. A comprehensive investigation of potential adaptive scanning techniques compatible with the RPAR architecture has to be con-

ducted. A first step could involve the use of high-fidelity simulations to evaluate adaptive scanning techniques exercising different tradeoffs, and their impact on the scan time, spatial sampling, or the quality of estimates. The FB-CONOPS could serve as the basis for studying these adaptive scanning techniques, and their potential benefits in terms of meeting future radar functional requirements. The next step could involve the development and implementation of a real-time scheduler capable of supporting an adaptive CONOPS. One of the main challenges for the use of adaptive scanning techniques with RPAR is the constantly changing set of beam positions to be scanned. That is, the limited visible region of a PAR antenna coupled with the mechanical rotation of the RPAR's pedestal limits the available time an adaptive algorithm has to operate on meteorological echoes of interest. As indicated in this dissertation, slow rotation speeds will favor the use of adaptive techniques.

A critical element for the deployment of an affordable network of RPARs is the design of a specific radar architecture that supports the CONOPS. That is, with a few candidate RPAR CONOPS capable of meeting the requirements, an evaluation of the most cost-effective implementation for the RPAR system that supports the CONOPS must be pursued. One of the open questions is related to the aperture size that would be required to meet spatial resolution requirements as a function of the CONOPS. While the use of MCS leads to a reduction in the size of the aperture that meets angular requirements, the use of digital beamforming (and techniques such as DB) increases it. These techniques counteract each other (i.e., one reduces the effective HPBW, the other one increases it), therefore, it is important to consider both effects when designing a specific RPAR architecture to meet the RFR. Further, several channels are needed to form multiple simultaneous receive beams. Depending on the number of simultaneous beams needed, the architecture could be based

on overlapped sub-arrays in two dimensions [33] (such as the ATD), overlapped sub-arrays in one dimension and digital channels in the other, or a fully digital array [132, 133]. The level of digitization will be dictated by the functional radar requirements and the capabilities needed to implement the CONOPS. Rigorous research on potential RPAR architectures and their associated CONOPS, capable of meeting the demanding functional requirements will be of high value.

References

[1] D. S. Zrnic and A. V. Ryzhkov, "Polarimetry for Weather Surveillance Radars," *Bulletin of the American Meteorological Society*, vol. 80, no. 3, pp. 389–406, Mar. 1999. DOI: 10.1175/1520-0477(1999)080⟨0389:PFWSR⟩2.0.CO;2.

[2] J. M. Straka, D. S. Zrnić, and A. V. Ryzhkov, "Bulk Hydrometeor Classification and Quantification Using Polarimetric Radar Data: Synthesis of Relations," *Journal of Applied Meteorology*, vol. 39, no. 8, pp. 1341–1372, Aug. 2000. DOI: 10.1175/1520-0450(2000)039⟨1341:BHCAQU⟩2.0.CO;2.

[3] H. S. Park, A. V. Ryzhkov, D. S. Zrnić, and K.-E. Kim, "The Hydrometeor Classification Algorithm for the Polarimetric WSR-88D: Description and Application to an MCS," *Weather and Forecasting*, vol. 24, no. 3, pp. 730–748, Jun. 2009. DOI: 10.1175/2008WAF2222205.1.

[4] R. A. Brown, V. T. Wood, and D. Sirmans, "Improved Tornado Detection Using Simulated and Actual WSR-88D Data with Enhanced Resolution," *Journal of Atmospheric and Oceanic Technology*, vol. 19, no. 11, pp. 1759–1771, Nov. 2002. DOI: 10.1175/1520-0426(2002)019⟨1759:ITDUSA⟩2.0.CO;2.

[5]   I. R. Ivić, D. S. Zrnić, and T.-Y. Yu, "The Use of Coherency to Improve Signal Detection in Dual-Polarization Weather Radars," *Journal of Atmospheric and Oceanic Technology*, vol. 26, no. 11, pp. 2474–2487, Nov. 2009. DOI: 10.1175/2009JTECHA1154.1.

[6]   I. R. Ivić, C. Curtis, and S. M. Torres, "Radial-Based Noise Power Estimation for Weather Radars," *Journal of Atmospheric and Oceanic Technology*, vol. 30, no. 12, pp. 2737–2753, Dec. 2013. DOI: 10.1175/JTECH-D-13-00008.1.

[7]   S. M. Torres and D. A. Warde, "Ground Clutter Mitigation for Weather Radars Using the Autocorrelation Spectral Density," *Journal of Atmospheric and Oceanic Technology*, vol. 31, no. 10, pp. 2049–2066, Oct. 2014. DOI: 10.1175/JTECH-D-13-00117.1.

[8]   J. M. Kurdzo, E. R. Williams, D. J. Smalley, B. J. Bennett, D. C. Patterson, M. S. Veillette, and M. F. Donovan, "Polarimetric Observations of Chaff Using the WSR-88D Network," *Journal of Applied Meteorology and Climatology*, vol. 57, no. 5, pp. 1063–1081, Apr. 2018. DOI: 10.1175/JAMC-D-17-0191.1.

[9]   D. Schvartzman and C. D. Curtis, "Signal processing and radar characteristics (sparc) simulator: A flexible dual-polarization weather-radar signal simulation framework based on preexisting radar-variable data," *IEEE Journal of Selected Topics in Applied Earth Observations and Remote Sensing*, vol. 12, no. 1, pp. 135–150, Jan. 2019. DOI: 10.1109/JSTARS.2018.2885614.

[10] I. R. Ivić, "A Simple Hybrid Technique to Reduce Bias of Copolar Correlation Coefficient Estimates," *Journal of Atmospheric and Oceanic Technology*, vol. 36, no. 9, pp. 1813–1833, Sep. 2019. DOI: 10.1175/JTECH-D-18-0226.1.

[11] D. Schvartzman, S. M. Torres, and D. Warde, "The Hybrid-Scan Estimators: Exploiting WSR-88D Split Cuts to Improve the Quality of Polarimetric-Variable Estimates," *Journal of Atmospheric and Oceanic Technology*, vol. 37, no. 2, pp. 299–315, Jan. 2020. DOI: 10.1175/JTECH-D-19-0071.1.

[12] F. Nai, J. Boettcher, C. Curtis, D. Schvartzman, and S. Torres, "The Impact of Elevation Sidelobe Contamination on Radar Data Quality for Operational Interpretation," *Journal of Applied Meteorology and Climatology*, vol. 59, no. 4, pp. 707–724, Apr. 2020. DOI: 10.1175/JAMC-D-19-0092.1.

[13] K. M. Simmons and D. Sutter, "WSR-88D radar, tornado warning, and tornado casualties," vol. 20, pp. 301–310, 2005.

[14] C. NEXRAD, N. Council, D. Studies, and B. Climate, *Weather Radar Technology Beyond NEXRAD*. National Academies Press, 2002.

[15] R. M. Steadham, R. A. Brown, and V. T. Wood, "Prospects for faster and denser WSR-88D scanning strategies," in *18th Int. Conf. on Interactive Information and Processing Systems (IIPS) for Meteorology, Oceanography, and Hydrology*, Orlando, FL, Amer. Meteor. Soc., J3.16, 2002.

[16] P. L. Heinselman and S. Torres, "High-Temporal-Resolution Capabilities of the National Weather Radar Testbed Phased-Array Radar," *J. Appl. Meteor. and Climatology*, vol. 50, pp. 579–593, 2011.

[17] P. L. Heinselman, D. L. Priegnitz, K. L. Manross, T. M. Smith, and R. W. Adams, "Rapid Sampling of Severe Storms by the National Weather Radar Testbed Phased Array Radar," *Weather and Forecasting*, vol. 23, no. 5, pp. 808–824, Oct. 2008. DOI: 10.1175/2008WAF2007071.1.

[18] K. A. Wilson, P. L. Heinselman, C. M. Kuster, D. M. Kingfield, and Z. Kang, "Forecaster Performance and Workload: Does Radar Update Time Matter?" *Weather and Forecasting*, vol. 32, no. 1, pp. 253–274, Jan. 2017. DOI: 10.1175/WAF-D-16-0157.1.

[19] K. Hondl and M. Weber, "Noaa's meteorological phased array radar research program," in *2019 IEEE International Symposium on Phased Array System & Technology (PAST)*, IEEE, 2019, pp. 1–6.

[20] M. E. Weber, "Meteorological phased array radar research at noaa's national severe storms laboratory," in *2019 IEEE International Conference on Microwaves, Antennas, Communications and Electronic Systems (COMCAS)*, Nov. 2019, pp. 1–6. DOI: 10.1109/COMCAS44984.2019.8958067.

[21] D. S. Zrnic, J. F. Kimpel, D. E. Forsyth, A. Shapiro, G. Crain, R. Ferek, J. Heimmer, W. Benner, F. T. J. McNellis, and R. J. Vogt, "Agile-Beam Phased Array Radar for Weather Observations," *Bulletin of the American Meteorological Society*, vol. 88, no. 11, pp. 1753–1766, Nov. 2007. DOI: 10.1175/BAMS-88-11-1753.

[22] R. L. Haupt and Y. Rahmat-Samii, "Antenna array developments: A perspective on the past, present and future," *IEEE Antennas and Propagation Magazine*, vol. 57, no. 1, pp. 86–96, Feb. 2015. DOI: 10.1109/MAP.2015.2397154.

[23] S. M. Torres, R. Adams, C. D. Curtis, E. Forren, D. E. Forsyth, I. R. Ivić, D. Priegnitz, J. Thompson, and D. A. Warde, "Adaptive-weather-surveillance and multifunction capabilities of the national weather radar testbed phased array radar," *Proceedings of the IEEE*, vol. 104, no. 3, pp. 660–672, Mar. 2016. DOI: 10.1109/JPROC.2015.2484288.

[24] T.-Y. Yu, M. B. Orescanin, C. D. Curtis, D. S. Zrnić, and D. E. Forsyth, "Beam Multiplexing Using the Phased-Array Weather Radar," *Journal of Atmospheric and Oceanic Technology*, vol. 24, no. 4, pp. 616–626, Apr. 2007. DOI: 10.1175/JTECH2052.1.

[25] H. B. Bluestein, M. M. French, I. PopStefanija, R. T. Bluth, and J. B. Knorr, "A Mobile, Phased-Array Doppler Radar For The Study of Severe Convective Storms: THE MWR-05XP," *Bulletin of the American Meteorological Society*, vol. 91, no. 5, pp. 579–600, May 2010. DOI: 10.1175/2009BAMS2914.1.

[26] J. Wurman, D. Dowell, Y. Richardson, P. Markowski, E. Rasmussen, D. Burgess, L. Wicker, and H. B. Bluestein, "The Second Verification of the Origins of Rotation in Tornadoes Experiment: VORTEX2," *Bulletin of the American Meteorological Society*, vol. 93, no. 8, pp. 1147–1170, Aug. 2012. DOI: 10.1175/BAMS-D-11-00010.1.

[27] C. A. Kerr and X. Wang, "Ensemble-Based Targeted Observation Method Applied to Radar Radial Velocity Observations on Idealized Supercell Low-Level Rotation Forecasts: A Proof of Concept," *Monthly Weather Review*, vol. 148, no. 3, pp. 877–890, Feb. 2020. DOI: 10.1175/MWR-D-19-0197.1.

[28] D. E. Forsyth, J. F. Kimpel, D. S. Zrnic, R. Ferek, J. F. Heimmer, T. McNellis, J. E. Crain, A. M. Shapiro, J. D. Belville, and W. Benner, "2.8 building the national weather radar testbed phased-array," 2003.

[29] D. E. Forsyth, J. F. Kimpel, D. S. Zrnic, R. Ferek, J. F. Heimmer, T. McNellis, J. E. Crain, A. M. Shapiro, R. J. Vogt, and W. Benner, "The national weather radar testbed (phased-array)," in *32nd Conference on Radar Meteorology*, 2005, pp. 24–29.

[30] D. E. Forsyth, J. F. Kimpel, D. S. Zrnic, R. Ferek, J. F. Heimmer, T. McNellis, J. E. Crain, A. M. Shapiro, R. J. Vogt, and W. Benner, "Progress report on the National Weather Radar Testbed (phased-array) becomes operational," in *21st Int. Conf. on Interactive Information and Processing Systems (IIPS) for Meteorology, Oceanography, and Hydrology*, ser. San Diego, CA, Amer. Meteor. Soc., CD-ROM, 19.5, 2005.

[31] D. Zrnic, V. Melnikov, and R. Doviak, "Issues and challenges for polarimetric measurement of weather with an agile beam phased array radar," Tech. Rep., 2012, p. 117.

[32] J. E. Stailey and K. D. Hondl, "Multifunction phased array radar for aircraft and weather surveillance," *Proceedings of the IEEE*, vol. 104, no. 3, pp. 649–659, Mar. 2016. DOI: 10.1109/JPROC.2015.2491179.

[33] M. D. Conway, D. D. Russel, A. Morris, and C. Parry, "Multifunction phased array radar advanced technology demonstrator nearfield test results," in *2018 IEEE Radar Conference (RadarConf18)*, Apr. 2018, pp. 1412–1415. DOI: 10.1109/RADAR.2018.8378771.

[34] S. Torres, T. Buckman, C. Curtis, E. Forren, S. Gregg, I. Ivic, R. Mendoza, D. Schvartzman, C. Schwarz, D. Wasielewski, *et al.*, "Towards an operational demonstration of the first full-scale polarimetric phased-array radar," in *39th International Conference on Radar Meteorology*, 2019.

[35] S. M. Torres, C. D. Curtis, and D. Schvartzman, "Requirement-Driven Design of Pulse Compression Waveforms for Weather Radars," *Journal of Atmospheric and Oceanic Technology*, vol. 34, no. 6, pp. 1351–1369, Jun. 2017. DOI: 10.1175/JTECH-D-16-0231.1.

[36] D. Schvartzman and S. Torres, "Design of practical pulse compression waveforms for polarimetric phased array radar. preprints," in *39th International Conference on Radar Meteorology*, 2019.

[37] J. S. Herd, S. M. Duffy, and H. Steyskal, "Design considerations and results for an overlapped subarray radar antenna," in *2005 IEEE Aerospace Conference*, Mar. 2005, pp. 1087–1092. DOI: 10.1109/AERO.2005.1559399.

[38] NOAA/NWS, "Radar functional requirement," NOAA/NWS Internal Rep., Tech. Rep., 2015.

[39] B. Palumbo and A. Cucci, "Array antenna with multiple, independently scanned beams for a 3d radar," in *1977 Antennas and Propagation Society*

International Symposium, vol. 15, Jun. 1977, pp. 185–188. DOI: 10.1109/ APS.1977.1147771.

[40] B. Palumbo, "Some examples of systems developments in italy based on phased array technology," in *Proceedings of International Symposium on Phased Array Systems and Technology*, Oct. 1996, pp. 444–449. DOI: 10. 1109/PAST.1996.566134.

[41] E. Brookner, "Phased array radars-past, present and future," in *RADAR 2002*, Oct. 2002, pp. 104–113. DOI: 10.1109/RADAR.2002.1174663.

[42] E. Yoshikawa, T. Ushio, Z. Kawasaki, S. Yoshida, T. Morimoto, F. Mizu- tani, and M. Wada, "Mmse beam forming on fast-scanning phased array weather radar," *IEEE Transactions on Geoscience and Remote Sensing*, vol. 51, no. 5, pp. 3077–3088, May 2013. DOI: 10.1109/TGRS.2012. 2211607.

[43] T. Ushio, S. Shimamura, T. Wu, H. Kikuchi, E. Yoshikawa, F. Mizutani, M. Wada, S. Satoh, and T. Iguchi, "Development and observation of the phased array radar at x band," in *2014 XXXIth URSI General Assembly and Scientific Symposium (URSI GASS)*, Aug. 2014, pp. 1–4. DOI: 10.1109/ URSIGASS.2014.6929643.

[44] J. M. Kurdzo, F. Nai, D. J. Bodine, T. A. Bonin, R. D. Palmer, B. L. Cheong, J. Lujan, A. Mahre, and A. D. Byrd, "Observations of Severe Local Storms and Tornadoes with the Atmospheric Imaging Radar," *Bulletin of the Amer- ican Meteorological Society*, vol. 98, no. 5, pp. 915–935, May 2017. DOI: 10.1175/BAMS-D-15-00266.1.

[45]   K. A. Orzel and S. J. Frasier, "Weather observation by an electronically scanned dual-polarization phase-tilt radar," *IEEE Transactions on Geoscience and Remote Sensing*, vol. 56, no. 5, pp. 2722–2734, May 2018. DOI: 10.1109/TGRS.2017.2782480.

[46]   I. Ivić and D. Schvartzman, "A first look at the atd data corrections. preprints," in *39th International Conference on Radar Meteorology*, 2019, pp. 2–06.

[47]   I. R. Ivić and D. Schvartzman, "Weather calibration efforts on the advanced technology demonstrator," in *100th American Meteorological Society Annual Meeting*, AMS, 2020.

[48]   L. Lei, G. Zhang, R. J. Doviak, and S. Karimkashi, "Comparison of theoretical biases in estimating polarimetric properties of precipitation with weather radar using parabolic reflector, or planar and cylindrical arrays," *IEEE Transactions on Geoscience and Remote Sensing*, vol. 53, no. 8, pp. 4313–4327, Aug. 2015. DOI: 10.1109/TGRS.2015.2395714.

[49]   C. Fulton, J. L. Salazar, Y. Zhang, G. Zhang, R. Kelly, J. Meier, M. McCord, D. Schmidt, A. D. Byrd, L. M. Bhowmik, S. Karimkashi, D. S. Zrnic, R. J. Doviak, A. Zahrai, M. Yeary, and R. D. Palmer, "Cylindrical polarimetric phased array radar: Beamforming and calibration for weather applications," *IEEE Transactions on Geoscience and Remote Sensing*, vol. 55, no. 5, pp. 2827–2841, May 2017. DOI: 10.1109/TGRS.2017.2655023.

[50]   M. E. Weber, J. Y. N. Cho, and H. G. Thomas, "Command and control for multifunction phased array radar," *IEEE Transactions on Geoscience and*

Remote Sensing, vol. 55, no. 10, pp. 5899–5912, 2017. DOI: 10.1109/TGRS. 2017.2716935.

[51]   M. Sachidananda and D. S. Zrnic, "Systematic Phase Codes for Resolving Range Overlaid Signals in a Doppler Weather Radar," *Journal of Atmospheric and Oceanic Technology*, vol. 16, no. 10, pp. 1351–1363, Oct. 1999. DOI: 10.1175/1520-0426(1999)016⟨1351:SPCFRR⟩2.0.CO;2.

[52]   R. J. Doviak and D. Zrnic, *Doppler radar and weather observations*. Courier Corporation, 2006.

[53]   M. R. Kumjian and A. V. Ryzhkov, "Polarimetric Signatures in Supercell Thunderstorms," *Journal of Applied Meteorology and Climatology*, vol. 47, no. 7, pp. 1940–1961, Jul. 2008. DOI: 10.1175/2007JAMC1874.1.

[54]   I. R. Ivić, "Options for polarimetrie variable measurements on the mpar advanced technology demonstrator," in *2018 IEEE Radar Conference (RadarConf18)*, Apr. 2018, pp. 0129–0134. DOI: 10.1109/RADAR.2018.8378544.

[55]   C. Fulton, J. Salazar, D. Zrnic, D. Mirkovic, I. Ivic, and D. Doviak, "Polarimetrie phased array calibration for large-scale multi-mission radar applications," in *2018 IEEE Radar Conference (RadarConf18)*, Apr. 2018, pp. 1272–1277. DOI: 10.1109/RADAR.2018.8378746.

[56]   I. Ivić, C. Curtis, E. Forren, R. Mendoza, D. Schvartzman, S. Torres, D. J. Wasielewski, and F. A. Zahrai, "An overview of weather calibration for the advanced technology demonstrator," in *2019 IEEE International Sympo-*

sium on Phased Array System Technology (PAST), Oct. 2019, pp. 1–7. DOI: 10.1109/PAST43306.2019.9021053.

[57] I. R. Ivić, "Effects of phase coding on doppler spectra in ppar weather radar," *IEEE Transactions on Geoscience and Remote Sensing*, vol. 56, no. 4, pp. 2043–2065, Apr. 2018. DOI: 10.1109/TGRS.2017.2772962.

[58] S. D. Blunt and E. L. Mokole, "Overview of radar waveform diversity," *IEEE Aerospace and Electronic Systems Magazine*, vol. 31, no. 11, pp. 2–42, Nov. 2016. DOI: 10.1109/MAES.2016.160071.

[59] F. O'Hora and J. Bech, "Improving weather radar observations using pulse-compression techniques," *Meteorological Applications*, vol. 14, no. 4, pp. 389–401, 2007. DOI: 10.1002/met.38.

[60] B. L. Cheong, R. Kelley, R. D. Palmer, Y. Zhang, M. Yeary, and T. Yu, "Px-1000: A solid-state polarimetric x-band weather radar and time–frequency multiplexed waveform for blind range mitigation," *IEEE Transactions on Instrumentation and Measurement*, vol. 62, no. 11, pp. 3064–3072, Nov. 2013. DOI: 10.1109/TIM.2013.2270046.

[61] J. M. Kurdzo, B. L. Cheong, R. D. Palmer, G. Zhang, and J. B. Meier, "A Pulse Compression Waveform for Improved-Sensitivity Weather Radar Observations," *Journal of Atmospheric and Oceanic Technology*, vol. 31, no. 12, pp. 2713–2731, Dec. 2014. DOI: 10.1175/JTECH-D-13-00021.1.

[62] G. Brylev, V. Melnikov, N. Mikhailov, G. Schukin, and I. Tarabukin, "Current state of radar meteorology in russia," *COST 75 Weather Radar Systems*, pp. 11–18, 1995.

[63] A. L. Pazmany, J. B. Mead, H. B. Bluestein, J. C. Snyder, and J. B. Houser, "A Mobile Rapid-Scanning X-band Polarimetric (RaXPol) Doppler Radar System," *Journal of Atmospheric and Oceanic Technology*, vol. 30, no. 7, pp. 1398–1413, Jul. 2013. DOI: 10.1175/JTECH-D-12-00166.1.

[64] B. Laird, "On ambiguity resolution by random phase processing(of cluttered meteorological radar signals)," in *Conference on Radar Meteorology, 20 th, Boston, MA*, 1981, pp. 327–331.

[65] D. Zrinc and P. Mahapatra, "Two methods of ambiguity resolution in pulse doppler weather radars," *IEEE Transactions on Aerospace and Electronic Systems*, vol. AES-21, no. 4, pp. 470–483, Jul. 1985. DOI: 10.1109/TAES.1985.310635.

[66] C. Frush, R. J. Doviak, M. Sachidananda, and D. S. Zrnić, "Application of the SZ Phase Code to Mitigate Range–Velocity Ambiguities in Weather Radars," *Journal of Atmospheric and Oceanic Technology*, vol. 19, no. 4, pp. 413–430, Apr. 2002. DOI: 10 . 1175 / 1520 - 0426(2002) 019⟨0413 : AOTSPC⟩2.0.CO;2.

[67] I. R. Ivić and R. J. Doviak, "Evaluation of phase coding to mitigate differential reflectivity bias in polarimetric par," *IEEE Transactions on Geoscience and Remote Sensing*, vol. 54, no. 1, pp. 431–451, Jan. 2016. DOI: 10.1109/TGRS.2015.2459047.

[68] I. R. Ivić, "Phase code to mitigate the copolar correlation coefficient bias in ppar weather radar," *IEEE Transactions on Geoscience and Remote Sensing*, vol. 55, no. 4, pp. 2144–2166, Apr. 2017. DOI: 10.1109/TGRS.2016. 2637720.

[69] R. J. Doviak, V. Bringi, A. Ryzhkov, A. Zahrai, and D. Zrnić, "Considerations for Polarimetric Upgrades to Operational WSR-88D Radars," *Journal of Atmospheric and Oceanic Technology*, vol. 17, no. 3, pp. 257–278, Mar. 2000. DOI: 10.1175/1520-0426(2000)017⟨0257:CFPUTO⟩2.0.CO;2.

[70] V. M. Melnikov and D. Zrnic, "Simultaneous transmission mode for the polarimetric wsr-88d: Statistical biases and standard deviations of polarimetric variables," Tech. Rep., 2004, pp. 1–84.

[71] A. V. Ryzhkov, T. J. Schuur, D. W. Burgess, P. L. Heinselman, S. E. Giangrande, and D. S. Zrnic, "The Joint Polarization Experiment: Polarimetric Rainfall Measurements and Hydrometeor Classification," *Bulletin of the American Meteorological Society*, vol. 86, no. 6, pp. 809–824, Jun. 2005. DOI: 10.1175/BAMS-86-6-809.

[72] A. Hopf, J. Bourgeois, P. Drake, and T. Flynn, "Raytheon polarimetric x-band phased array radar: Single and netted radar system," *Amer. Meteor. Soc. Annual Mtg*, 2015.

[73] H. Kikuchi, T. Suezawa, T. Ushio, N. Takahashi, H. Hanado, K. Nakagawa, M. Osada, T. Maesaka, K. Iwanami, K. Yoshimi, F. Mizutani, M. Wada, and Y. Hobara, "Initial observations for precipitation cores with x-band dual polarized phased array weather radar," *IEEE Transactions on Geoscience*

and Remote Sensing, vol. 58, no. 5, pp. 3657–3666, May 2020. DOI: 10.
1109/TGRS.2019.2959628.

[74] D. Zrnić, R. Doviak, G. Zhang, and A. Ryzhkov, "Bias in Differential Reflectivity due to Cross Coupling through the Radiation Patterns of Polarimetric Weather Radars," *Journal of Atmospheric and Oceanic Technology*, vol. 27, no. 10, pp. 1624–1637, Oct. 2010. DOI: 10.1175/2010JTECHA1350.1.

[75] V. Chandrasekar and R. J. Keeler, "Antenna Pattern Analysis and Measurements for Multiparameter Radars," *Journal of Atmospheric and Oceanic Technology*, vol. 10, no. 5, pp. 674–683, Oct. 1993. DOI: 10.1175/1520-0426(1993)010⟨0674:APAAMF⟩2.0.CO;2.

[76] A. L. Pazmany, J. C. Galloway, J. B. Mead, I. Popstefanija, R. E. McIntosh, and H. W. Bluestein, "Polarization Diversity Pulse-Pair Technique for Millimeter-WaveDoppler Radar Measurements of Severe Storm Features," *Journal of Atmospheric and Oceanic Technology*, vol. 16, no. 12, pp. 1900–1911, Dec. 1999. DOI: 10.1175/1520-0426(1999)016⟨1900:PDPPTF⟩2.0.CO;2.

[77] V. M. Melnikov and D. S. Zrnić, "On the Alternate Transmission Mode for Polarimetric Phased Array Weather Radar," *Journal of Atmospheric and Oceanic Technology*, vol. 32, no. 2, pp. 220–233, Feb. 2015. DOI: 10.1175/JTECH-D-13-00176.1.

[78] M. Sachidananda and D. S. Zrnić, "Efficient Processing of Alternately Polarized Radar Signals," *Journal of Atmospheric and Oceanic Technology*,

vol. 6, no. 1, pp. 173–181, Feb. 1989. DOI: 10.1175/1520-0426(1989) 006⟨0173:EPOAPR⟩2.0.CO;2.

[79] C. M. Kuster, J. C. Snyder, T. J. Schuur, T. T. Lindley, P. L. Heinselman, J. C. Furtado, J. W. Brogden, and R. Toomey, "Rapid-Update Radar Observations of ZDR Column Depth and Its Use in the Warning Decision Process," *Weather and Forecasting*, vol. 34, no. 4, pp. 1173–1188, Aug. 2019. DOI: 10.1175/WAF-D-19-0024.1.

[80] P. Barton, "Digital beam forming for radar," *IEE Proceedings F - Communications, Radar and Signal Processing*, vol. 127, no. 4, pp. 266–277, Aug. 1980. DOI: 10.1049/ip-f-1:19800041.

[81] H. Steyskal, "Digital beamforming-an emerging technology," in *MILCOM 88, 21st Century Military Communications - What's Possible?'. Conference record. Military Communications Conference*, Oct. 1988, 399–403 vol.2. DOI: 10.1109/MILCOM.1988.13422.

[82] M. Chryssomallis, "Smart antennas," *IEEE Antennas and Propagation Magazine*, vol. 42, no. 3, pp. 129–136, Jun. 2000. DOI: 10.1109/74.848965.

[83] B. D. Van Veen and K. M. Buckley, "Beamforming: A versatile approach to spatial filtering," *IEEE ASSP Magazine*, vol. 5, no. 2, pp. 4–24, Apr. 1988. DOI: 10.1109/53.665.

[84] S. H. Talisa, K. W. O'Haver, T. M. Comberiate, M. D. Sharp, and O. F. Somerlock, "Benefits of digital phased array radars," *Proceedings of the*

IEEE, vol. 104, no. 3, pp. 530–543, Mar. 2016. DOI: 10.1109/JPROC.2016. 2515842.

[85] P. M. Peterson, N. I. Durlach, W. M. Rabinowitz, and P. M. Zurek, "Multimicrophone adaptive beamforming for interference reduction in hearing aids.," eng, *Journal of rehabilitation research and development*, vol. 24, pp. 103–10, 4 Fall 1987.

[86] B. Isom, R. Palmer, R. Kelley, J. Meier, D. Bodine, M. Yeary, B.-L. Cheong, Y. Zhang, T.-Y. Yu, and M. I. Biggerstaff, "The Atmospheric Imaging Radar: Simultaneous Volumetric Observations Using a Phased Array Weather Radar," *Journal of Atmospheric and Oceanic Technology*, vol. 30, no. 4, pp. 655–675, Apr. 2013. DOI: 10.1175/JTECH-D-12-00063.1.

[87] C. D. Curtis, M. Yeary, and J. L. Lake, "Adaptive nullforming to mitigate ground clutter on the national weather radar testbed phased array radar," *IEEE Transactions on Geoscience and Remote Sensing*, vol. 54, no. 3, pp. 1282–1291, Mar. 2016. DOI: 10.1109/TGRS.2015.2477300.

[88] F. Nai, S. M. Torres, and R. D. Palmer, "Adaptive beamspace processing for phased-array weather radars," *IEEE Transactions on Geoscience and Remote Sensing*, vol. 54, no. 10, pp. 5688–5698, Oct. 2016. DOI: 10.1109/ TGRS.2016.2570138.

[89] R. J. Mailloux, *Phased array antenna handbook*. Artech house, 2017.

[90] S. M. Torres and D. Schvartzman, "A Simulation Framework to Support the Design and Evaluation of Adaptive Scanning for Phased-Array Weather Radars," *Journal of Atmospheric and Oceanic Technology*, 2020.

[91] P. L. Heinselman, D. L. Priegnitz, K. L. Manross, T. M. Smith, and R. W. Adams, "Rapid sampling of severe storms by the National Weather Radar Testbed phased-array radar," *Wea. Forecasting*, vol. 23, pp. 808–824, 2008.

[92] K. A. Bowden, P. L. Heinselman, D. M. Kingfield, and R. P. Thomas, "Impacts of phased array radar data on forecaster performance during severe hail and wind events," *Weather and Forecasting*, no. 2015, 2015.

[93] P. L. Heinselman, D. S. LaDue, and H. Lazrus, "Exploring impacts of rapid-scan radar data on nws warning decisions," *Weather and Forecasting*, vol. 27, no. 4, pp. 1031–1044, 2012.

[94] J. N. Chrisman, "Automated volume scan evaluation and termination (avset)," in *34th Conference on Radar Meteorology*, 2009.

[95] D. McLaughlin, D. Pepyne, V. Chandrasekar, B. Philips, J. Kurose, M. Zink, K. Droegemeier, S. Cruz-Pol, F. Junyent, J. Brotzge, D. Westbrook, N. Bharadwaj, Y. Wang, E. Lyons, K. Hondl, Y. Liu, E. Knapp, M. Xue, A. Hopf, K. Kloesel, A. DeFonzo, P. Kollias, K. Brewster, R. Contreras, B. Dolan, T. Djaferis, E. Insanic, S. Frasier, and F. Carr, "Short-Wavelength Technology and the Potential For Distributed Networks of Small Radar Systems," *Bulletin of the American Meteorological Society*, vol. 90, no. 12, pp. 1797–1818, Dec. 2009. DOI: 10.1175/2009BAMS2507.1.

[96] D. Schvartzman, S. Torres, and T.-Y. Yu, "Weather Radar Spatiotemporal Saliency: A First Look at an Information Theory–Based Human Attention Model Adapted to Reflectivity Images," *Journal of Atmospheric and Oceanic Technology*, vol. 34, no. 1, pp. 137–152, Jan. 2017. DOI: 10.1175/JTECH-D-16-0092.1.

[97] D. S. Zrnic and R. J. Doviak, "Effective antenna pattern of scanning radars," *IEEE Transactions on Aerospace and Electronic Systems*, vol. AES-12, no. 5, pp. 551–555, Sep. 1976. DOI: 10.1109/TAES.1976.308254.

[98] R. A. Brown, L. R. Lemon, and D. W. Burgess, "Tornado Detection by Pulsed Doppler Radar," *Monthly Weather Review*, vol. 106, no. 1, pp. 29–38, Jan. 1978. DOI: $10.1175/1520\text{-}0493(1978)106\langle0029\text{:TDBPDR}\rangle2.0.$ CO;2.

[99] R. A. Brown and V. T. Wood, "Simulated Vortex Detection Using a Four-Face Phased-Array Doppler Radar," *Weather and Forecasting*, vol. 27, no. 6, pp. 1598–1603, Dec. 2012. DOI: 10.1175/WAF-D-12-00059.1.

[100] V. Kluckers, "Beam-shaping with active phased array radars," in *2008 International Conference on Radar*, Sep. 2008, pp. 177–182. DOI: 10.1109/RADAR.2008.4653913.

[101] H. L. Van Trees, *Optimum array processing: Part IV of detection, estimation, and modulation theory*. John Wiley & Sons, 2004.

[102] F. Nai, "On the potential of adaptive beamforming for phased-array weather radar," Ph.D. dissertation, 2017.

[103] M. Weber, J. Cho, J. Flavin, J. Herd, and M. Vai, "Multi-function phased array radar for us civil-sector surveillance needs," in *32nd Conf. on Radar Meteorology, Albuquerque, New Mex., 24–29 Oct*, 2005.

[104] D. Schvartzman and S. M. Torres, "Distributed beams: A technique to reduce the scan time of an active rotating phased array radar system," in *100th American Meteorological Society Annual Meeting*, AMS, 2020.

[105] F. M. Handbook, "Doppler radar meteorological observations, part c, wsr-88d products and algorithms," Office of the Federal Coordinator for Meteorology, Tech. Rep., 1991.

[106] J. C. Kirk, "Motion compensation for synthetic aperture radar," *IEEE Transactions on Aerospace and Electronic Systems*, vol. AES-11, no. 3, pp. 338–348, May 1975. DOI: 10.1109/TAES.1975.308083.

[107] D. C. Law, S. A. McLaughlin, M. J. Post, B. L. Weber, D. C. Welsh, D. E. Wolfe, and D. A. Merritt, "An Electronically Stabilized Phased Array System for Shipborne Atmospheric Wind Profiling," *Journal of Atmospheric and Oceanic Technology*, vol. 19, no. 6, pp. 924–933, Jun. 2002. DOI: 10. 1175/1520-0426(2002)019⟨0924:AESPAS⟩2.0.CO;2.

[108] I. R. Ivić, "An Approach to Simulate the Effects of Antenna Patterns on Polarimetric Variable Estimates," *Journal of Atmospheric and Oceanic Technology*, vol. 34, no. 9, pp. 1907–1934, Sep. 2017. DOI: 10.1175/JTECH-D-17-0015.1.

[109] M. Galletti and D. S. Zrnic, "Bias in copolar correlation coefficient caused by antenna radiation patterns," *IEEE Transactions on Geoscience and Remote Sensing*, vol. 49, no. 6, pp. 2274–2280, Jun. 2011. DOI: 10.1109/TGRS.2010.2095019.

[110] R. C. Hansen, *Phased array antennas*. John Wiley & Sons, 2009, vol. 213.

[111] C. Miller, "Minimizing the effects of phase quantization errors in an electronically scanned array," in *Proc. 1964 Symp. Electronically Scanned Phased Arrays and Applications*, vol. 1, 1964, pp. 17–38.

[112] K. Carver, W. Cooper, and W. Stutzman, "Beam-pointing errors of planar-phased arrays," *IEEE Transactions on Antennas and Propagation*, vol. 21, no. 2, pp. 199–202, Mar. 1973. DOI: 10.1109/TAP.1973.1140434.

[113] M. I. Skolnik, *Radar handbook*. McGraw-Hill Professional, 2008.

[114] M. C. Leifer, V. Chandrasekar, and E. Perl, "Dual polarized array approaches for mpar air traffic and weather radar applications," in *2013 IEEE International Symposium on Phased Array Systems and Technology*, Oct. 2013, pp. 485–489. DOI: 10.1109/ARRAY.2013.6731876.

[115] G. C. Brown, J. C. Kerce, and M. A. Mitchell, "Extreme beam broadening using phase only pattern synthesis," in *Fourth IEEE Workshop on Sensor Array and Multichannel Processing, 2006.*, Jul. 2006, pp. 36–39. DOI: 10.1109/SAM.2006.1706079.

[116] R. G. Frehlich and M. J. Yadlowsky, "Performance of Mean-Frequency Estimators for Doppler Radar and Lidar," *Journal of Atmospheric and Oceanic Technology*, vol. 11, no. 5, pp. 1217–1230, Oct. 1994. DOI: 10.1175/1520-0426(1994)011⟨1217:POMFEF⟩2.0.CO;2.

[117] A. Mancini, R. M. Lebrón, and J. L. Salazar, "The impact of a wet s -band radome on dual-polarized phased-array radar system performance," *IEEE Transactions on Antennas and Propagation*, vol. 67, no. 1, pp. 207–220, Jan. 2019. DOI: 10.1109/TAP.2018.2876733.

[118] W. H. Heiss, D. L. McGrew, and D. Sirmans, "Nexrad: Next generation weather radar (wsr-88d)," *Microwave Journal*, vol. 33, no. 1, pp. 79–89, 1990.

[119] NOAA, "Federal meteorological handbook no. 11: Doppler radar meteorological observations, part d: Wsr-88d unit description and operational applications." Tech. Rep., 2006.

[120] S. M. Torres, C. D. Curtis, E. Forren, S. Gregg, I. R. Ivic, J. R. Mendoza, D. Schvartzman, C. Schwarz, D. Wasielewski, and A. Zahrai, "An update on the advanced technology demonstrator at the national severe storms laboratory," in *100th American Meteorological Society Annual Meeting*, AMS, 2020.

[121] V. M. Melnikov, R. J. Doviak, and D. S. Zrnić, "A method to increase the scanning rate of phased-array weather radar," *IEEE Transactions on Geoscience and Remote Sensing*, vol. 53, no. 10, pp. 5634–5643, Oct. 2015. DOI: 10.1109/TGRS.2015.2426704.

[122] H. Pruppacher and J. Klett, "Microstructure of atmospheric clouds and precipitation," in *Microphysics of Clouds and Precipitation*. Dordrecht: Springer Netherlands, 2010, pp. 10–73. DOI: 10.1007/978-0-306-48100-0_2.

[123] D. S. Zrnić and A. Ryzhkov, "Advantages of Rain Measurements Using Specific Differential Phase," *Journal of Atmospheric and Oceanic Technology*, vol. 13, no. 2, pp. 454–464, Apr. 1996. DOI: 10.1175/1520-0426(1996) 013⟨0454:AORMUS⟩2.0.CO;2.

[124] A. Ryzhkov and D. Zrnić, "Assessment of Rainfall Measurement That Uses Specific Differential Phase," *Journal of Applied Meteorology*, vol. 35, no. 11, pp. 2080–2090, Nov. 1996. DOI: 10.1175/1520-0450(1996) 035⟨2080:AORMTU⟩2.0.CO;2.

[125] A. V. Ryzhkov and D. S. Zrnic, "Discrimination between Rain and Snow with a Polarimetric Radar," *Journal of Applied Meteorology*, vol. 37, no. 10, pp. 1228–1240, Oct. 1998. DOI: 10.1175/1520-0450(1998)037⟨1228: DBRASW⟩2.0.CO;2.

[126] D. S. Zrnić, V. N. Bringi, N. Balakrishnan, K. Aydin, V. Chandrasekar, and J. Hubbert, "Polarimetric Measurements in a Severe Hailstorm," *Monthly Weather Review*, vol. 121, no. 8, pp. 2223–2238, Aug. 1993. DOI: 10.1175/ 1520-0493(1993)121⟨2223:PMIASH⟩2.0.CO;2.

[127] D. S. Zrnić, T. D. Keenan, L. D. Carey, and P. May, "Sensitivity Analysis of Polarimetric Variables at a 5-cm Wavelength in Rain," *Journal of Applied*

Meteorology, vol. 39, no. 9, pp. 1514–1526, Sep. 2000. DOI: 10.1175/1520-0450(2000)039⟨1514:SAOPVA⟩2.0.CO;2.

[128] R. C. Gonzalez, R. E. Woods, and S. L. Eddins, *Digital image processing using MATLAB*. Pearson Education India, 2004.

[129] I. R. Ivić, "On the Use of a Radial-Based Noise Power Estimation Technique to Improve Estimates of the Correlation Coefficient on Dual-Polarization Weather Radars," *Journal of Atmospheric and Oceanic Technology*, vol. 31, no. 9, pp. 1867–1880, Sep. 2014. DOI: 10.1175/JTECH-D-14-00052.1.

[130] C. D. Curtis and S. M. Torres, "Adaptive Range Oversampling to Achieve Faster Scanning on the National Weather Radar Testbed Phased-Array Radar," *Journal of Atmospheric and Oceanic Technology*, vol. 28, no. 12, pp. 1581–1597, Dec. 2011. DOI: 10.1175/JTECH-D-10-05042.1.

[131] M. E. Weber, V. Melnikov, D. Zrnić, K. Hondl, R. Zellner, and B. Hudson, "Experimental Validation of the Multibeam Technique for Rapid-Scan, Meteorological Phased-Array Radar," in *100th American Meteorological Society Annual Meeting*, AMS, 2020.

[132] C. Fulton, M. Yeary, D. Thompson, J. Lake, and A. Mitchell, "Digital phased arrays: Challenges and opportunities," *Proceedings of the IEEE*, vol. 104, no. 3, pp. 487–503, Mar. 2016. DOI: 10.1109/JPROC.2015.2501804.

[133]   M. Yeary, R. Palmer, C. Fulton, J. Salazar, and H. Sigmarsson, "Recent advances on an s-band all-digital mobile phased array radar," in *2019 IEEE International Symposium on Phased Array System Technology (PAST)*, Oct. 2019, pp. 1–5. DOI: 10.1109/PAST43306.2019.9020988.

Appendix A

Acronyms

4F-PAR Four-faced Phased Array Radar

ADAPTS Adaptive Digital Signal Processing Algorithm for PAR Timely Scans

AHV Alternate transmission of horizontal and vertical polarizations

AIR Atmospheric Imaging Radar

ATD Advanced Technology Demonstrator

AVSET Automated Volume Scan Evaluation and Termination Automated Volume Scan Evaluation and Termination

BMCS Broadside Motion-Compensated Steering

BMX Beam MultipleXing

CD Continuous Doppler

CIMMS Cooperative Institute for Mesoscale Meteorological Studies

CONOPS Concept of Operations

CPI Coherent Processing Interval

CPPAR Cylindrical Polarimetric Phased Array Radar

CS Continuous Surveillance

DB Distributed Beams

FAA Federal Aviation Administration

FB-MCS Forward-looking and Back-scanning MCS

FBT Forward-looking and Back-scanning Technique

H Horizontal

HPBW Half-Power Beamwidth

HSE Hybrid-Scan Estimators

IOC Initial Operating Capabilities

MBT Multi-Beam Technique

MCS Motion-Compensated Steering

MIT-LL Massachusetts Institute of Technology-Lincoln Laboratory

MPAR Multi-Function Phased Array Radar

NEXRAD Next-Generation Radar

NOAA National Oceanic and Atmospheric Administration

NSSL National Severe Storms Laboratory

NWRT National Weather Radar Testbed

NWS National Weather Service

PAR Phased Array Radar

PPI Plane-Position Indicator

PRT Pulse Repetition Time

PSL Peak Sidelobe Level

QSHV Quasi Simultaneous transmission of Horizontal and Vertical polarizations

RFR Radar Functional Requirements

RPAR Rotating Phased Array Radar

RR Rotating-reflector Radar

SD Standard Deviation

SNR Signal-to-Noise Ratio

SENSR Spectrum Efficient National Surveillance Radar

SHV Simultaneous transmission of Horizontal and Vertical polarizations

V Vertical

VCP Volume Coverage Pattern

WSR-88D Weather Surveillance Radar - 1988 Doppler

Appendix B

General earth-relative MCS Pointing Angles

To account for antenna tilt on the calculation of MCS steering angles, it is first noted that each location ϕ, θ, r in spherical coordinates can be expressed in the Cartesian system as

$$x = r \sin \theta \cos \phi \quad y = r \sin \theta \sin \phi \quad z = r \cos \theta \tag{B.1}$$

If the antenna is tilted by θ_T, each location with coordinates (x, y, z) in the Cartesian coordinate system referenced to the ground has the corresponding location (x_A, y_A, z_A) in the Cartesian system referenced to the antenna. Given ϕ, θ, r, the location (x_A, y_A, z_A) can be found using the rotation matrix as

$$\begin{bmatrix} x_A \\ y_A \\ z_A \end{bmatrix} = \begin{bmatrix} \cos \theta_T & 0 & \sin \theta_T \\ 0 & 1 & 0 \\ -\sin \theta_T & 0 & \cos \theta_T \end{bmatrix} \begin{bmatrix} x \\ y \\ z \end{bmatrix} =$$

$$\begin{bmatrix} r \sin \theta \cos \phi \cos \theta_T + r \cos \theta \sin \theta_T \\ r \sin \theta \sin \phi \\ -r \sin \theta \cos \phi \sin \theta_T + r \cos \theta \cos \theta_T \end{bmatrix} . \tag{B.2}$$

Then, each location ϕ, θ in spherical coordinates tied to the ground has the corresponding location ϕ^A, θ^A in spherical coordinates referenced to the antenna as

$$\phi^A = \arctan\left(\frac{y_A}{x_A}\right) =$$
$$\arctan\left(\frac{\sin\theta\sin\phi}{\sin\theta\cos\phi\cos\theta_T + \cos\theta\sin\theta_T}\right).$$
$$\theta^A = \arccos\left(\frac{z_A}{\sqrt{x_A^2 + y_A^2 + z_A^2}}\right) =$$
$$\arccos\left(-\sin\theta\cos\phi\sin\theta_T + \cos\theta\cos\theta_T\right).$$

(B.3)

Thus, if desired scan angle is at ϕ_0, θ_0 (in the spherical coordinates referenced to the ground) the commanded location to which the tilted array must steer the beam, to point at ϕ_0, θ_0, is found using B.3. Following the same rationale, each location ϕ^A, θ^A in spherical coordinates referenced to the antenna has the corresponding location ϕ, θ in spherical coordinates tied to the ground as

$$\phi = \arctan\left(\frac{\sin\theta^A\sin\phi^A}{\sin\theta^A\cos\phi^A\cos\theta_T^A - \cos\theta^A\sin\theta_T}\right)$$
$$\theta = \arccos\left(\sin\theta^A\cos\phi^A\sin\theta_T + \cos\theta_A\cos\theta_T\right).$$

(B.4)